Title
Deformation Mechanisms of Gum Metals Under Nanoindentation

Author
Sankaran, Rohini

Publication Date
2015

Peer reviewed|Thesis/dissertation

Deformation Mechanisms of Gum Metals Under Nanoindentation

By

Rohini Priya Sankaran

A dissertation submitted in partial satisfaction of the

requirements for the degree of

Doctor of Philosophy

in

Engineering - Materials Science and Engineering

in the

Graduate Division

of the

University of California, Berkeley

Committee in charge:

Professor J. W. Morris, Jr., Co-Chair
Professor Andrew M. Minor, Co-Chair
Professor Sanjay Govindjee

Summer 2015

Deformation Mechanisms of Gum Metals Under Nanoindentation

by

Rohini Priya Sankaran

Abstract

Deformation Mechanisms of Gum Metals Under Nanoindentation

by

Rohini Priya Sankaran

Doctor of Philosophy in Engineering - Materials Science and Engineering

University of California, Berkeley

Professor J. W. Morris, Jr., Co-Chair

Professor Andrew M. Minor, Co-Chair

Gum Metal is a set of multi-component β-Ti alloys designed and developed by Toyota Central R&D Labs in 2003 to have a nearly zero shear modulus in the <111> direction. After significant amounts of cold-work (>90%), these alloys were found to have yield strengths at a significant fraction of the predicted ideal strengths and exhibited very little work hardening. It has been speculated that this mechanical behavior may be realized through an ideal shear mechanism as opposed to conventional plastic deformation mechanisms, such as slip, and that such a mechanism may be realized through a defect structure termed "nanodisturbance". It is furthermore theorized that for near ideal strength to be attained, dislocations need to be pinned at sufficiently high stresses. It is the search for these defects and pinning points that motivates the present study. However, the mechanism of plastic deformation and the true origin of specific defect structures unique to gum metals is still controversial, mainly due to the complexity of the β-Ti alloy system and the heavily distorted lattice exhibited in cold worked gum metals, rendering interpretation of images difficult.

Accordingly, the first aim of this study is to clarify the starting as-received microstructures of gum metal alloys through conventional transmission electron microscopy (TEM) and aberration-corrected high resolution scanning transmission electron microscopy with high-angle annular dark field detector (HAADF-HRSTEM) imaging. To elucidate the effects of β-stability and starting microstructure on the deformation behavior of gum metals and thus to provide adequate context for potentially novel deformation structures, we investigate three alloy conditions: gum metal that has undergone solution heat treatment (STGM), gum metal that has been heavily cold worked (CWGM), and a solution treated alloy of nominal gum metal composition, but leaner in β-stabilizing content (ST Ref-1). In order to directly relate observed defect structures to applied loading, we perform *ex-situ* nanoindentation. Nanoindentation is a convenient method as the plastic deformation is localized and probes a nominally defect free volume of the material. We subsequently characterize the defect structures in these alloys with both conventional TEM and

advanced techniques such as HAADF HRSTEM and nanoprobe diffraction. These advanced techniques allow for a more thorough understanding of the observed deformation features.

The main findings from this investigation are as follows. As expected we observe that a non-equilibrium phase, ω, is present in the leaner β-stabilized alloy, ST Ref-1. We do not find any direct evidence of secondary phases in STGM, and we find the α phase in CWGM, along with lath microstructure with subgrain structure consisting of dislocation cell networks. Upon nanoindentation, we find twinning accompanied by ω nucleation on the twin boundary in ST Ref-1 samples. This result is consistent with previous findings and is reasonable considering the alloy is unstable with respect to ω transformation. We find deformation nanotwinning in cold worked gum metals under nanoindentation, which is initially surprising. We argue that when viewed as a nanocrystalline material, such a deformation mechanism is consistent with previous work, and furthermore, a deformation nanotwinned structure does not preclude an ideal shear mechanism from operating in the alloy. Lastly, we observe continuous lattice rotations in STGM under nanoindentation via nanoprobe diffraction. With this technique, for the first time we can demonstrate that the lattice rotations are truly continuous at the nanoscale. We can quantify this lattice rotation, and find that even though the rotation is large, it may be mediated by a reasonable geometrically necessary dislocation density, and note that similar rotations are typically observed in other materials under nanoindentation. HRSTEM and conventional TEM data confirm the presence of dislocations in regions that have sustained large lattice rotations. Finally, we report on the nature of indirectly observed "pinning points" in STGM under nanoindentation that was reported in a previous study. We find through ADF/HAADF STEM that the "pinning points" which cause dislocation bowing in STGM under nanoindentation are actually other dislocations with the line direction normal to the TEM foil, and, in support of this finding, we also observe other in-plane dislocation-dislocation interactions that is responsible for resultant bowing. We observe no direct evidence of any secondary phases, twinning, or nanodisturbances in the STGM case, and the majority of deformation features can be explained by conventional slip mechanism. However, it remains a possibility that an ideal shear mechanism may be accompanying conventional slip in STGMs that may account for the truly continuous nature of the lattice rotations.

To my parents Drs. K. K. Sankaran and D. V. Sankaran

and my sister Ranjani Sankaran

Acknowledgements

There are many people to thank for the work included in this manuscript.

I would like to acknowledge my fellow graduate students in the Department of Materials Science and Engineering at UC Berkeley. As a whole group, their talents are manifold. Through classes, study sessions, and simple informal conversation, I have learned something from each student regarding how to be a better scientist, and I also wish to express my gratitude for their friendship. I have also learned the finer points of experimental science through observing my fellow colleagues in the Minor and Morris groups. I am grateful for the friendship, guidance, and sympathetic ears of former elder graduate students Dr. Matt Lowry and Dr. Christopher Kinney, and my good friend and colleague, Julian Sabisch. I have also been greatly inspired by the experimental work of Prof. Qian Yu and Claire Chisholm.

I am most appreciative of the classes I took with Prof. Komvopolous of the Mechanical Engineering Department and Prof. Govindjee of Civil Engineering. Their deformation behavior and continuum mechanics classes are among the best two classes I have ever taken in all my years of being a student: the clarity with which they taught, the generosity of time and patience with students, and the clever and thoughtful problems they assigned were excellent and cemented my understanding of solid mechanics. I also want to think Prof. K for serving on my qualifying exam committee, and Prof. Govindjee for collaborating with me regarding the nanoindentation experiment through simulations, our extremely thoughtful discussions, and for serving on my dissertation committee.

I am very grateful for the funding I have received from my advisor Prof. J. W. Morris, Jr. and thank him for the opportunity to research the ever-enigmatic Gum Metal alloy system. I am grateful to my co-advisor Prof. Andrew M. Minor for his scientific guidance, invaluable experimental planning, and genuine moral support as I went through the Ph.D. program. I also want to thank LBL and the technical staff at NCEM for supporting my experiments. Specifically I would like to thank Dr. Karen Bustillo, Dr. Peter Ercius, Dr. Jim Ciston, Dr. Alpha N'Diaye, and Dr. Mary Scott for their generous technical help and advice while working at NCEM. I am also very lucky to have been trained by and to collaborate with former NCEM scientist Prof. Velimir "Mimo" Radmilovic. Mimo always congratulated me for even the smallest of successes with respect to TEM sample preparation and atomic resolution imaging, and his ever-positive attitude helped me get through the tougher days during my time here. I am also grateful to Prof. Oscar Dubon for funding my last two semesters in which I dedicated my time to analysis and dissertation writing, and Ms. Meltem Erol for helping coordinate this dissertation funding.

I am indebted to my collaborators and mentors, who I refer to as "the post-Docs" (although they are no longer post-docs now). The work presented here was facilitated by the unfailing help, support, and encouragement of Dr. Burak Ozdol, Dr. Christoph Gammer, Dr. Colin Ophus, and Prof. Josh Kacher. Dr. Gammer's nanoprobe diffraction routine for the TitanX directly facilitated the acquisition of Orientation Image Maps of Gum Metal under Nanoindentation presented here. I am, again, indebted to Burak and Colin, who were

instrumental in helping me organize my thoughts for determining the origin of contrast in HRSTEM from embedded precipitates in gum metals. I thank Josh and Burak for their scientific guidance, friendship, and sense of humor. I sincerely thank Colin for guiding me through the world of MATLAB coding and simulations: skills, which will undoubtedly serve me well for the rest of my life. The most rewarding time during my tenure at Berkeley was being able learn from, discuss ideas, and work as a team with this group of scientists.

I would like to thank my closest friends who have in one way or another helped and supported me through these last few years with their genuine friendship, which I hope will endure for many years to come: Dr. John Heron, Kevin Wang, Ravi Singh, Urusa Alaan, Julian Sabisch and Mary Clare Masters, M.D. Finally, special thanks to Edward Cassidy Clark for your unwavering support and constructive advice always.

And, of course, my sincerest gratitude to my parents K. K. Sankaran and D. V. Sankaran and my sister Ranjani Sankaran for helping me attain this goal with their unconditional love and support. Thank you, Dad, for introducing me to field of Materials Science and Engineering, even though I found out later on you had originally wanted to be a geologist! And thank you again, Mom and Dad, for communicating to me in different ways that if someone has a will and puts in hard work, they can accomplish anything. It is this simple belief that I can understand anything if I put in the effort that has enabled me come this far in my academic career.

My hope is to make my family proud by contributing something of value to humanity. My papers and this manuscript are but humble steps towards this end.

1 Introduction

Titanium alloys possess a good combination of low density, superior corrosion resistance and biocompatibility and are thus attractive materials for structural applications in aerospace, automotive, and biomedical implant industries. Through thoughtful alloying and processing, a variety of titanium alloys with a range of microstructures and properties suitable for these industries has been developed. In particular, beta (β) – stabilized Ti-Nb alloys have attracted attention in recent years because of their low elastic moduli, biocompatibility, superelasticity, and shape-memory behavior [1,2,3]. Among the most actively researched of this family of alloys is the "Gum Metal" alloy that was developed by Toyota R&D over ten years ago [4]. This alloy set is distinguished by its low shear modulus in the <111>β direction, high yield strength, and unusual deformation behavior and accompanying defect structures. When mechanically tested in the severely cold worked condition, this alloy exhibits a shear strength that seemed to approach the ideal value at elastic instability ($0.11G_{<111>}$)[5] given the calculated elastic constants available at the time [6,7]. Experimental images of the microstructures of the deformed alloys seemed to support the notion that an ideal shear mechanism was operating during plastic deformation, most notably via giant fault formation and atomic–scale "nanodisturbances" [4,8,9].

Significant research has been underway in recent years to elucidate these proposed mechanisms of plastic deformation in Gum Metals. The difficulty of characterizing the microstructures of gum metal in the cold worked condition has precluded a thorough and unambiguous understanding of the causes of its unusual mechanical behavior. The present study aims to understand the mechanisms of the deformation behavior by a thorough atomic scale characterization of the defect structure of gum metals deformed under nanoindentation.

It is well known that the deformation behavior of titanium alloys is influenced by the starting microstructure. In beta-stabilized Ti alloys in particular, phase transformations also occur as a result of deformation, which further complicates the interpretation of the experimental observations. To aid in the understanding of the results presented in this work, this chapter begins with a brief overview of the classification, metallurgy and deformation behavior of titanium alloys. This is followed by a brief discussion of the previously reported experimental observations and theoretical interpretations of the behavior of gum metal, thereby setting the context for the present investigation.

1.1 Physical Metallurgy of Titanium Alloys

Pure titanium occurs in two allotropic forms at atmospheric pressure – alpha, α (HCP), is stable until 882°C above which the beta, β (BCC), phase is stable. Titanium alloys are classified based on which phase is primarily stabilized by the alloying elements, which also determines the shape of the phase diagram. Technical multicomponent Ti alloys are typically classified by which phases are present at room temperature, an immediate description that is more relevant in an engineering context than indication of the form of the phase diagram. On this basis, titanium alloys are generally classified as α, α + β and β alloys, with further subdivisions, such as near-α, near-β, and metastable β depending on the

proximity of the composition to the α-β transus line, as outlined in Figure 1.1. α-alloys contain fully or predominantly the HCP phase and are alloyed with α-stabilizers or neutral elements. If some β-stabilizing elements are added but the alloy remains in the HCP phase, the alloy is referred to as near-α. α + β alloys have some combination of both the HCP and BCC phases. When enough β-stabilizing elements are added that the β-phase does not martensitically transform upon quenching to room temperature but still lies in the α + β field, the alloy is metastable-β. Referring to Figure 1.1, the composition for a metastable-β alloy would be to the right of the martensitic start line (Ms) at room temperature, but still in the two-phase field. Stable β alloys are those that lie in the β-field at room temperature [10].

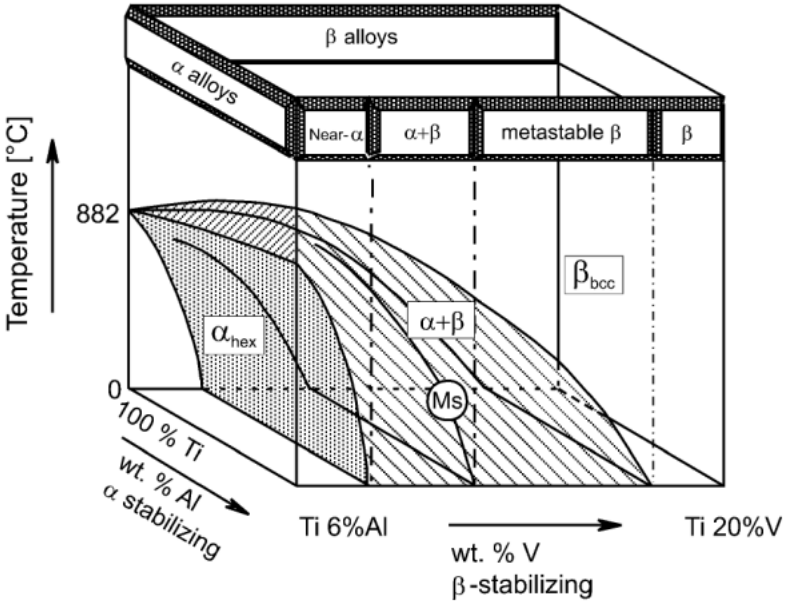

Figure 1.1: Classification scheme of technical multicomponent Titanium alloys based on which phases are present near room temperature, namely α, α + β, metastable β alloys, and β alloys. Gum Metal is considered a metastable β alloy. From Ref. [10]

β- stabilized alloys are classified as β-isomorphous or β-eutectoid systems. β-isomorphous systems are those in which the alloying element is completely soluble in the β phase over some arbitrary temperature range, typically about the allotropic transformation temperature of pure Ti, and has limited solubility in the α phase. A schematic pseudo-binary phase diagram for β-isomorphous Ti alloy is shown in Figure 1.2. Unlike β-eutectoid alloys, these systems do not form intermetallics from the eutectoidal decomposition of the β phase. Alloying elements that form β-isomorphous systems are typically Group 5 and Group 6 elements such as V, Nb, Ta, and Mo [11]. Figure 1.1, shown for Ti-V alloys, is a schematic of a phase diagram for β-isomorphous systems containing α-stabilizing elements, in this case Al.

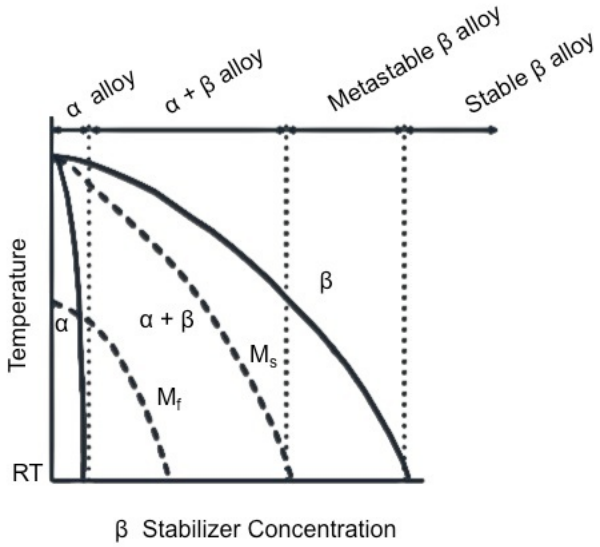

Figure 1.2: Schematic pseudo-binary β-isomorphous phase diagram

Gum Metal is considered a **technical multicomponent metastable-β alloy** since after solution heat treatment it is completely composed of the β phase at room temperature, but based upon the amount of Nb stabilizing content, it is presumably left of the β transus line. Its pseudo-binary phase diagram is thought to be similar to that for β-stabilized isomorphous alloy, schematically shown in Figure 1.2, as niobium (Nb) is the primary alloying addition. Thus the phase diagram of GM can also be most likely classified as **β-isomorphous**. Both these classification schemes are useful as a first step in understanding the Gum Metal alloy.

For the alloys of interest here, Gum Metal (GM) and its compositionally related alloys, the primary alloying addition is the β-isomorphous alloying element niobium (Nb). Table 1 gives the compositions of the main Gum Metal alloy and its compositionally related alloys, termed "Ref-1" and "Ref-3", as given by Toyota.

Table 1: Composition breakdown in weight (atomic) percent of Gum Metal and its related alloys as given by Toyota.

Weight Percent (atomic percent) of Alloying Elements in Gum Metals					
Alloy	Ti	Nb	Ta	Zr	O
Gum Metal	59.1 (73.5)	35.9 (23)	2 (.7)	2.7 (2.0)	.3 (1.2)
Ref-1	63.1 (76.6)	31.9 (20)	2 (.6)	2.7 (1.7)	.3 (1.1)
Ref-3	55.3 (70.4)	39.7 (26)	2 (.7)	2.7 (1.8)	.3 (1.1)

The phase diagram of GM would presumably look very similar to the phase diagram of a β-isomorphous system given that the main alloying element is the β-stabilizing element Nb. The Ti-Nb diagram is presented in Figure 1.3 [12] and can also be used as a schematic phase diagram and qualitative guide for understanding the phase stability of GM and its adjacent compositions.

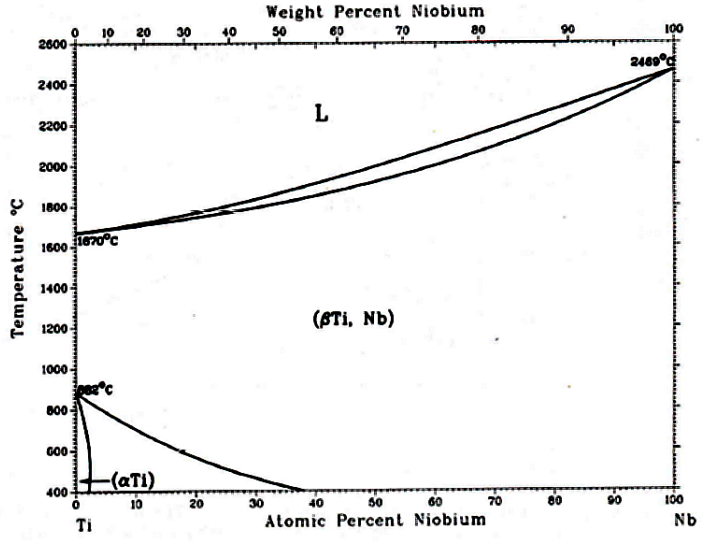

Figure 1.3: Experimentally derived phase diagram for binary alloy Ti-Nb from Ref. [12].

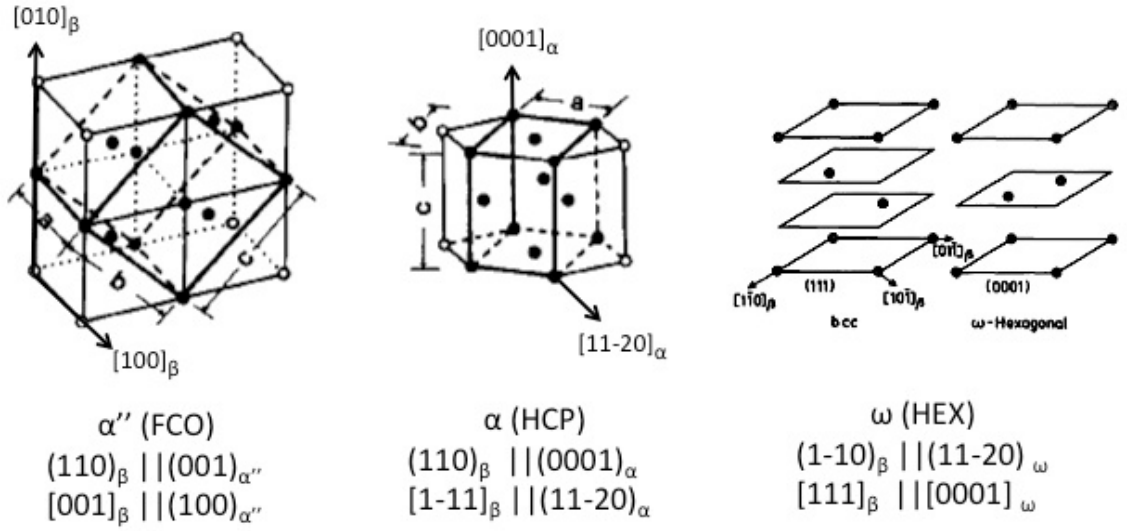

Figure 1.4: Orientation relationships of metastable phases in titanium alloys with respect to the parent BCC lattice. In the first two models, α-HCP and β-BCC phases are drawn with thin lines and open circles and the α'' - FCO phase is outlined with heavy lines and closed circles.

The most common non-equilibrium phases observed in β-Titanium alloys are the α' (HCP), ω (Hexagonal), and α'' (FCO) phases. The crystallography of these phases and its relationship to the parent β (BCC) unit cell is given in Figure 1.4 (adapted from [13] and [14]).

1.2 Deformation Mechanisms of β-Ti Alloys and Gum Metals

It is well known that the starting microstructure and phase stability of β-Ti alloys greatly influence the plastic deformation mechanism, and this will be a key concept in

understanding the results of this research. Typically alloys that are *unstable* with respect to martensitic transformation (that is, the quenched condition contains non-equilibrium phases) have previously been shown to deform via twinning or stress induced martensitic phases. As the β-stability increases with additional alloying content, the deformation mechanism has traditionally been observed to change to conventional slip [15]. If the microstructure contains non-equilibrium phases, these phases can either serve as obstacles to slip or as nucleation sites for other stress induced martensitic phases. This is the typical trend observed in β-Titanium alloys.

Gum Metals are unique in that they have been designed from first principles to have a particular composition and β-stabilizing content that places them seemingly on the boundary between these two regimes: it is not an unstable alloy in the quenched condition, but instead has been designed to practically be on the border of β-stability. It is well known that the β-stability of Ti alloys is correlated with the shear modulus [16] which in turn implies a functionally low ideal strength. When Gum Metals were initially tested, they indeed seemed to exhibit extraordinary properties including: 1) a lack of work hardening in both the tensile and Vickers hardness tests with increased cold work ratio, and 2) a yield strength that is a significant fraction of the calculated ideal strength. This lack of work hardening, and the initial notion that Gum Metals were deforming near or at ideal strength, coupled with defect structures in which the plastic deformation seemed very localized, led to the notion of a novel plastic deformation mechanism via idea shear that is mediated neither by dislocations nor by another conventional mechanism. Rather, this mechanism was hypothesized to be via "ideal shear." This can be described as two planes shearing past each other without the aid of a dislocation, and could be thought of as planar mechanical melting and subsequent recrystallization, where the only evidence left behind may be a line defect, similar to an edge dislocation. The atomic columns on either side of the sheared plane may not line up in registry following recrystallization, and the resultant lattice displacement is not necessarily an integral or rational fraction of the lattice parameter. Such a defect left behind has been termed a "nanodisturbance," and is claimed to have been directly observed in HRTEM images of heavily worked gum metals. It is noted that this is not the typical way to define "nanodisturbances", but it is probably a more instructive explanation than the typical definition ubiquitous in the literature: "dipoles of partial dislocations with non-quantized burgers vector" [9]. Another hypothesis that may explain the lack of work hardening and the relatively large yield stresses was the idea that any dislocations residing in gum metals must be pinned by particles at sufficiently high stresses. The bowing of dislocations in nanoindented solution treated gum metals was strong evidence that such pinning may be occurring. It is the search for these theorized defects and particles, and their relation to the plastic deformation in gum metals, that motivates the experiments performed in this study.

1.3 Motivation and Methods

In an effort to confirm the existence of these theorized "nanodisturbances" and pinning points, we image deformation structures of gum metals with both conventional TEM imaging and advanced characterization techniques that allow for direct observations of the atomic lattice. In particular, we use aberration-corrected HRSTEM imaging to probe the deformation structures of Gum Metals. Originally nanodisturbances were imaged through HRTEM. However, this technique is quite sensitive to defocus value, thickness and other parameters that result in contrast reversals rendering image interpretation difficult, especially of atomic resolution images of heavily deformed materials. It should be noted that it is common practice to interpret contrast in HRTEM (phase contrast) images as approximately indicative of the relationship between atomic columns. However, if knowledge of the exact atomic positions is required, direct interpretation of white contrast as atoms is typically discouraged without the aid of simulations or exit wave reconstruction. Thus, we use the HAADF-HRSTEM technique to image the deformed alloys at atomic resolution, where image intensity is typically proportional to Z^2. We do find in this study that it may, in certain instances, be more appropriate to regard HAADF images as indicative of projected atomic potential, but in general the interpretation of atomic resolution HAADF images is considerably more straightforward than phase contrast images.

Probing the deformation response via nanoindentation seemed prudent in that the plastic deformation happens within a very localized region. Thus, we can relate any deformation structures directly to the nanoindentation process. Furthermore, as we are trying to probe the material at its theoretical strength, nanoindentation is an attractive choice as it probes nominally defect free volumes, as directly demonstrated via *in-situ* testing [17].

1.4 Contents

This dissertation is divided into four main chapters:

- Chapter 2 contains a thorough microstructural and atomic-scale analysis of the as-received microstructures of the three alloys.
- Chapters 3, 4, and 5 concern solution treated–reference 1 (ST Ref-1) sample, cold worked gum metal (CWGM), and solution treated gum metal (STGM), respectively. These chapters present results and analysis of deformation structures and mechanical data related to the respective alloy under nanoindentation. From testing these alloys, we can determine the effect of β-stability and the effect of cold-work on the deformation mechanism. Sufficient background and context for each alloy is given in the individual chapters rather than in the introduction to explain the relevant deformation mechanism.

The general findings in Chapters 3 and 4 is that the observed defect structures of each alloy under nanoindentation is consistent with previous studies regarding the effect of β-stability and cold working on the plastic deformation mechanism of the respective alloy. In Chapter 5, in which we investigate STGMs, we find that the features observed under the nanoindent through nanoprobe diffraction are also consistent with features found in previous studies of materials deformed via nanoindentation. We find no direct evidence of

nanodisturbances in any of the observations, rather we do find direct evidence that indicates conventional slip is operating in gum metals. Furthermore, we determine that the pinning points responsible for dislocation bowing in STGMs under nanoindentation are from dislocations oriented normal to the TEM foil. We do note that defect structures observed do not necessarily rule out the possibility that ideal shear on a local scale is occurring in the gum metal alloys during plastic deformation. The results of this research will hopefully reveal the intrinsic complexity of deformation mechanisms operating in β-Titanium alloys that has understandably led to the ongoing controversy surrounding the plastic deformation mechanisms of Gum Metals.

2 Observation of microstructure and secondary phases in Gum Metals in as-received condition

2.1 Introduction

The starting microstructure in β-Ti alloys has a significant influence in their operating deformation mechanisms [18]. Thus, to determine and understand the deformation mechanisms operating in Gum Metals, a thorough analysis of the starting microstructure must be performed. Without this knowledge, it will be very difficult to try to explain the measured mechanical test data and the resultant deformation microstructures. Some of the important microstructural parameters relevant for analyzing the mechanical data obtained from *ex-situ* nanoindentation are the characteristics of the primary matrix phase including the morphology and texture/orientation distribution of the grains and the type and density of any pre-existing defects (e.g. dislocations) as well as the presence, type and morphology of secondary phases. This information is gleaned through various characterization and imaging methods, which in the current investigation include EBSD, conventional BF/DF TEM and HRTEM imaging, and more sophisticated TEM experiments including aberration-corrected HAADF HRSTEM. Where TEM images give ambiguous contrast, simulations can guide interpretation.

2.2 Materials and Methods

All material used in this investigation was supplied in the form of round bar specimens with the nominal compositions given in Table 1. The bars were fabricated by Toyota Central R&D Laboratories, Nagakute, Japan via powder processing according to the procedures discussed in reference [4]. Specifically, elemental powders are cold isostatically pressed into cylindrical form, sintered at 1300°C, hot forged at 1150°C, and solution-treated in Ar at 900°C. Severe cold work is imparted to Gum Metal via rotary swaging at room temperature by 90%, and is referred to as CWGM. Solution-treated Gum Metal (STGM) applies to the material that has been solution-treated in air for 30 minutes at 9008C after being severely cold-worked. In the latter case, the surface oxide is peeled off after solution-treatment.

Samples for both EBSD and TEM imaging were initially prepared in the same manner: samples were precision sawed perpendicular to the original swaging axis (unless otherwise specified) into discs of ~300μm thickness and disc cut to 3mm diameter. Samples were then mechanically ground to ~100μm thickness and polished to 4000grit with SiC paper.

To prepare samples for EBSD scanning, the remaining mechanical damage layer must be removed. To achieve this, one-sided jet polishing with a Fischione Model 1010 twin-jet polisher was performed. An electrolyte solution with nominal composition of 4.8 vol% perchloric acid, 28 vol% butanol, and 68 vol% methanol was used with jet polishing parameters of about -35 to -30°C at 30-45V for ~3min. A time limit is set to ensure that sample is not perforated as in regular jet polishing. One-sided electropolishing was performed prior to EBSD analysis to ensure a damage free surface for scanning than mechanical polishing can provide. This was achieved by covering one side of the sample

with non-adhesive Teflon® tape to prevent polishing action. Polish of the other side was avoided to enable mounting of the sample on an SEM stage. EBSD measurements were acquired on a Zeiss EVO SEM with 25kV beam voltage. For STRef-1, the scan was acquired with square grid at ~2.8μm step size, and for CWRef-3, the scan was acquired with hexagonal grid at ~1.1μm step size.

To prepare samples for TEM and HRTEM/HRSTEM imaging, after the mechanical polishing step was completed, the samples underwent conventional two-sided twin-jet polishing using the same equipment and similar parameters as used for electropolishing step, except that the sample was jet polished until perforation. All conventional TEM imaging was performed on a JEOL 3010 TEM at 300kV at LBNL-NCEM unless otherwise specified as performed on a JEOL 2011 TEM at 200kV (UC Berkeley, Dept. of MSE). HAADF-HRSTEM was performed on a modified FEI Titan with a CEOS probe aberration corrector at 300 kV with a probe size of ~0.5 Å and probe convergence semi-angle of 17.2 mrad. Specific HAADF inner collection angle was set to ~53 mrad and the other HAADF detection parameters are discussed further in Section 2.3.3.

2.3 Results

2.3.1 EBSD data: Grain morphology and <110> fiber texture

Electron Back Scatter Diffraction (EBSD) technique is well suited for microstructural analysis of metallurgical specimens and typically follows characterization by optical microscopy. In this technique, an electron probe in an SEM is rastered across the sample with the EBSD signal recorded by a detector at a 70° angle with respect to horizontal. The signal from a single probe position on a relatively damage-free surface will look similar to that in Figure 2.1b. To form the pattern, an initial incoherent scattering event must occur from electron beam-sample interaction. The resultant incoherently scattered electron, if travelling at a proper Bragg angle with respect to certain *hkl* planes, subsequently diffracts from this particular set of planes. The wavevector of the incoherently scattered electron can be any trajectory, but only those with a scattered wavevector that is inclined at a proper Bragg angle with respect to those *hkl* planes can diffract. The resultant possible diffraction paths form a cone with angle θ_{Bragg} with respect to *hkl* planes since the incoming incoherently scattered electrons can come in at a range of incident angles from the initial scattering event. The resultant cone of outgoing diffracted electron wavevectors is termed a Kossel cone, and for a given set of *hkl* planes, there are two cones (the other from diffraction off equivalent –*h*-*k*-*l* planes). The intersection of the cones on the EBSD detector forms the characteristic lines on the detector, called a "Kikuchi pattern", where the trace of the diffracting set of planes lies in the middle of the two lines. [19].

Figure 2.1 shows the resultant EBSD data for the ST Ref-1 sample. The electropolishing process preferentially etched the grain boundaries as observed in the secondary electron image (taken in the SEM) in Figure 2.1a and created a relatively flat surface with slight pitting. A typical Kikuchi pattern from the sample is of high quality and given in Figure 2.1b. Grain boundary map and Inverse Pole figure map in Figure 2.1c, d show that the sample is comprised of equiaxed grains 20-70 nanometers wide with an expected <110>$_\beta$ out-of-plane orientation.

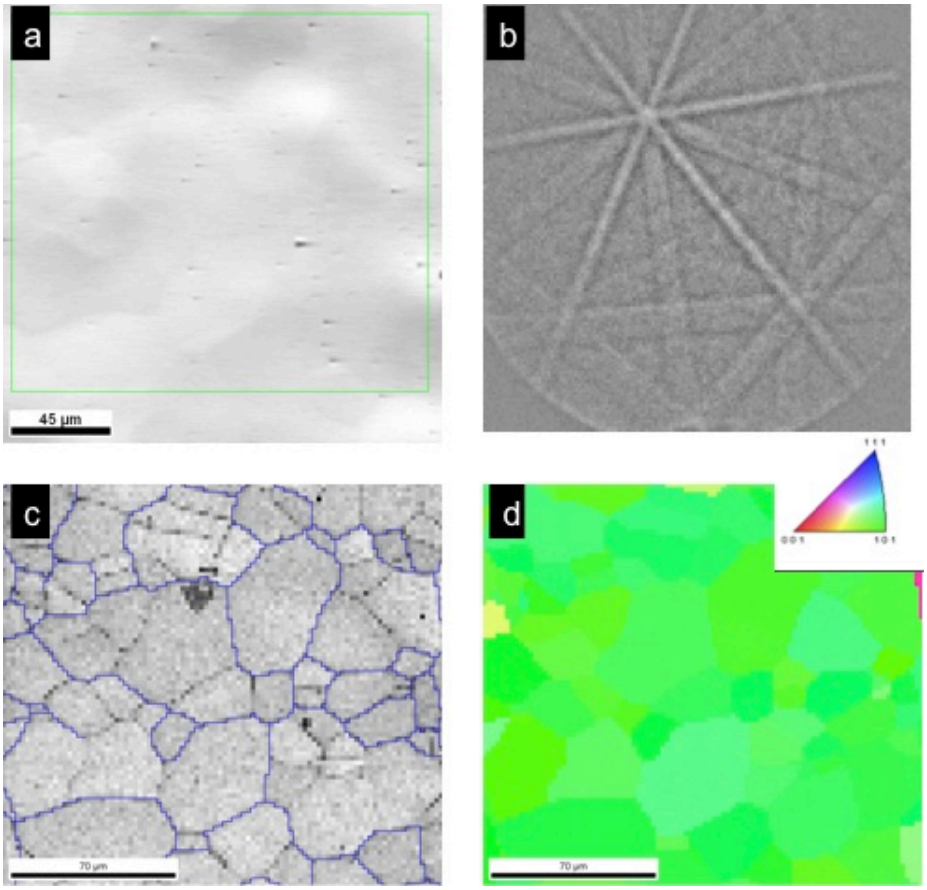

Figure 2.1: SEM and EBSD data for Ref-1 sample. 1a: SEM image of region to be scanned, 1b: typical Kikuchi map from sample 1c: Grain boundary map shows grains to be 20-70nm wide, 1d: Inverse pole figure map shows sample to have <110> fiber texture

The SEM imaging and EBSD data for the CW Ref-3 (higher Nb content than typical GMs) is provided in Figure 2.2. The SED image in Figure 2.2a shows an overview of the sample in which it appears relatively flat over the observed area. In Figure 2.2b, after the sample is tilted, it is clear that the sample surface is actually wavy. It is assumed that some preferential etching occurred at regions where the sample was under the highest stress from the swaging process, resulting in a wavy pattern characteristic of the underlying grain and defect structure.

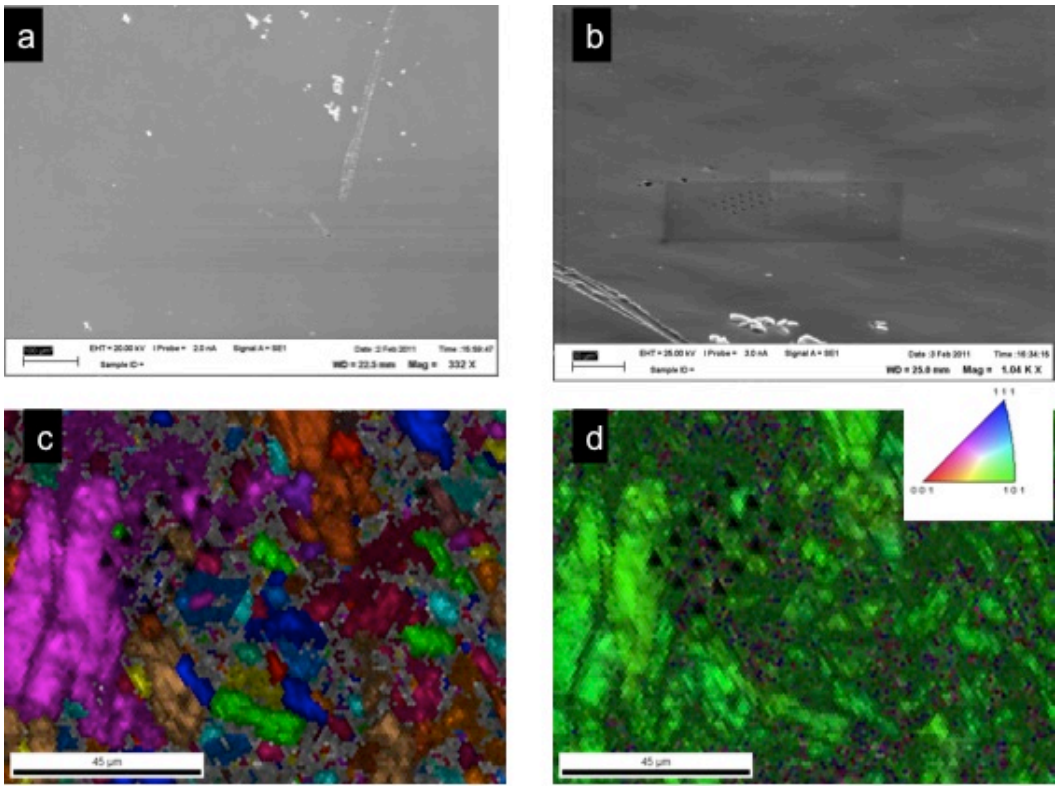

Figure 2.2: a) and b) SED images taken in SEM of the surface of the CWGM Ref-3. b) tilted sample shows surface waviness responsible for some regions of poor quality in the EBSD maps presented in c) and d). c) gives unique grain map showing complex cold worked grain structure and d) is inverse pole figure, where the sample is shown to have nominally <110> fiber texture.

It should be noted that the array of nanoindents that is pictured was present originally for the purpose of attempting to perform EBSD within these localized deformed regions. Unfortunately, the nanoindents are too steep to detect a strong EBSD signal. A better experiment to determine local orientation after localized indentation would be to perform a shallow, wide Vickers indent as opposed to nanoindentation.

Figure 2.2c and Figure 2.2d confirm that the sample has been heavily deformed. Figure 2.2c gives a unique grain map, showing the various sizes and shapes of the grains, and it is clear that some marbled texture is apparent, which is consistent with the results included in Refs. [4,20]. Figure 2.2d is the inverse pole figure map for the out-of-plane orientation and demonstrates that a <110>-fiber texture results from the swaging process. It should be pointed out that the STGMs used in this investigation undergo the solution anneal treatment after the swaging process. The lack of data from certain regions of the scanned area, denoted by gray coloring, is due to the large amount of deformation sustained by the sample that makes it difficult to produce a perfectly flat specimen for EBSD scanning from the electropolish method. Variations of the surface normal due to uneven surface change the effective angle of incidence on the specimen, which is tilted to ~70°. If variation in

height is too much, some areas do not exhibit diffraction patterns, while other areas will give distorted patterns for which the orientation software will provide a poor match based on the lowered quality of the Kikuchi bands [21].

The observed grain sizes, recrystallized and marbled grain morphologies, and nominally <110>-fiber texture are consistent with the many optical microscopy and EBSD studies conducted on Gum Metals [4,22,23,24]. While the samples scanned are not of "on-composition" Gum Metals and differ by having slightly less or more niobium content, the resulting microstructures are very similar to their Gum Metal counterparts. This similarity is apparent in the optical microscopy study by Furuta et al. [24], in which microstructural studies are performed on ST and CW specimens with slightly varying amounts of niobium (30, 32, 34, 36wt%), where the standard amount for Gum Metal is 36wt% and the rest of the alloying additions are equivalent. In this study, the authors in Ref [24] observe for all samples a drastic change from "marble-like" texture with filamentary grains to recrystallized microstructure upon solution heat treatment, and the microstructures across samples is very similar. Thus, we can take the EBSD data from Figure 2.1and Figure 2.2 as representative of the initial microstructure of all ST samples and CW samples.

2.3.2 Conventional TEM data: Observing secondary phases and sub-grain structures

2.3.2.1 ST Ref-1: (Possible) ω_{ath} phase

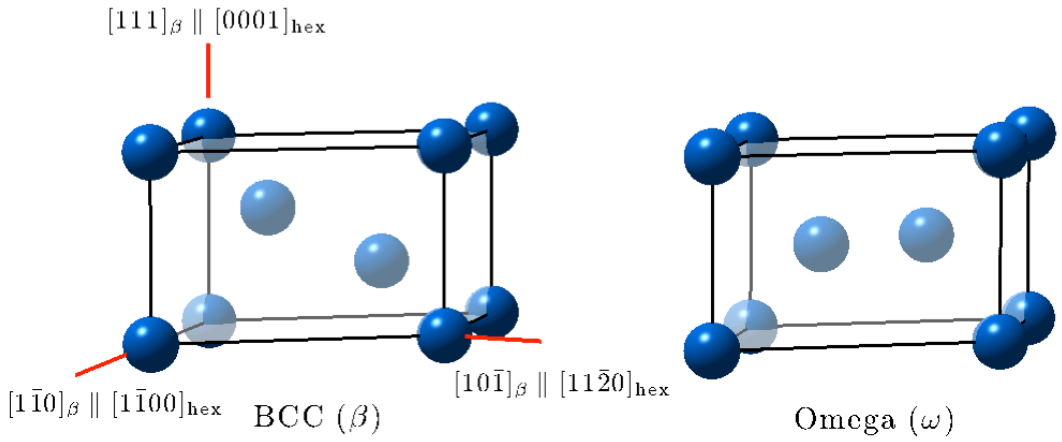

Figure 2.3: Crystallographic relationship between BCC (**β**) and Omega phase (ω) is {111}β || (0001)ω; <10-1> β|| <11-20>ω. The ω phase shown is ideal hexagonal structure. The formation of ω_{ath} phase is thought to involve shuffle of atoms via collapse of consecutive pairs of {111}**β** planes.

The ST Ref-1 sample contains less niobium content than the typical Gum Metal alloy composition, 20at% as opposed to 23at%. As discussed in Chapter 1, niobium is a β-stabilizer in Ti alloys, so it is expected that this particular sample may be unstable with respect to phase transformation. Using the schematic pseudo-binary equilibrium phase diagram for β-isomorphous Ti alloys as a guide shown in Figure 1.2 one would expect an alloy leaner in β-stabilizer content to possibly transform to the α phase upon quenching to room temperature, as the samples in the current investigation were designed to lie on or

near the boundary between α+β and β region. Upon quenching, however, martensitic phases form as opposed to equilibrium phases and microstructures. In a study by Moffat and Larbalesiter [25] on binary Ti-Nb alloys, it was found that the β-ω transition upon quenching occurs between 25 and 60at%Nb and that α'' (FCO) forms between 20 and 25at%Nb. For alloys with Nb content above 60at%, the alloy remains β phase upon quenching. Thus, we expect a similar behavior to occur in ST-Ref1 alloys and Gum metals. Even though the compositional values for the cutoffs between each regime may not be the same, we expect that the alloy leaner in Niobium content (ST Ref-1) will contain ω or α'' phase, and alloys with higher Nb content should either contain less volume fraction of ω phase or exist completely as the β phase.

The ω phase that forms upon quenching is typically termed athermal ω, or ω_{ath}, as the phase transformation that occurs from the β phase to the ω phase upon quenching is thought to be (mostly) displacive in nature. Such a transformation is similar to martensitic phase transformations as it is also not formed through typical nucleation and growth processes. The difference between the β-ω transition and β- α' or α'' transformations is that the exact mechanism of β-ω transition is theorized to require a displacement wave of **K** = 2/3<111> with an amplitude that allows shuffle of {222} planes by ½{222} which would be mediated by an intrinsic soft phonon mode in BCC structure that enables easy {112}-type shear [26]. This transformation results in the widely accepted orientation relationship $\{111\}_\beta$ || $(0001)_\omega$; $<10\text{-}1>_\beta$|| $<11\text{-}20>_\omega$. The amplitude of displacement given (½{222}) results in an ideal hexagonal structure with space group P6/mmm. One ideal hexagonal ω variant (out of four possible) is shown along side a hexagonal unit cell of BCC in Figure 2.3 in which the structure shown has undergone complete collapse of the middle $\{111\}_\beta$ planes, and thus, the atoms are located at the (0,0,0), (1/3, 2/3, 1/2) and (2/3, 1/3, 1/2) positions. From the figure it is seen that the ω phase can be simply described by a BCC structure in which there is a "collapse" of consecutive pairs of $<111>_\beta$ planes. To form the trigonal ω phase (space group P-3m1), the collapse does not go to completion and the z-position of the internal atoms ranges from (1/3, 2/3, 1/2+z) and (2/3, 1/3, 1/2 –z) where $0 < z < 1/6$; when $z = 1/6$, the BCC phase is formed. The trigonal phase forms typically in higher solute content alloys [27] and in rapidly cooled samples where partial collapse results [28]. Furthermore the ω_{ath} phase has also been observed to have particle-like as opposed to plate-like morphology. Due to the differences in mechanism of origin and differences in morphology, the ω phase is typically not termed a martensitic phase like α' or α'' phases, except in instances where the non-diffusional and composition-invariant nature of the mechanism of formation is being emphasized [29].

Initial selected area diffraction pattern from the $<110>_\beta$ zone axis of ST-Ref1 yields super structure spots in $1/3<112>_\beta$-type positions as shown in Figure 2.4a. These spots are typically associated with all four variants of the ω_{ath} phase. A dark field image shown in Figure 2.4b is taken with one of the circled superlattice reflections (associated with $[1\text{-}11]_\omega$ spot) and reveals a homogeneous distribution of nanoscopic secondary particles, most likely the ω_{ath} phase. Individual [110]β (|||[110]ω) ZA diffraction patterns for each variant are given in **Appendix B.1**. Total Diffraction pattern for all 4 variants is given in Figure 2.5, where the blue spots are from the BCC matrix and the red spots emanate from the ω variants.

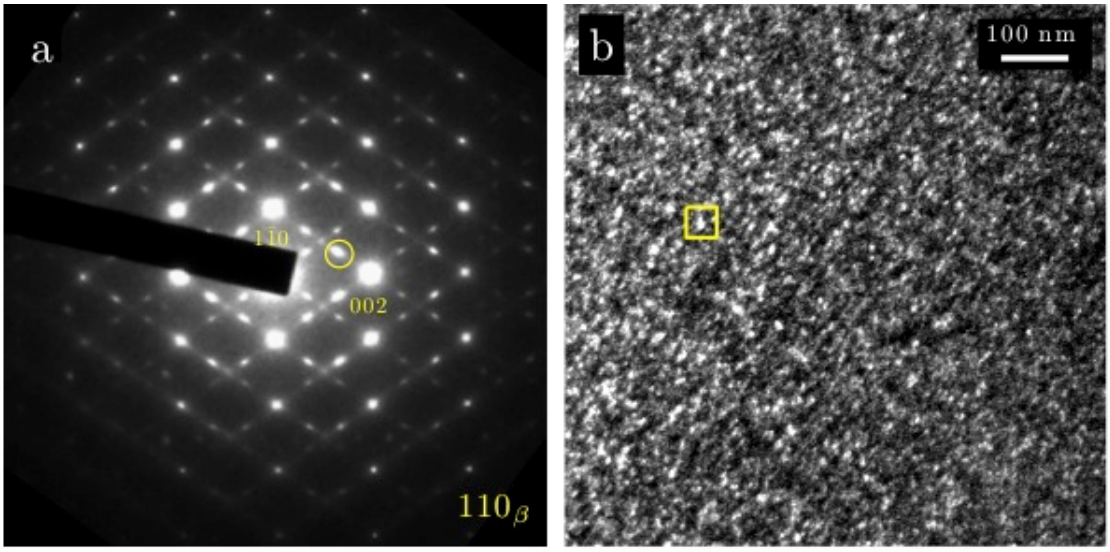

Figure 2.4: a) Experimental Diffraction Pattern taken from [110]β zone axis demonstrates existence of more than one variant of the ω phase. Dark field image taken from ω-type spot circled in a) shows nanometer-sized ω precipitates

Note a few differences between the kinematical simulation and the experimental image in Figure 2.4a. First, the kinematical diffraction pattern has fewer ω spots than the experimental pattern. The extra spots in the experimental diffraction pattern are from dynamical diffraction phenomenon and would otherwise be excluded if the sample were thinner, as dynamical diffraction effects imply multiple scattering events occur in the sample. The dark field image was specifically taken using a spot associated with kinematical diffraction. Second, the diffraction "spots" in the experimental pattern are elongated in <112>$_\beta$ -type directions, whereas they are circular spots in the simulations. The shape of the ω_{ath} precipitates is typically ellipsoidal with long axis along <111>$_\beta$, and it is the opinion of the author that the nanoscopic size along with the elongated shape creates the slight streaking seen in the ω spots. These streaked spots, when related to a discrete precipitate structure that can be imaged as in Figure 2.4b, have been similarly rationalized in the literature as due to individual rows of ω particles or the individual particles themselves [27 p. 45]. The streaking extends to ½<112>$_\beta$ –type positions for both variants due to its small size, and it is observed that there is some intensity where they overlap at this position. The ½<112>$_\beta$ –type positions are typically associated with the α' phase, but a dark field image taken with this spot revealed a lack of precipitates. Thus, any appreciable intensity at this spot is considered to be due to overlapping ω-streaking from the different variants. Notice further that the discrete ω spots are also accompanied by "diffuse" streaking in the [112]β-type directions, discussed further in the next section.

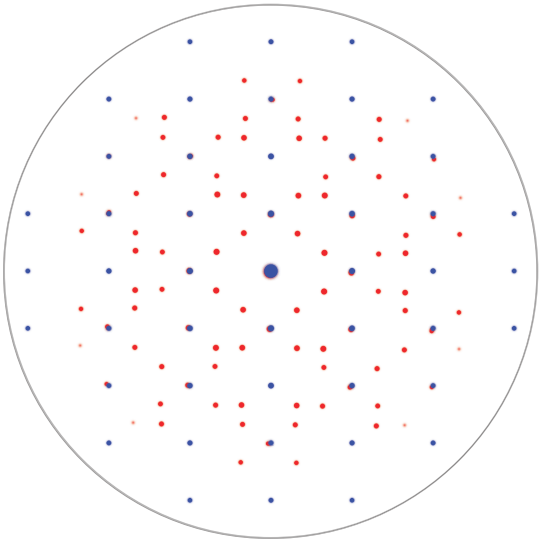

Figure 2.5 Kinematical Diffraction pattern of $[110]_\beta$ |||$[110]_\omega$ simulated in Crystal Maker Software (Single Crystal package). Here the red denotes the ω phase (all variants) and the blue denotes spots from the BCC β-Ti phase. Compare to **Figure 2.4**a

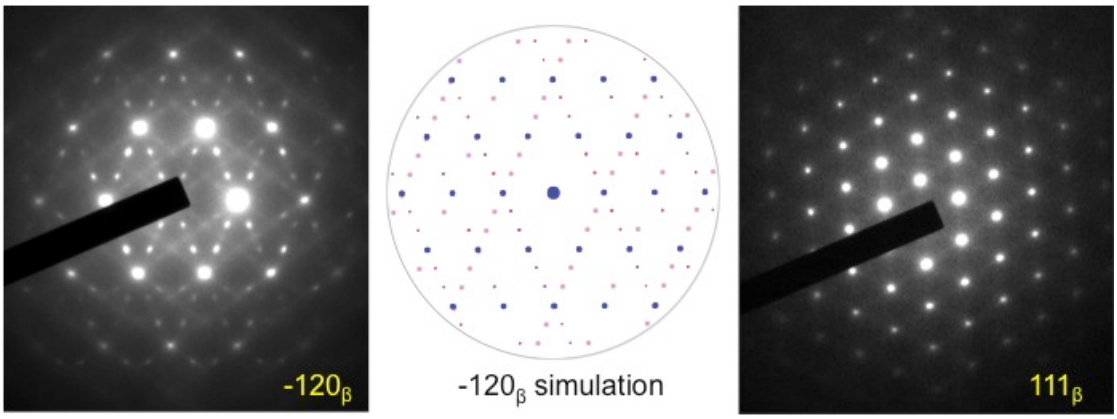

Figure 2.6: Experimental DPs taken from different zone axes. (Left and middle) DP and kinematical DP simulation of the [-120]β zone axes confirms possible existence of ω phase (BCC: blue, ω: purple). Extra spots in experimental due to dynamical diffraction. (Right) <111>β DP does not exhibit extra spots, consistent with ω phase.

Diffraction patterns from other β zone axes were taken to confirm the existence of ω phase in the ST Ref-1 sample. Diffraction pattern of [-120]β axis taken on JEOL 2011 is given in Figure 2.6. The kinematical diffraction simulation of the [-120]β phase with all four ω variants is given in the central image, where the blue spots are the BCC matrix and the purple spots are from the variants of the ω phase. The simulation confirms the presence of the ω phase, where the extra spots in the experimental pattern are from dynamical diffraction effects similar to those seen in the <110>β DP. In this particular zone, two variants fall identically on a subset of BCC matrix spots, while the other two have their own particular set of spots distinct from the BCC spots as outlined in **Appendix B.2.1**. With these two particular diffraction patterns, it is difficult to verify exactly which variants, if all,

are present, but given that if ω is present it is the athermal kind, we can infer that all variants should be present. To complete the description of this phase, a diffraction pattern from <111>β zone is presented in the last image in Figure 2.6. The fact that we observe no extraneous spots is consistent with our hypothesis that the ω phase is present. There is some streaking present between spots, which has been observed in previous studies, including for a similar Zr-Nb alloy by Dawson et al. in [30]. The streaking in that study was explained as originating from rows of quenched-in ω precipitates.

Thus we initially believe the ST-Ref1 sample to contain nanoscopic, ellipsoidal particles of trigonal ω_{ath} phase based on conventional TEM SAD and dark field imaging and observations from previous studies. Further in depth TEM images and diffraction patterns of ST-Ref1 can be found in **Appendix C.1**.

2.3.2.2 STGM: ω streaking, absence of secondary phases.

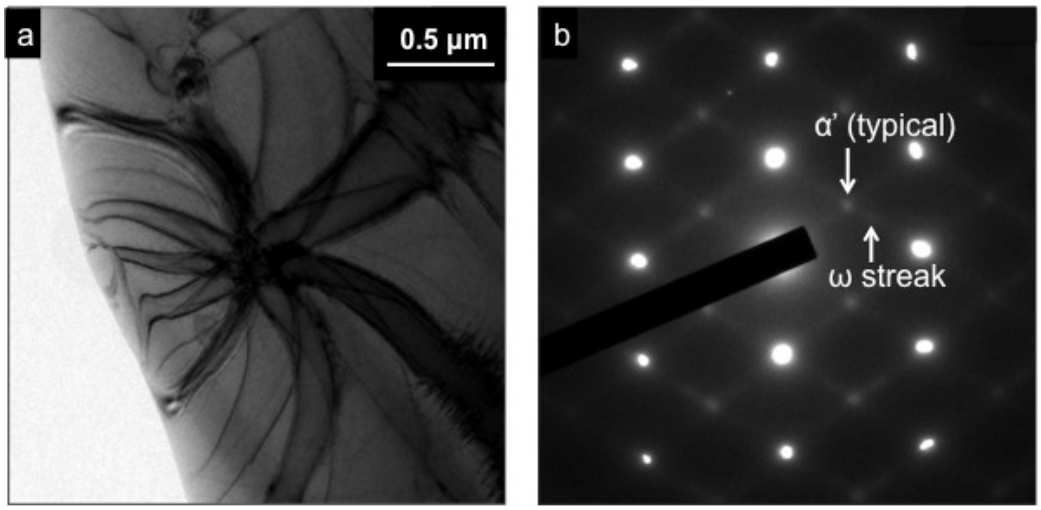

Figure 2.7: (left) conventional bright field image of STGM, from which SAD was performed. (right) SADP of region on left reveals reciprocal lattice streaking. No discrete precipitate structures could be imaged from any secondary reflections, and it is assumed the streaking is due to lattice-modulation via soft phonon. Any appreciable intensity at the α' spots is thought to be due to overlap of streaks. It is thus assumed there are no secondary phases present.

Preliminary TEM investigation of STGM yielded streaked diffraction patterns as indicated in the selected area diffraction pattern in Figure 2.7 taken from the region on the left. Subsequent dark field imaging taken of the ω streaks and spot associated with the α' phase yielded no observable intensity in real space emanating from discrete precipitate structure. This result is consistent with that in a Gum Metal study conducted by Talling et al. in which they could not image the ω phase from dark field imaging of the streaks for a similarly solution annealed sample [31].

There is still some controversy regarding whether the origin of the streaks is indeed from an actual discrete precipitate structure of ω phase, or whether the streaks are phonon, or lattice-modulated, mediated due to an intrinsic instability of the BCC phase. Where the streaks are diffuse and possible precipitates are not directly image-able, the phase is

termed “diffuse ω” due to the diffuse scattering that can be observed as in Figure 2.7. A thorough review of the initial ω literature can be found in “Metal Properties Handbook: Titanium Alloys” [27, p.43-47]. In this chapter, the authors support a lattice-dynamical model to explain ω phase formation. Initially, the proposed mechanism for ω formation was a “linear fault” mechanism, which indicates that the ω phase forms from equal and opposite shear on adjacent pairs of (110)β planes that ultimately result in displacement of atoms along <111>β-type directions. This mechanism immediately justified various observations of the ω phase, including the observations that ω structures appear elongated along <111>β directions. While this mechanism provides a simple means of describing the final structure and its relation to the parent BCC lattice, it does not completely explain the reversible nature of the β-ω transition nor satisfactorily indicate where the compositional boundaries lie between discrete ω phase and “diffuse” ω with respect to the transition between discrete spots and streaks in reciprocal space. Initially such streaking was thought to originate from rows of particles or individual particles themselves. Later on, however, a phonon-mediated model was proposed by de Fontaine et al. [32] that more thoroughly explained observations of the ω phase. It was argued that a longitudinal phonon with wavevector **K =** 2/3<111> can describe the partial collapse and continuum nature of the β-ω transition with respect to temperature and composition and can also explain the diffuse intensity present in the diffraction pattern where a discrete precipitate structure cannot be found. Electron scattering simulations of a Ti_{85}-V_{15} alloy from first-principles calculations performed by Hanlumyuang et al. [33] supports the idea that streaking in the diffraction pattern could indeed be phonon mediated. The authors observe that lines of intensity observable along <112>**β** - type directions are due to the lattice modulation resulting from an intrinsic soft-phonon mode present in leaner **β**-stabilized alloys. Based on the lack of directly observable precipitates and that the most recent literature suggest that lattice-dynamical effects can account for reciprocal lattice streaks, it is concluded that there are no secondary phases present in the STGM sample. This is further supported via HRSTEM imaging in Section 2.3.3.1. Extra images and diffraction patterns of the STGM sample can be found in **Appendix C.1**.

2.3.2.3 CWGM: Lath structure and dislocation cell networks

Cold Worked Gum Metal (CWGM), as will be demonstrated in this section, can be difficult to characterize as it has been heavily cold swaged with a reduction of cross section area by 90%. Initial conventional TEM images are given in Figure 2.8 and Figure 2.9. These samples have been cut perpendicular to the swaged axis, and thus should nominally be in <110>β orientation. Figure 2.8(left) is a BF image of a typical region which exhibits non-uniform grain sizes, diffuse contrast features, and moiré fringes. SADP (right) taken from this region indicates that heavy rotation has been sustained within the sample after undergoing swaging. Some regions of the sample, despite being cut perpendicular to the swaged axis, contain lath microstructure as shown in Figure 2.9. Figure 2.9a is a TEM BF image and Figure 2.9b is the dark field image taken from the reflection circled in green on the inset DP. Figure 2.9c contains an enlarged image of the elongated grain that is lit up in Figure 2.9b and demonstrates mottled contrast, possibly due to an intricate sub-grain structure mediated by low-angle tilt boundaries. Such sub-grain formation is common in

materials that have endured severe plastic deformation [34], although the exact reason for this mottled contrast is not immediately clear from the dark field imaging alone.

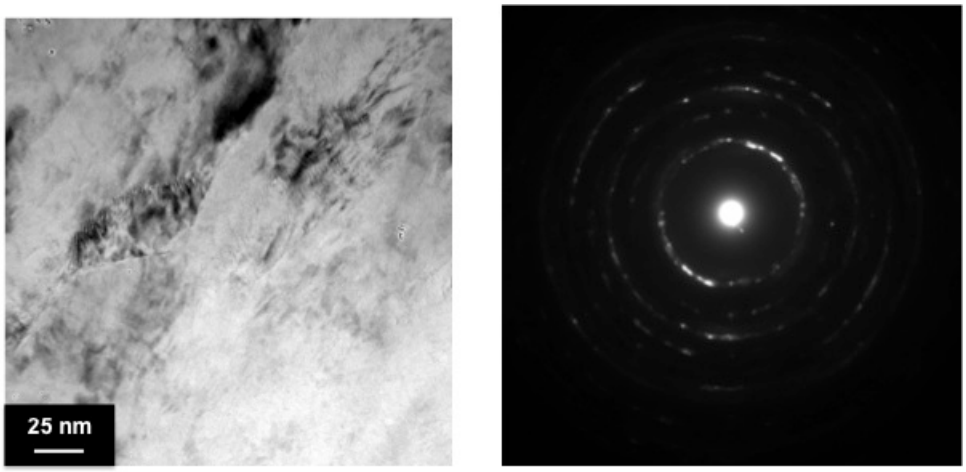

Figure 2.8: (left) BF TEM image of CWGM cut perpendicular to swaged axis demonstrates non-uniform grain sizes, complex diffraction contrast features and Moiré fringes. (right) SADP of region indicates heavy a rotation has been incurred by sample (taken with JEOL 2011)

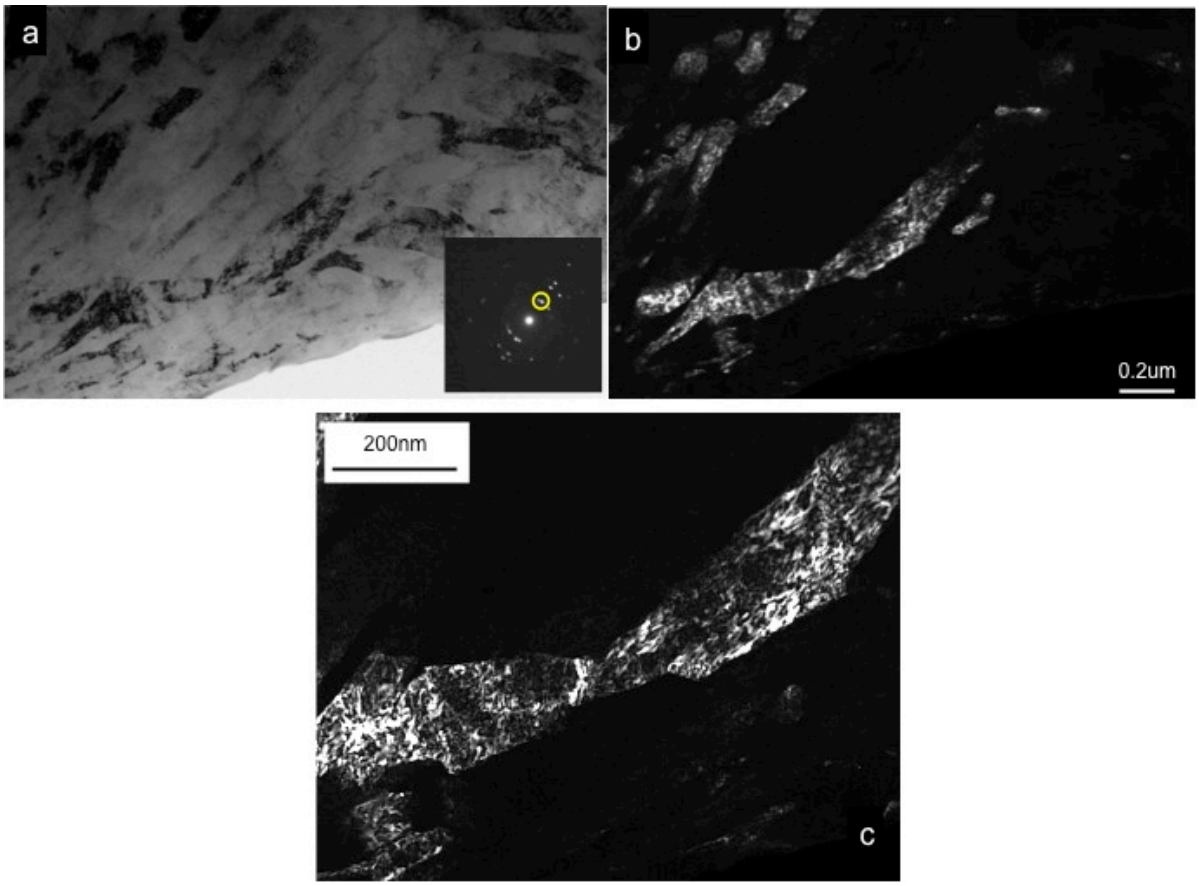

Figure 2.9: a) and b) are bright field and dark field images respectively demonstrating elongated grain microstructure. c) is a close-up of the elongated grain in b) and exhibits "mottled" contrast, intricate sub-grain structure, possible emanating from low-angle tilt boundaries, similar to dislocation cell network structures found in severely deformed materials.

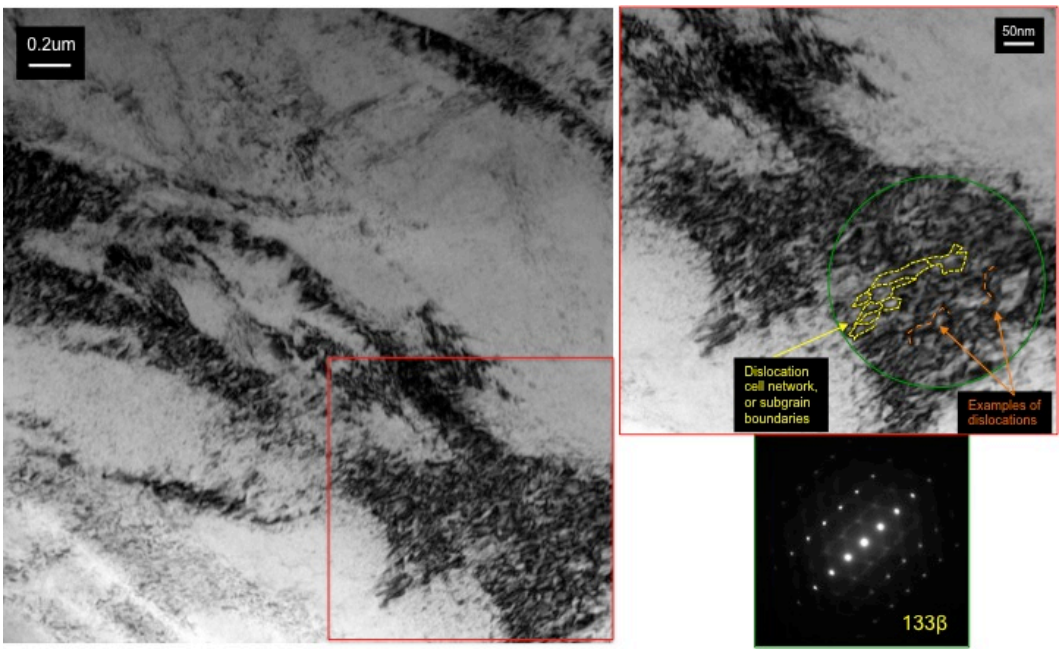

Figure 2.10: (left) typical bright field image of lath type grains with complex contrast features within. (right, top) possible sub-grain boundaries mediated by dislocations are outlined in dotted yellow, underscoring the existence of dislocations / dislocation cell networks in cold worked gum metals, example dislocations are outlined in dotted orange. (right, bottom) SADP of region encircled in green demonstrates that the region is of nominally one orientation, {133}β and contains streaking but no discrete secondary phase reflections.

Figure 2.10(left) is another BF image of CWGM. BF image on the right is a magnified view of part of the mottled region outlined in red and the DP inset indicates the entire dark region (encircled in green) to be {133}β diffraction condition. Thus, despite the mottled contrast, regions of the same diffraction contrast which appear mostly dark are nominally oriented along the same zone axis and thus part of the same original grain. A region within one grain is circled in green in the BF image on the right. This mottled region appears to contain linear defects which appear to be a network of dislocations in which the dislocations are not straight, short segmented, and form the boundary of sub-grains as outlined by dotted yellow lines. The sub-grains appear to be 50-100nm in diameter. While not definitive proof, this is very convincing evidence that dislocations are present in cold worked gum metals**,** consistent with the evidence found in [35] and our understanding that severely plastically deformed materials form dislocation cell network structures. This TEM evidence counters the claims in the original Saito et al. paper that Cold Worked Gum Metals do not contain dislocations [4]. It is understandable that initially the interpretation of such images may have led people to claim that there were "virtually no dislocations present" since the complex contrast present in such severely deformed materials at and within grain and sub-grain boundaries may preclude immediate identification of the boundaries themselves [36]. Indeed it has been explicitly claimed that the distorted lattice that forms upon cold working gum metals renders any line defects to be extremely difficult to image [37,38]. Perhaps it is better to claim "there are no easily characterize-able dislocations in cold worked gum metals" as the dislocations are short, kinked segments in complex networked structures, which precludes conventional g•b analysis. Without immediate Burgers vector analysis available, it is admittedly difficult to ensure that the kinked dark

line features outlined in dotted yellow in Figure 2.10(right) in such samples denotes a boundary, a dislocation, or a combination of both (e.g. dislocation cell network). Furthermore, the anomalous mechanical data of Gum Metals, which indicated a lack of work hardening, along with one HRTEM image found in CWGMs indicated the existence of "nanodisturbances". While, it may certainly be the case that another defect structure, such as this "nanodisturbance" defect, is able to account for the anomalous mechanical properties of gum metals and is the defect structure through which GMs deform, it is important to note that generation and movement of such a defect should be accompanied by typical dislocation motion simply given the dislocation cell network evidence in Figure 2.10. It should be noted that Kuramoto et al. also observed sub-micrometer subgrains in CWGM, but speculated that their formation was due to division of grains via giant faults (ideal-shear generated defects) and not dislocations [8].

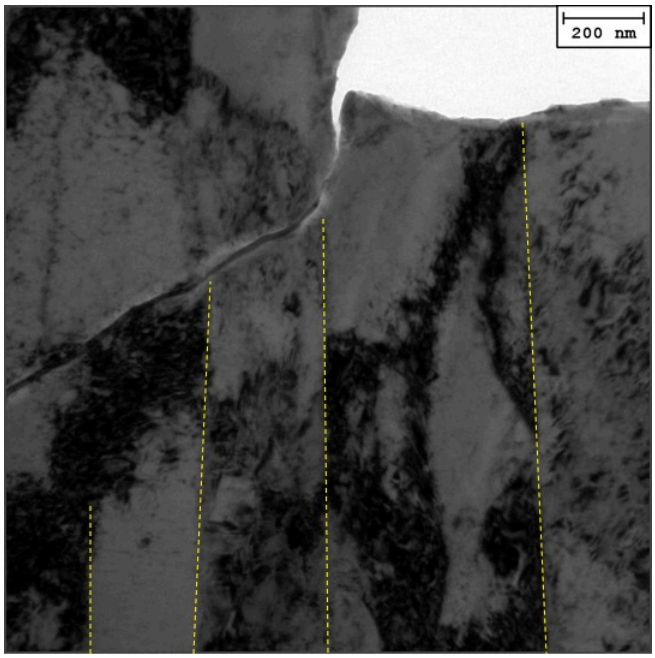

Figure 2.11: BF image of CWGM sample that has been previously cut parallel to swaged axis clearly reveals lath microstructure with complex substructure and exhibits straight, parallel grain boundaries. Taken with JEOL 2011.

Figure 2.11 is a TEM BF image of a CWGM sample that has been cut parallel to the swaging axis. The lath structure that forms upon heavy swaging is outlined in yellow and these grains are presumably elongated in the direction of swaging. Laths are ~200-300nm in width. Complex substructure exhibited within lath is similar to that found in Figure 2.9c. However, unlike the sample that has been cut perpendicular to the swaging axis, lath structure in Figure 2.11 has well defined, straight grain boundaries.

In summary, CWGMs do not clearly contain secondary phases as observed from conventional TEM imaging. 90% CWGMs contain a complex microstructure: large lath structures and elongated grains with sub-grain structures mediated by dislocation cell network structures typically found in severe plastically deformed (SPD) materials.

2.3.3 HRSTEM data: Direct Atomic Imaging of secondary phases

In anticipation of characterizing the nanoindentation test results and to explore the possibility of the existence of a theorized "nanodisturbance" defect in cold worked gum metals, HRSTEM imaging was performed on as-received samples as "control" specimens. Initial nanoindentation work on ST GM seemed to indicate the presence of pinning points [39] and initial HRTEM work on 90% CW GM seemed to indicate the presence of a line defect with non-quantized burgers vector [4,9], also termed "nanodisturbance."

The applicability and appropriateness of HREM experimentation for imaging a line defect is discussed in Section 3.4.3.1. Despite the difficulties involved in imaging a line defect in HREM, the recent advances in spherical-aberration correction allows for higher probe currents and convergence angles so that it is possible to image atomic columns that are separated by sub-angstrom distances [40]. This recent advancement makes HRSTEM imaging an attractive tool for understanding potentially complex atomic-scale defects. Furthermore, use of HAADF detector for atomic scale imaging is particularly attractive for its typically straightforward interpretation where the intensity is thought to scale with Z^2 [41]. For this reason we use HAADF imaging over phase contrast imaging. Atomic resolution images obtained via phase contrast imaging, or HRTEM technique, are less straightforward to interpret and typically require simulations and through focal reconstruction to determine exact atomic positions [42]. A generally accepted rule of thumb to ensure the validity of Z-contrast interpretation in HAADF imaging (that is, the recorded signal is dominated by incoherent scattering) is to use an inner detector collection semi-angle, θ_i, which is at least three times the probe convergence semi-angle, α [43]; thus the HAADF signal in the following images was collected at an inner collection semi-angle of ~53 mrad and an outer collection semi-angle of ~318 mrad using a probe convergence of 17.2mrad, unless otherwise specified. However, as will be illustrated through multislice HRSTEM simulations in Section 2.3.3.1, the interpretation that HAADF intensity is simply a monotonic function of atomic number might not be the case for an alloy containing multiple phases.

2.3.3.1 ST Ref-1: Tri-layer periodicity of ω phase in HRSTEM confirmed via multi-slice simulations

Note: Parts of this section are taken from Sankaran et al. [44] and are reproduced here with consent of all co-authors. Initial HRSTEM images Figure 2.12 and Figure 2.13, along with Figure 2.4, were originally included in the Project Report for fulfillment of M.S. degree in Materials Science and Engineering at UC Berkeley. However, subsequent HRSTEM simulations and analysis reversed our initial interpretation of the raw HRSTEM data that was stated in the original M.S. project report. The finalized version of HRSTEM interpretation of ω phase was submitted to Philosophical Magazine and this section contains portions from this manuscript.

2.3.3.1.1 Background and Context

It is noted that contemporaneous studies, specifically a study by Sabol, Marvel, Watanabe and others [45], observed the same tri-layer contrast of ω phase in HAADF imaging experiments of β-Ti alloys. This particular manuscript was published six months after our

Philosophical Magazine paper [44] was published online. The authors of Ref. [45] claimed (emphasis added):

"Since the HAADF-STEM images were acquired at 90–370 mrad, which are true HAADF conditions, ***it can be confidently stated that the relative average intensities are directly attributed to atomic number (Z) contrast****. It is more obvious in Figure 3c that particular atomic columns are occupied by one or multiple alloying elements, which give rise to the three different average intensities. However, without atomic resolution chemical analysis, the precise distributions and site occupancies of the five elements in the three different layers cannot be determined. Further investigations are needed to determine if ω is ordered and which elements occupy the trilayer sites."*

The authors of this study claimed chemical ordering because of the persuasive "rule-of-thumb" argument regarding intensity being proportional to Z^2, and it should be noted that the belief that HRSTEM images are directly interpretable in terms of Z-contrast is very strong. However, this generally only holds true for simple mono-phase systems and thin samples; for any other systems, HAADF can be thought of to first order as *sum of projected potential*, but simulations should still guide HAADF interpretation. It should also be noted that after [45] was published, the specific contrast motif generated by the ω phase in HAADF images was termed "tri-layer periodicity".

Given that HAADF imaging of the ω phase is an active area of research, typically used to gain insight into the β-ω transformation, a study was recently published (June 2015) by a group from Cambridge to clear up the controversy regarding ω phase HAADF contrast interpretation [46]. The results of Bennett et al. confirm our interpretation that the tri-layer periodicity originates from the omega structure. The authors confirmed the interpretation via additional multislice simulations and experimental EELS data to ensure that no chemical ordering is generating the observed contrast. In the following section, we demonstrate our extensive thought process in determining that the true origin of tri-layer periodicity observed in HAADF images of unstable β-Ti alloys is the ω phase.

2.3.3.1.2 HAADF data

Atomic resolution HAADF images, shown in Figure 2.12 were taken along the $<110>_\beta$ zone to confirm that a given particle, such as that outlined in yellow in Figure 2.4b, consists of the ω phase, and we observed three types of atomistic motifs. Figure 2.12a reveals a region of the crystal in which brighter and less-bright atomic columns alternate in an ordered pattern; that is, every third column along the $[002]_\beta$ direction (or every third $(-11-2)_\beta$ plane trace) indicated in Figure 2.12a is brighter than the other two intermediate columns, which appear dim. All atoms appear to be in registry and not displaced. A similar contrast motif is shown in Figure 2.12b in which every third atomic column is also slightly brighter. However, this motif differs from the previous one in that the dimmer columns are streaked in a $<111>_\beta$ –type direction, indicated by the arrow as the $[-111]_\beta$ direction. Furthermore, the brighter atomic columns along the $[-111]_\beta$ are not surrounded by diffuse intensity and appear stark with respect to the dimmer columns. Most strikingly, the precipitate in Figure 2.12c exhibits discrete partial collapse of the $\{111\}_\beta$ planes, which is considered direct evidence of the trigonal ω phase [16].

To complete the description of these possibly distinct structures, an atomic-resolution HAADF image from a second zone axis, [210]β, was captured and is presented in Figure 2.13. Within this one region, about 12 nm x 12 nm in area, three motifs are also observed and are shown in the figure. The precipitate in region 'a' contains atomic columns of slightly brighter contrast along the trace of every third (1-2-1)β plane, with the dimmer atomic columns appearing to be in registry with the BCC lattice. In the 'b' region, a similar contrast motif is observed along with faint streaking of atomic columns in between planes along the [-125]β direction. Similar to the motif in Figure 2.12b, no discrete atomic collapse is observed. Region 'c' indicates a trigonal ω phase with partially collapsed atomic columns evident along the trace of the (1-21)β plane in the [-125]β direction as indicated in the figure. In the case of this collapse, atomic shifts are still occurring along the [111]β direction, and we are simply observing the projection of this collapse when viewing along the <210>β zone axis so that the collapse appears along this [-125]β direction. Thus, by tilting to the [210]β zone axis, we again observe three atomic motif types in the material, similar to those found in Figure 2.12 a-c.

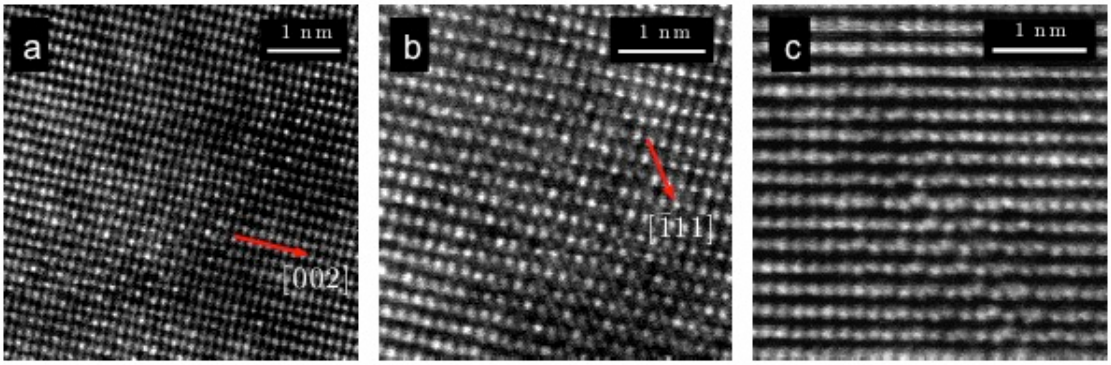

Figure 2.12: Probe-corrected HAADF-HRSTEM images (a-c) were obtained and reveal three atomic motifs. For the precipitate in a), every third atomic column along the [200]β direction is twice as bright and all atoms appear to be in registry with the BCC lattice. In b) a similar contrast motif is present along with atomic streaking of the dimmer columns in the [-111]β direction. No such contrast motif is present in c) and atomic columns show discrete displacement in the [-111]β direction.

We note that there are "extra" superstructure reflections present in the [210]β FFT that would not be present for the trigonal ω or ideal hexagonal ω phases. However, the FFT of a high-resolution image simply gives information about the contrast periodicity present in the image only. Without knowledge of the true origin of the periodic contrast, such spots cannot be associated with any particular phases or chemical ordering. We also note that the intensity of the columns in regions 'a' and 'b' of Figure 2.13 is not as strong as in Figure 2.12a and Figure 2.12b; however, we think this is a straightforward consequence of the sample tilt. The specimen developed a nominally <110>β orientation after undergoing cold-swaging and subsequent annealing. Given that the precipitate is most likely sandwiched by matrix material, tilting from <110>β to the higher order zone axis, <210>β (~18°), would most likely increase the through-thickness of the sample. Additional matrix material will obscure atomic columns of a precipitate structure, thereby decreasing the apparent contrast.

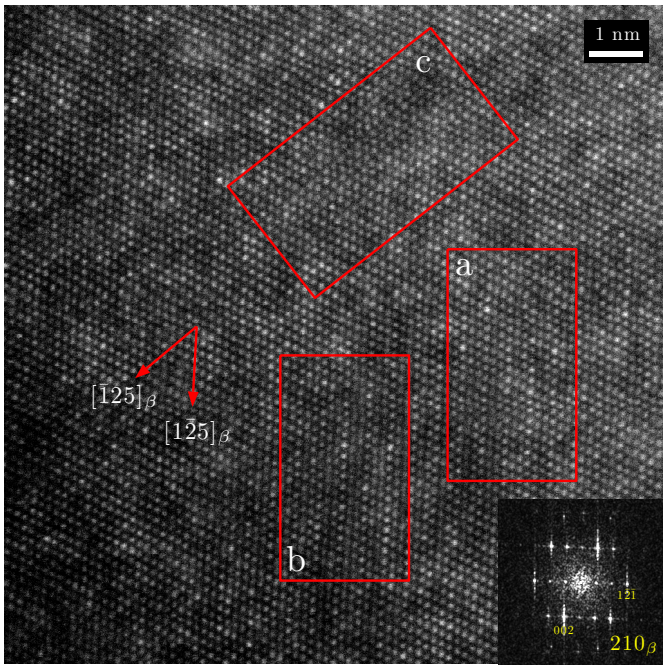

Figure 2.13: A HAADF image taken from one region along the $[210]_\beta$ zone also reveals the presence of three atomistic motifs. In region a), every third atomic column is brighter along the $[1\text{-}2\text{-}1]_\beta$ direction and the atoms appear to be in registry with the BCC lattice, similar to Fig. 1c. The same contrast motif appears in region b) and is also accompanied by atomic streaking of the dimmer columns in the $[1\text{-}25]_\beta$ direction. Lastly, the precipitate in region c) demonstrates discrete atomic displacement.

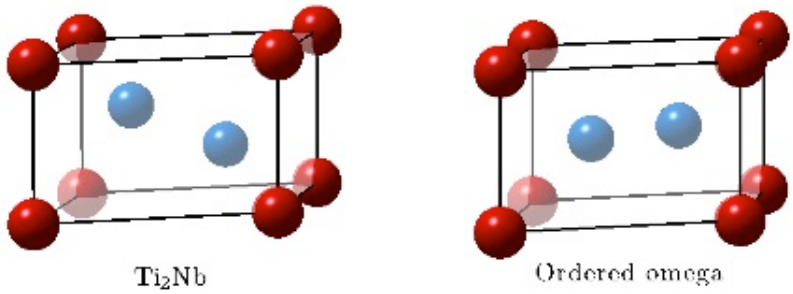

Figure 2.14: Atomic models of possible structures that could account for the motifs in **Figure 2.12** are presented here and in **Figure 2.3**(right) where atomic species are red: Nb and Ti: blue. The hexagonal cell of the BCC matrix is provided in **Figure 2.3**(left) for comparison along with the crystallographic relationship to the hypothesized structures, all of which can be described by a hexagonal unit cell. Since HAADF imaging is z-sensitive, the atomic contrast observed in the experimental data could be due to niobium ordering. The possible structures include the trigonal or ideal ω phase, ordered Ti2Nb, and an "ordered omega" structure.

The ω phase model included in Figure 2.3(right) and the models in Figure 2.14 outline the atomic structures of the most likely candidates that could account for each of the atomic motifs imaged in Figure 2.12. The hexagonal cell of the BCC titanium matrix is outlined in Figure 2.3(right) and gives the crystallographic orientation relationship of the BCC matrix with the three possible candidates, all of which can be described by a hexagonal unit cell as well. Since the HAADF-HRSTEM technique is Z-sensitive, the precipitates in Figure 2.12a, b and Figure 2.13 region 'a', region 'b' could be interpreted as containing atomic columns populated preferentially by an element that is heavier than titanium. The only plausible candidate atom would be niobium, since it is the only alloying element whose

concentration (~20 atom percent) is sufficient to fill planes over significant regions of the crystal. Furthermore, the atomic columns in Figure 2.12a and Figure 2.13 region 'a' appear to be in registry with the BCC lattice, indicating no direct evidence of collapse of the {111}-type planes. Thus, this phase at first appears to be a result of simple ordering via atomic rearrangement on the BCC background lattice. A possible structure responsible for these ordered domains can be described by niobium ordering along the <111> direction in the BCC matrix in which Nb atoms preferentially fill every third (111)β plane yielding the stoichiometric composition Ti_2Nb. The unit cell of this hypothesized ordered phase is shown in Figure 2.14(left) This theorized phase would have a trigonal crystal structure (space group P-3m1) with a general matrix/precipitate orientation relationship of {111}BCC||{0001}Ti_2Nb and <110>BCC||<11-20>Ti2Nb. In this structure, the niobium atoms fill the basal planes, occupying (0,0,0) position, and the titanium atoms appear at the (1/3, 2/3, 2/3) and (2/3, 1/3, 1/3) positions, as given in Figure 2.14(left).

The motif observed in Figure 2.12c and Figure 2.13 region 'c' contains partial collapse of $\{111\}_\beta$ – type planes with no significant contrast variation. As discussed previously, the ω phase is thought to form from the BCC phase through either complete or partial collapse of the $\{111\}_\beta$ planes through a shuffle mechanism, resulting in the hexagonal (space group P6/mmm) or trigonal ω (space group P-3m1) phase, respectively [26]. We hypothesize that the structure responsible for this motif would be an unordered trigonal ω phase due to the partial collapse observed. This is consistent with previous observations that quenched-in, embryonic ω_{ath} is typically trigonal and does not undergo full collapse of $\{111\}_\beta$, and our original interpretation of the DP and dark field image as discussed in Section 2.3.2.1.

Lastly, there is another structure that could account for the motif, which includes streaking in the $<111>_\beta$ direction accompanied by contrast variation as observed in Figure 2.12b and Figure 2.13 region 'b': the hypothesized structure could contain niobium ordering, similar to that in the Ti_2Nb structure and could also contain $\{111\}_\beta$ planes in a partial state of collapse, similar to the ω phase. In this case, the niobium atoms fill the basal planes, occupying the (0,0,0) position, and the titanium atoms are displaced from the BCC matrix similar to that in the trigonal ω phase. For the purposes of this paper, we term this hypothesized structure "ordered omega." All of the hexagonal structures presented in Figure 2.3 and Figure 2.14, given that all four variants are present, would yield the same $[110]_\beta$ electron diffraction pattern shown in Figure 2.4a.

We again note that there should be systematic absences for the ideal hexagonal and trigonal ω phases along the <110>β zone, but those reflections are typically present on account of dynamical diffraction, or multiple scattering effects. However, the spots associated with dynamical diffraction for the ω phase are kinematical reflections for both the Ti_2Nb phase and the ordered ω phase on account of the chemical ordering present. This is apparent in the kinematical simulation of a <110>β||<11-20>Ti_2Nb diffraction pattern given Figure 2.15. Only one variant is simulated and demonstrates no systematic absences exist in the presence of the chemical ordering described above. Blue is Ti_2Nb and purple is the BCC phase (which overlaps Ti_2Nb reflections).

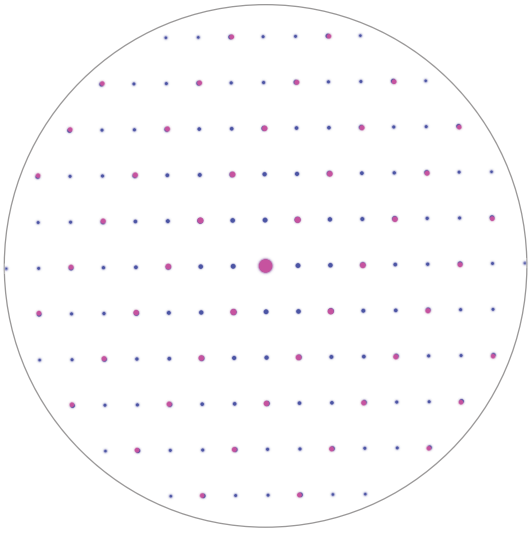

Figure 2.15: Kinematical DP simulation of <110>β||<11-20>Ti_2Nb Zone Axis for one variant demonstrates no systematic absences occur in DP for ordered Ti_2Nb phase along this zone.

2.3.3.1.3 *Multislice simulations*

To test the validity of the hypothesized structures outlined in Figure 2.3 and Figure 2.14, spectroscopic analysis would ordinarily be used to verify niobium ordering but is precluded here owing to the atomic scale dimensions of the precipitates. Furthermore, a diffraction pattern along the <111>β zone axis should yield superstructure spots on account of chemical ordering, but we did not observe any extra reflections as shown in Figure 2.6(right). However, the lack of such evidence does not exclude the possibility that niobium ordering is occurring as the volume fraction of any ordered precipitates could be low enough that the intensity of the superstructure spots may not be easily visible. Thus our main questions remain: can all atomistic motifs observed in Figure 2.12(a-c) be explained by the widely observed ω phase, and, if so, can we then rule out the possibility of niobium ordering?

In order to answer these questions, we performed HRSTEM simulations of each structure using the multislice algorithm outlined in Kirkland (1998) in which the dynamical scattering of electrons is derived from a physical optics viewpoint [47]. The Matlab code used to simulate the structures is given in **Appendix A.2**. To more accurately describe the sample, we simulated a sandwich structure, in which the precipitate is embedded within the β-titanium matrix, and another structure in which the precipitate lies on the specimen surface. These structures are shown in Figure 2.16. The matrix material was simulated as pure Ti in the BCC phase. For the precipitate, we simulated a range of structures in which we varied the amount of [111]β collapse and niobium ordering, shown in a collapse-ordering continuum in Figure 2.16. Here, the amount of collapse is indicated by the 'c' parameter labeled for each row, where c = 0 indicates no collapse (BCC structure); c =1 indicates full collapse of the <111>β planes (ideal hexagonal ω); and 0 < c < 1 indicates partial collapse (trigonal ω). To simulate the case where the ordering is not fully stoichiometric, the amount of niobium ordering in the precipitate was varied, and this is

indicated by the stoichiometry listed for each column. The extreme case, full collapse (c = 1) accompanied by full niobium ordering (Ti_2Nb stoichiometry), yields the exact description for the "ordered omega" structure. For the main simulation parameters, we simulated a [110]β oriented STEM image using the crystallographic relationships specified in Figure 2.3, using the same microscope parameters as used in the experiment: a convergence angle of 17.2 mrad, 300 kV accelerating voltage, and a HAADF inner angle of 53 mrad. Since we used a probe-corrected microscope, we assumed all aberration coefficients to be zero and a probe defocus of 0 nm. Two frozen phonons were also used in simulation.

The results of the simulations are given in Figure 2.16. First, we attempted to simulate a structure that would most closely match the motif found in Figure 2.12a to determine if the ω phase, rather than atomic ordering, could be responsible for the observed contrast. That is, since the atomic columns do not look streaked or displaced, there is no immediate evidence that indicates an ω-like collapse in the motif. To determine the best simulation parameters, we calculated the mean unit cell within the precipitate region. From this cell, we determined the average intensity ratio between the dimmer and brighter atomic columns to be ~0.55, that is the dimmer columns are about half as bright as the brightest atomic columns. We used this ratio as a semi-quantitative guide to determine the simulation parameters that yielded the best match with the experimental data in Figure 2.12a. We determined that a foil thickness of roughly 30 nm with the precipitate spanning 30% of the foil thickness provided the best match. The result of this simulation is given in the top row of Figure 2.16. First, we notice that the intensity ratio of the brighter to dimmer columns monotonically increases with the amount of collapse and niobium ordering in a continuous manner. Furthermore, we immediately notice that the fully ordered Ti_2Nb structure (top right) and fully collapsed ω (bottom left) precipitates look quite similar, except for a slight contrast effect noticeable in the ω structure along the trace of the (11-2)β plane that is not present for a niobium ordered structure: when the sample contains an ω structure, there is a lack of diffuse intensity around the brighter columns. Surprisingly, the atomic collapse of the ω structures is not readily visible. Instead, the only evidence that collapse has occurred is the presence of a diffuse intensity surrounding the dimmer columns that does not surround the brighter columns. This contrast effect can be directly related to the sum of the projected potential. Thus, from these simulations, we find that the discrete atomic displacement in the ω structures can be obscured when the precipitate is embedded, and instead the collapse only results in dimmer columns surrounded by diffuse intensity. The simulated peak intensity ratio between brighter and dimmer atomic columns for ideal ω (c = 1, Ti) is ~ 0.6 and for Ti2Nb (c = 0) is ~ 0.7. These values closely match that of the experimental data, but the Ti2Nb (c = 0) structure is a slightly poorer match. A few of the structures containing both niobium ordering and collapse provide as good a match as the ideal ω phase. The intensity difference between columns is most pronounced in the "ordered ω" (c = 1, Ti2Nb) structure at the extreme bottom right of the figure, with an intensity ratio of ~ 0.5. Qualitatively, both an ideal ω phase and a Ti_2Nb structure could account for the motif observed in Figure 2.12a, and it remains a possibility that a mixture of both ordering and collapse is occurring.

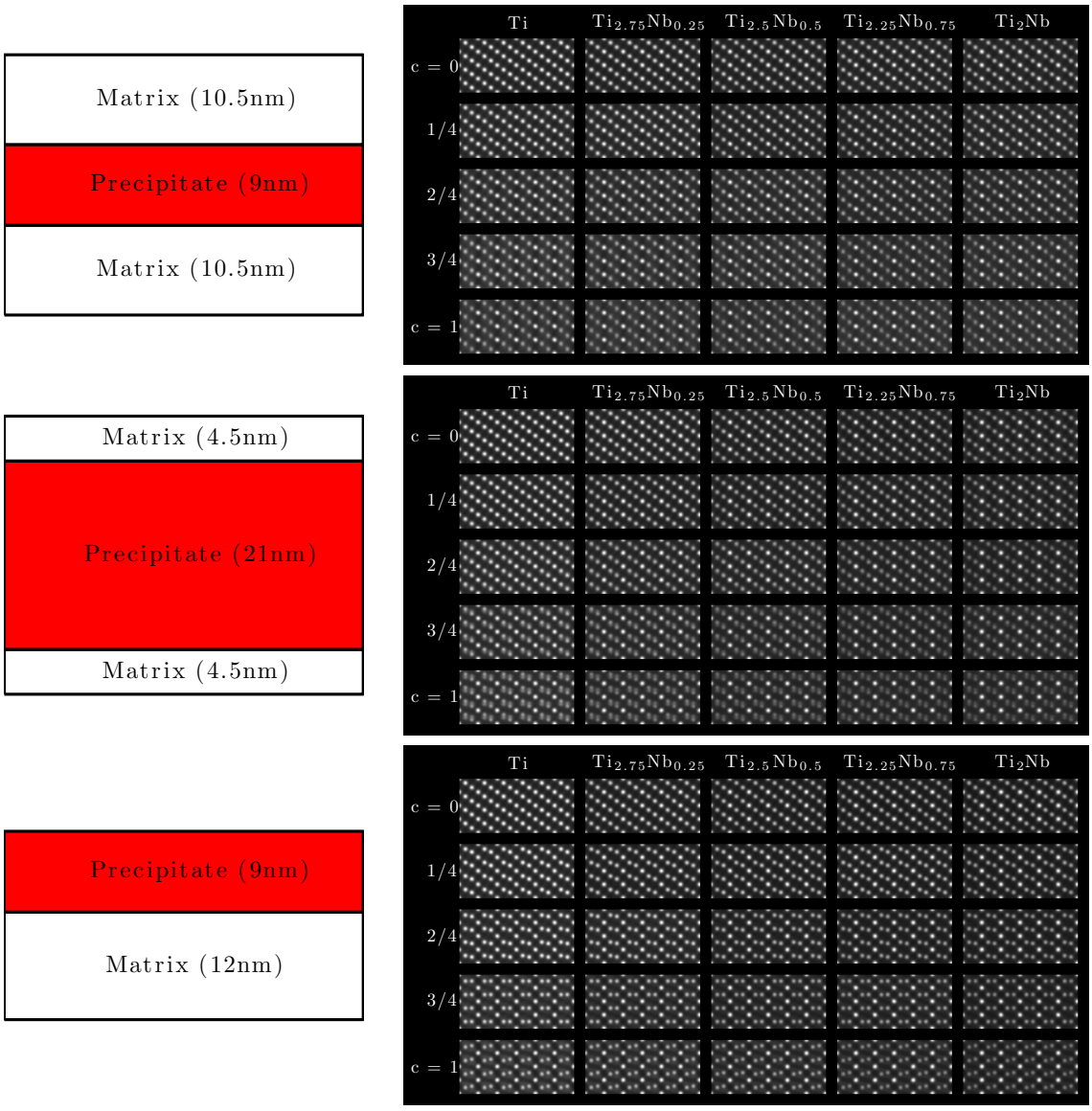

Figure 2.16: Specimen geometry and resultant multislice STEM simulations are presented. The matrix is simulated as pure BCC-Ti and the precipitate phase is varied according to a collapse parameter 'c', and the amount of niobium ordering. (Top Row) 30 nm thick foil with embedded precipitate demonstrates that collapse with no ordering (c = 1, Ti) yields a similar motif to that in **Figure 2.12**a. Combinations of collapse accompanied with niobium ordering also provide a match with respect to the peak intensity ratio measured for the precipitate in **Figure 2.12**a. (Middle Row) 30 nm thick foil with 21nm embedded precipitate shows streaking of atomic columns, like that seen in **Figure 2.12**b, and can be interpreted as collapse of $<111>_{\beta}$-type planes. (Bottom Row) To re-create the motif in **Figure 2.12**c, the precipitate phase was placed at the surface of the specimen in the simulation. The best qualitative match for this motif is an unordered trigonal omega phase (c = 2/4, Ti). See manuscript for simulation parameters**.**

When the embedded precipitate is roughly 20 nm long, or takes up 70% of the foil thickness, a streaking effect from the collapse in the ω phase becomes pronounced, as observed in the simulation provided in the middle row of Figure 2.16. The contrast between atomic columns from large collapse ($c \geq 2/4$) is now distinct from that of niobium ordering, which does not contain this streaking effect, as seen in the simulation of Ti_2Nb (c = 0). By comparing the simulations containing pure omega structures (Ti, left column) with the motif in Figure 2.12b, we conclude that the precipitate in the experimental data is

exhibiting partial <111>β collapse. As to whether niobium ordering is also involved, we again determined the mean unit cell within the precipitate region in Figure 2.12b. From this cell, we calculated the average intensity ratio between the dimmer and brighter columns to be ~ 0.9. Thus, the pure ω structures (c ≥ 2/4, Ti) provide a better fit than structures containing collapse accompanied with Nb-ordering, since the intensity difference between columns in Figure 2.12b is not as large.

In the last simulation, presented in the bottom row of Figure 2.16, we placed the precipitate at the surface of the sample. The mean unit cell of the precipitate calculated from the experimental image demonstrates no significant contrast variations between atomic columns and has a measured collapse of ~ 40%. We find that the simulated precipitate/matrix combination containing a collapse of c = 2/4 and no niobium ordering (pure Ti) is the best match for the motif in Figure 2.12c. It is interesting to note that when the precipitate is placed at the top of the foil and the probe is focused onto the surface, counterintuitive motifs can arise as shown in the bottom row where c = 1. In these simulated images, the displacement of the atoms has gone beyond full collapse resulting in an "anti-collapse" motif. This effect demonstrates the sensitivity of the image contrast with respect to the probe focus and precipitate position: the probe, focused at the surface where the precipitate is located, has been dramatically altered after propagation through the precipitate. When the altered probe subsequently encounters the BCC matrix, the scattering profile results in the counter-intuitive motif shown.

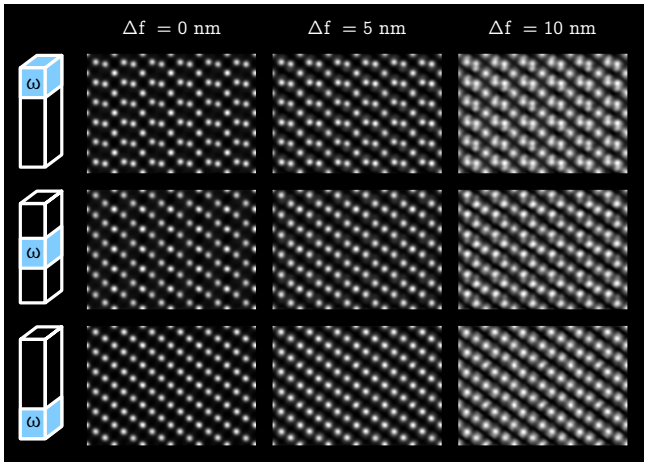

Figure 2.17: Here we present multislice STEM simulations to demonstrate the effect of defocus, Δf, and position of an unordered trigonal ω (c = 2/4, Ti) precipitate in the BCC-Ti Matrix on image contrast. The total foil thickness is 30 nm and the precipitate thickness is 9 nm. When the probe is focused on the surface (Δf = 0 nm) or slightly below (Δf = 5 nm) and the precipitate sits at the surface, the ωphase is immediately visible. When precipitate position is moved away from the surface under these defocus conditions, the ω precipitate is obscured. A slight streaking effect is the only evidence that the omega phase is present when the ω precipitate is completely embedded and the probe defocus is 5 nm. Furthermore, when the probe is focused below the surface further, (Δf=10 nm), counter-intuitive motifs occur, specifically a doubled-peak pattern can occur.

To understand the effect of probe defocus on resultant contrast, we performed simulations in which we changed both the location of an ideal hexagonal ω precipitate in the matrix and the probe defocus value. Results of simulations are given in Figure 2.17 and clearly demonstrate that different defocus values and precipitate locations can yield distinct and complex atomic motifs. The collapse motif only occurs when the precipitate and probe focus lie at the specimen surface (Δf = 0 nm). It is also observed that the ω precipitate can

become easily obscured when positioned below the surface of the specimen. Only when the probe is focused on the surface (Δf = 0 nm) or slightly below (Δf = 5 nm) and the precipitate is at the surface, the omega phase is immediately visible. However, when the probe defocus is large (Δf=10 nm) and the precipitate lies at the surface, a counter-intuitive doubled-peak pattern can occur.

2.3.3.1.4 *Discussion*

To summarize the previous section, the atomic motif in Figure 2.12a could be caused by an embedded trigonal omega precipitate, niobium ordering, or a combination of both. The precipitate in Figure 2.12b has undergone partial or full collapse of the [111]β planes, but niobium ordering is probably not also occurring since the peak contrast intensity ratio is too small. Lastly, the precipitate in Figure 2.12c can be fully explained by a partially collapsed trigonal omega phase with no chemical ordering involved. Thus, while each experimentally observed motif can be explained by varying the thickness and position of an omega phase with a particular collapse parameter within the matrix, niobium ordering still remains a possibility in this system, specifically for the precipitate shown in Figure 2.12a.

With respect to previous investigations, the Ti-Nb system is not known to contain ordered phases [48]. The only metastable phases that are known to form in this system are the martensitic α and α'', and the ω phases. Interestingly, there is one reference to an ordered Ti2Nb phase by Balcerzak and Sass in 1972 [49], who observed ordered spots in the diffraction pattern for aged Ti-18at%Nb. Despite this strong evidence of ordered ω, the "physically appealing" Ti2Nb phase did not agree with previously obtained X-ray data. The fact that ordering has not been reported previously may be due to the fact that it appears to be a strain-stabilized metastable structure with nanoscale dimensions, and therefore it is difficult to identify (Balcerzak and Sass [49] may well have seen it, but they could not unambiguously identify it.) It may also be relevant that our alloy, which has the composition Ti-20.0Nb-0.6Ta-1.7Zr-1.1O at.%, contains additions of Ta, Zr and O that are not present in the Ti-Nb binary. One or more of these may participate in the ordered phase and help to stabilize its structure.

2.3.3.1.5 *Summary*

If we adopt the simplest interpretation of these results and take into account the recent study by Bennett et al. [46], we determine that the nanoscale precipitates are indeed partially-collapsed trigonal ω phase.

Finally, we note there is a growing use of aberration-corrected STEM under HAADF conditions to study ω transformations and the role of ω in the microstructural evolution in β-Ti alloys. However, as shown in the present work, if the ω phase has dimensions smaller than the TEM foil thickness and occurs in a multi-component alloy, the resultant images could yield counter-intuitive or ambiguous motifs and caution should be taken in interpreting HAADF images as simply monotonic measurements of atomic number. In order to validate any interpretations, one must either perform multislice simulations or obtain further experimental data with complementary characterization techniques. Furthermore, we note that where HAADF conditions might fail to help unambiguously identify a particular phase, bright-field STEM may be useful as the motifs are distinguishable.

2.3.3.2 ST GM: No direct observation of any secondary phases

HRSTEM images were also taken of STGM gum metal samples and the vast majority of images contained no extraneous spots in the FFT and periodic contrast motifs in the real space images that would otherwise indicate composition fluctuations or chemical ordering. Representative images are provided in Figure 2.18 and confirm the notion that annealed GM samples contain no secondary phases and contain a negligible amount of defects. Vertical streaking of spots contained in FFT is due to rastering artifact from STEM imaging.

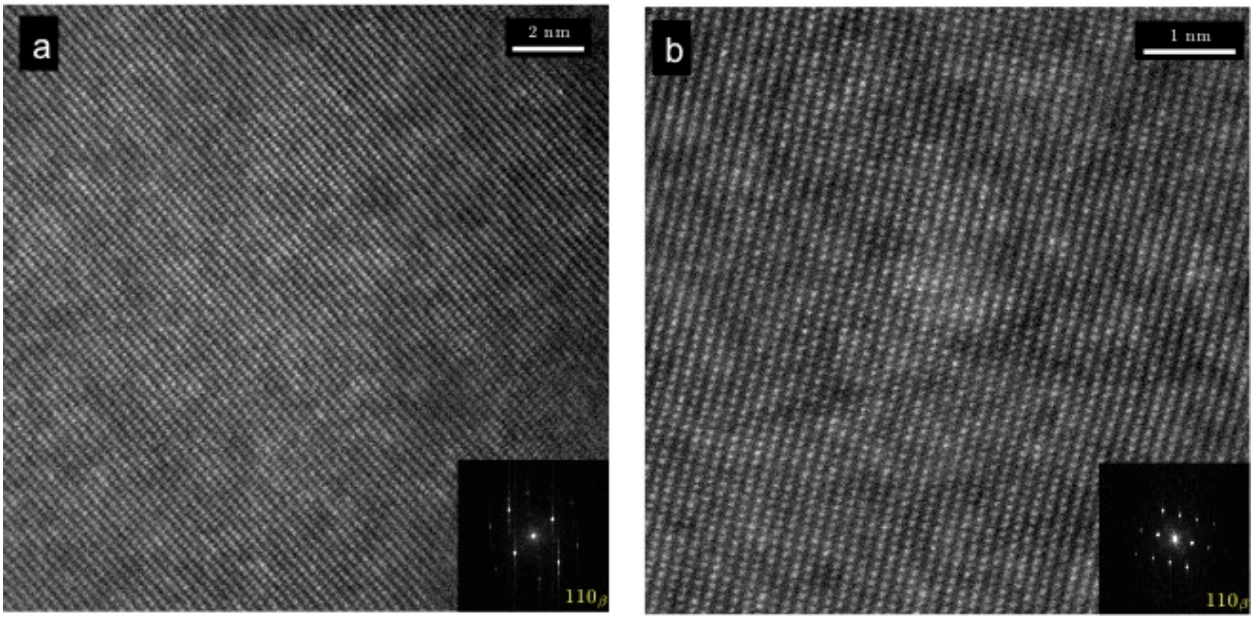

Figure 2.18: HAADF images taken of ST GM samples indicate no presence of secondary phases.

For the sake of completeness and in anticipation of nanoindentation test results in Chapter 5, Figure 2.19 demonstrates a rare occurrence of faint secondary spots in FFT from HAADF image of STGM. Figure 2.19(top) position of extra reflections is encircled in yellow. There are two main features in the image, outlined in rectangles in Figure 2.19(bottom) that could explain the origin of extra peaks. In the upper right black rectangle, there are what appear to be extra atomic columns in between (1-10)β planes. Furthermore, we observe boundary in which there seems to be a stark change in contrast, the precise nature of which is unknown but thought to be different thickness of passive oxide layer on sample surface, which may result in fuzzy contrast and contrast change. Linked Fourier Transform Method (**Appendix A.1)** was performed to determine the origin of extra spots. Results of Linked FT method are given in Figure 2.19. It is clear that the region that contains extra atomic columns does not contribute to extra reflections, but the region with contrast reversal does. The extra columns could be due to local lattice tilt of the planes, possibly from presence of screw dislocation resulting in Eshelby twist [19, p. 454], but the rotation may be too small to appear distinct from fundamental reflections in the FFT.

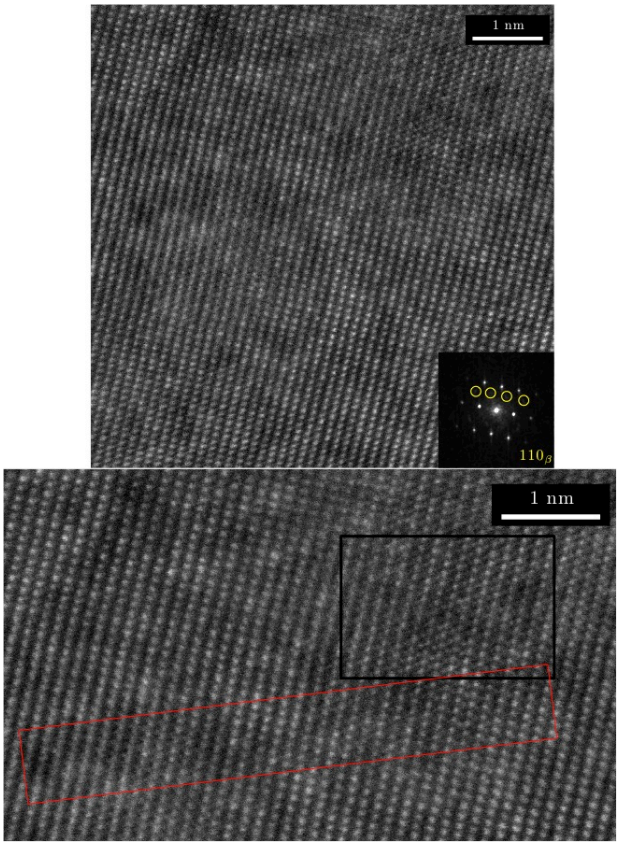

Figure 2.19: Top: FFT of HAADF image of STGM shows existence of faint extra reflections circled in yellow. Bottom: Possible origin of extra reflections could be extra atomic columns (black rectangle) or from contrast change (red rectangle)

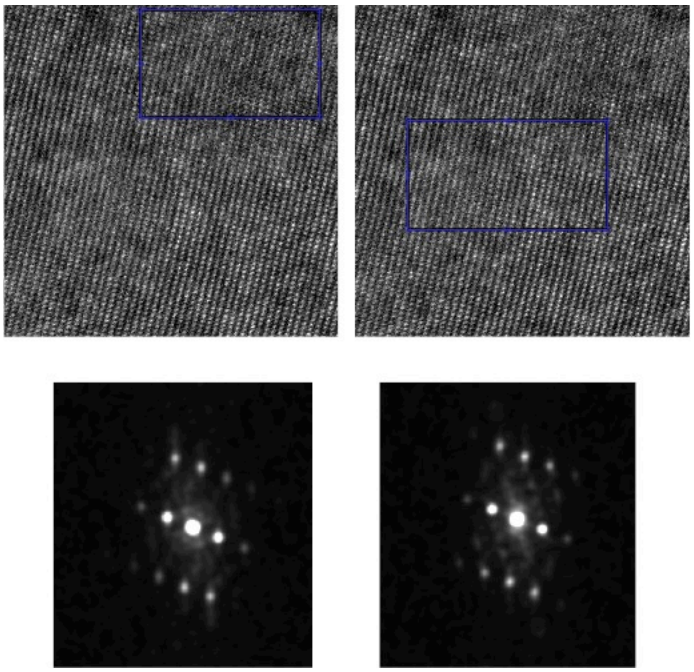

Figure 2.20: Linked FFTs of the image in **Figure 2.19**. (Left) The region with extra atomic columns yields no extra reflections in the FFT. (Right) The region with contrast change exhibits the extra reflections.

2.3.3.3 CWGM: α phase and complex sub-grain structure

As demonstrated in Section 2.3.2.3, the cold worked gum metal microstructure is extremely complex exhibiting a lath microstructure with nanometer sized subgrains appearing similar to dislocation cell network structures found in severely cold worked materials. Initial HAADF investigation of samples cut parallel to the swaging axis confirms sub-grain structure as demonstrated in Figure 2.21 and Figure 2.22. White contrast in the image is equivalent to diffraction contrast, which can be present at the collection angles used. In Figure 2.21, large laths oriented parallel to the swaging axis are apparent, and a complex internal structure, consisting of dislocation threads intermixed with bend contours, can be seen. An interesting v-shaped structure can be seen at the bottom of the image and could possibly be a martensitic structure or twin.

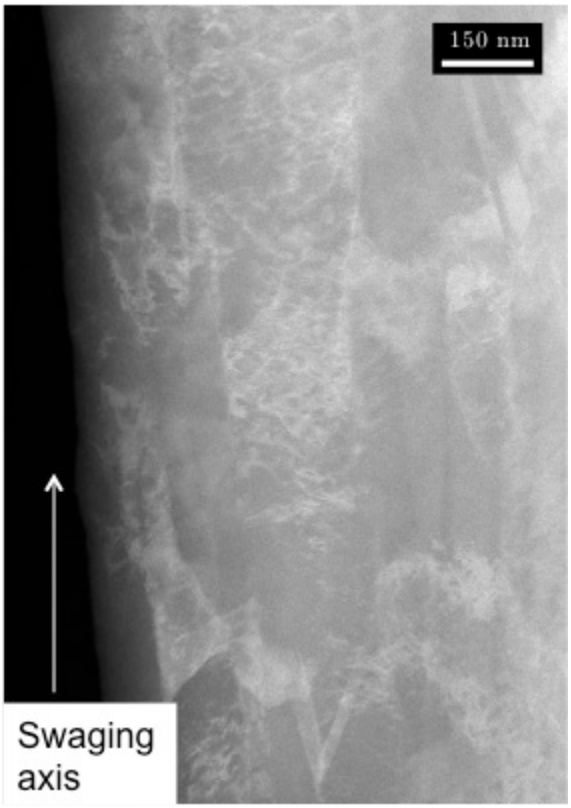

Figure 2.21: Low magnification HAADF image of CWGM cut parallel to the swaged axis gives moderate diffraction contrast that reveals lath structure and complex internal grain structure. Bend contours are also present in the image that are not indicative of sample feature, but it can be difficult to distinguish.

In Figure 2.22, a small lath about 50nm in width is positioned on zone axis and subsequently imaged at higher magnifications. The image on the right is a higher magnification image of the lath and appears to contain nanometer subgrains within the lath. The subgrain boundaries are outlined in the figure and appear to be about 5-15nm in diameter. Lattice fringes are visible in the image, and the subgrain boundaries appear to be small angle boundaries as each of the subgrains largely appears to be close to the [001]β zone axis as the fringes are still apparent. Adjacent subgrains are only slightly tilted off zone with respect to each other.

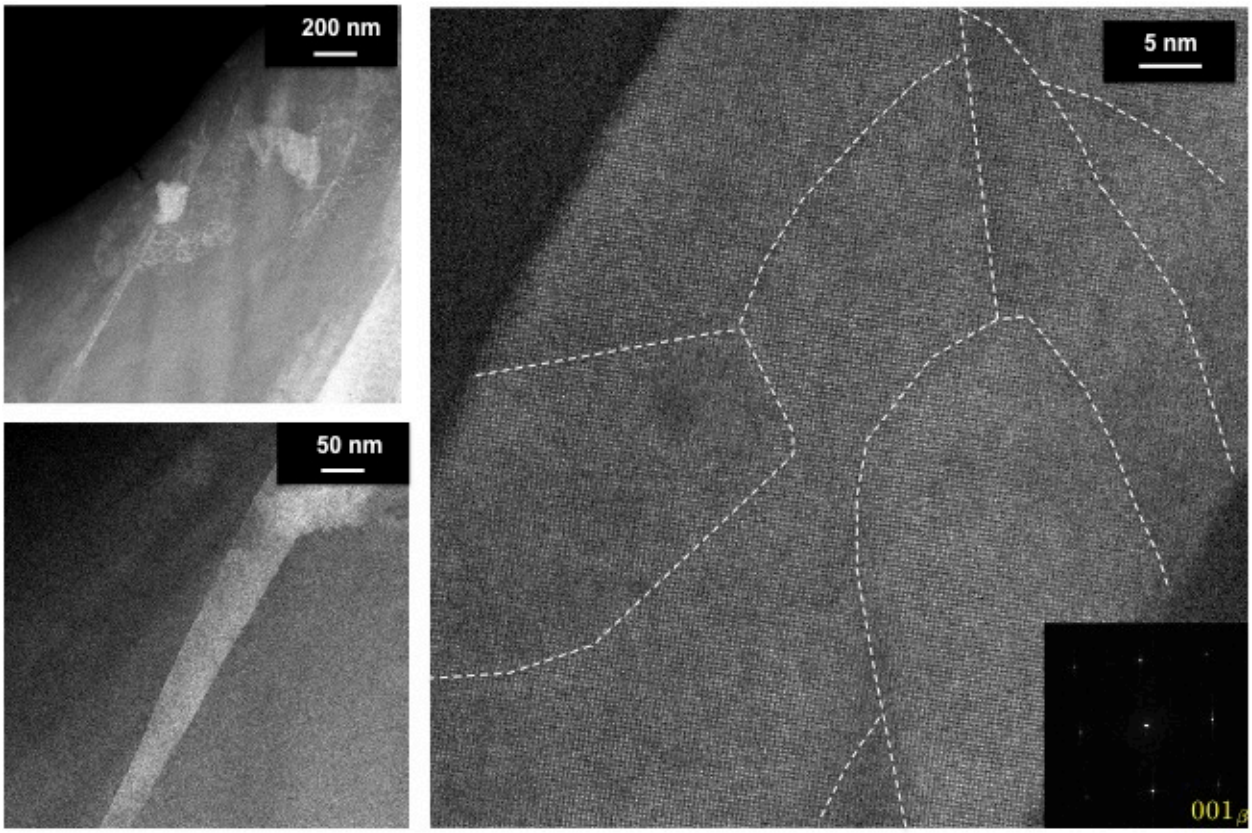

Figure 2.22: Thin lath is imaged at successively higher magnifications in HAADF imaging mode. Left two images are lower magnification images of the lath. On the right, the image is taken at a higher magnification and lattice fringes can be observed. Boundaries between subgrains are denoted where there appears to be a contrast change and change in clarity of fringes. Boundaries thus appear to be small angle tilt boundaries and appear similar in shape and size to the subgrain structure outlined in **Figure 2.10**.

Further atomic imaging of the region within the lath was performed, and we find evidence in the FFT of superstructure reflections. The origin of the reflections is outlined by the red boxed region in the lower left of the image. A higher magnification image of the region of interest is given on the left. Within this region, we find that along a [110]β type direction, every other atom is considerably brighter than its neighbors. Or equivalently, we see that every other (110)β trace is brighter, and furthermore note that the plane trace in the middle is streaked. Line intensity profile scans of an area within the region of interest and in the matrix are given in the upper left, where the colors correlate with the respective areas outlined in the image. We see in the line intensity profile scans that the atomic columns in the region of interest are roughly a third brighter than the dimmer columns. We learn from Section 2.3.3.1 that intensity periodicities in HAADF imaging do not necessarily originate from presence of atoms with higher atomic number, but can be indicative of an embedded precipitate that changes the projected potential. In this case, it is most likely a small, embedded precipitate that contributes to the observed contrast. Typical martensitic phases in β-Ti alloy are ω, α' and α''. The ω and α'' phase would not yield superstructure reflections in the observed locations. We thus turn our attention to the α phase as a potential candidate for the secondary phase. The schematic presented in Figure 2.24 gives the orientation of the basal plane of the HCP α' phase with respect to four

unit cells of the BCC phase. The orientation relationship between the β and α phases is known to be approximately $\{001\}_\beta||\{0001\}_\alpha$ | $<11\text{-}1>_\beta||<11\text{-}20>_\alpha$ [29, p. 47] and termed a "Burgers orientation relationship" as it was theoretically deduced by Burgers in 1947. In the schematic, the red dots represent atom positions for a BCC lattice, and the green dots give the atom positions for the HCP phase. It is clear from the schematic that the α phase can be described as a structure that results when atoms on every other {110}β-type plane parallel to the basal plane undergo a slight displacement in a direction perpendicular to the [110]β direction of an amount that yields an ideal c/a ratio ($0.177a_0$). Figure 2.25 gives a top down view (or [001] zone axis view) that demonstrates the difference in atom

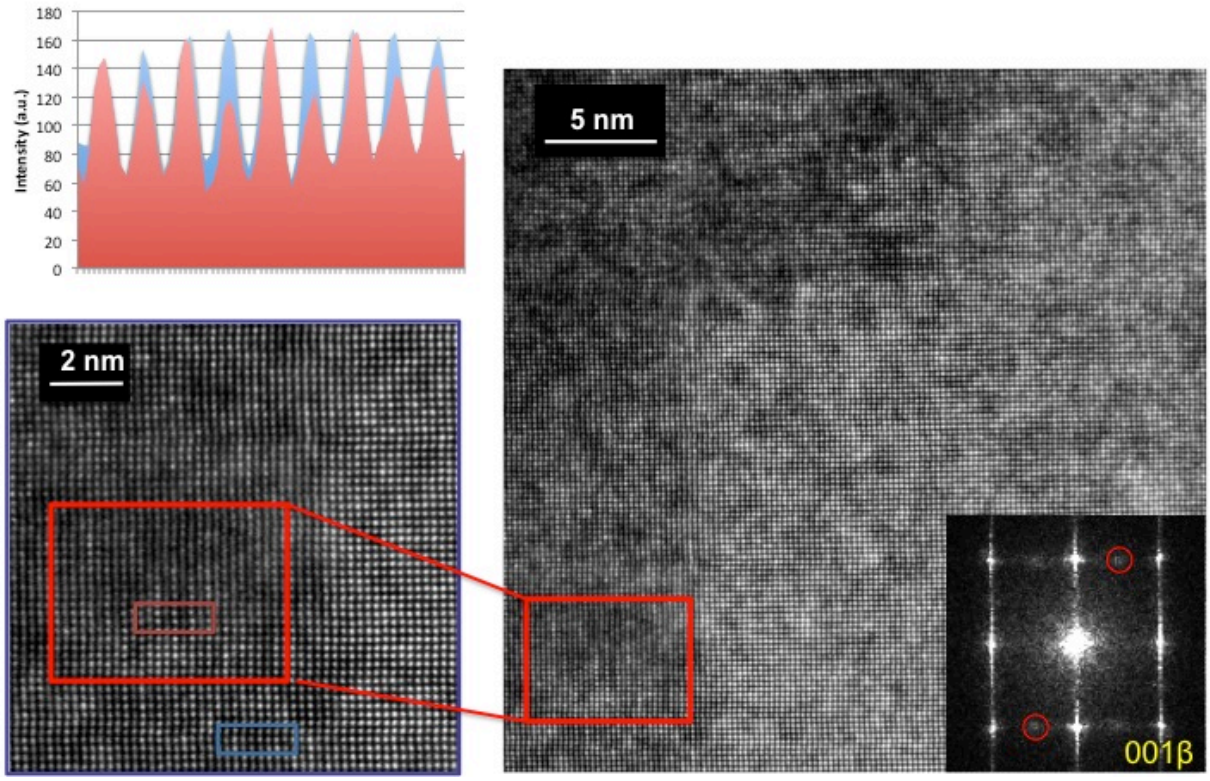

Figure 2.23: Atomic resolution HAADF imaging and line intensity profile graph confirm existence of small α particle. (Right) [001]β zone HAADF atomic image of lath presented in **Figure 2.22.** (lower left) higher magnification of ROI (red box) reveals every other (110)type plane trace is brighter. Line intensity profile of region in particle and matrix confirms that the intensity variation is unique to the particle phase, where the every other column in the [110]β direction is ~1/3 brighter than its adjacent neighboring atoms.

positions between the α and β phases that may result in the contrast periodicity observed in which every other atomic column in the [1-10]β direction is brighter and the middle column is streaked. Where the atoms are brighter, the atoms in the α phase are in registry with the atoms in the β phase. Where the atoms are not in registry due to inclusion of the α phase, the column is "fuzzy" and the plane trace is streaked.

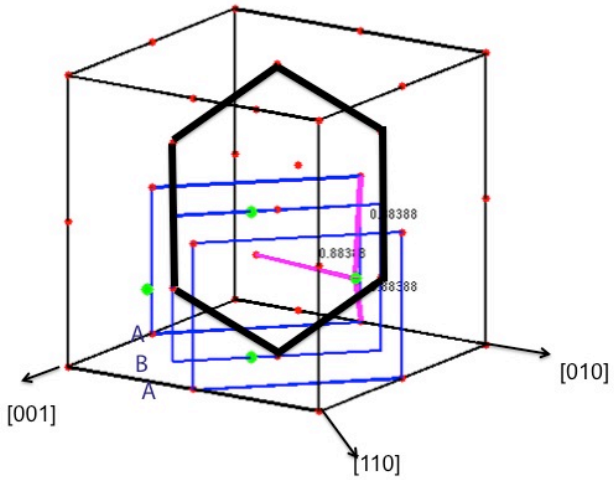

Figure 2.24 Schematic of relationship between α phase basal plane (black hexagon) and 4 BCC unit cells. Red dots denote BCC positions and green denote a few of the HCP positions. HCP structure can be described as displacement of BCC atom in [1-10]β directions on every other (110) plane in the specific orientation shown here.

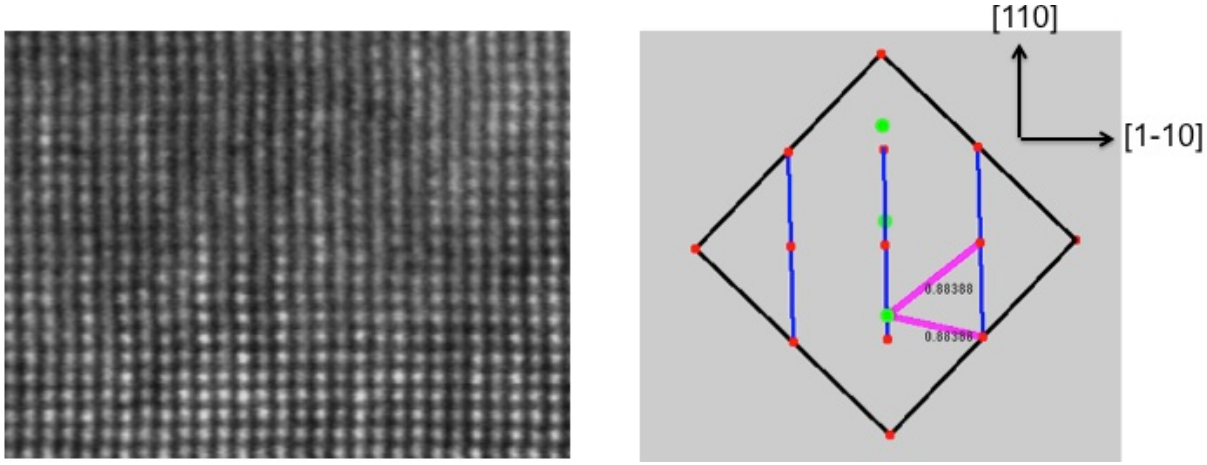

Figure 2.25. Schematic in **Figure 2.24** is rotated to [001]β zone axis as seen on the right, where the green atoms are displaced in the HCP phase from the red atoms on BCC lattice sites. It's very likely that where the atoms do not line up in registry yields the contrast periodicity observed in (left) [taken from inset in **Figure 2.24**]. Thus we conclude that observe contrast motif is due to embedded α precipitate.

To ensure the embedded precipitate is indeed the α phase, we perform kinematical diffraction simulations using Crystal Maker software for the [001]β zone axis. For the α phase we use space group P63/mmc, equilibrium lattice parameters of a =2.95Å and c= 4.68 Å for α-Ti, and Wyckoff positions x=1/3, y=2/3 and z=1/4 to generate HCP structure. We first note there are a total of 12 variants of α phase possible in β: 4 {110}β planes x 3 close-packed directions in the α phase. For each close-packed direction, the diffraction pattern will be the same, and furthermore, the 4 [110]-type directions will only yield two distinct patterns (e.g. the (110)β and (-1-10)β planes given as parallel to the basal plane will yield identical structures.) Thus, we are left with two unique patterns that are given in Figure 2.26. We find that the relationship between the β peaks and secondary α reflections is the same as that observed in the FFT, consistent with 1 main type of variant present (6

possible, as they are degenerate). We note that in the simulation, an ideal c/a ratio and equilibrium lattice parameter for HCP Ti was used, but that an embedded precipitate would likely not have the ideal c/a ratio or equilibrium lattice parameter as the α phase would be a coherent particle. This would account for the slight difference in reflection positions between the α phase and the β phase in the diffraction simulations. Also note that the Crystal Maker software uses a 3-index notation for all structures, including hexagonal unit cells, and the zone axis, shown as $[110]_{\alpha}$ is equivalent to $[11\text{-}20]_{\alpha}$ in 4 index notation.

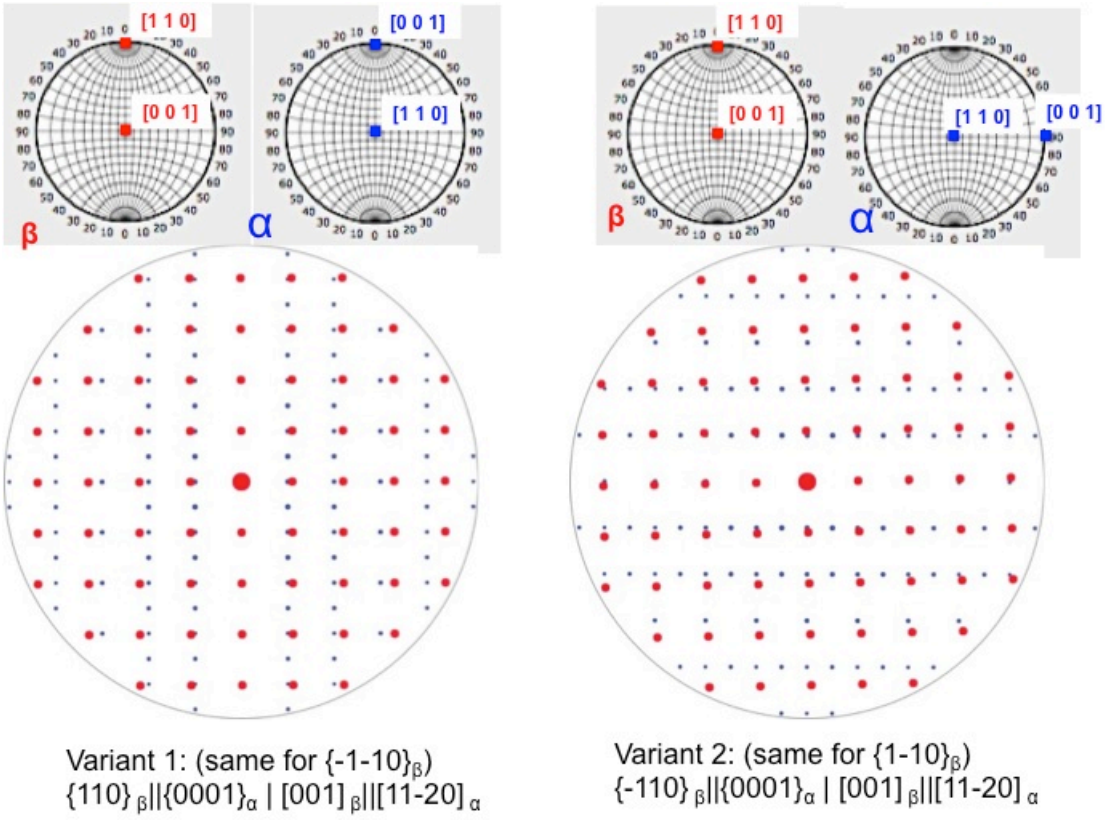

Figure 2.26: Kinematical diffraction pattern simulations of [001]β zone axis with two main variants of α phase. Red lattice is BCC pattern and blue is HCP pattern. The simulations are consistent with the observed superstructure reflections in the FFT of **Figure 2.23** implying the region imaged contains one α variant type.

A different region of the same CWGM sample was imaged and is presented in Figure 2.27. Again, we observe nanometer-width subgrain boundaries as outlined in the figure, and notice that the inset FFT does not reveal any appreciable intensity in α spots. However, upon performing linked FFT analysis we find at least two distinct α variants are present in the sample within a small region. The results are shown in Figure 2.28 and show that multiple regions exhibit α structure spots.

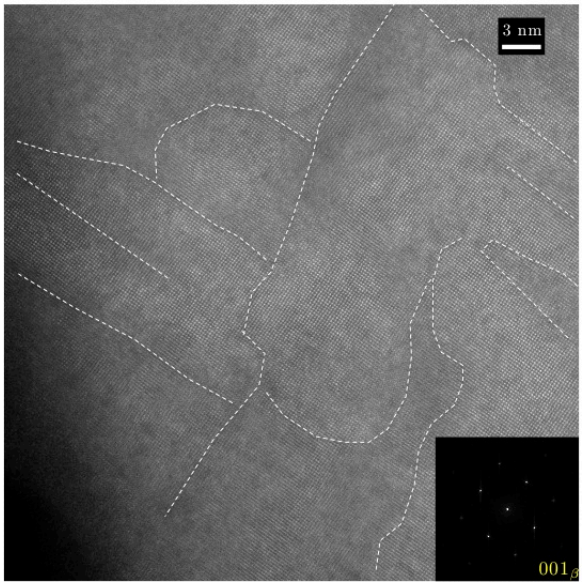

Figure 2.27: Another HAADF image of the CWGM sample with subgrain boundaries outlined. Note almost no intensity is observed at α positions within the FFT, indicating any α particle present must be very small.

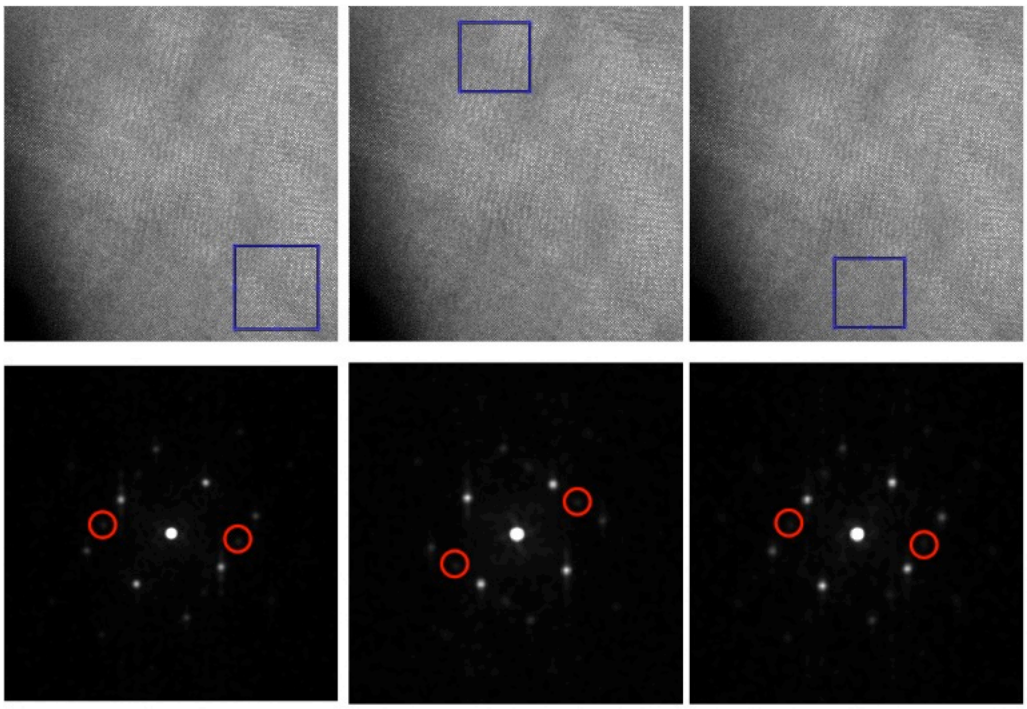

Figure 2.28: Linked FFT analysis of image in **Figure 2.27** shows there are at least two distinct variants present in the sample.

2.3.3.3.1 Discussion

A major focus of the experimental effort has been the identification of the nanosized precipitates that decorate the matrix and may interfere with dislocation motion. Other groups have also found evidence of secondary phases in TEM investigations of CWGMs. Yano et al. [50] found evidence of ω phase in energy filtered TEM and Talling et al. found evidence of α'' and ω plates in the gum metals [31]. From the data presented here, we can only state that small, coherent alpha particles are present. The result is consistent with previously obtained SAXS data [51] that indicates cold worked gum metals contain particles of 1nm diameter. We believe they may have been observing this α phase.

Given that the α particles appear small, coherent, and not associated with any typical martensitic morphology, we speculate that the α spontaneously nucleates during swaging. It has been reported previously that fine scale α precipitates can occur upon cold working of metastable β-Ti alloys even at ambient temperature [52], and we reason that such a process could have occurred here. We also speculate that these particles may explain the non-linear pseudo-elasticity observed in Gum Metals through variant reorientation upon applied stress.

2.4 Summary

Results from the TEM and HRSTEM imaging presented in the current chapter are succinctly summarized in Figure 2.29 below.

As-Received Condition	Solution Treated Alloys			Cold Worked (Swaged) Alloys		
Composition	Ref-1	GM	Ref-3	Ref-1	GM	Ref-3
Grain Morphology/ Texture	▪ Typical recrystallized microstructure ▪ Equiaxed grains ~20-70um width ▪ <110> Fiber Texture			▪ Marbled microstructure viewed along <110> (extent of marble depends on composition) ▪ Lath grains elongated in the <110> swaged direction		
Secondary Phases	nm-sized ω_{ath}	None (<112> streaks)		α'	α''; (<112> streaks)	
Initial Defects	Negligible (grain boundaries)			Dislocation Cell Network Subgrains		

Figure 2.29: Summary of initial microstructural and atomic scale investigation of Gum Metal alloys. Refer to **Table 1** for specific composition of alloys.

3 Zigzag mechanical twinning and deformation-induced omega in solution treated–ref1 (STGM) under nanoindentation

3.1 Introduction

In the current study, we report a zigzag deformation twinning morphology accompanied by stress-induced omega (ω) phase on the twin boundary under nanoindentation. There are multiple plastic deformation mechanisms that can operate in BCC alloys that have purportedly been observed in a variety of Ti-based GM alloys including conventional slip [53,54], twinning [55,31] and stress-induced phase transformations (ω or α'') [55,31]. Another theorized deformation mechanism reported in GM is the controversial ideal-shear, dislocation-free mechanism mediated by shear bands via nanodisturbance generation [4,9]. To be clear, all the cited studies use the specific composition of Gum Metal Ti-23Nb-0.7Ta-2Zr-1.20 (at%), but use different processing methods to synthesize the material. Only the studies conducted in [4,9,8], indicating a dislocation-free mechanism, use the original material from Toyota. In order to elucidate our understanding of the controversial dislocation-free deformation mechanism that may be operating in GM, we first want to determine how off-composition, Nb-lean STGM (ST-Ref 1) responds to applied stress under nanoindentation and if this response adheres to the more conventional deformation mechanisms that have been observed in other GM variants. Furthermore, if the response is one that is widely observed, we want to determine how similar the mechanism is to those previously observed in GM material. We find that this alloy, like other β-Ti alloys, exhibits mechanical twinning but with unique morphological and crystallographic characteristics under nanoindentation. Specifically, this alloy exhibits nano-sized zigzag {112}<111> twins with a deformation-induced ω phase nucleating at the twin boundary, a specific deformation mechanism that has only been previously reported in two studies of plastically deformed alloys of gum metal composition [56,57].

3.2 Deformation Twinning in Metastable β-Ti Alloys

Multiple, complex deformations mechanism can operate in β-Ti alloys, which in general depend on the β stability of the alloy [18], presence and structure of secondary phases [15 58], the extent of deformation in the initial condition, and how the stress is applied (e.g. strain rate, compression/tensile, crystallographic direction of applied stress, etc.)

For metastable β-Ti alloys with compositions near the M_s line (martensite start temperature), the main deformation mode is either mechanical twinning or formation of stress-induced martensitic phases. These modes are preferred over other deformation mechanisms as β stability decreases. It is well known that as the β phase stability increases upon alloying with β- stabilizers (such as Nb or O), the deformation mode transitions from twinning to dislocation slip [59]. Dependence of deformation mode on β phase stability in binary Ti-V, Ti-Mo and Ti-Nb β-Ti alloys was observed by Hanada et al. [15] across a range of β stabilizer amounts. The main observations of Hanada et al. indicated that twinning (specifically {332}<11-3> type) occurs in *unstable* β-Ti Alloys (those containing the athermal omega (ω_{ath}) phase upon quench), and that where stress-induced ω phase is

observed, it is thought to be accompanied or induced by this twinning mode. They observe that an increase in β-stability results in twinning as the primary deformation mode and is unaccompanied by any stress–induced phases. They also specifically report that as β-stability is increased further, conventional slip is observed.

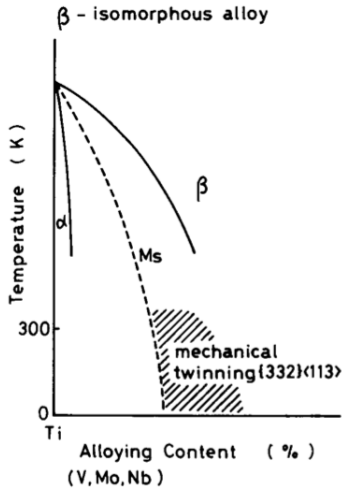

Figure 3.1: Schematic of deformation mode for metastable isomorphous β-Ti Alloys. From Reference [15]. It was initially believed only {332}<113> twinning mode was active in unstable and metastable β-Ti Alloys, but other modes have been observed since.

3.2.1 Crystallography of Twinning in BCC Ti Alloy

Twinning in materials is characterized by the presence of a reflection plane or 180° rotation axis that relates matrix and twin lattices. A twinned lattice that is reoriented with respect to the parent lattice results from atomic displacement equivalent to a shearing movement of an amount that is some integral fraction of the lattice parameter along the sheared direction [60]. Twin geometries are formally defined by the following notation system: the mirror plane is K_1 (also the "invariant plane") and the shear direction is given as $\boldsymbol{\eta}_1$. In the twinned lattice, another invariant plane with respect to the matrix is given as K_2. Plane of shear, s, contains $\mathbf{N}(K_1)$, $\mathbf{N}(K_2)$, and $\boldsymbol{\eta}_1$, with the characteristic vector $\boldsymbol{\eta}_2$ defined as the vector of intersection of s and K_2. Based on specific mathematical properties of these quantities (rational or irrational) and their relationships, twins are classified into different types. A particular twinning system is denoted by the {hkl}<uvw> notation where {hkl} defines the twin plane or mirror plane and <uvw> gives the displacement direction of the atoms in the twinned lattice. This notation is shown in Figure 3.2 for the example of the {112}<111>type twin commonly found in BCC alloys (adapted from [61]).

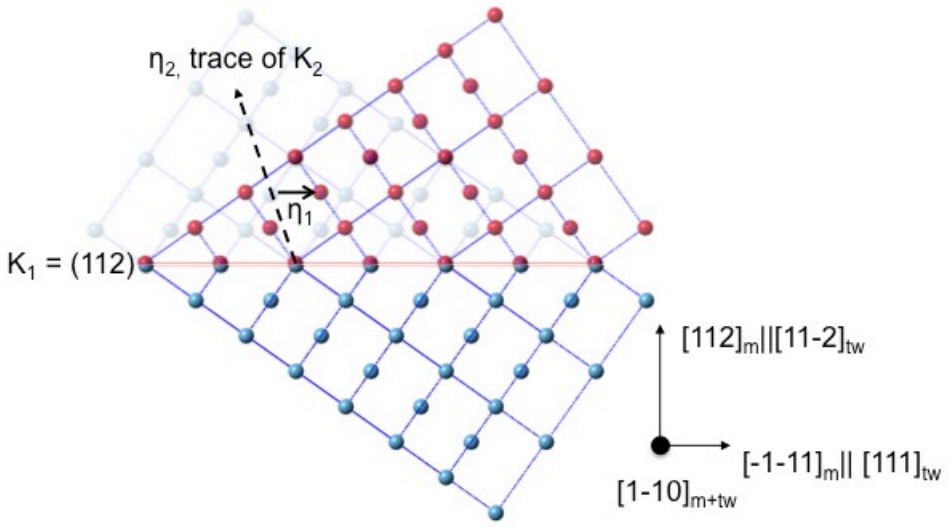

Figure 3.2: Schematic diagram of {112}<111>-type twin in BCC alloys with formal twinning notation system. Figure adapted from [61].

In the particular case of twinning in beta and metastable β-Ti alloys, only certain twin geometries have been observed. The most commonly observed systems are the {332}<11$\bar{3}$> and the {112}<111> types in BCC materials. For BCC materials, lattice shuffle is required for {332}<113> twinning whereas the {112}<111> type only requires shear movement. However, {332}<11$\bar{3}$> deformation twinning is more widely observed than the {112}<111> type of twinning for metastable β-Ti alloys. This has been recently explained by Tobe et al. [62] as a consequence of the low elastic shear modulus c' ($(c_{11}-c_{12})/2$) in metastable β-Ti alloys that would result in a modulated tetragonal structure in the material due to easy shear on parallel {110} planes in the <011> type directions. The modulated structure, shown in Figure 3.3, would require less shuffling of atoms for {332}<11$\bar{3}$> type twinning than for the {112}<111> twinning type. In the case of gum metal and gum metal-like alloys studied here, it has been proposed by Yang et al. [63] that Ti -22.4Nb-0.73Ta-2.0Zr-1.34O(at%) contains the critical Nb composition, below which {332}<11$\bar{3}$> would be the preferred twinning type. A similar alloy with increased Nb content would be more stable and as such the {112}<111> twinning type would be preferred. Conceivably, the increased stability would be correlated with increased shear modulus through increased alloying content of the beta stabilizing element Nb, leading to {112}<111> preferred twinning.

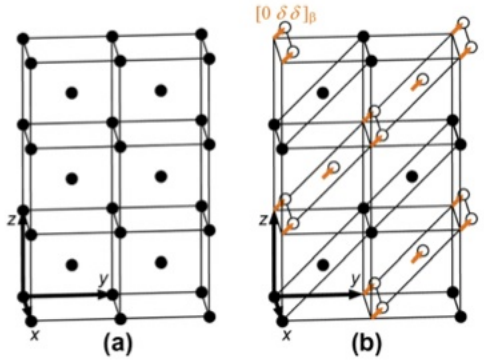

Figure 3.3: Schematic of (a) BCC unit cells and (b) modulated BCC structure that theoretically occurs in metastable β Ti alloys that are lean in β-stabilizing content as a consequence of the low elastic shear modulus. Note every other {110}-type plane is slightly displaced in the modulated structure. Taken from [62].

3.3 Sample Preparation and Methods

The material used in this investigation was supplied in the form of round bar specimens with a nominal composition of 76.6Ti-20.0Nb-0.6Ta-1.7Zr-1.1O at.% (63.1Ti-31.9Nb-2.0Ta-2.7Zr-0.3O wt. %), termed "Ref-1". The bars were fabricated by Toyota Central R&D Laboratories, Nagakute, Japan via powder processing according to the procedures discussed in Chapter 2 and reference [4].

The solution-annealed bars were cut perpendicular to the swaging direction into discs of ~300μm thickness and disc cut to 3mm diameter. Samples were then mechanically polished to ~100μm thickness with SiC paper. A polished surface for nanoindentation was prepared through one-sided jet polishing with a Fischione Model 1010 twin-jet using an electrolyte solution of 4.8 vol% perchloric acid, 28 vol% butanol, and 68 vol% methanol at -28°C and 38V for ~3min (ensuring that the sample is not perforated as in regular jet polishing). One-sided electropolishing was performed prior to nanoindentation to provide flatter surface than mechanical polishing and was achieved by covering one side of the sample with non-adhesive, light transparent, Teflon® tape to prevent polishing action. A flatter, damage-free surface will yield more reliable nanoindentation data and increases yield of electron transparent, plan-view indents upon one-sided jet polishing where the sample is thinned from the backside for subsequent TEM analysis.

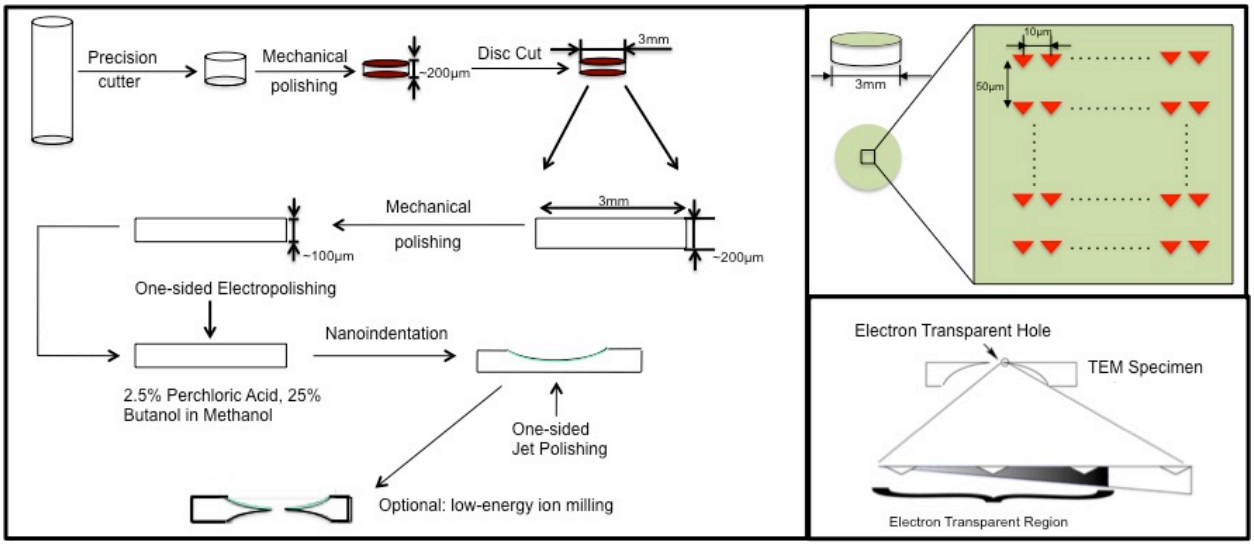

Figure 3.4: TEM Sample preparation workflow for nanoindented Ref-1 Sample, in which sample is electropolished on one side, undergoes nanoindentation, and then finally one-sided jet polished from the back to thin the indents to electron transparency. Depending on the suitability of indents for atomic resolution imaging, further low-energy ion milling was performed as stated in the manuscript. The two figures on the right are adapted from Ref. [39].

Nanoindentation of the electropolished surface was performed *ex-situ* in a Hysitron Triboindenter© fitted with a triangular, diamond Berkovich tip. Nanoindentation was performed for the purpose of imparting heavy, localized plastic deformation in a nominally defect free sample volume. It is believed that the maximum shear stresses are generated underneath the nanoindenter tip, and if this nanometer volume is nominally dislocation

free, as it would be for an annealed/solution treated sample, the shear stress generated in the sample prior to plastic deformation would approach the theoretical shear stress limit of the material [64]. Any subsequent plasticity should theoretically be due to a homogenous nucleation of dislocations in the material if other deformation mechanisms are not activated (e.g. twinning and stress-induced phases). This theory is supported by the experiments of Minor et al. [17] upon *in situ* TEM indentation of an aluminum sample in which nucleation of dislocations appeared underneath the indenter tip at shear stresses approaching the ideal strength.

3.3.1 Nanoindentation: Motivation and methods

Thus, for the Ref-1 sample that has been annealed, we want to determine the deformation response under nanoindentation and determine how the beta-stability might change the deformation mode between the ST Ref-1 and Gum Metal samples. For nanoindentation of ST and CW Gum Metals, we theorize the resultant plastic deformation is occurring via ideal shear. Subsequent TEM characterization of the plastic zone underneath the indent should yield insight into the nature of the local defect structures responsible for the large plastic strains endured and should elucidate the deformation mechanism which allows near-ideal shear strength to be achieved in these materials. For the ST Ref-1 sample, if another deformation mode is observed, it would be thought that the mode is activated before the ideal strength can be reached via nanoindentation. The mode of deformation activated in the ST-Ref1 would conceivably be due to the instability of the BCC phase in this sample, which would not be present in on-composition Gum Metal.

Figure 3.4 gives a schematic of the sample preparation procedure for subsequent TEM analysis. 500 indents, as shown in Figure 3.4, were performed to ensure that a few (~10-15 indents) would be suitably electron transparent for subsequent TEM analysis. They were spaced nominally 50μm by 10μm apart, as stated in Ref. [39]. Figure 3.5 shows the Hysitron Triboindenter® setup (left), along with scanning probe microscopy (SPM) images (right). Top right is the Ref-1 sample nanoindented on an electropolished surface, and bottom right is the sample nanoindented on a mechanically polished surface that has not been subsequently electropolished prior to indentation. Surface roughness of the non-electropolished sample is clear. The initial electropolish prior to nanoindentation, along with the large number of indents (~500), increases the chances of obtaining an indent that is electron transparent upon jet polishing. Indentation was performed under load control with a maximum load of 8mN at a loading/unloading rate of 800μN/s with a hold of 5 seconds.

3.3.2 TEM: sample preparation and methods

After nanoindentation was performed, the sample was jet polished from one side to ensure the nanoindents were electron transparent for subsequent TEM analysis, where the side that underwent nanoindentation was covered again with non-adhesive Teflon® tape to prevent polishing the indents away. The samples were jet polished in a similar manner as in the previous electropolishing step: a Fischione Model 1010 twin-jet polisher was used to create the electron transparent sample with electrolyte solution of 4.8 vol% perchloric acid, 28 vol% butanol, and 68 vol% methanol at -30°C and 47V until perforation (~4:30min).

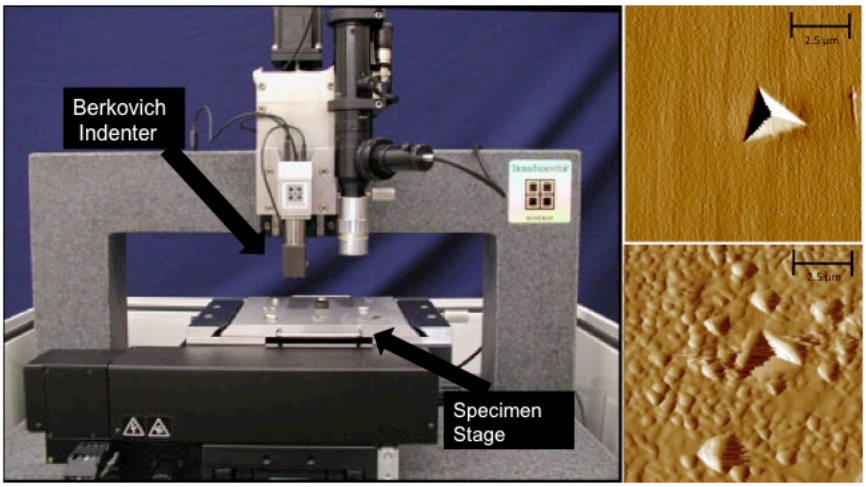

Figure 3.5: (Left) Setup of Hysitron Triboindenter® with Berkovich tip. (Top Right) SPM image of surface of sample after indentation that has been electropolished. (Bottom Right) SPM image of sample surface that was not initially electropolished prior to nanoindentation. Scanning size is 10um x 10um for each SPM image.

Initial TEM analysis was performed on a JEOL 3010 microscope at 300 kV. Selection of suitable indents for subsequent high resolution HAADF-HRSTEM was performed on a modified FEI Titan with a CEOS probe aberration corrector at 300 kV with a probe size of 0.5 Å and probe convergence semi-angle of 17.2 mrad. HAADF signal was collected at an inner collection semi-angle of ~53 mrad, unless otherwise stated.

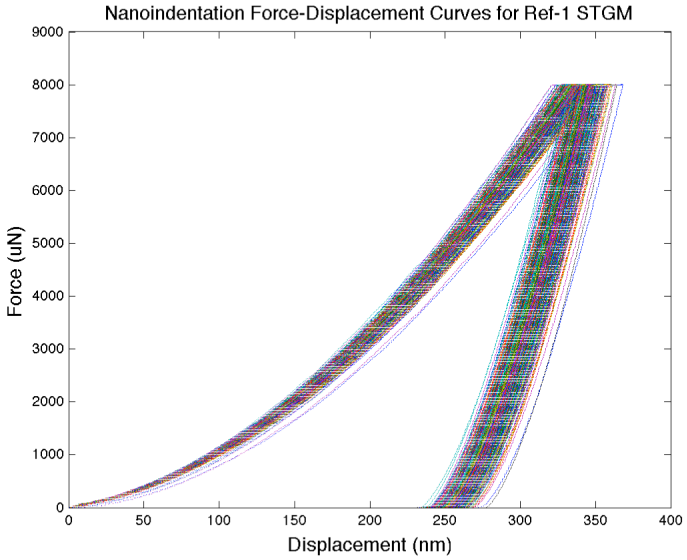

Figure 3.6: Load-Displacement curves for Ref-1 sample, ~500 indentation curves, achieved with load-control function on Hysitron Triboindenter® with max load of 8mN. E_r of 76.5 GPa and H of 4.1 was calculated, but due to the creep observed at the max load, these values are semi-quantitative guides only. No obvious pop-ins are observed so onset of initial plasticity is unclear from the data and could very well be initiated near the start of loading.

3.4 Results

3.4.1 Nanoindentation Data

The load-displacement curves are given in Figure 3.6. Reduced modulus (E_r) of 76.5GPa and H of 4.14GPa was measured using analytical procedure outlined in Oliver and Pharr [65], which is built-into Hysitron® analysis software (further discussion of nanoindentation is given in **Appendix D**). It is unclear where the onset of plasticity occurs, as there are no discrete pop-in features observed. However, the lack of pop-in feature does not necessarily indicate that plastic deformation is not occurring, and it is possible that plasticity initiates near the beginning of loading [64,66]. Indeed, from subsequent *ex*-situ TEM observations, we can be certain plastic deformation has occurred as we later observe residual indent impression in the sample [67].

Creep, or visco-plastic, behavior is also observed during the hold portion of the loading procedure and is apparent by the increase in the penetrating depth while there is no increase in load at the top of the curve. This creep behavior influences the maximum penetrating depth and changes the initial slope of the unloading portion of the curve, and thus changes the calculated E_r and H values from their real values [68]. Furthermore, determination of E_r via the Oliver and Pharr method assumes Hertzian contact between the probe and the sample, but as we know that plastic deformation has occurred, this assumption is not completely applicable [69]. As we are more concerned with plastic deformation mechanisms, which should not change at the relevant loading rates and hold times used, we thus only use the measured values as a general, semi-quantitative guide in our understanding of the mechanical response of the material. It is more important that a nominally defect free volume is sampled for mechanical testing, which is most likely occurring in the nanoindentation test as discussed previously.

3.4.2 Conventional TEM Data

Initial TEM images of indents after one-sided jet polishing procedure are given in Figure 3.7. An amorphous hydrocarbon film that remains after the jet polishing process is observed within the indent (and is most likely covering the top and bottom of the TEM foil). This film is easily removed during subsequent ion milling as seen in Figure 3.10. Consistent with the images of nanoindents in STGM by Withey et al. [39], we observe hairpin dislocations emanating from the boundary of the indentation pit. Also consistent with the results of Withey et al. [39] is the observation of cellular "domains" in the pit of the indent. As will be

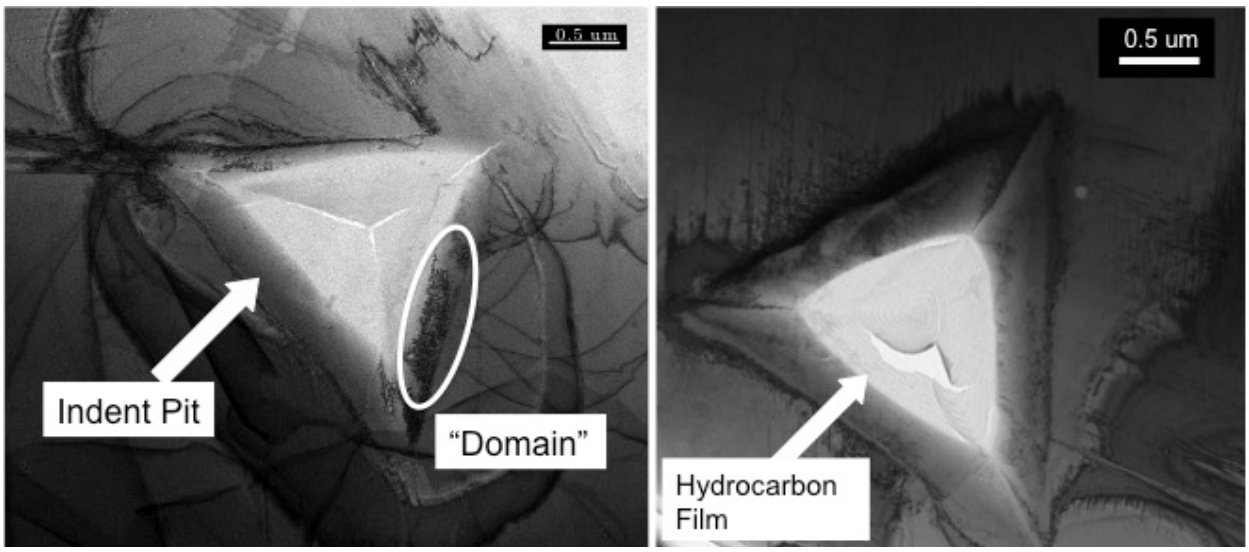

Figure 3.7: Initial TEM images of indents prior to low-energy ion milling. Observation of cellular domain structure and hairpin dislocations is consistent with that of Withey et al. [39]

discussed later in this in Chapter 5, we believe that the domains are simply regions where the lattice has rotated away from its original orientation. Such rotation comes about from the changing loading axis as the indenter penetrates the material during the indentation process, which activates different slip systems. Such phenomenon was observed in both simulations and experiments conducted by Zaafarani et al. in FCC copper samples [70]. In the images of Withey et al. [39], it is initially unclear what accounts for granular-like internal structure of the cellular domains, and what particular defect structures are present within the pit of the nanoindent that would account for the rotations and heavy plastic deformation endured.

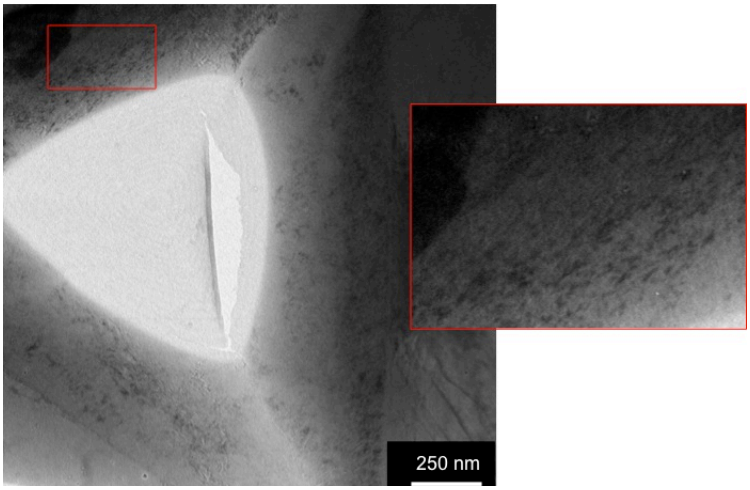

Figure 3.8: TEM image of indentation pit. Higher magnification image (Right) inside indent pit reveals mottled contrast. Origin of nanometer-scale contrast is not immediately identifiable in these images, but is theorized to be short dislocation segments. Samples for atomic resolution imaging were subsequently made owing to the nanoscale dimensions of the defect structures.

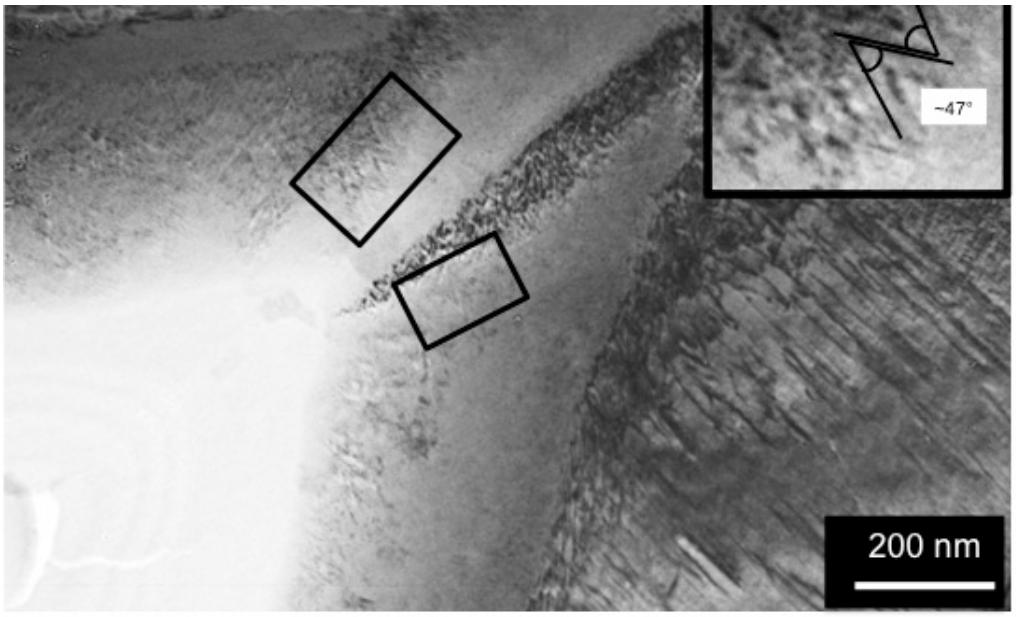

Figure 3.9: (Main) TEM image of nanoscale zigzag, or v-shaped, and linear defect morphologies are observed in the pit of another indent. Such morphologies are generally associated with martensitic and twinning defect structures, but their exact nature is difficult to assess with conventional TEM imaging. (Upper Right) Blown up view of the left rectangle in which the angle of zigzag has been roughly measured to be ~50° and ~47°

Higher magnification bright-field TEM images inside the pit of the indent were taken in order to clarify the origin of mottled contrast inside the indent. An image of the mottled structure is provided in Figure 3.8, but its exact nature is unclear. We theorize these defect structures to be dislocations that are not exactly at the correct tilt to be visualized clearly, with adjacent regions most likely slightly rotated with respect to each other, in addition to simply being short segments. TEM images of nanoindentation of STGM in Chapter 5, reveal similar structures to be, most likely, dislocations that are difficult to clearly image and characterize due to the continuous nature of the lattice rotations within the indent pit. The small, short nature of these defects, along with the fact that they may be in a continuously rotated domain, make it extremely difficult to determine the exact character of such defects using conventional g•b analysis. Note that a similar phenomenon is most likely occurring in as-received CWGMs, where the lattice is distorted from the heavy swaging, which possibly precludes the imaging of defects [37,38] and may have led to the initial conclusion that gum metals contain "virtually no dislocations" [4].

Along with mottled contrast and rotated domain structure, there are interesting V-shaped and straight-line morphologies of nanometer scale thickness that are observed within the indent pit. Such V-shaped or zig-zag morphologies have been observed in other β-Ti alloys originating from {111}<112>-type twins or shock-induced/mechanically-induced ω phase and α'' (FCO) features [63, 31] and is a commonly observed morphology for lenticular martensitic defect structures [71]. Owing to the nanometer-scale dimensions of the structures, however, determining their exact nature proves difficult with conventional TEM imaging. From the image, we roughly measure the angle of the V-shaped structures to be ~50° and ~47°. We determined that higher resolution imaging is necessary to identify the exact nature of the observed structures.

Before atomic resolution imaging can be attempted, however, further sample preparation is required to remove the hydrocarbon layer and thin the indentation pits further. Low-energy ion milling to clean and further thin the sample was performed on Leica Res 101

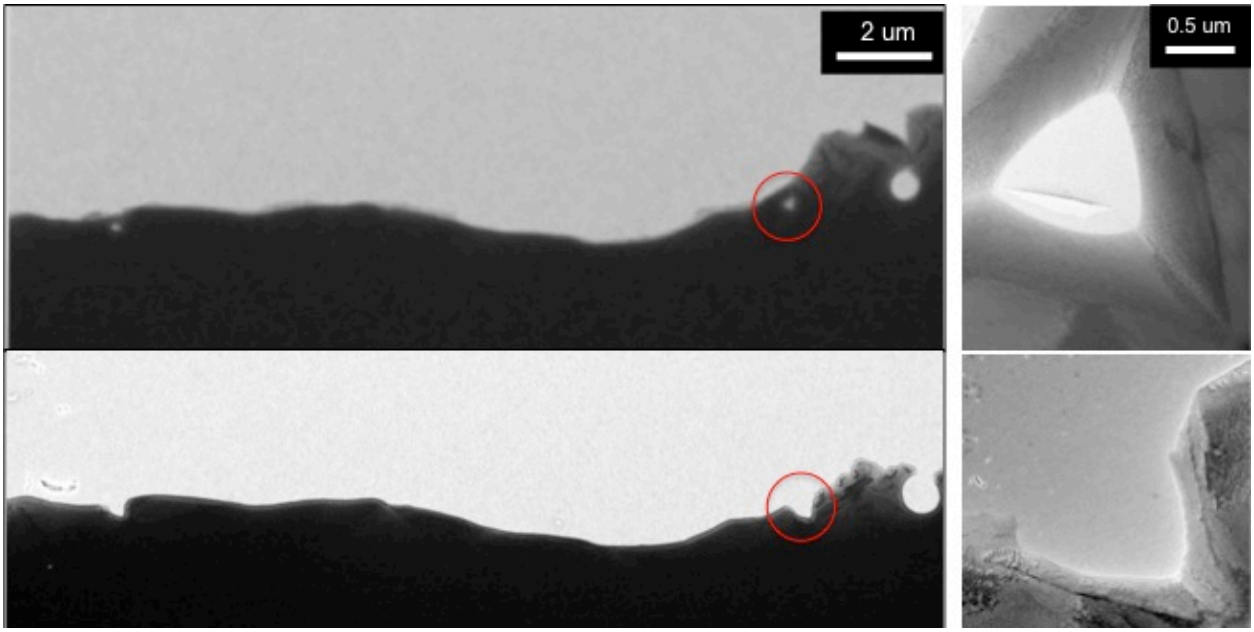

Figure 3.10: (Top) Bright Field TEM images after jet polishing prior to low energy ion milling. Suitable indents are selected for further high resolution imaging. (Top Right) Hydrocarbon layer is present, seen in middle of indent. (Bottom) TEM images of sample after low energy milling thins the indents and removes layer of hydrocarbon.

"Baltec". Milling of previously jet polished samples was performed at 2kV, 1.2-1.5mA, -8°/8° gun tilt, ~30min-1hour depending on which nanoindents are desired for subsequent HRSTEM imaging (the further away the possible indents are from the coastline, the longer milling that has to be performed). However, it can be difficult to ensure that a particular indent will be milled such that it is precisely on the coastline: it is possible to mill away indents that were previously imaged in the TEM, and even if the indent appears on the coastline, it is possible that it still maybe too thick or angled too steeply from the indentation process to be imaged at atomic resolution (however, in this case, it is still wise to use low-resolution ADF-STEM imaging as discussed in **Section 3.4.3.1**). Thus, it is not always easy or possible to identify and thin a particular indent for subsequent HRSTEM imaging, which is why the particular indent in Figure 3.9 was not subsequently imaged in the TEAM 0.5. However, the indent imaged in Figure 3.10 was imaged in HRSTEM, and other indents from other samples were subsequently imaged as well and are presented in **Section 3.4.3:** HRSTEM Data.

Higher magnification TEM images of the indent in Figure 3.10 (bottom right) are given in Figure 3.11. Each image from left to bottom right is taken at higher magnifications, with each successive image focusing on the region inside the boxed area of the previous image. A complex contrast feature is present in the indent of the pit, which, as discussed in Chapter 5, may be short segments of dislocations that are all in slightly varying imaging conditions due to the continuous nature of the lattice rotations in the pit of the indent, and thus exhibiting different black/white contrast features. In this particular indent, no zig-zag or V-shaped structures were directly observed, possibly because the sample tilt was not in a favorable condition for the structures to be visualized.

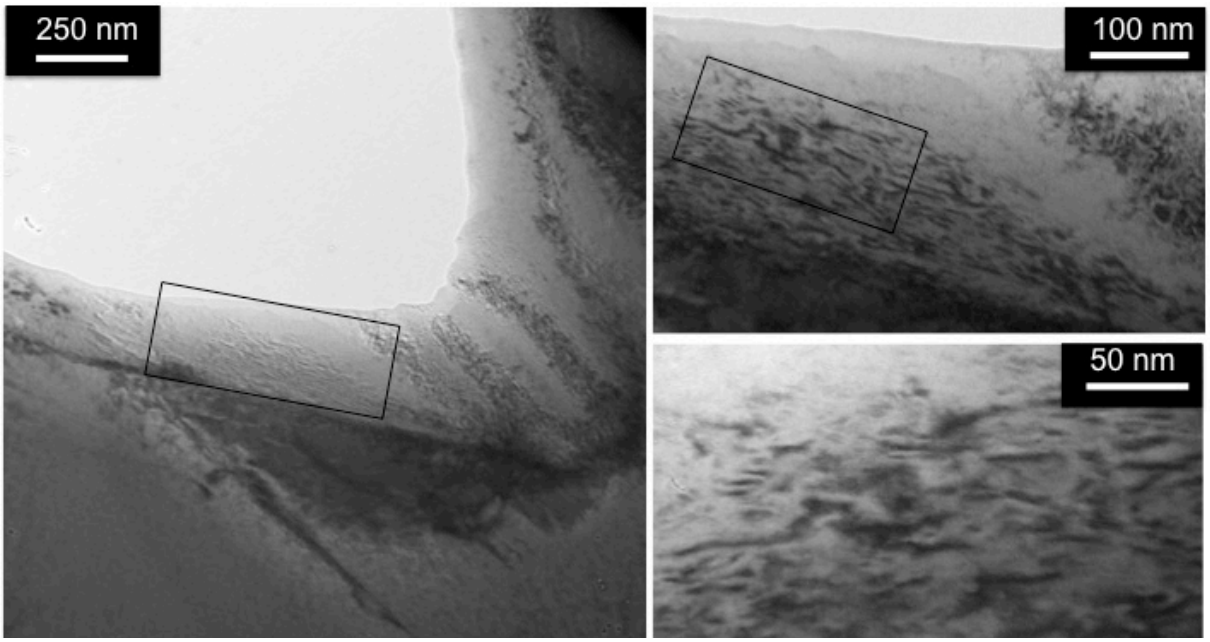

Figure 3.11: Higher magnification images of the indent in **Figure 3.10**. Increasing magnification from left to upper right to lower right of the region contained in the boxed area. The region imaged here is observed to contain complex black/white contrast features that are thought to be dislocations in different imaging conditions.

3.4.3 HRSTEM Data

Subsequent HRSTEM imaging of the particular indent shown in Figure 3.10 and Figure 3.11 did not yield any twinning structures. The ω phase was imaged inside the indent pit as shown in Figure 3.12. However, as the phase did not have any particular morphology, was not associated with any other defect structures, and multiple variants are observed in a small region, the imaged ω precipitates most likely originated from the original quench in the as-received conditions. Thus, these precipitates are identified as athermal ω (ω_{ath}) phase. We determine that the ω phase is present due to the tri-layer contrast periodicity [44, 46](as discussed in Chapter 2) present in both images in Figure 3.12. Since the total area of imaged material in HRSTEM experiment was only a small fraction of the entire

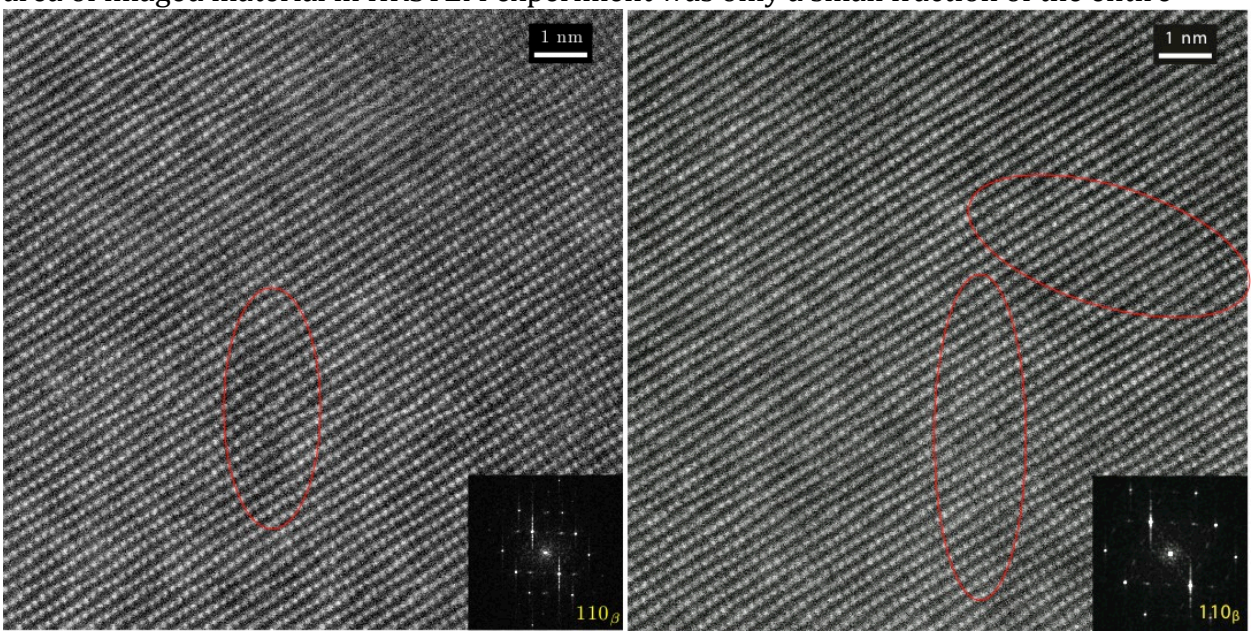

Figure 3.12: Atomic Resolution HRSTEM images from within the indent pit (same indent as **Figure 3.10** and **Figure 3.11**) show only ω_{ath} precipitates that are from the as-received condition. (Left) Tri-layer periodicity in the image denotes one variant of the ω phase, outlined in Red. (Right) The tri-layer periodicity can be difficult to discern in the real space image, but the fact that at least two distinguishable variants are present is clear from the FT inset.

indent pit, with the imaging performed mostly near the coastline at the thinnest regions, it is quite possible that we simply failed to image any twinning/martensitic structures that may have been present in the indent pit. Of course, it is also quite possible that this particular indent did not exhibit such a deformation feature.

3.4.3.1 On the use of HAADF HRSTEM technique for Nanoindentation Results

For the purposes of determining the nature of the deformation zigzag features, atomic resolution imaging is a useful experiment. For all other features and contained defects of the nanoindent, it may not be the optimal experiment. It was theorized in [39] that for indents in STGM, there may be nanoscopic dislocation pinning points, perhaps of a secondary, martensitic phase, outside the boundary of the indent pit and also that "nanodisturbance" defects [4,9] may be present in the nanoindents of STGM which facilitate the continuous rotations observed in the indent pit. Initial evidence of such atomic-scale defects naturally led us to try atomic resolution imaging experiments to determine the nature of such theorized nanometer-to-atomic scale defects, although we

note that the nanodisturbance defect should not be present in the Ref-1 sample because of its different stability characteristics (Ref-1 material is *unstable* with respect to ω transformation). Further discussion regarding the nanoindents in STGM is found in Chapter 5.

It should be noted that the ST-Ref1 samples were heavily rotated within the indent pit (as expected [70]) such that the HRSTEM imaging experiment required careful tilting to bring even adjacent areas inside the pit onto zone axis for best atomic imaging condition during the experiment. Paradoxically, the regions that are best for atomic resolution imaging are typically small areas in which the least deformation has occurred such that the majority of atoms line up in registry along the atomic columns being imaged. In this case, it should be noted that the areas imaged with good atomic resolution may not be representative of the most deformed regions.

In any case, "fuzzy" contrast is sometimes observed from heavily deformed samples as observed in Figure 3.13 (which is of the same indent shown in Figure 3.10-3.12. Figure 3.13 demonstrates that deformed materials can be difficult to image and interpret at atomic resolution as the fuzzy regions could be due to a) heavy deformation, in which case, any atomic scale defects are difficult to discern with this technique b) dirt/carbon contamination on the surface, and c) local thickness difference/preferential etching in some regions, which could conceivably happen given that the sample has undergone local rotation from the indentation process before undergoing jet polishing.

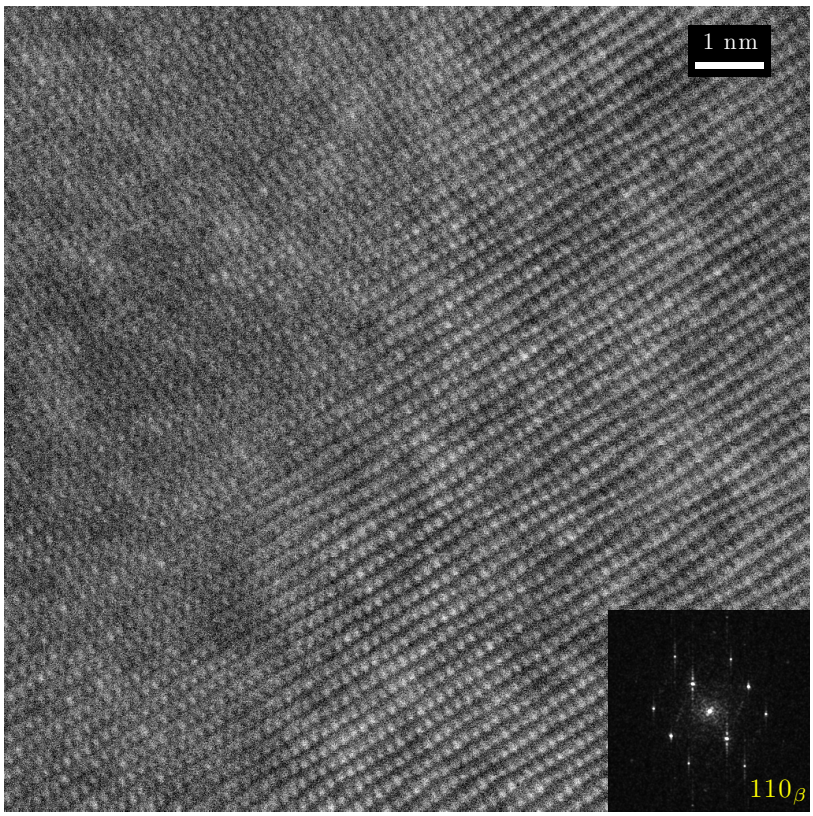

Figure 3.13: Atomic resolution image of region within indent demonstrates areas of "fuzzy regions" (pictured on the left) that could be due to local rotation, dirt, thickness difference, thick oxide layer, or from being precisely an area that has incurred heavy deformation.

More advanced experiments (e.g. defocus series, tomography) could be performed along with post-image analysis and simulations in order to gain any useable data from such deformed or "fuzzy" regions, but in these cases, the experimenter should have a very clear hypothesis and precise crystallographic model in mind to determine the best imaging conditions and specific experimental variables to be tuned. Furthermore, the HRSTEM technique at atomic magnification will not clearly resolve the dislocation structures (or any line defect defined by a Burgers vector) possibly observed in Figure 3.8 and Figure 3.11, unless a) part of the dislocation line is precisely being imaged end-on such that the Burgers circuit can be drawn for the edge component of an end-on line defect [72] or b) the Eshelby-twist phenomenon for screw dislocations is observed in the form of twisted atomic columns [73] (which otherwise cannot be observed from a projected image where the Burgers vector is parallel to the incident beam). Otherwise, for any dislocation line or line defect that is not viewed end on, any displacement or deviation from perfect position in atomic column will be obscured due to electron channeling in STEM mode except on the thinnest, most pristine samples [74], which would probably not be the case for a heavily deformed sample. To reiterate, due to channeling effect and considering the sampled volume of material by electron beam as shown schematically in Figure 3.14, only line defects that are straight and parallel to the electron beam can be reliably imaged in atomic resolution (without further simulations to guide interpretation), and then only for non-screw component. Thus, one should not perform HREM imaging simply to try to observe or precisely identify any theoretical line defect defined by a Burgers vector without a specific physical model at hand or without prior simulations to suggest optimal imaging conditions. This advice, indeed, applies to any attempted experimental imaging of "nanodisturbances". A better method to determine the characteristics of dislocations or "nanodisturbance" structures observed in the pit of the indent would be medium magnification ADF STEM. This method may yield useful results along with more conventional dark field imaging techniques, which utilize diffraction contrast, as opposed to mass/thickness contrast for HAADF STEM, to visualize the line of the defect. Presently, however, there may be no best direct imaging technique to characterize a theoretical nanoscopic defect such as a "nanodisturbance"; perhaps imaging such a defect requires more sophisticated experiments coupled with modeling and simulations.

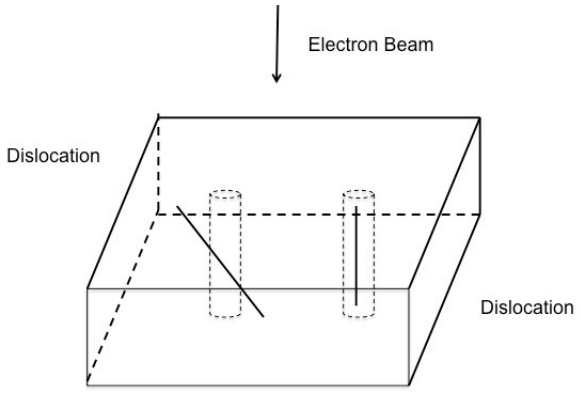

Figure 3.14: Schematic diagram of electron beam traversing through a sample with differently inclined dislocations. Only line defects parallel to the electron beam may be more easily observed in HREM imaging than an inclined line defect (see manuscript for details). Dotted cylinders are regions where the electron beam interacts with the sample. Adapted from [74].

3.4.3.2 Direct observation of Twinning with deformation-induced ω particle at twin boundary

We determine to find the nature of the zigzag structures observed in Figure 3.9 via HRSTEM imaging. We looked at a different sample than the ones imaged in the previous HRSTEM images. As shown in Figure 3.15, extra spots are observed in the inset Fourier Transform. To determine the origin of the peaks, two methods can be used: spot-masking the FFT and performing an inverse Fourier Transform of the mask to determine location of origin of peaks, or a quicker, less-artifact prone method of simply taking the Fourier Transform at various locations to determine which regions most likely correspond with certain peaks observed in the overall FFT. Linked Fourier Transform method coded with MATLAB (**Appendix A.1**) is used for this analysis. Results of the analysis are given in Figure 3.15 which show the existence of a region, outlined as the yellow lath, which is still the BCC phase but rotated with respect to the adjacent regions. This rotation is measured to be roughly 70° from the FFT, consistent with the previously calculated 70.53° misorientation angle about the <110>β direction for {112}<111> type twins in BCC materials [63]. Through further linked FFT analysis and by looking directly at the image itself, the boundary of the twin lath is where the {1-10} lattice fringes end on either side and continue on the other side in a rotated configuration. The boxed region in the upper right contains similar peaks and information contained in the FFT of the entire image shown in the lower right inset, implying it contains a twinned region. No clear boundary is visible in the real space image itself, making this boxed region harder to interpret and analyze.

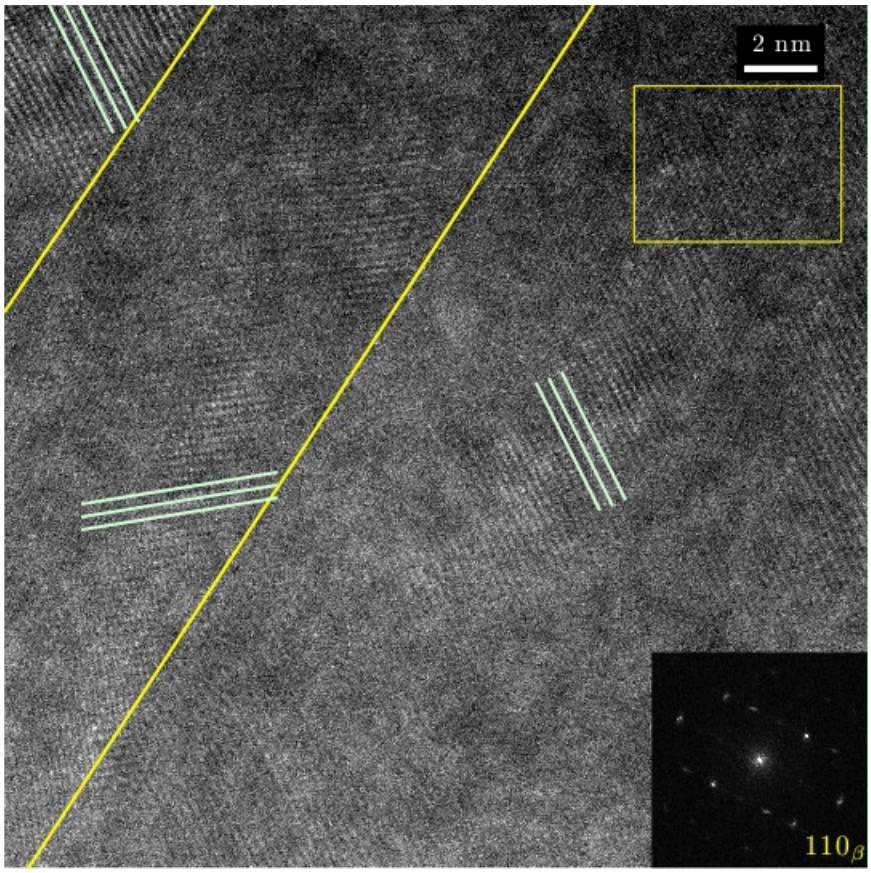

Figure 3.15: HRSTEM image of region within indent taken from another sample than that of the previous HRSTEM images. The inset Fourier Transform exhibits extra peaks that are not expected from a single<110>β zone. Further analysis (**Figure 3.16**) indicates nanometer (~10nm) width twin is responsible for extra peaks, such as the lath outlined in yellow. Region within yellow box contains twinning peaks as well but with no obvious real space boundaries. Green lines indicate (1-10) plane traces

The determination from the given data that the imaged regions are in fact twins is not as immediately obvious as one would expect. As discussed in Chapter 2, the Ref-1 composition is unstable with respect to the ω transformation upon quenching, and thus

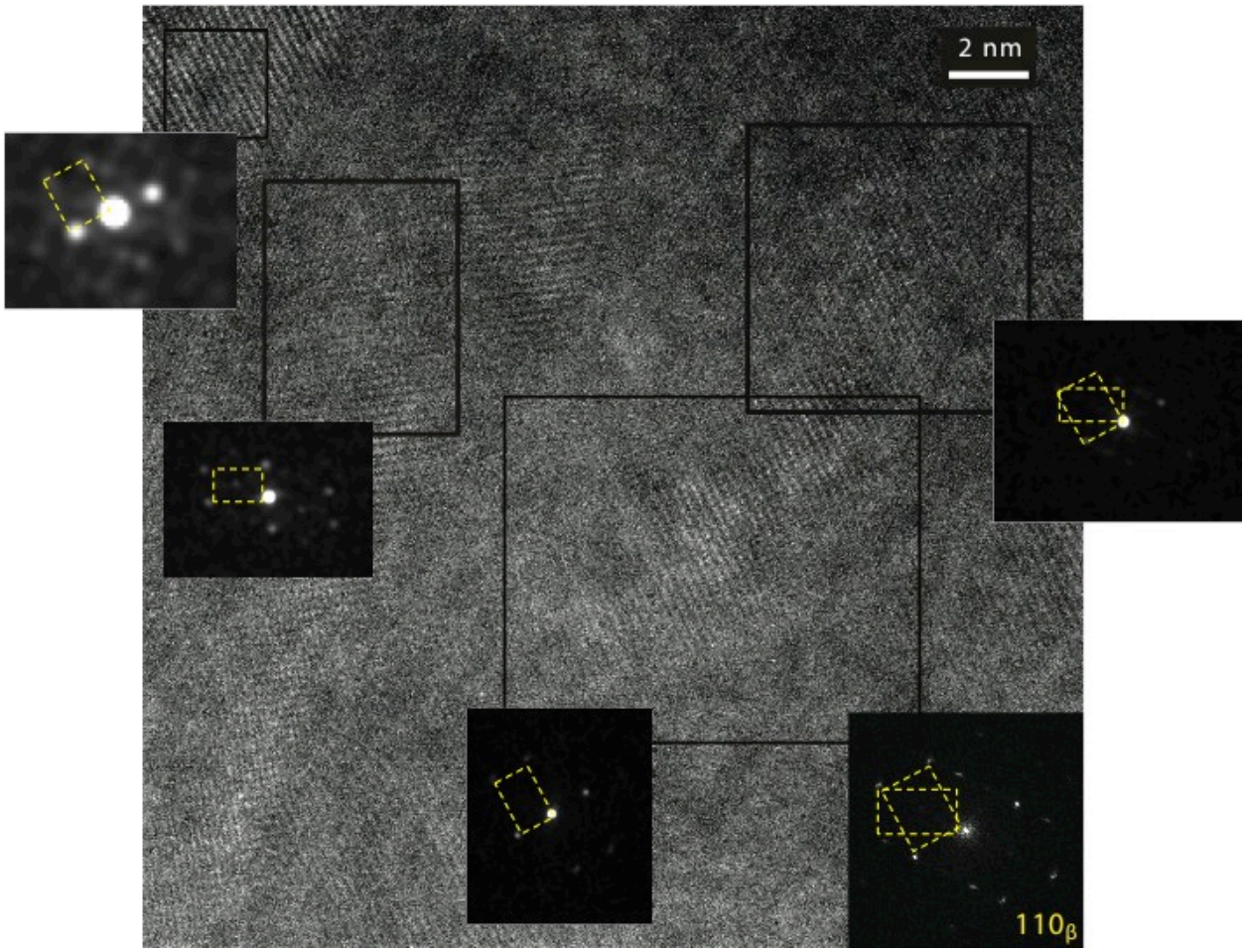

Figure 3.16: Linked Fourier Transform Analysis of **Figure 3.15** reveals twinning. Moving from upper left to lower right, we see the second region contains a different orientation than the other adjacent two regions. The region in the upper right is more complex, containing both orientations in a small region. Extra spot in the second FFT in the ½[112]-type positions (typically associated with alpha phase) most likely emanates from mid-boundary region. The rotation angle between motifs is ~70°, consistent with known twinning geometry for {112}<111> type twin in BCC materials.

contains nanometer-sized islands of ω_{ath} phase [44]. Considering that there are four variants of the ω phase, and that only two are observable from [110] ZA (the other two being degenerate for a total of two sets of superstructure peaks, as discussed in Chapter 2), the number of possible peak locations with respect to the ω phase is manifold, notwithstanding adding those from another rotated domain, itself with its own 2 sets of ω phase peaks. A couple of facts help us understand why the peak number is reduced in the FFTs of the HRSTEM images. Firstly, small regions imaged may have only one of the possible variants as directly observable via tri-layer periodicity or discrete collapse (depending on location and size of precipitate as discussed in Chapter 2). It is the tri-layer periodicity itself and/or the discrete collapse that yields intensities at the given ω phase positions. Secondly, the twins themselves are small and may not contain appreciable

amounts of the ω phase (although it has been suggested that where twin domains form with respect to regions previously containing the ω_{ath} phase, the ω is destroyed and subsequently reforms as discussed in [58]). Thus we may expect only one or two variants from the parent phase and very little or none in the twinned region. Furthermore, as discussed later in this chapter, due to the nature of the twins exhibiting deformation-induced ω phase at the boundary, there is another possibility: it is actually most likely that the FFT will have highest intensity peaks (after the matrix and twin BCC peaks) dominated by the peaks from the variant of the deformation-induced ω itself as opposed to the ω_{ath} precipitates, yielding only one strong variant.

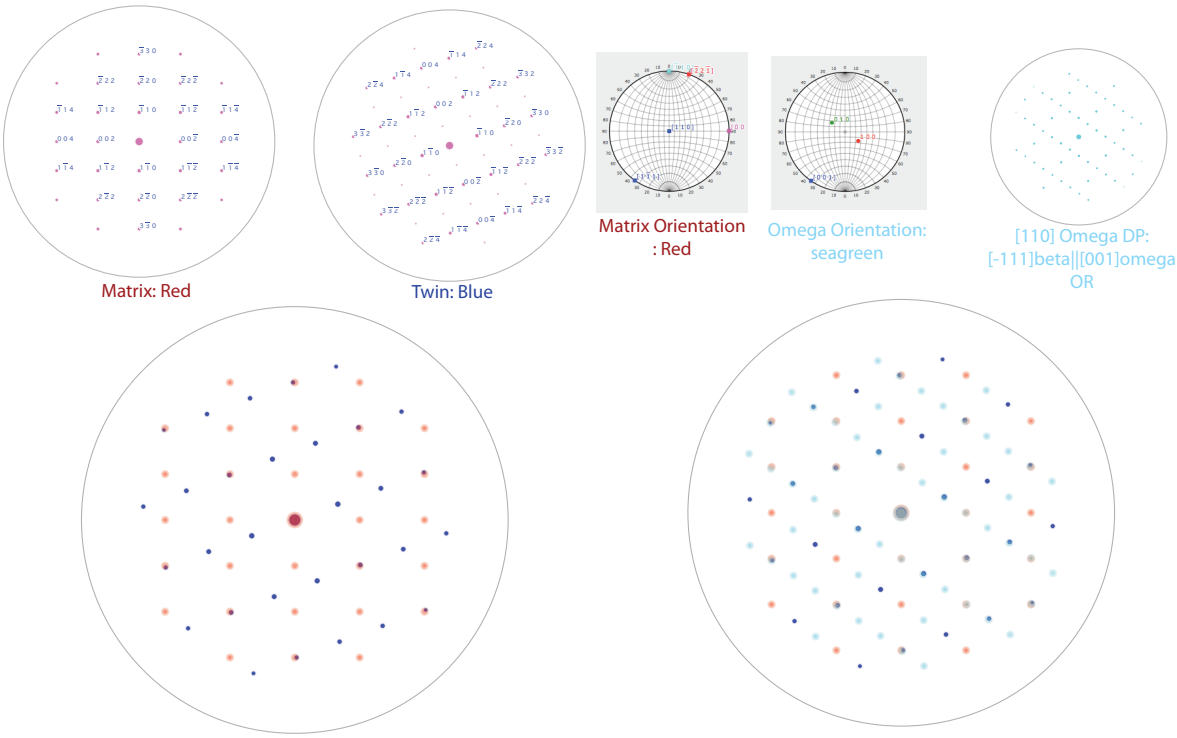

Figure 3.17: {112}<111>-twin kinematical diffraction pattern shown on the left. On the right, the same DP with one variant of the ideal hexagonal omega phase included to account for most of the spots given in the FFT inset of **Figure 3.15**. Notice how all the diffraction peaks of the twin are included in the peaks of the omega diffraction pattern: hence morphology of defect and direct lattice observations are key to deducing such a twin exists when analyzing only the [110] orientation. Furthermore, such spots from the twin will typically be greater in intensity than the omega spots themselves.

Whatever the case may be for the region imaged in Figure 3.16, we can recreate the overall FFT pattern through kinematical diffraction simulations using Crystal Maker software and the ideal Hexagonal omega phase with space group P6/mmm (which is indistinguishable from trigonal omega in [110]β zone axis). To be clear, the FFT and the diffraction pattern are two separate entities entirely, where the diffraction pattern gives information on the periodicities contained within the projected atomic potential of the crystal, and the Fourier Transform of atomic resolution image merely gives information about the intensity periodicities contained within this image. A diffraction pattern may be used to interpret an FFT only if the origin of contrast within the HRSTEM image is known or can be narrowed to a few reasonable possibilities, as is the case here. Results of the simulation are given in Figure 3.17, with the total diffraction pattern including parent, twin and ω variant in the

lower right DP. Indeed we find that one variant of the omega phase (contained in the parent matrix) present with a {112}<111> type twin allows us to recreate the pattern we observe in the FFT of the image as given in the lower right inset of Figure 3.15. Because the ω reflections in the FFT are strong and indicate only one variant, the ω phase contained in the sample is most likely a deformation-induced ω-plate, although it is not directly observed in the HRSTEM image in Figure 3.16.

As can be seen in the simulated DPs in Figure 3.17, all reflections from the twin overlap with ω spots from the one variant, which "obscures" the twin in the FFT. Thus, determination of whether a {112}<111> twin is actually present in the HRSTEM image will depend on a few factors: a) quality of direct lattice imaging, b) morphology of defect (ellipsoidal, straight, or V-shaped), c) shape of the Fourier peaks, and d) intensities of secondary reflections. Related to c), typically ω_{ath} precipitates are small and elongated along {112}-type directions and thus may result in streaked reflections in the FFT. A large, single variant ω plate will have a rounder peak shape due to its larger size. Related to d), if ω peaks for a single variant have varying intensities, then we can deduce the higher intensity peaks are due to twin contribution, otherwise the intensity of ω-only reflections should be identical (where the ω reflections do not overlap with the matrix spots). Of course, a SAD experiment or direct lattice imaging would provide definitive proof that twinning is indeed present. If the twins were large enough to perform SAD, there would be

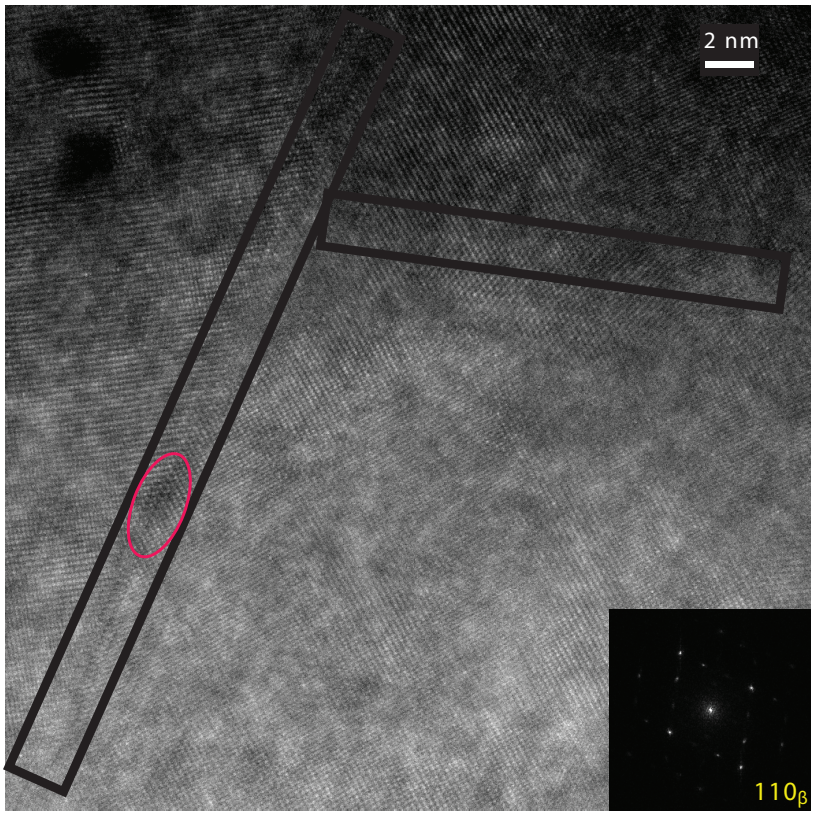

Figure 3.18: HRSTEM image of same sample as that in **Figure 3.15** at an adjacent area. ω lath on the twin boundary (left rectangle) is clear from the discrete collapse, which exhibits >1/4 collapse as observe inside red ellipse. Entire imaged region is heavily deformed and contains complex twinning structures and morphologies that cannot be clearly imaged at the same sample tilt condition due to heavy local rotation. On the other twin boundary, outlined in the black rectangle on the right, an ω plate is present

an obvious 70.53° misorientation angle about the [110] zone axis. However, given that the size of the twin laths here are nm-wide, adjacent and in a continuously rotated nanoindentation pit, this experiment was not easy to perform.

Indeed, as shown in Figure 3.18, an omega plate can be observed in the left black rectangle, as hypothesized from the DP simulations. This precipitate continues to the image edge, separating the image into primarily twinned and un-twinned regions. The twin can be easily identified by noticing the ~70° tilt between the (1-10) plane traces). The diagonal streaking in Figure 3.15 that seemed to delineate a wide boundary between different rotated crystal domains probably has its origin from the existence of an ω lath on this boundary, as typical HRSTEM images of the ω phase demonstrate streaking feature in {111}-type directions. Figure 3.18 contains interesting features regarding the complex morphology of the twinning and deformation, but is difficult to analyze further as the entire region could not be imaged directly at the same sample tilt conditions.

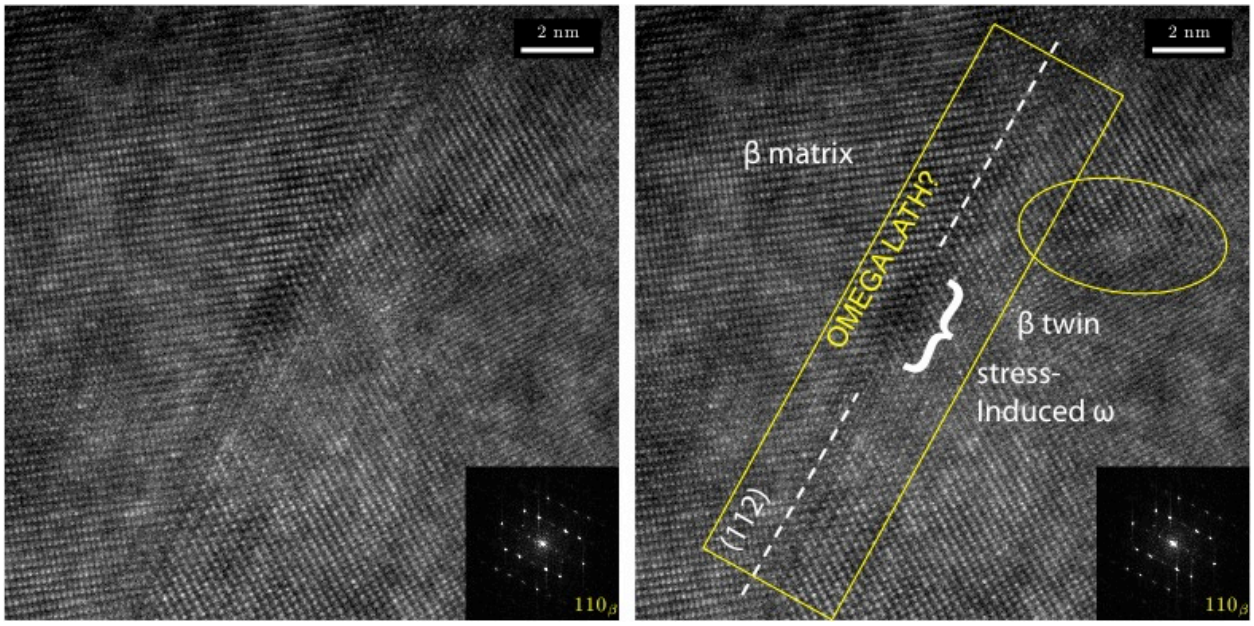

Figure 3.19: HRSTEM image clearly showing omega particle or lath on the twin boundary. The collapse of the $\{111\}_\beta$ planes that occurs in ω phase is obvious, in contrast to how ω_{ath} phase appears in HRSTEM conditions (see **Figure 3.12** where the discrete collapse is not typically observed due to small amount of collapse and small size. This leads to the conclusion it is most likely deformation-induced ω particle given its appearance and placement along deformation twin boundary. Yellow ellipse contains another ω particle: it is unclear whether this is ω_{ath} or pressure-induced ω.

Part of the ω lath separating the matrix and twin domains is more clearly imaged in Figure 3.19: after careful tilting, the matrix, twin and part of the ω lath are imaged on zone axis. Note the two images in Figure 3.19 are the same, but the image has been annotated in the right figure. The ω lath appears to have the typical orientation relationship of $(-1010)_\omega$ $||(211)_\beta$, $[0\text{-}112]_\omega$ $||[1\text{-}10]_\beta$ but appears to have a habit plane of (112)-type which is distinct from the typical habit plane ω_{ath} of $(-1010)_\omega$ $||(111)$.

In the middle of the ω lath, discrete collapse is evident. Typically the ω_{ath} phase precipitates only have barely visible collapse, if any at all. This is due to its small size and

nature of the mechanism of formation that leads to impartial collapse [28]. Thus, ω_{ath} does not typically have an ideal hexagonal structure, but has only undergone partial collapse of the {111}-type planes, much less than the amount exhibited in the bracketed region of Figure 3.19. We believe that the ω phase may extend out further than this local region (identified by the bracket in the image) due to the existence of tri-layer periodicity bordering the twin boundary (mostly to the right of the boundary). We do not know if the large discrete collapse is maintained as the phase extends further into the twinned region. We know that discrete collapse can be obscured by matrix columns depending on the position of ω particle and defocus value (as discussed in Chapter 2) [44]. If simply less collapse has occurred and the phase tapers off, it is not immediately clear why only a part of the ω lath has undergone larger, almost complete collapse. Due to the complicated defect features (overlapping twin and ω plate) present in the image, it is difficult to know if the ω lath extends wider than the "lath" region outlined by the yellow rectangle.

Higher magnification image of the ω phase is given in Figure 3.20. As discussed above, the ω lath imaged seems to contain regions that have undergone larger collapse than typical

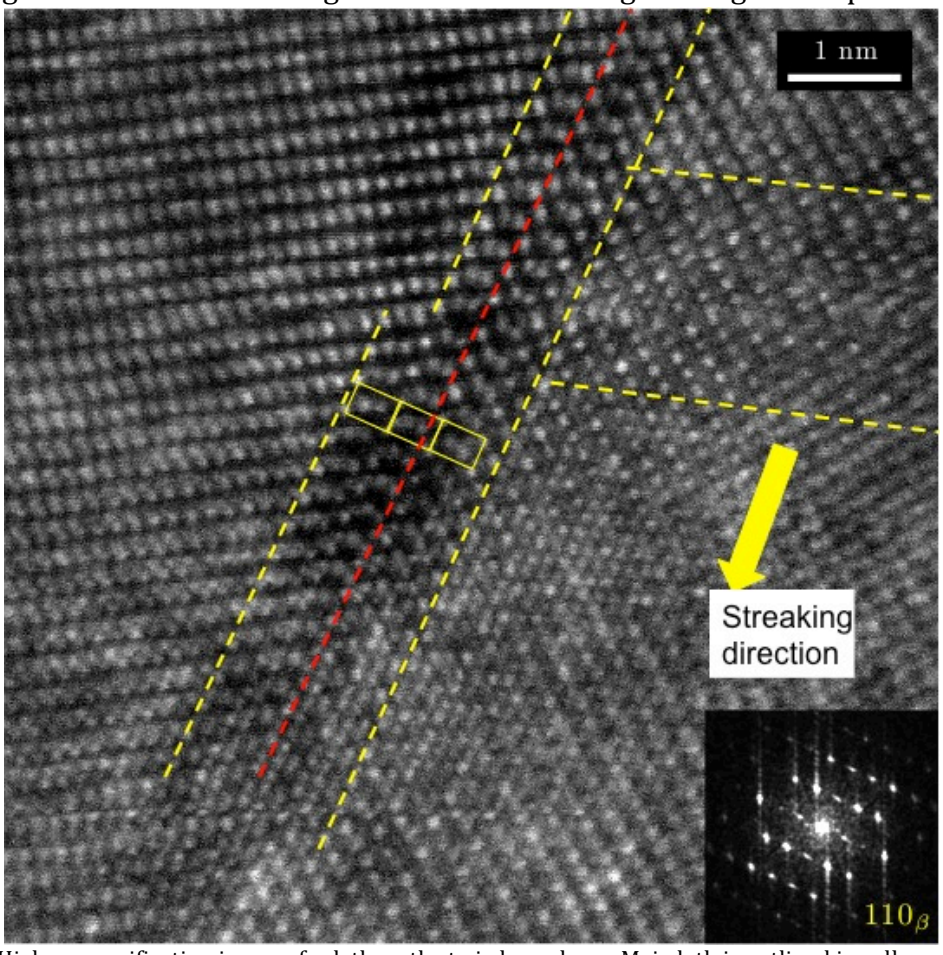

Figure 3.20: Higher magnification image of ω lath on the twin boundary. Main lath is outlined in yellow and contains instances of discrete collapse of {111} type planes, >50% as observed with in the yellow rectangles. The red dotted line indicates the mirror plane of the twin. The lath may extend laterally outward, as indicated by streaking in the twinned region. Extra ω lath is also outlined in dotted yellow, but it is unclear if this lath is related to the ω lath at the twin boundary.

ω_{ath} precipitates. The collapse in some places is even observed to be nearly complete as observed within the outlined cells. The location of the twin plane is given as a dotted red line and follows the trace of (112)-type plane. A second ω lath is outlined within the twinned region, but it is not clear if this is also a pressure-induced ω lath or an original ω_{ath} particle. As discussed above, the primary ω lath may also extend beyond the dotted lines as indicated by the streaking observed in the twinned region.

In summary, the imaged ω phase seems to be an elongated lath or plate at the boundary of a deformation twin, exhibiting a {112}type habit plane with relatively-large discrete collapse. This leads us to believe that it was nucleated on the boundary during twin formation and that it is not an ω_{ath} precipitate.

3.5 Discussion

Plate-like morphology of relatively large size has typically been observed only for mechanically-induced ω phase [29, p. 500], indicating that the observed ω plate may have been induced by the mechanical loading. A similar, if not identical, deformation mechanism - - deformation-induced ω phase formed on {112}<111>-type deformation twin boundary-- has been reported in two other studies: a) cold swaged Gum Metal with typical composition Ti-23Nb-0.7Ta-2Zr-1.2O at% as observed by Xing et al. [56] and b)3.5% cold rolled and uniaxial tension samples of Ti– 36Nb–1.4Ta–2.8Zr–0.3O (wt.%) (close to typical Gum Metal composition) alloy as observed by Lai et al. in 2015 [57].

In the study by Xing et al. [56], HRTEM investigation revealed ω regions and plates accompanied by thin {112}<111>-type lamellar twinning. Their alloy, unlike the one used in this study, does not contain ω_{ath} after quench, implying any observed ω must have been nucleated from mechanical loading. Figure 3.21 features an image from the investigation to underscore the similarity of their results to those found in the current study. They claim, citing evidence from previous study [75], that the typical mechanically induced {332}<113> twin system found in unstable β alloys is suppressed in these alloys due to the addition of oxygen which interferes with the shuffle and shear mechanism necessary to produce this twinning system. Furthermore, they argue that as oxygen in β-Ti alloys serves as a solute strengthener and increases the critical stress needed to activate slip, the deformation mechanism favored in these alloys is twinning over conventional slip. Thus, we can understand why the {112}<111> type twinning system is favored as a deformation mechanism in the alloys studied in this investigation.

What remains unclear is how the mechanically-induced ω particle forms, and why it occurs on a {112}<111> twin boundary. Xing et al. [56], again citing evidence from a previous study by Hsiung et al. [76], argue that a dislocation-based mechanism may explain the formation of the mechanically-induced ω particle and why the ω particle is accompanied by the {112}<111> twinning system. The study by Hsiung et al. [76] that the authors cite investigates the formation of stress-induced phases accompanied by {112}<111>-type twinning in shock-loaded BCC Ta alloys. While the ω phase and BCC twin structures are morphologically unrelated in the study by Hsiung et al. [76], contrary to the findings in the current study, they report them as competing mechanisms in the same alloy under shock loading. The mechanism for {112}<111>-type twinning in BCC materials can be described

by a/6<111> shear on successive {112} planes. They argue that the mechanism for formation of deformation-induced ω phase can be described similarly, except that the shear amount is inhomogeneous on successive {112} planes. While some believe a shuffle mechanism can account for the formation of the deformation-induced ω laths via shear due to the lattice instability that is intrinsic to metastable β-Ti alloys [29], Hsiung et al. [76] suggest that their formation is due to dissociation of a/6<111> edge dislocations into differently sized partials. The latter mechanism is able account for the observed volume fractions of the different deformation structures based on the fact that the partials that ultimately form the ω phase are expected to move more slowly, resulting in smaller ω phases and larger {112}<111> twin lamellae. In any case, due to their similar mechanistic origins that involve shearing on successive {112} beta planes, Xing et al [56] and Hsiung et al. [76] argue that it is reasonable that both structures may accompany each other under deformation in their respective BCC alloy systems.

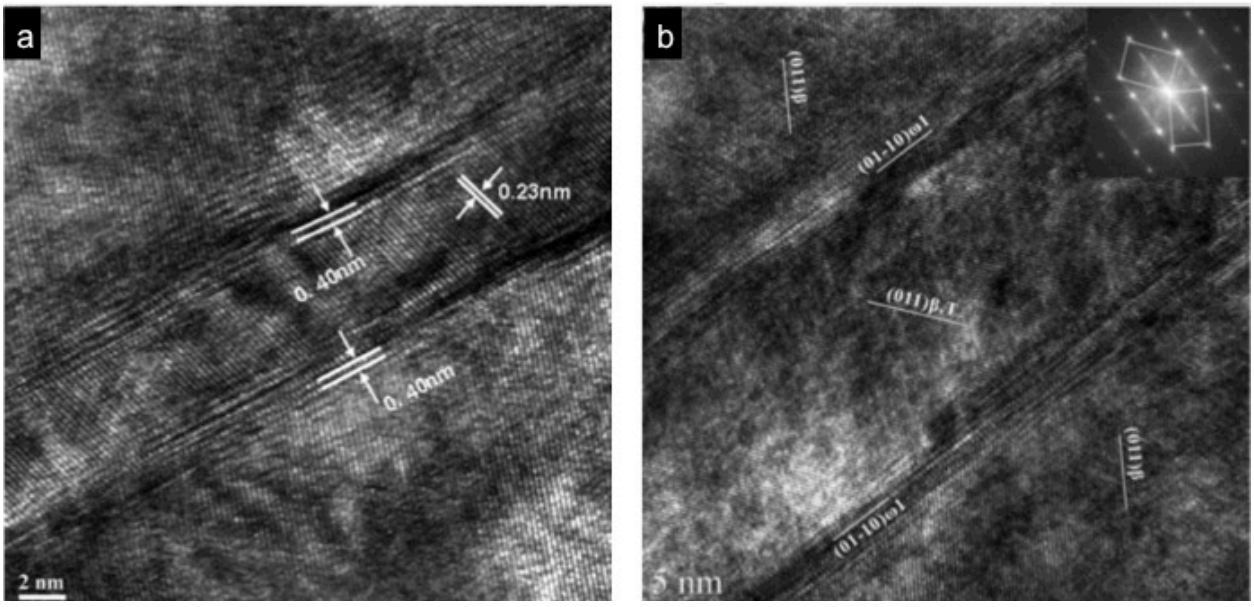

Figure 3.21: HRTEM images from (a) Ref [56] and (b) Ref [57] show evidence of ω plates present on {112}<111>type twin boundary, similar to that observed in this study.

Lai et al. [57] find similar deformation-induced ω laths on the twin boundary, as shown in Figure 3.21b. As they observe the ω-plate twin boundary morphology for both cold-rolled and tensile specimens, they argue that the deformation-induced ω transformation is independent of macroscopic stress state. It is important to note that the alloy in this study did contain previous islands of ω_{ath}, but the authors argue that the cold-rolling and tensile process are performed at too low temperatures and are performed in too short a time period for nanosized ω particles to transform into plates. The authors perform *ab initio* calculations to calculate energetics of the β to ω transformation path and find that due to an energy barrier, it is unlikely that the ω phase can spontaneously transform from the β phase, as speculated in [29]. However, their calculations, using the mechanistic model for twinning and ω transformation outlined by Hsiung et al [76], support the notion that if a local stress is present to move adjacent {112} planes in the <111> direction by some

minimum amount, the energy barrier may be overcome. Thus, they argue that the twinning that occurs under deformation is responsible for ultimately inducing the nucleation of the ω plates. It is the same shearing stress that forms the twin that also allows the energy barrier to be overcome to nucleate the ω phase, explaining why it is found at the twin boundary.

3.6 Summary

In this investigation, we have found that ST Ref-1 material deforms under nanoindentation via zigzag <112>{111} twinning with ω phase nucleating on twin boundary. This is confirmed with atomic resolution HRSTEM observations and kinematical diffraction pattern simulations. We reason that {112}<111> twinning occurs over {332}<113> twinning due to either, or a combination of, the Nb stabilizer content in this alloy and the addition of oxygen. Even though this material is unstable with respect to ω_{ath} formation, it may still have enough Nb stabilizing content to prevent the alloy from having a modulated tetragonal structure that would allow for easy formation of {332}<113> twinning over {112}<111> twinning. Oxygen also may prevent extra lattice shuffle required for {332}<113> twinning. Oxygen also increases the shear stress required for slip, so we expect twinning as a main deformation mode in this material. ω phase is thought to not spontaneously form on the twin boundary via intrinsic instability of the alloy due to a large energy barrier. However, local shear may allow this barrier to be overcome. Thus, as a {112}<111> twin lamella is formed, ω nucleation may be easily induced, explaining the observations here that plate-like ω phase forms at the twin boundary.

4 Deformation nanotwinning (DNT) in cold worked Gum Metal (CWGM) under nanoindentation

4.1 Introduction

In the current study, we report that deformation nanotwinning (DNT) is observed in cold worked gum metals (CWGM) under nanoindentation. While deformation twinning occurs in ST Ref-1 under nanoindentation (as reported in Chapter 3), we note that the twinning in this material is correlated with the β instability resulting from lower Nb content. As STGM does not exhibit ω_{ath} or twinning under nanoindentation (Chapter 5), we do not believe the origin of DNTs in CWGM to be the same as that for the ST Ref-1 case, as CWGM should have similar β stability characteristics of STGM due to having the same composition. Furthermore, the truly nanoscale width of the twins imaged in this study, along with a unique morphology, leads us to believe that it is the microstructure of the cold worked gum metals that contributes directly to the DNT mechanism. Nanocrystalline (NC) materials have been shown to deform similarly via deformation nanotwinning. While CWGMs differ in a few ways from NCs, specifically in that they do not have a homogenous grain size, we believe a similar mechanism to that operating in NCs may be responsible for the DNTs observed in CWGMs. The main theories regarding DNTs in NC materials include emission of partial dislocation from grain boundaries and nanoscale multiplane shear (NMS) via nanodisturbance generation. We cannot be sure which mechanism is operating in the CWGM alloy investigated in the current study. However, with respect to the NMS theory, we find that the observation of DNTs in CWGM is not necessarily inconsistent with the notion that gum metals deform via an ideal-shear mechanism.

4.2 Sample Preparation

The material used in this investigation was supplied in the form of round bar specimens with a nominal composition of 73.5Ti-23.0Nb-0.7Ta-2.0Zr-1.2O at.% (59.1Ti-35.9Nb-2.0Ta-2.7Zr-0.3O wt. %), termed "CWGM" for "cold worked- gum metal composition". The bars were fabricated by Toyota Central R&D Laboratories, Nagakute, Japan via powder processing according to the procedures discussed in Chapter 2 [4].

The cold worked bars were cut perpendicular to the swaging direction into discs of ~300μm thickness and disc cut to 3mm diameter. Samples were then mechanically polished to ~110μm thickness with SiC paper. A polished surface for nanoindentation was prepared through one-sided jet polishing with a Fischione Model 1010 twin-jet polisher using an electrolyte solution of 4.4vol% of 70% perchloric acid, 29.3 vol% butanol, and 66.3vol% methanol at -30°C and 50V for ~1 min. (ensuring the sample is not perforated as in regular jet polishing). Further discussion involving details and explanations for these specific sample preparation steps are found in Section 3.3 and discuss how one-sided electropolish is achieved. Nanoindentation of the electropolished surface was performed *ex-situ* in a Hysitron Triboindenter© fitted with a triangular, diamond Berkovich tip. Figure 3.5 in Section 3.3 shows Hysitron Triboindenter® setup (left), along with typical SPM images (right). 2000 indents, as opposed to 500 indents as performed previously on ST

Ref-1 (Section 3.3), were performed to ensure that a handful (~10-15) of indents would be suitably electron transparent for subsequent TEM analysis. They were spaced nominally 30μm by 10μm apart in a pattern of 40 rows by 50 columns. The 10μm spacing between columns is demonstrated in the DF TEM image of a jet polished sample in Figure 4.1, and adjacent rows are not visible in the field of view. Indentation was performed under load control with a max load of 27mN at a loading/unloading rate of 5mN/s with a hold of 5 seconds.

Figure 3.4 in Section 3.3 gives a schematic of the sample preparation procedure for subsequent TEM analysis. After nanoindentation was performed, the sample was jet polished from one side to ensure the nanoindents were electron transparent for subsequent TEM analysis, where the side that underwent nanoindentation was covered again with non-adhesive Teflon® tape to prevent polishing the indents away. The samples were jet polished in a similar manner as in the previous electropolishing step: a Fischione Model 1010 twin-jet polisher was used to create the electron transparent sample using a similar etchant as performed in the electropolishing step at -35°C and 50V(24mA) until perforation (~1:30min).

Before further conventional TEM or atomic resolution imaging can be attempted, however, further sample preparation is required to remove the hydrocarbon layer (as seen in the middle of the left indent in Figure 4.1) and thin the indentation pits further. Low-energy ion milling to clean and further thin the sample was performed on Leica Res 101 "Baltec", and further discussion of this method is outlined in Section 3.3. Milling of the previously jet polished TEM sample was performed in two steps: a milling step was performed at 3kV, 1.5mA for 32 minutes and a cleaning step was performed subsequently at 2kV, 1.2mA for 10 min. Both steps were performed with -8°/8° gun tilt and 1.5 rpm sample rotation.

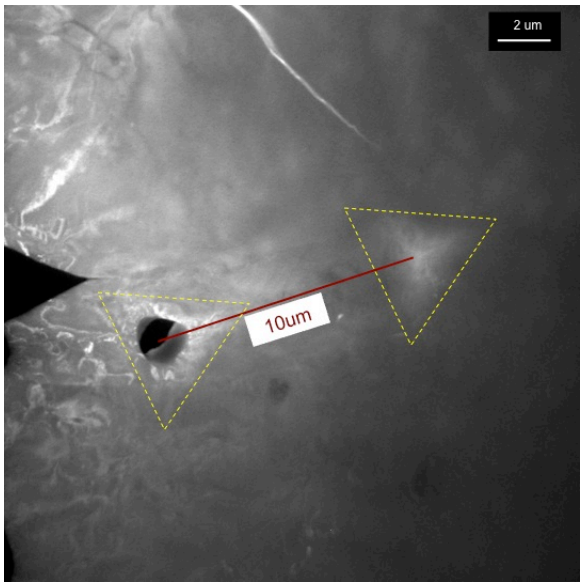

Figure 4.1: DF TEM image of CWGM after jet polishing demonstrates nanoindents were spaced 10um apart (in rows, which were spaced 50um apart) and that visible nanoindents are typically not on the thinnest regions of the coastline Hydrocarbon layer is observed in the middle of the left indent. Subsequent low-energy milling was performed to remove hydrocarbon layer and thin the indentations further.

After low energy milling, further TEM analysis was performed on a JEOL 3010 microscope at 300 kV. Suitably thin indents were imaged with atomic resolution HAADF-HRSTEM technique performed on a modified FEI Titan with a CEOS probe aberration corrector at 300 kV with a typical probe size of 0.5 Å and probe convergence semi-angle of 17.2 mrad. HAADF signal was collected at an inner collection semi-angle of ~53 mrad, unless otherwise stated.

4.3 Results

4.3.1 Nanoindentation data

The load-displacement (F-d) curves are given in Figure 4.2. As stated in Section 4.2, 2000 indents were attempted on the sample. The top two figures are the load-displacement curves for all reliable indents with outliers removed from the final figures. The indentation experiment yielded 1926 reliable indentations. Unreliable indentation data could be caused by surface imperfections that give unrepresentative F-d curves or where the indentation equipment timed out and could not perform an indent due to local surface unevenness. The total F-d data are split into two sets to make description and visualization easier. In the top two figures, the F-d curves for a set of 200 indents is plotted as a particular color as indicated in the legend. The indentation experiment is set up such that indentation is performed row by row with 50 indents each per row. Thus, indents 1-200 will have been performed in roughly the same local region of the sample (e.g. bottom 4 rows), and the data is presented this way to enable easier visualization of trends and artifacts with respect to sample coordinates. For indents 1000-1926 (right), all indentation data is similar as the curves lie on top of one another. For indents 1-999(left), many indents out of the first 400 indents performed demonstrate an increased slope at higher loads that deviates from the typical exponential form of the loading curve [77]. The bottom two figures are sample indent curves where this deviation is noticeable and the point of deviation is indicated by red arrows. It is most likely that this deviation from exponential loading curve is related to sample mounting. The sample itself is mounted to an AFM mount with Crystalbond™, a low melting-point polymer adhesive. The AFM mount is then magnetically attached to the sample stage, shown in Figure 3.5. It is possible that there is some compliance from the adhesive during loading and that the maximum displacement has been met at locations where the slope of the F-d curve increases if the adhesive is not of homogenous thickness under sample. At places where the local compliance changes mid-indentation, either the sample is undergoing full indentation (without associated movement from the compliance of the adhesive) or it could be a substrate (stage/AFM mount) effect. As both the stage and the CWGM sample are hard materials compared to the polymer, it is difficult to determine exactly which scenario is occurring [78]. Typically, the Crystalbond™ adhesive is melted at a high enough temperature to create a thin liquid layer, but if the melting temperature is not kept high enough during sample mounting, the polymer thickness may not be homogenous leading to the increased slope effect indicated in [77] It is important to note this artifact and clarify that the deviation is probably not indicative of a mechanical response from the sample itself. This effect was not observed in the Ref-1 sample since the max load for that experiment was 8mN. Furthermore, out of 2000 indents, only ~75 indents demonstrated this effect and they were located in a particular region of the sample, supporting the notion that the effect is most likely due to local sample mounting conditions.

From the data, we calculate reduced modulus (E_r) of 76GPa (standard deviation 6GPa) of and H of 3.0GPa (standard deviation 0.15GPa) using the analytical procedure outlined in [65] for depth-sensing nanoindentation, with further details given in Section 3.4.1and **Appendix D**. Given that the deviation described in the previous paragraph does not affect the slope of the unloading portion of the curve, we take the E_r value to be a good semi-quantitative guide. It is also consistent with the value of 76.5GPa measured for the Ref-1 sample given in Section 3.4.1. However, the hardness between the two samples is quite different: 3.0GPa for CWGM and 4.14GPa for the Ref-1 sample. It has been previously reported that aged Ti-Mn alloys demonstrate a drastic increase in hardness due to presence of the ω_{iso} phase [79], and the same increase has been observed for aged Ti-V alloys [80], thought to be due to the typical precipitation hardening effect. Vickers hardness was measured by Saito et al. [81] for the GM composition over a range of cold working ratios, and it was found that cold working had little to no effect on the hardness, an observation which partly spurred the notion that GMs are "super plastic" and "do not contain dislocations". Thus, they measure Vickers hardness to be 250Hv for both STGM and CWGM, which may be converted to an approximate nanoindentation hardness of 2.65GPa [67 (p. 191), 82]. This value is reasonably close to the measured nanoindentation hardness value of 3.0GPa, but may be larger due to the cold working (which of course, could not be explained if an ideal shear mechanism were *solely* operating in the material during plastic deformation.)

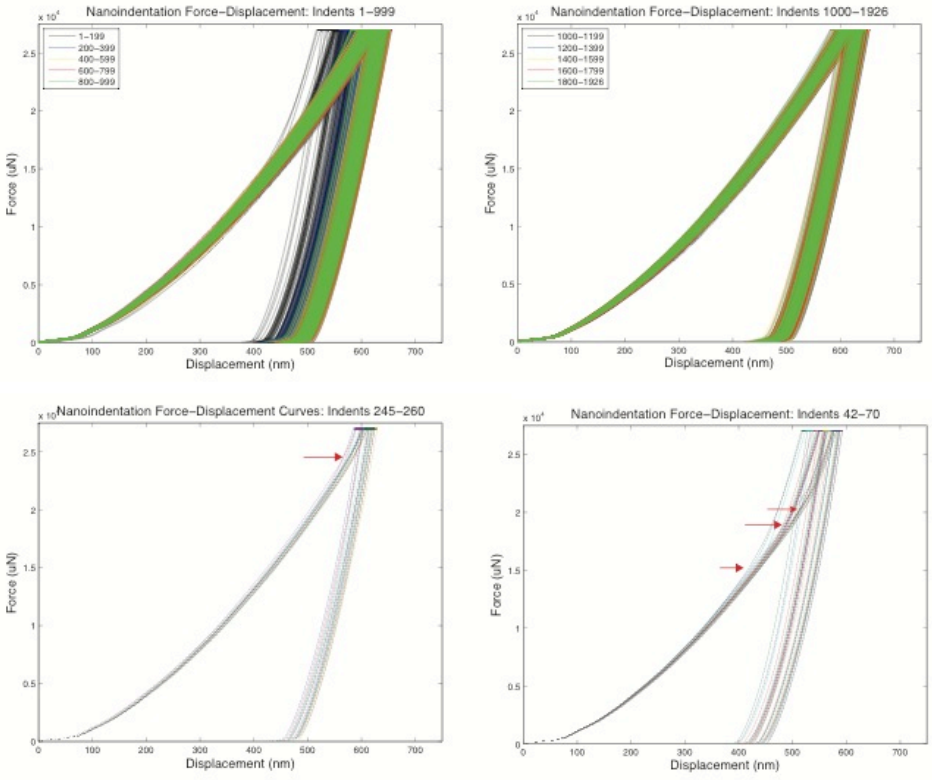

Figure 4.2: (top) Load-Displacement curves for CWGM sample achieved via load-control function on Hysitron Triboindenter® with max load of 27mN. Er of 76.4GPa and H of 3.0GPa was calculated. (bottom)Anamalous deviation from exponential loading curve and increased slope for a small subset of indents is thought to be caused by sample mounting effect as explained in text.

4.3.2 Conventional TEM data

Initial low magnification TEM image of the CWGM nanoindented sample is given in Figure 4.3 after the sample has undergone low energy milling in the Baltec. The image is similar to that given in Figure 3.10 in which a few of the indents are situated on the coastline and thus thin enough for TEM imaging. The distance between the two indents is measured at 60μm, as the row in between did not have visible indents due to sample thickness. The indent circled in yellow is imaged at higher magnification as shown in Figure 4.4. BF image is given in Figure 4.4a with the indent outlined in yellow and the dark field image in Figure 4.4b shows a couple of straight line defects along with bend contours that are lit up in the image. Otherwise, not many defects are observable in this particular image. Additional dark field images are provided in Figure 4.5. Figure 4.5a contains no noticeable defects, however, indents pictured in b) and c) contain straight and zigzag shaped defect structures. Since the indent is slightly difficult to identify in Figure 4.5c, it has been outlined in dotted yellow, and outlines of lath grain boundaries have been outlined in red. A magnified view of the region enclosed in the green box in c) is pictured in Figure 4.5d. The zigzag features have straight boundaries and are 20-70nm in width. They appear distinct from the zigzag features pictured in Section 3.4.2 in Figure 3.9 in the CWGM samples, the features are visible over a wider area of the indentation pit.

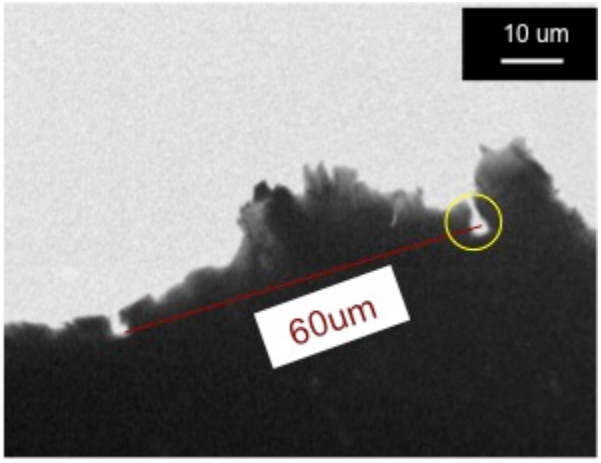

Figure 4.3: Low magnification TEM image of CWGM sample after low energy milling yields indents on sample coastline. The indents pictured are two rows, or 60um, apart, where the middle row is too thick for any indents to be visible in the image.

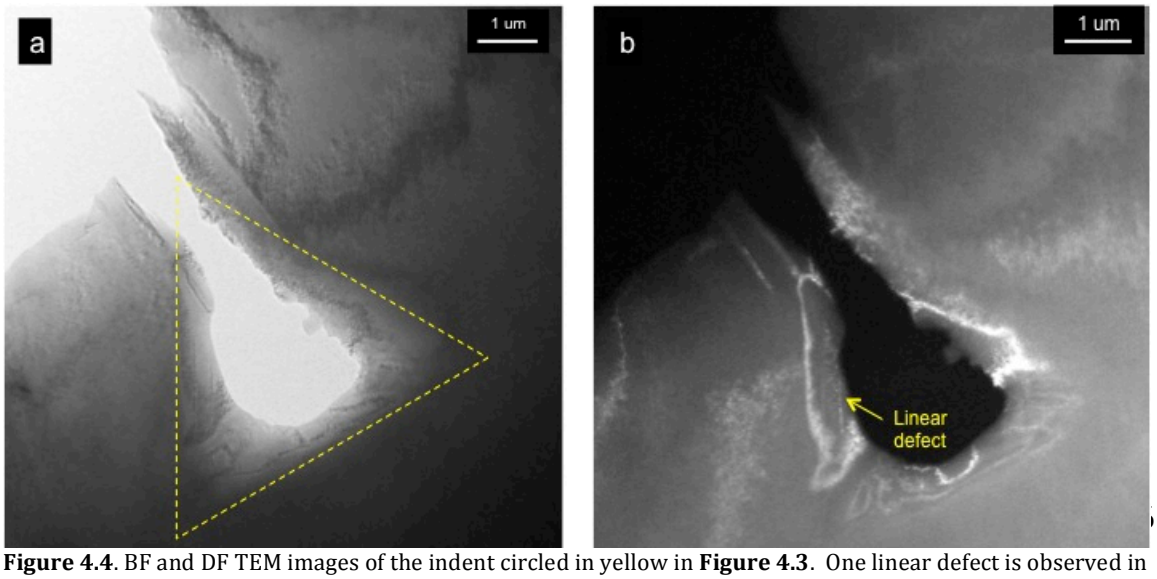

Figure 4.4. BF and DF TEM images of the indent circled in yellow in **Figure 4.3**. One linear defect is observed in the dark field image b), but otherwise at this sample, not many defects are observed.

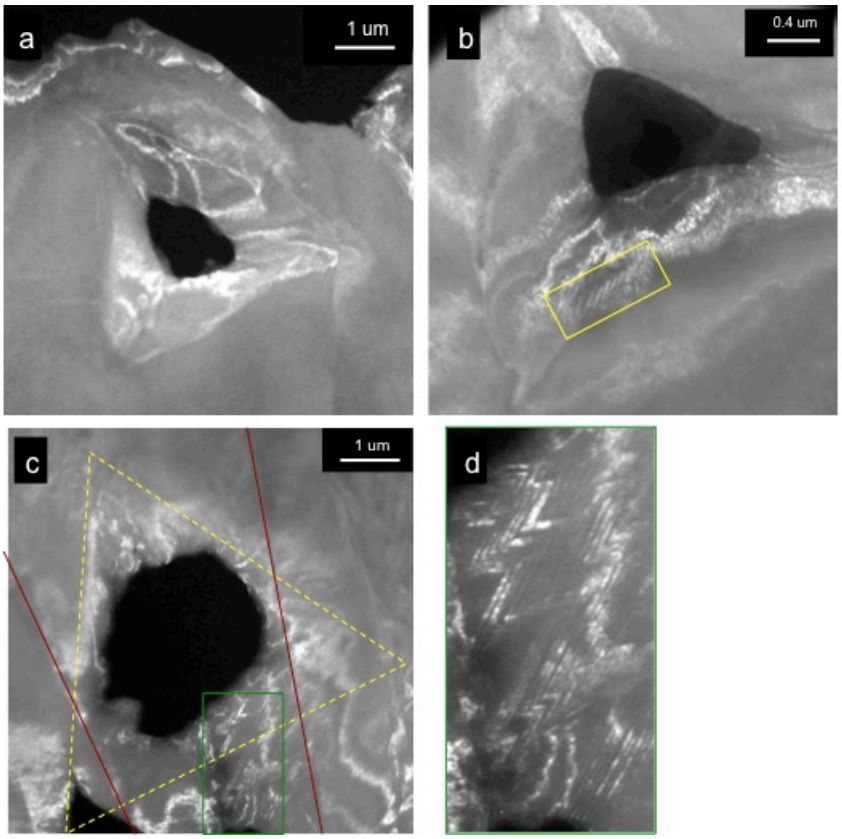

Figure 4.5: a)-c) Dark field images are presented of different indents with different defect microstructures visible under the given imaging conditions. a) no obvious defect microstructure present within the indent pit. b) straight, linear defects present within the pit of the indent <100nm wide. c) zigzag features of 30-70 nm width appear within indentation pit.

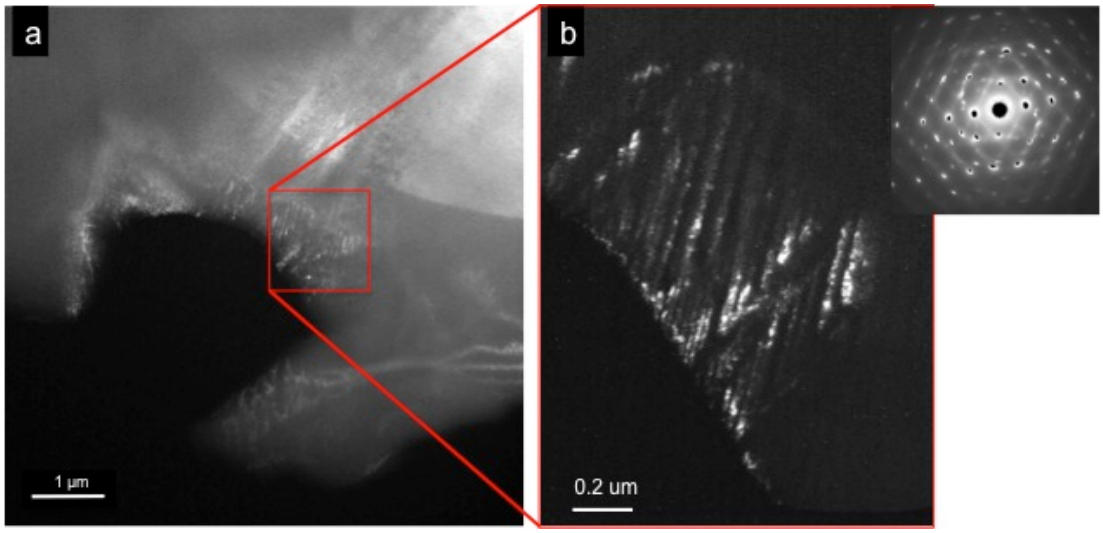

Figure 4.6: Dark field images taken of deformation structure inside indent pit reveals nm-size zigzag defect structures. b) shows a magnified view of the outlined region in a) where the defects have bright intensity. The DP inset is from region contain defect structures in b). The DP contains a complex composition of different lattices that is difficult to analyze.

Another dark field image is presented in Figure 4.6 in which the indent pit also contains zigzag defect features. A close-up view of the features is given in Figure 4.6b, and the features are observed to be zigzag, lath-like features with straight boundaries that are <100nm in width as in Figure 4.5d. A selected area diffraction pattern of the region in Figure 4.6b is presented adjacent to the image. The zone axis appears to be nominally <113>β, however, there are many extra reflections in the diffraction pattern that are hard to identify. These extra reflections are possibly due to the overlapping and rotation of misoriented adjacent grains (as discussed in Chapter 2), which could be compounded by the rotation that can occur in GMs under nanoindentation (as discussed in Chapter 5). The defect structure presented is observed to have a zigzag morphology similar to the imaged features in Chapter 3 that turned out to be {112}<111> twins. The diffraction pattern, however, clearly contains another misoriented lattice and the extra spots look more similar to spots from an adjacent rotated grain than from a twinning effect. Further sample tilting may have helped. However, due to the nanometer scale of the defect laths, SAD experiment proved difficult in the precise identification of the defect structure. Dark field imaging was more successful, but without proper identification of the reflections in the DP, the images were difficult interpret with respect to identification of the defect structure.

4.3.3 HRSTEM data

In order to accurately identify the defect structures observed in Figure 4.5c, d and Figure 4.6, HAADF HRSTEM imaging was performed on TEAM 0.5 to obtain atomic resolution. Lower magnification images of the same indent in Figure 4.6 are presented in Figure 4.7. The right image is taken of the region indicated by yellow outline and exhibits the same straight, lath defect structure observed in Figure 4.7 as expected. The laths are observed to be much thinner than 100nm, with many being <50nm in thickness near the indent edge. HAADF images are thought to contain intensities related mainly to mass/thickness, as the quasi-elastic incoherent scattered electrons are deflected to the larger angles collected by the HAADF detector. However, with a large enough inner collection semi-angle, diffracted electrons may also be collected and can result in the diffraction contrast of the defect features that is apparent in Figure 4.7(right). Before investigating further, we note that jet polishing process can result in twin formations that are observed to emanate from the coastline as shown in **Appendix C.1**.[1] The laths imaged here, however, are much smaller (20-100nm), whereas the twinning artifact from jet polishing is around 100-200nm in thickness. Furthermore, the defect structure imaged in nanoindented CWGM can appear in different morphologies other than straight, such as zigzag shown in Figure 4.6 and Figure 4.7; are observed to be much denser than the twinning artifact; and can appear away from the coastline as in Figure 4.5b. Lastly, the twinning defects observed here are in or around the indentation pit, providing strong evidence that the feature is related to the mechanical response of the material and is not an artifact from the jet polishing process.

[1] These defects look similar to dislocations that are pinned by surface oxides upon electrolytic thinning [19, p. 453]. However, as the bend contours are not continuous between boundaries, we assume they are twins.

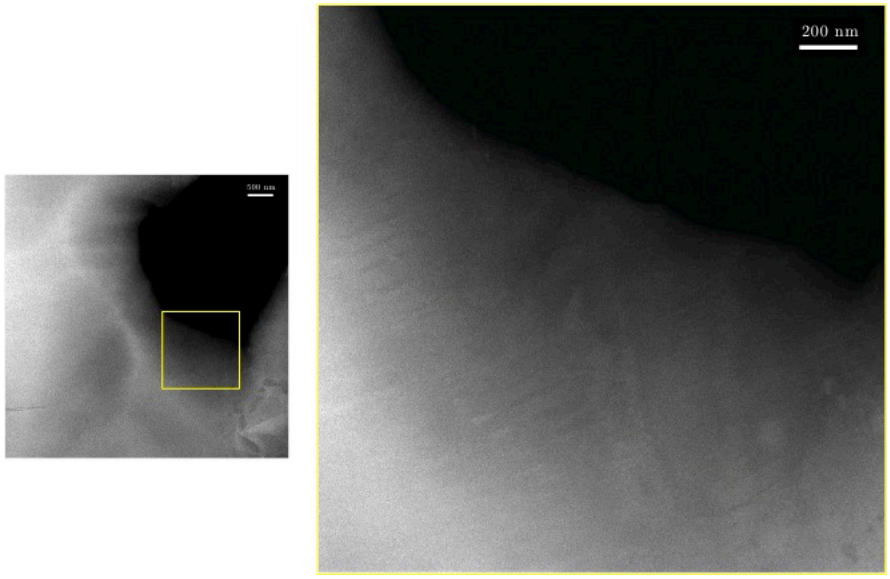

Figure 4.7: HAADF images of the indent presented in **Figure 4.6** are shown. (left) Overview of indent. Region in boxed area is imaged at higher magnification at right. (right) Straight, lath defect structure is apparent from diffraction contrast effect in HAADF image.

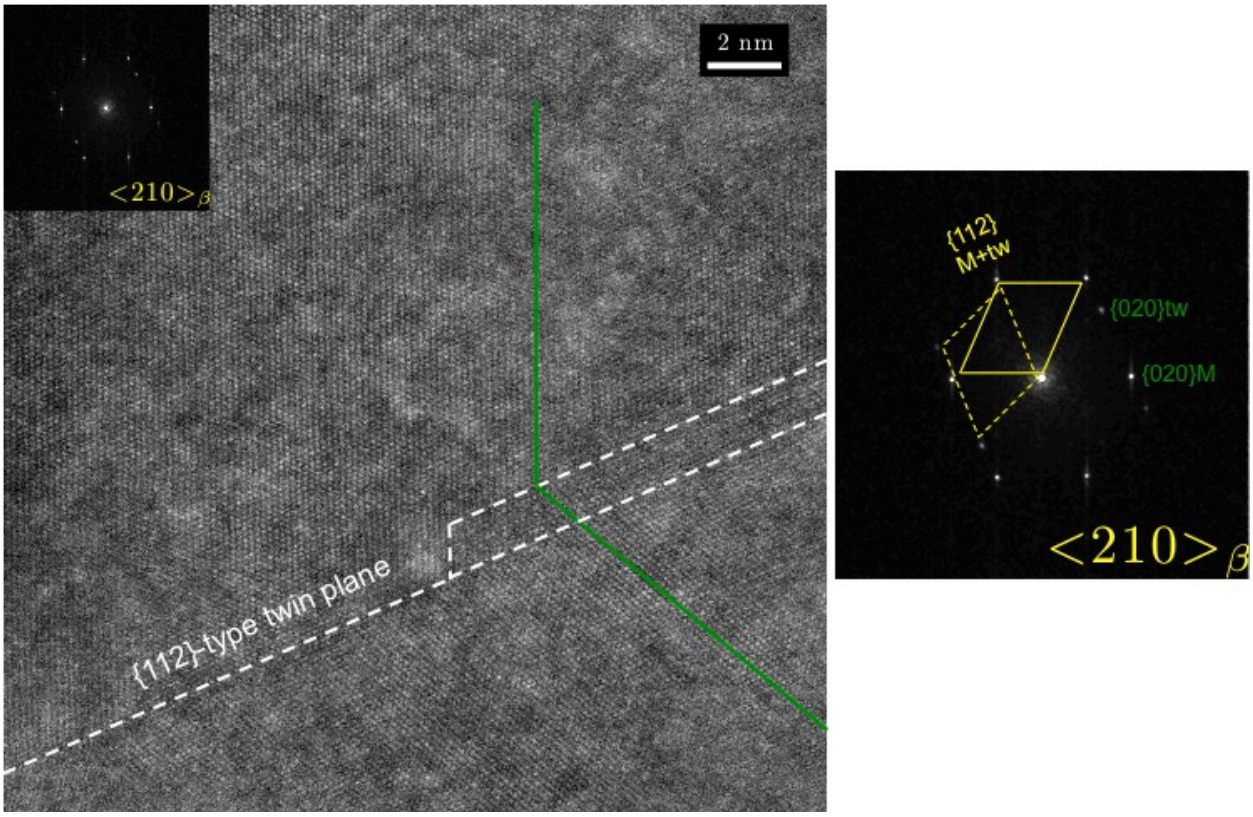

Figure 4.8: (left) HAADF atomic resolution image of <210>β-type zone is provided, and it appears the defect structures are twins since there is a mirror plane present about the {112}β-type plane trace. (right) magnified view of the FFT is provided along with the distinct lattices present. The (020) matrix and twin plane reflections are indicated that correspond to the green plane traces indicated in the atomic resolution image.

Atomic resolution HRSTEM images were captured of the defect structures and a lattice image of the straight, lath defects is provided in Figure 4.8(left). The zone axis imaged is a <210>-type zone, and immediately we observe direct evidence of a {112}-type mirror plane as outlined in the figure. Given the discussion in Chapter 3 regarding possible twinning systems present in BCC, we theorize the defect structures to be {112}<111>-type twins. Furthermore, we know that a sample with gum metal- composition contains more β-stabilizing content than ST-Ref-1 sample which exhibited {112}<111>-type twinning (as stated in Chapter 3). Thus it is very likely that CWGM would also exhibit a similar twinning system, as the {332}<113>-type twinning is usually only observed in unstable β-Ti alloys [62]. Figure 4.8(right) is a magnified view of the FFT of the image in which the twin lattice and matrix lattice are outlined. The plane traces in green in Figure 4.8(left), which correspond with the green reflections in the FFT inset, are of the (020) type planes.

We want to note that while the mirror plane is immediately apparent in the picture, there are parallel {112}-type plane traces that also seem to indicate mirroring, and the twin plane would appear to be kinked. Because it is a deformation twin that occurs in a previously cold worked gum metal sample, we expect the mirror plane may not be exactly straight and may follow a path that follows a boundary feature in the sample prior to nanoindentation.

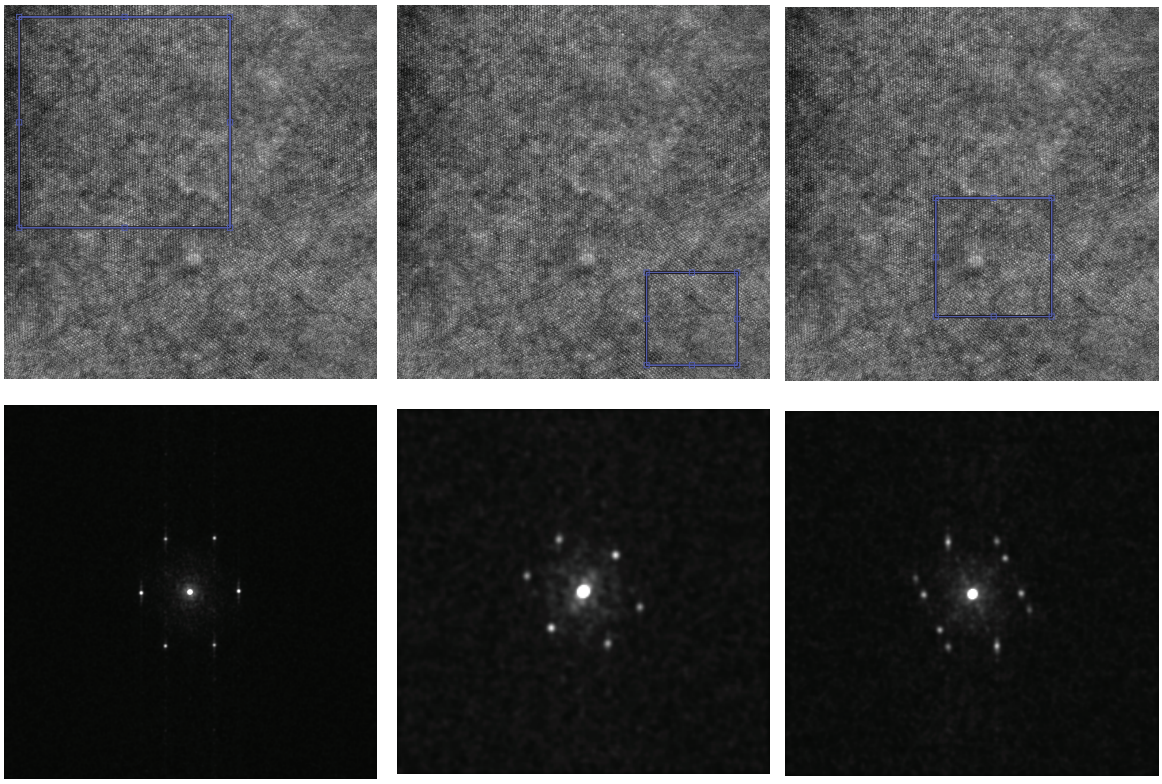

Figure 4.9: Linked Fourier transforms of boxed region is provided below each image. Atomic resolution image used for Fourier analysis is the same as that in **Figure 4.8**. (left) and (middle) FTs are taken of regions above and below twin boundary and indicate <210>β-type zones that are rotated with respect to each other. (right) FT of twin boundary region indicates overlap of the two discrete lattices.

It is well known that {112}<111>-type twins exhibit a 70.53° misorientation angle about the <110> zone axis. To verify that that the twin imaged in Figure 4.8(left) is indeed a {112}<111> twin, we perform Fourier filtering of the image and kinematical simulations. Fourier Transforms of selected areas of the atomic resolution image presented in Figure 4.8 are given in Figure 4.9. The region from which the Fourier transform is calculated is indicated in the blue box and the resultant FT is given below the image (FTs calculated with Matlab routine given in **Appendix A.1**). In Figure 4.9(left), the FT was taken above the twin boundary, for Figure 4.9(middle) FT was taken below, and in the last image, the FT is taken of the region containing the twin boundary. We note that two distinct lattices that are rotated with respect to each other are indeed present in each region as clearly indicated by the FTs. The distinct lattices are also outlined in the FT in Figure 4.8(right).

Now that is has been directly established that the extra reflections in the FT observed in Figure 4.8 indeed emanate from a twinned lattice, we set out to verify that the twin pattern given in the FTs of Figure 4.8(right) and Figure 4.9(right) is what would be expected from a {112}<111> type twin as imaged from a <210>-type zone axis. In other words, we want to verify that the measured misorientation angle, ~48°, is consistent with the misorientation angle expected for a {112}<111> twin along a <210>β zone. Kinematical simulations

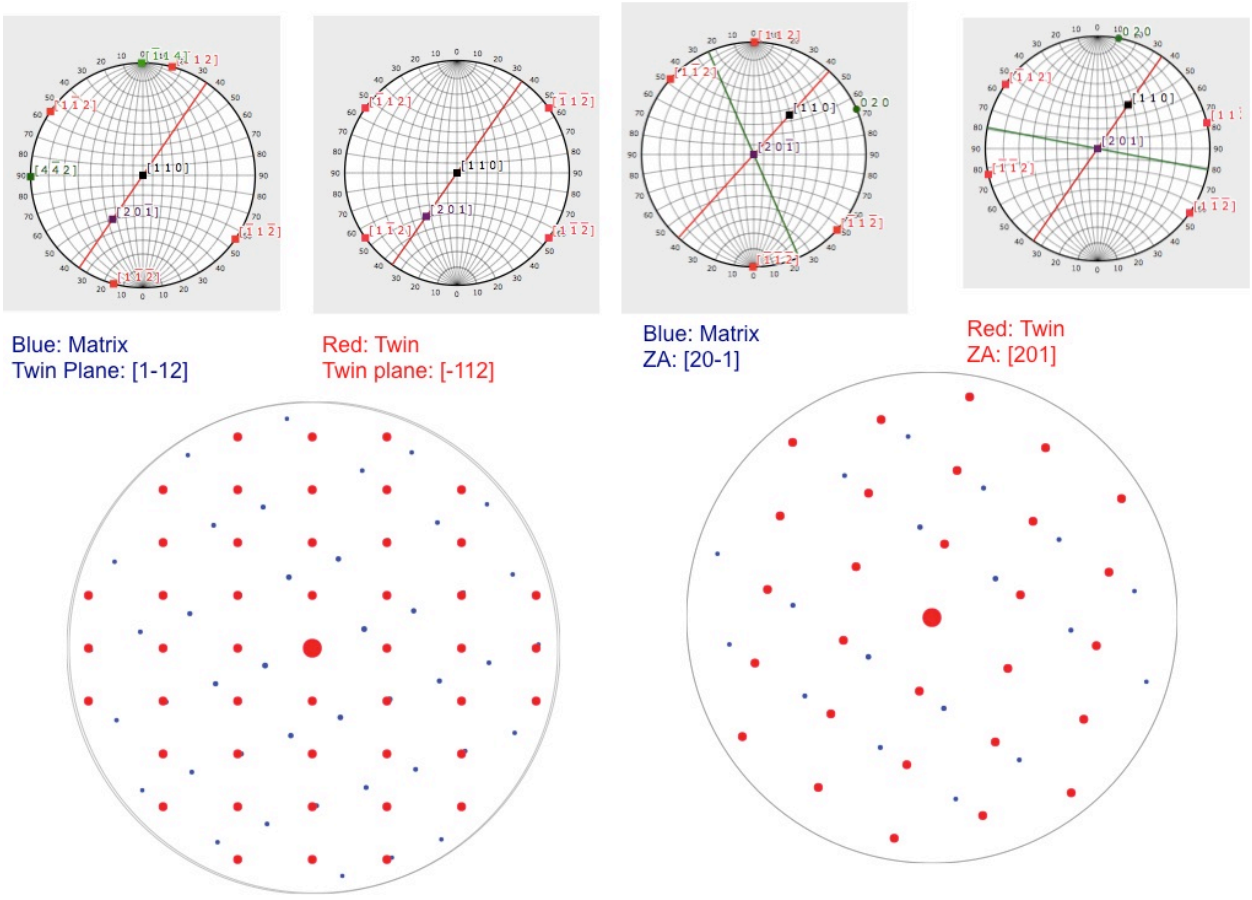

Figure 4.10: Kinematical simulations of <112>{111} type twin as viewed along $[110]_{Matrix}$ ||$[110]_{Tw}$ (left) and $[20\text{-}1]_{Matrix}$ ||$[201]_{Tw}$ (right) are presented, with respective pole figures given above. The <210>type simulated diffraction pattern of material containing {112}<111> type twin is seen to match the FT provided in **Figure 4.8**(right). See text for further details. Simulations prepared with Crystal Maker software.

performed in Crystal Maker Software (Single Crystal package) are provided in Figure 4.10. The pole figure maps give the relative orientations of the matrix and twin for the simulated diffraction pattern beneath. In Figure 4.10(left) a $[110]_{Matrix}||[110]_{twin}$ ZA containing {112}<111>-type twin reflections is given as a reference. Next, the matrix and twin lattices are rotated 50° about their respective twin plane poles, where $\mathbf{N}(1\text{-}12)_{Matrix}||\mathbf{N}(\text{-}112)_{Twin.}$ The resulting rotation yields the diffraction pattern for the desired zone axis of <210>β type, which in this particular case is $[20\text{-}1]_{Matrix}||[201]_{twin.}$ We find the kinematical diffraction simulation of the <210>β zone matches exactly the pattern observed in the FT of the atomic resolution image. Furthermore, the misorientation angle can be directly measured from the pole figure about the <210>type zone and is given as ~50° (the minimum rotation angle required to reorient the twin lattice as identical to the matrix lattice). Finally, to enable direct comparison with the atomic resolution image, in Figure 4.8(left) the trace of the (020) type planes for both the matrix and the twin have been outlined in the <210>-type pole figures. The angle between the planes measured on the pole figures matches the angle measured between the planes in the image (~132°). The angle between the (020) plane traces contains the same geometrical information as the misorientation angle quoted (180°-132° = 48°), but it may be easier to visualize the angle between the (020) lattice traces in the atomic resolution image than the misorientation angle in the FFT, and so the angle between the (020) plane traces is explicitly stated here. Another HAADF image is presented in Figure 4.11 that demonstrates the thin nature of the twin structures. The particular twin lath imaged is about 15nm in thickness.

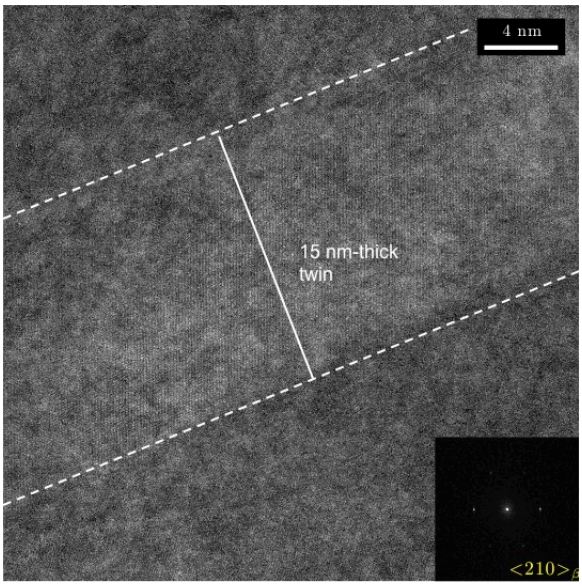

Figure 4.11: HAADF image of deformation nanotwin (DNT). DNT is approximately 15nm in width

From direct atomic resolution images along with linked FFT analysis and kinematical diffraction simulations, we are confident that the observed defects are deformation nanotwins (DNTs) 15nm-70nm in width that are of {112}<111>-type.

4.4 Discussion

For the ST Ref-1 sample, deformation mechanism under nanoindentation loading was found to be twinning with ω nucleation on twin boundary as discussed in Chapter 3. Twinning is theorized to occur over slip in ST Ref-1 sample due to relatively low β-stabilizing content. It is a well known trend that upon increasing the β-stabilizer content in β-Ti alloys, the operating deformation mechanism changes from stressed-induced martensite (SIM) and twinning to conventional deformation slip as discussed in Chapter 3. In Chapter 5, we report that no twinning features are observed after nanoindentation of STGM. CWGM, the alloy reported in this section, has the same composition as STGM as shown in Table 1. Thus, based on β-stability characteristics of the CWGM alloy, we do not expect twinning as a deformation feature. Based on the results of the STGM work, we expect conventional slip, but since we do not observe it, we theorize that it is the microstructure that is developed upon coldworking that directly influences the deformation behavior of this alloy under nanoindentation. Thus the question remains: what is the mechanism by which deformation nanotwinning (DNT) occurs in CWGM that would explain why it is not observed in the STGM or ST Ref-1 alloys?

4.4.1 Brief literature review regarding deformation mechanisms and structures in gum metals

Before discussing the possible mechanisms that may induce the specific deformation mechanism observed in this study, DNTs, we want to first give a brief overview of the general deformation mechanisms of gum metals that have been previously theorized and observed. The operating deformation mechanism that accounts for the anomalous plastic deformation properties of Gum Metals, specifically of CWGMs, has been debated in the literature since the original Saito et al. [4] paper was published in 2003. This paper, and follow-up theoretical and experimental papers, claimed that a dislocation-free, ideal shear mechanism was responsible for the observed mechanical properties and complementary defect structures of both cold worked and solution treated gum metals. Specifically, some of the observed anomalous properties that seem to preclude a conventional deformation mechanism is the lack of work hardening in stress-strain tensile curves [4], a lack of increase in Vickers hardness with increasing cold-work ratio [81], and a tensile strength near the calculated ideal strength [4] as supported by the calculations in [6].

A short comment should be made on the calculated ideal strength, which has been controversial as well. Various research groups have either calculated or measured the elastic constants of Gum Metals in an attempt to prove or disprove that the alloy yields when its theoretical shear stress is reached. All calculations use the derived relation $.11*G_{<111>}$ for ideal shear strength in BCC metals as presented in Krenn et al. [5]. The theoretical ideal tensile strength of a Ti_{75}-V_{25} alloy at 0K, as calculated by Li et al. [6], is 1.8GPa and is comparable to the measured value of yield in tension of 1.8GPa at 77K in Gum Metal [4]. Elastic constants of Gum Metals were also calculated by Ikehata el al. [7] using first principles, and a theoretical value of ideal shear strength using these values is explicitly stated as 1.2GPa in Kuramoto et al. [8]. It should be noted that this value of 1.2GPa for ideal shear strength is comparable to the tensile strength of 1.2GPa for CWGMs, and would thus imply ideal strength is not being achieved in shear. Furthermore, Talling et al [37] experimentally determined the elastic constants of Gum Metal and from these values calculate an ideal shear strength of 2.25GPa, which is still larger than the measured

tensile strength of 1.2GPa for CWGM. From the tensile yield strength, an approximate maximum shear stress at yield for polycrystalline materials can be computed: 0.5*1.2GPa = 600MPa [83][2], which implies bulk ideal shear is not theoretically possible if one assumes the theoretical ideal shear strength of anything above this value, as explicitly stated by Talling et al [31]. Even though it is not likely that Gum Metals are deforming solely through an ideal shear mechanism, and certainly not deforming in the bulk at ideal strength, the maximum shear stress at yield is still a considerable fraction of the ideal strength. In any case, it should be noted that determination and agreement on the elastic constants of Gum Metals between research groups has been controversial, and thus not all groups agree that ideal strength in shear is being achieved in the alloy upon plastic deformation.

Nevertheless, the notion of a dislocation-free ideal shear mechanism was seemingly supported by direct TEM observations of defect structures found in deformed solution treated samples and as-received cold-worked samples. Specifically giant faults were observed in TEM after tensile testing of STGMs, which seemed to be unaccompanied by the presence of dislocations [8]. Further, atomic resolution images of as-received cold worked gum metals seemed to indicate localized areas of pure shear, or, in other words, the presence of line defects with non-integer, "non quantized" burgers vector quantities [4, 8]. The images of these defect structures, along with an apparent lack of dislocations related to deformation, directly led to the notion of a new defect structure termed "nanodisturbances" as theoretically defined in [9] and [84]. It should be noted that authors of [31,38] claim that a highly distorted lattice may obscure line defects and render them hard to characterize, as stated in 3.4.3.1, and that dislocations still may be present. Furthermore, as given in Figure 2.10, there are clearly dislocations present in CWGM, but they are admittedly difficult to fully characterize.

This theorized defect of "nanodisturbance" was initially thought to explain the anomalous measured mechanical properties listed previously. Very few studies, however, have investigated the mechanical response, either *in-situ* or *ex-situ,* of CWGMs, as most initial studies focused on a thorough investigation of the as-received cold worked microstructure, which is controversial and difficult to analyze in and of itself. Of the few studies, the most notable that examine the deformation structures in tested CWGM samples include *in-situ* atomic resolution HRTEM tensile testing [85], *in-situ* TEM nanopillar compression testing [86], and *ex-situ* nanoindentation [39] very similar to the current study. In the study conducted by Cui et al. [85], the authors claim that nanodisturbances are generated and can be restored during elastic deformation of CWGM, and this mechanism can ultimately explain the non-linear elasticity observed. (Although, it should be noted that now many groups are in agreement that α'' appears upon elastic loading and that a reversible martensitic transformation is responsible for the pseudo elasticity present in CWGMs [31]). The study by Withey et al. [86] observed no motion of dislocations upon compression testing of nano-pillars and found shear bands were present during deformation, reminiscent of the seemingly dislocation-free, ideal shear-mediated, giant fault structures observed in bulk tensile testing of STGMs in [39]. The study most similar to the current

[2] For a polycrystalline material, the factor is reduced further to ~1/3 due to statistical distribution of grain orientations, but we neglect this here.

investigation conducted also by Withey et al. found a lack of dislocations in or around the indent pit and that previous domains seemed to have broken into nano-cellular domains within the indent pit. They explicitly state that no twinning was observed, but the exact nature of the crystallographic relationship between the cellular domains was not clear from the diffraction patterns. There are a few reasons that may explain the stark difference in observed deformation structures between the Withey et al. study [39] and the current one: 1) the TEM image of the CWGM nanoindentation pit in Fig. 9 in [39] indicates that much of the nanoindentation pit has been milled away, so it is possible that observations were made primarily of material surrounding the indent pit or 2) The indentation force applied in the material was much lower at 8mN compared to 27mN in the current study. It is conceivable that the stresses applied in the previous study may not have been large enough to activate the twinning mechanism observed here.

Other investigations, however, claimed conventional plastic deformation mechanisms, such as dislocation slip and twinning, must be operating in gum metals given the TEM observations of as-received rolled and worked samples. Specifically, Talling et al. [31] found evidence of twins, stress-induced ω plates, and dislocations when observing as-received cold-rolled Gum Metal specimens in the TEM. A similar finding was presented by Xing et al. [87], in which dislocations were imaged in atomic resolution HRTEM experiment in as-received CWGM. Furthermore, the increased yield strength upon cold working in gum metal specimens as observed in tensile curves presented in [31] cannot be adequately explained by a nanodisturbance/giant fault mechanism, as explicitly pointed out in the investigation. Finally, *in-situ* TEM tensile testing of STGM was performed by Castany et al. [53], which provided direct observations of dislocation slip during the test. Thus, how Gum Metals deform, via ideal shear, conventional plastic deformation mechanism, or a combination, is still a very controversial topic.

For the material investigated here, CWGM, under the specific loading condition of nanoindentation, the relevant question is whether a conventional dislocation slip mechanism or an ideal-shear mechanism can explain the observed Deformation Nano-Twinning (DNT). DNTs are frequently observed upon deformation of nanocrystalline (NC) materials [88]. As DNTs are typically observed to emanate from grain boundaries (GBs) in NC materials, they are thought to form from emission of partial dislocations from grain boundaries [89]. Another mechanism has been put forward to explain DNT formation in NC materials by Ovid'ko [88] that does not require dislocations pre-existing on every slip plane at GBs. Rather this mechanism, termed nanoscale multiplane shear (NMS), involves ideal shear in nano-sized volumes. It's important to note that as-received CWGM that has been worked via rotary swaging does not have a homogenous distribution of truly nano-sized grains as found in typical NC materials, but as shown in Chapter 2 and in Figure 4.12(left) it contains a hierarchical, complex microstructure containing long, lath-like grains (~100-400nm in width) with nanometer sized subgrains (30-50nm in width)-possibly formed by dislocation cell network structures. Thus, CWGMs could be considered to contain nanosized grains, albeit with a non-homogeneous size distribution. Furthermore, other features of the DNTs in CWGMs presented here, such as loss of coherent nature of twin boundary and step-features, observed in Figure 4.8(left), are also observed in DNTs of NC materials [89].

In the NMS theory put forward by Ovid'ko [88], dislocation dipoles with non-crystallographic, small burgers vectors, or "nanodisturbances", are simultaneously nucleated under action of shear stress and quickly grow to have burgers vector of requisite partial dislocation. Overview of this mechanism is provided in the schematic in Figure 4.12(right). Through calculation of the energetics of this mechanism, Ovid'ko found that the shear stresses required for the activation of NMS in NC materials is quite high, but could conceivably be achieved under indenter loading, as is the case in the current investigation, and may possibly be aided by the fact that the theorized ideal strength of Gum Metals is relatively low. The large shear stresses required may explain why this defect structure is observed in the current investigation but not by Withey et al. [39] where the indentation force applied was much lower. As the NTs formed via this mechanism would be fully contained within a nanograin, and the nanotwins formed in the material in the current study seem to traverse through the entire grain (not confined to the sub-grains), justification has to be made to apply this theory to a material that has larger grains than those found in nanocrystalline materials. Thus, we bring attention to this theorized NMS mechanism only to underscore that the DNT deformation structure found in CWGMs under nanoindentation is not necessarily counter to the notion that an ideal shear mechanism via nanodisturbance generation is operating in this material. That is, the DNT structure observed in CWGMs under nanoindentation is consistent with both an ideal-shear mechanism via "nanodisturbance" generation and also with conventional slip, as supported by previous studies on deformation of nanocrystalline materials. Thus, the evidence of this twin structure does not necessarily imply that ideal-shear is not occurring: DNT formation here may still be consistent with the previous results and observations of ideal shear mechanisms and defects in GMs.

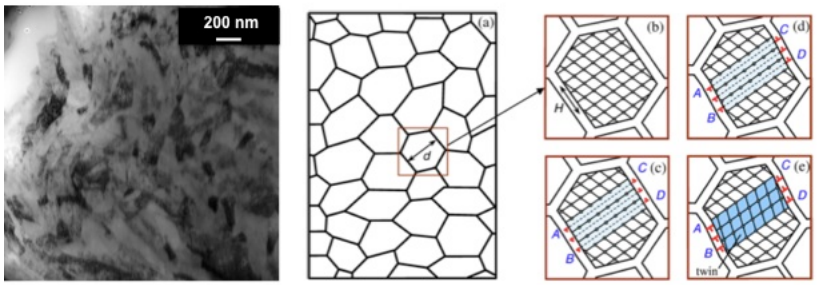

Figure 4.12: (left) BF TEM of grain structure in gum metals, where grains are elongated, but only 100-200nm in width, with some sub-grain, 100nm-sized features similar to nanocrystalline materials. Due to low magnification, Dislocation cell network structure is not observed in this image, but is present in CWGMs. (right) schematic of nanoscale multiplane shear (NMS) mechanism taken from [88]. Upon applied stress, nanodisturbances are generated at the GBs, grow to become partial dislocations that then generate nanotwins within the nanograin.

Either or both mechanisms, NMS and partial dislocation emission from GBs, which are theorized to induce deformation nanotwinning NC materials, may be operating in CWGMs under nanoindentation. The twinning observed in ST Ref-1 sample in Chapter 3 was different morphologically in terms of the density of the twins and apparent size of the twin laths. These particular morphological features were difficult to determine in the ST Ref-1 sample, but the twinning in the CWGM sample certainly has a different character than that in ST Ref-1 and seems to contain much smaller twin laths that are adjacent to each other in

rows. Furthermore, kinking in twin boundaries was observed here and no evidence was found of ω particles on the boundary, unlike in the ST Ref-1 case. No twinning was observed in the STGM case (Chapter 5), so the origin of twinning over slip in the CWGM case should not be due to β instability as it is for the ST Ref-1 case. Thus we are confident that the mechanism inducing DNTs in this case would be distinct from the mechanism inducing twinning in the ST Ref-1 case. We believe the mechanism responsible for DNTs in CWGM is mediated by a mechanism responsible for DNTs in typical nanocrystalline materials, which could be either partial dislocation movement or NMS via nanodisturbance generation.

4.5 Summary

Through TEM and HRSTEM characterization, we have found {112}<111>type nanotwin features in CWGM under deformation in nanoindentation. These deformation nanotwins (DNTs) are found in the indent pit at high densities and are of 15-70nm width with both straight line and zigzag morphologies. The morphology and size of the twin laths, along with evidence that STGM does not exhibit twinning under nanoindentation, lead us to believe that a distinct mechanism from that operating in ST Ref-1 sample is responsible for the DNTs observed here. We believe that the mechanism would be similar to that which is responsible for DNTs in nanocrystalline (NC) materials, especially given the heavily cold worked texture that develops in Gum Metals. The two main theories regarding the mechanisms responsible for DNT formation in NC materials are partial dislocation emission from grain boundaries and nanoscale multiplane shear via nanodisturbance generation. We cannot conclusively state which mechanism is operating in CWGMs from the results in the current study, but we can state that a deformation nanotwinning structure in CWGMs is not necessarily inconsistent with the previous observations of Gum Metals that indicate an ideal shear mechanism is operating during plastic deformation.

5 Continuous lattice rotations in solution treated Gum Meal (STGM) under nanoindentation

5.1 Introduction

STGM, as has been discussed previously, contains no secondary phases and is not unstable with respect to ω transformation. Thus, based on the results and discussions from the previous chapter, we do not predict twinning as the principal deformation mechanism of STGMs under nanoindentation. Given what we know about deformation mechanisms of β-Ti alloys, we would typically assume conventional slip is operating. However, because of the extraordinary mechanical properties of Gum Metals, scientists have speculated an ideal shear mechanism may be occurring during plastic deformation in this alloy.

The primary motivation for performing nanoindentation on STGMs was initially to generate dislocations in order to observe possible pinning points that may be present in CWGMs as obstacles to dislocation motion, thereby allowing for large yield stresses to be attained, as well as to observe the resultant defect structures. A few surprising results were observed and reported in the study by Withey et al. [39], specifically that: 1. seemingly continuous rotations were observed in the pit of the indent (in which individual defects could not be resolved) and 2) the dislocations that were generated outside the nanoindentation pit indeed appeared to be bowed, suggesting pinning by obstacles. In this chapter, we prepare a nanoindented STGM sample for TEM analysis, similar to previous study, except that we perform the analysis in cross-section view to give a more complete picture of the deformation structure underneath the indent. We also add to the previous work by using more advanced methods, such as ADF/HAADF STEM and nanoprobe diffraction in order to answer the remaining questions: 1. What is the exact nature of the rotations underneath the indent? 2. Are they continuous at an atomic scale? 3. What defect structures can mediate the observed large, continuous rotations? 4. What is the nature of the obstacles that are pinning dislocations underneath the indent? The experiments and analysis contained in this chapter are devoted to answering these questions.

5.2 Materials and Methods

5.2.1 Sample preparation

The material used in this investigation was supplied in the form of round bar specimens with a nominal composition of 73.1Ti-23Nb-0.7Ta-2Zr-1.2O at.% (59.1Ti-35.9Nb-2Ta-2.7Zr-0.3O wt. %). The bars were fabricated by Toyota Central R&D Laboratories, Nagakute, Japan via powder processing according to the procedures discussed in Chapter 2reference [4].

The solution-annealed bars were cut perpendicular to the swaging direction into discs of ~300 μm thickness and disc cut to 3mm diameter. Samples were then mechanically polished to ~100 μm thickness with SiC paper. A polished surface for nanoindentation was prepared through one-sided jet polishing with a Fischione Model 1010 twin-jet using an electrolyte solution of 4 vol% perchloric acid, 25 vol% butanol, and 71 vol% methanol at -30°C and 42V for 2min. One-sided electropolishing was performed prior to nanoindentation to provide smoother, damage-free surface than mechanical polishing can

provide and was achieved by covering one side of the sample with non-adhesive Teflon® tape to prevent polishing action. A flatter, damage-free surface will yield more reliable nanoindentation data. Only one side was electropolished briefly both to yield a smooth surface for nanoindentation and to retain sufficient sample thickness to provide a sturdy base for nanoindentation. Subsequently, the electropolished side underwent nanoindentation.

Nanoindentation of the electropolished surface was performed *ex-situ* in a Hysitron Triboindenter© fitted with a triangular diamond Berkovich tip. Nanoindentation was performed for the purpose of imparting heavy, localized plastic deformation in a nominally defect free sample volume. The resultant plastic deformation is hypothesized to occur via ideal shear in Gum Metals. Subsequent TEM characterization of the plastic zone underneath the indent should yield insight into the nature of the local defect structures responsible for the large plastic strains endured and should elucidate the deformation mechanism which allows near-ideal shear strength to be achieved in these materials [8]. The sample was indented using a triangular load-control function with 25mN maximum load and a loading/unloading rate of 5mN/s.

The cross-section of the indent was prepared for TEM observation through the "*in-situ* lift-out technique" [90] using a FEI Strata dual beam SEM/FIB with Ga+ ion source equipped with Omniprobe micromanipulator. Sample preparation schematic is provided in Figure 5.1. The indent was first coated with a 2μm thick protective film of Pt and thinned to an initial thickness of 200nm at 30kV. After the lamellae was attached to the TEM grid, it was further milled and cleaned to a thickness of ~100nm at 6kV and 300pA.

It also should be noted that the sample preparation method here is different from that described in the previous chapters, as it involves FIB lift-out as opposed to a jet polishing method. It is well known that jet polishing can introduce twinning artifacts into samples. However, we also electrolytically thinned nanoindented STGM samples in a manner similar to that described in the previous chapters, and no evidence of twinning was found.

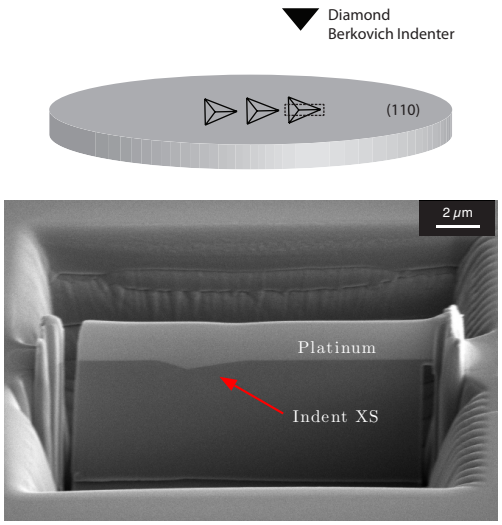

Figure 5.1: Schematic of *in-situ* lift-out process for TEM observation of nanoindentation in cross section is provided. (Top) Gum Metal cut perpendicular to the swaged axis and subjected to electropolishing was indented on the (110) surface. Sample containing region of interest was retrieved by cutting out the section of the indent within the dotted rectangle. (Below) SEM image of sample lamella after initial thinning to 200nm, but prior to lift-out and final cleaning, is shown.

5.2.2 Experimental facilities and parameters

Initial dislocation analysis and dark field imaging was performed on a JEOL 3010 microscope at 300 kV. All scanning nanoprobe diffraction experiments were performed on a FEI Titan operating at 300kV in STEM mode. During acquisition of the HAADF image, a diffraction pattern was acquired for every probe position. The three independent condenser lenses of the Titan microscope enable STEM imaging with various semi-convergence angles. In the present case, a sub-nanometer electron probe with a semi-convergence angle of ~0.9-1 mrad was used in nanoprobe mode. This yields diffraction patterns with non-overlapping spots while still enabling good spatial resolution (<1nm). The microscope was equipped with a Gatan Orius 830 diffraction camera that allowed for capture of full diffraction patterns with a resolution of 1024x1024 pixels at relatively fast acquisition times of only 0.1s. Pattern collection was achieved with custom software implemented in DigitalMicrograph. HAADF-HRSTEM was performed on a modified FEI Titan with a CEOS probe aberration corrector at 300 kV with a probe size of 0.5Å and probe convergence semi-angle of 17.2 mrad. HAADF signal was collected at an inner collection semi-angle of ~53 mrad.

5.2.3 Nanoprobe diffraction analysis algorithm

Diffraction pattern analysis was performed offline using custom MATLAB code. Peaks were located through a routine combining cross-correlation and high pass filtering. High pass filtering was necessary to remove internal structure of diffraction disks to enable more accurate determination of peak center. A peak-fitting algorithm was used on the original diffraction pattern image to refine the initial peak position determined from the cross correlation routine. Strain and rotation maps were then computed by calculating basis vectors for each pattern via a least squares approach. The deformation gradient tensor, **A**, was computed with respect to a reference lattice. This reference pattern was determined by calculating the median basis vectors from all the diffraction patterns included in the bottom half of the data set presented in Figure 5.18. Thus the color index represents deviation of rotation and strain from a nominally deformation-free part of the sample. The deformation tensor was decomposed into stretch and rotation matrices via singular value decomposition algorithm [91], such that

$$\boldsymbol{A} = \boldsymbol{U}\boldsymbol{H},$$

where U and H are rotation and stretch matrices, respectively. The rotation value, θ, can be computed from the matrix, since

$$\boldsymbol{U} = \begin{bmatrix} \cos\theta & -\sin\theta \\ \sin\theta & \cos\theta \end{bmatrix}.$$

We use the Biot strain measure, where

$$\boldsymbol{E} = \boldsymbol{H} - \mathbf{1}.$$

A note should be made that if the strain matrix is computed this way directly from the change in reciprocal lattice basis vectors, they would represent the strains in reciprocal

space. If the measured lattice basis vectors are determined from the diffraction patterns, the real space strains may be computed with $\boldsymbol{E}_{\mathbf{real\ space}} = \mathbf{1} - \boldsymbol{H}$.

5.3 Results

5.3.1 Nanoindentation Data

The resultant load-displacement curves obtained from the nanoindentation test, shown in Figure 5.2, are similar to those given in Withey et al. [39], in which no "pop-in" events are observed. Mean hardness measured is 2.63GPa with a standard deviation of 0.06GPa. This value is consistent with the experimentally measured Vickers hardness values of 250Hv obtained by Saito et al. [81]. This value is equivalent to 2.65GPa as stated in Section 4.3.1. As stated in Chapters 3 and 4, the hardness values measured for ST Ref-1 and CWGM were 4.14GPa and 3.0GPa, respectively. If the plastic deformation were mediated *solely* by an ideal shear mechanism, we would not expect the hardness to increase upon cold working, similar to the data obtained by Saito et al. [81] in which no increase in Vickers hardness values were observed with increasing cold working ratio. Otherwise, with respect to a conventional dislocation hardening mechanism, it seems reasonable that the hardness values increase from STGM to CWGM to ST-Ref1. That is, a worked alloy should be harder than a non-worked alloy due to repulsive interaction between dislocations that have been generated in the cold working process (CWGM), and a material that contains coherent precipitates may be harder still due to interactions of elastic strain fields surrounding particles and dislocations (ST Ref-1). This finding that the hardness has increased in CWGM compared to STGM would also seem to be consistent with the fact that CWGMs have a higher yield strength than STGMs as observed in the tensile curves [4], which would, typically, be attributed to the effect of work hardening through generation and interaction of dislocations and defects. The measured E_r value for STGM was much higher than that of the other two materials, exhibiting a Young's modulus of 91GPa as calculated using the

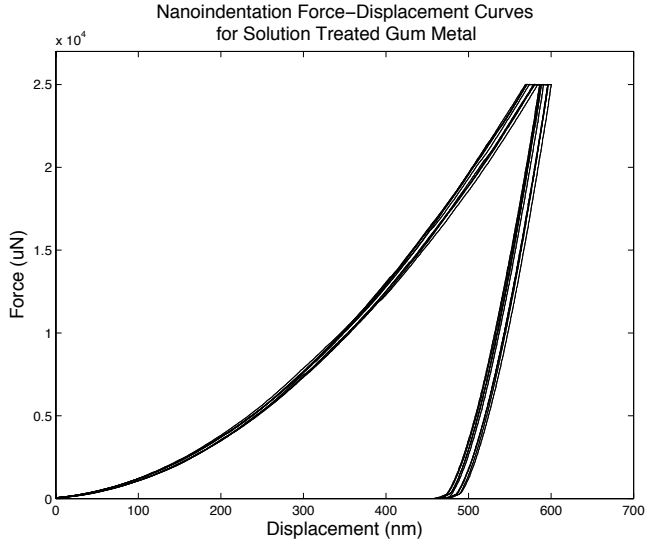

Figure 5.2: Load-Displacement curves for STGM sample, achieved with load-control function on Hysitron Triboindenter® with max load of 25mN. E_r of 91 GPa and H of 2.63GPa was calculated, but due to the creep observed at the max load, these values are semi-quantitative guides only. No obvious pop-ins are observed so onset of initial plasticity is unclear from the data and could very well be initiated near the start of loading

analytical method described in Section 3.4.1, whereas the modulus for CWGM was calculated as ~76GPa. It has been observed in the tensile loading curves of gum metals, that STGM exhibits a higher modulus value than CWGM, ~90GPa compared to ~48GPa. [4]. Thus our result is consistent with the increased modulus of STGM measured in the previous study. However, it is unclear presently why the ST Ref-1 sample would have a E_r less than that for STGM.

5.3.2 Conventional TEM results

Overview bright field TEM images of the entire indentation cross section are presented in Figure 5.3, each taken at different sample tilt angles. We observe in the first image that the contrast of defect structures within the indent is obscured by diffraction contrast effects, notably bend contours. The image on the right is taken at a different sample tilt in which the diffraction effects have been reduced. The original indent is filled with Pt during the lift-out procedure as indicated in the figure. We observe a high density of dislocations surrounding the indent, which extends 4-5μm below the indent, similar to the high dislocation density surrounding the indent pit observed by Withey et al. [39]. While these authors did not directly observe dislocations within the indent pit itself, the images presented in Figure 5.3 are at too low of magnification to determine whether dislocations are present directly beneath the indent. We observe two deformation features 3-4μm below the indent that we later identify as dislocation cells network structures in an initial stage of formation. We note that this result supports the conclusion given in Section 2.3.2.3 that the subgrain structure of CWGM consists of dislocation cell networks. Another feature has been highlighted in red, which seems to denote a boundary and we note its discrete step-like appearance here. We later identify such structure from nanoprobe diffraction analysis as a small-angle grain boundary that has most likely been formed upon deformation.

5.3.2.1 Dislocation analysis: Burgers and line vector determination

The movement of dislocations is the typical mechanism by which a material may respond to a high enough applied stress and deform, or change shape. Dislocations are line defects characterized by a Burgers vector, **b**, and a line direction**, u**, which together determine the slip plane on which the dislocations move. The dislocation has an associated strain field that distorts and bends surrounding lattice planes. It is the distortion of these planes, or the strain field, that changes the local diffraction condition allowing for the approximate position of the dislocation line to be determined upon imaging. Amplitudes of forward scattered and one diffracted beam in two-beam condition can be calculated with the Howie-Whelan equations, which can be modified to include an elastic distortion inside the material. After taking into account the lattice distortion, the amplitude of the diffracted beam associated with **g** will go to zero when g.b = 0.Thus, if we set up a two beam imaging condition by tilting the sample, where we include a diffracted beam associated with the g reflection that satisfies **g.b** = 0, the dislocation should be invisible. Determination of **b** is achieved through imaging with different diffracted beams in different zone axes and determining under which conditions the dislocations appear invisible. This imaging experiment is typically known as "**g** dot **b**" analysis. [19 p. 442-444]. The line vector **u** can be roughly determined by observing the projected directions of the dislocation lines under different imaging conditions. Knowledge of typical slip systems operating in the material

can enable a determination of u without requiring full trace analysis, as will be done here. Observed slip systems for BCC materials are slip planes {110}, {112}, {123} with burgers vector <111> type, or {110}<001> [92] (not commonly observed), where the {110}<111> is the most commonly observed type as it involves slip in the closest packed direction on the densest plane.

From the two bright field images given in Figure 5.4, we find four main dislocation types decorate the sample, and examples of these dislocations are given in the figure as colored lines, outlining the projected direction of that respective type of dislocation, except for those outlined by the red lines, which denote the boundaries of the dislocation cell network. We term the blue type as "H" for "horizontal", the yellow as "SL+SR" for "slant left and slant right", the purple as "V" for "vertical" and the dislocations within the red lines as "Web". Figure 5.4b is an image of the same approximate region in a), but at a different sample tilt to enable visualization of the other dislocation types not visible in image a). Outline of plane traces are given in the inset DP to establish the starting orientation for the subsequent **g.b** analysis.

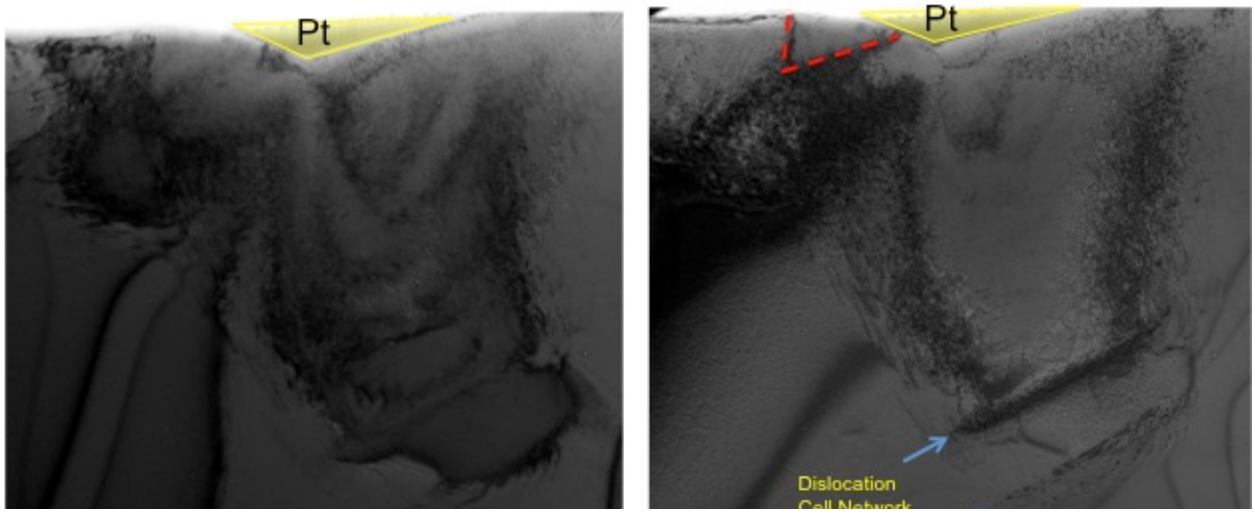

Figure 5.3. Bright field TEM images of the entirety of the indentation cross-section. Each image is of the same sample, taken at different sample tilt conditions to bring attention to pervasive diffraction contrast that can obscure deformation features, as evident in the left picture. There appears to be a high density of dislocations surrounding the indent. On the right, we observe initial stages of dislocation cell network formation well beneath the sample and the appearance of a small angle grain boundary directly adjacent to the nanoindentation surface.

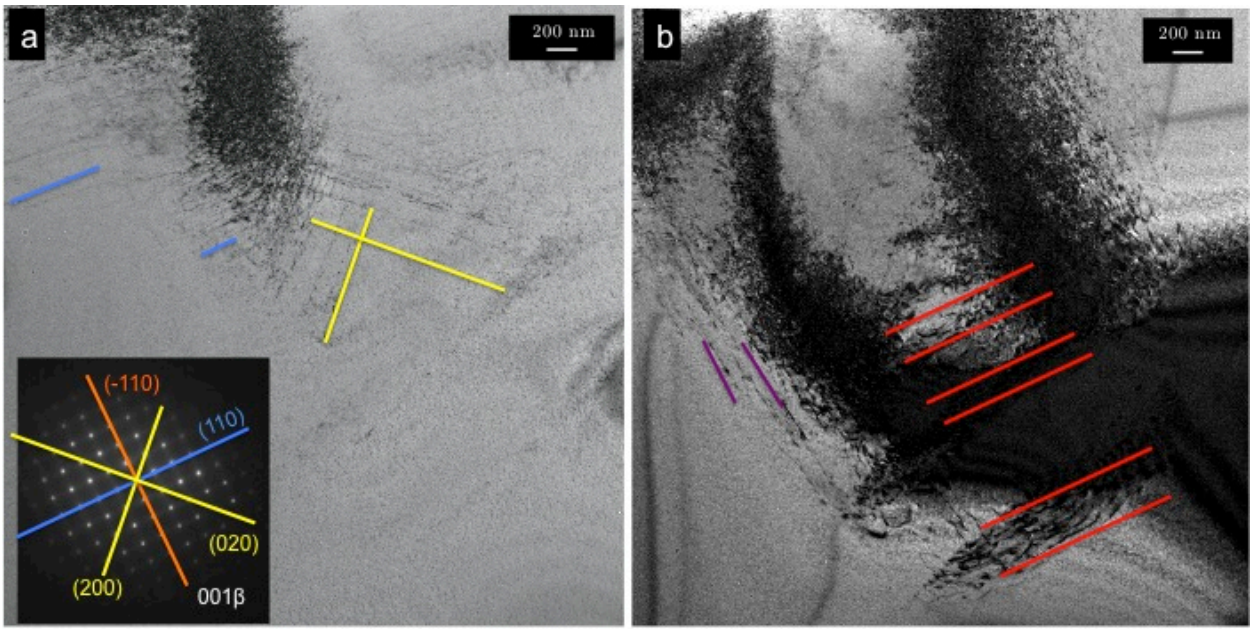

Figure 5.4: Four main types of dislocations lines can be viewed from the overview bright field images, where the blue is "H", horizontal, yellow is "SL+SR" for slant left and slant right, purple is "V" for vertical, and the red lines denote the boundaries of the dislocation cell network, in which we term the dislocations in this region "Web".

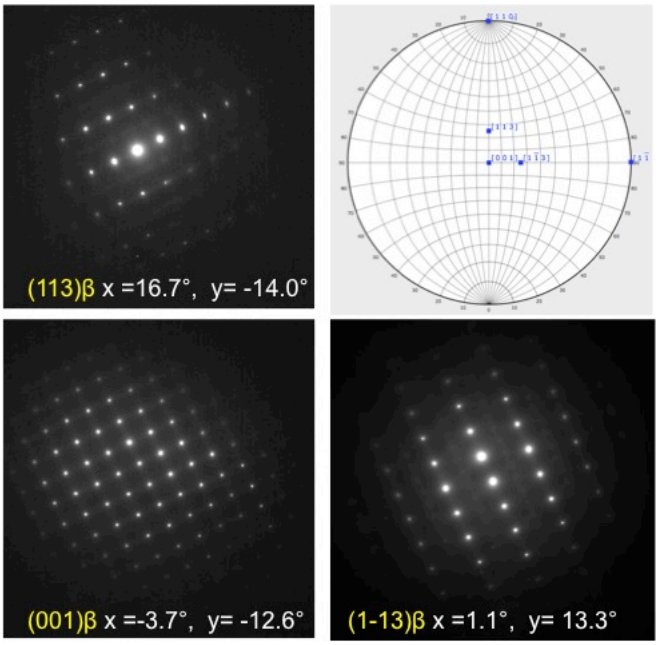

Figure 5.5: Orientation of zone axes with respect to sample/stage tilt. Stereographic projection of [001]β zone axis shown in the upper right gives relative orientation of the other zone axes used in the **g.b** experiment.

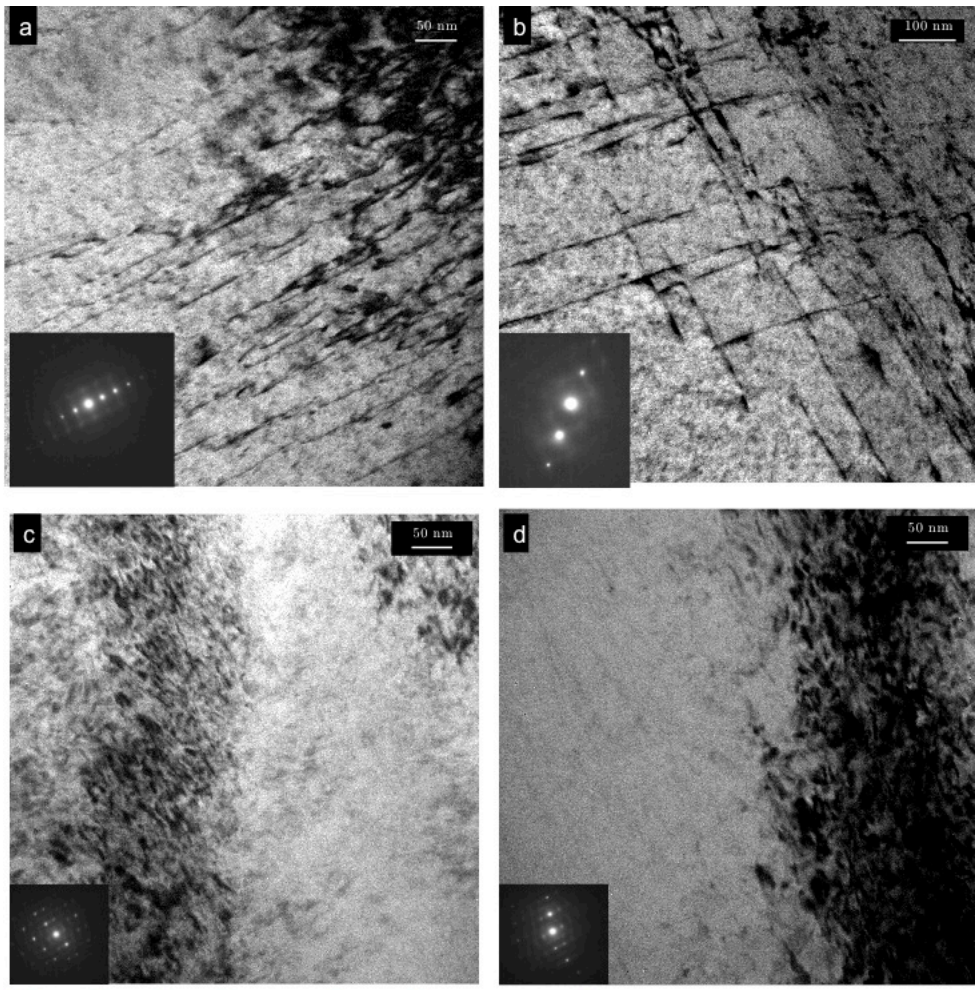

	X tilt	Y tilt	g vector	Zone	Visible?	Possible types based on g.b
a	1.6	-12.6°	-110	(001)	Yes (H) No (V)	-111 or 1-11 111 or -1 -11
b	4.2	-5.9	200	(001)	Yes (both)	No added info for <111> type
c	19.0	-5.5	-1-21	(113)	Yes(H) ?	1-11 -1-11 or 111
d	22.7	-11.3	21-1	(113)	No (H) Yes (V)	1-11 -1-11 or 111

Figure 5.6: g.b analysis for H and V – type dislocations. Further analysis from **g** = 2-1-1 in **Figure 5.9**, leads to determination that V-type dislocations have **b** = [111], but that cannot be deduced from the images in this figure alone.

5.3.2.1.1 **g.b** analysis of "H" and "V" dislocations

Figure 5.5 gives the orientation of the zone axes for the sample to enable easy determination of the condition of the diffracted beams. Figure 5.6 provides images of the "H" and "V" dislocations under specific two-beam imaging conditions as specified in the accompanying table. In Figure 5.6a, we find that H-dislocations are visible. We know BCC structures have the Burgers vector in <111> type directions, as these are the closest - packed directions in the BCC crystal structure, but <001> directions are possible as well. As the H, but not the V dislocations, are visible, we can narrow the possible Burgers vectors as shown in the table, and although not stated in the table, [010] and [001] vectors remain possible. Imaging with **g** = 200, as in Figure 5.6b, demonstrates that both dislocations types are visible. All <111> burgers types are visible under this condition, but only the [100] is visible out of the <100> types, so it actually narrows the possibilities further. We tilt the sample to nominally (113) zone axis for figures c, d and e. Figure c is an image taken with **g** = -1-21, and the H dislocations are faintly visible, implying the H-type must have Burgers vector of [1-11] direction. It is not clear whether the V-type dislocation are visible. Diffraction of higher order planes is weaker than lower order, so we expect the contrast to be reduced when imaging with higher order beams, and it can be difficult to judge whether a dislocation is visible or not. We verify this in figures d and e by imaging with **g =** 21-1. The fact that the H-type dislocations are invisible in both d and e is consistent with a Burgers vector in [1-11] direction (although it technically remains a possibility that the burgers vector is [001] type). The only way to rule this out is to image with **g =** [0-11] or [001], which is nearly impossible given the limitations of stage tilt). Again, the V-type dislocations in d) are very faint, and another region adjacent to the imaged region is pictured to show the visibility of these dislocations. From these last two image conditions, we cannot distinguish if the V-type has [-1-11] or [111] burgers vector. From subsequent analysis, shown in Figure 5.9, we later observe from **g**= -211 that the V dislocations are visible, and determine they have a Burgers vector of [111].

We can calculate the slip plane by deducing the line direction **u** from the images. From the image in Figure 5.9 near a [1-13] zone, we find the projected line of the V-dislocation has not changed from a nominally [001] zone implying V-type dislocations have a **u** = [110]. We calculate the slip plane as follows: **N**(slip plane) = **b** x **u**, where 'x' is the cross product operation. Thus, the slip plane for the V-type would be (-110), and they must be operating on (-110)[111] slip system. Our best guess for the dislocation line of both types, since they have the similar projected lengths, would be that they are equivalent. The H-type seem to follow a [1-10] direction, which would imply a line direction of [1-10] or [1-11]. Given that the V-type has been determined to have **u** = 110, we assume H-type has **u** = [1-10], yielding a slip plane of (110). Results of the analysis are given in Figure 5.10.

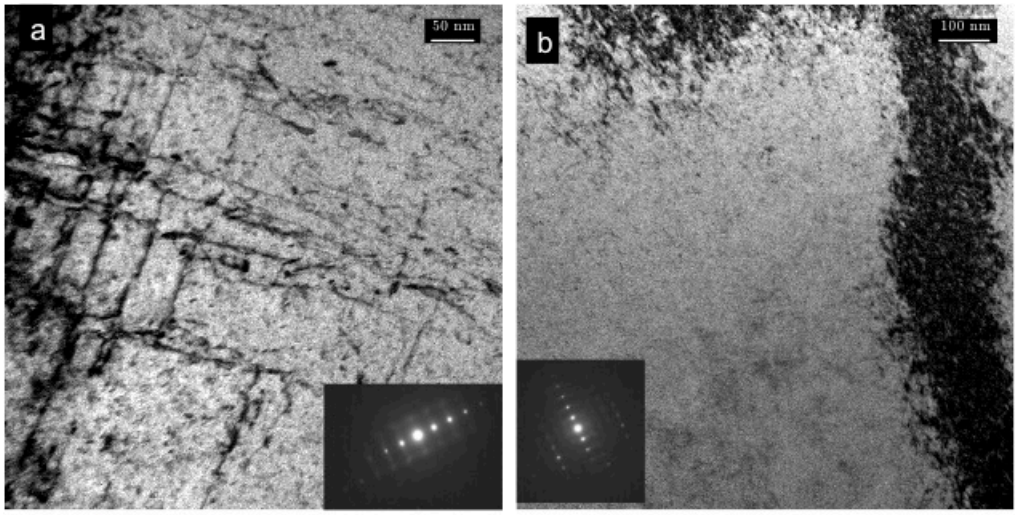

	X tilt	Y tilt	g vector	Zone	Visible?	Possible types based on g.b
a	1.6	-12.6°	-110	(001)	Yes (SL +SR)	-111 OR 1-11
b	-3.8	2.1	110	(001)	No (SL+SR)	-111 OR 1-11

Figure 5.7: From **g.b** analysis, we can determine the Burgers vector of these dislocations, SL and SR types are [-111] or [1-11]. From looking at the project line of the dislocation under different zone axes, we can deduce the line vector, **u** is [100] and [010], as demonstrated in **Figure 5.9**.

5.3.2.1.2 **g.b** analysis for "SL" and "SR" type dislocations

We perform a similar analysis for SL and SR type dislocations as provided in Figure 5.7. We determine that **b** for both SL and SR must be [-111] or [1-11] as they are both visible under **g** = -110 and invisible under **g** = 110 imaging conditions. We should still note it may be possible for the Burgers vector of these dislocations to be [100] or [010] type, as the **g** conditions used do not rule out this possibility. For the SR-type, the line direction **u** could either be [100] or [101] as the projected line vector follows a [100] direction. We subsequently deduce from **g**= -211 imaging condition, shown in Figure 5.9, that the line direction is [100]. This line direction would yield a slip plane of (01-1) for **b**= [-111] and (011) for **b** = [1-11] for SR.

For SL, the projected line direction follows the [010] direction, thus the line direction **u** could either be [010] or [011]. Given the subsequent imaging in Figure 5.9, we again can deduce that **u** = [010]. This yields a slip plane of (-10-1) for **b**= [-111] and (-101) for **b** = [1-11]. Results of this analysis are summarized in Figure 5.10.

5.3.2.1.3 **g.b** analysis of "Web" dislocations

We next find the character and slip plane of the "Web" dislocations found in the proto-dislocation cell network structures observed in Figure 5.3. Results of **g.b** analysis are provided in Figure 5.8. We first performed imaging in the [001]β zone axis. With **g** = 110 we find the dislocations visible, reducing the possibilities of the Burgers vectors to [111], [-1-11], and technically [100] and [010], although we do not include them in the table. Figure 5.8b with imaging condition **g** = 1-10 confirms the previous result. We tilt to a second zone axis, nominally (1-13)β. Figure 5.8c shows very faint lines of the dislocations under **g** = -211, whereas, in Figure 5.8d, they are completely invisible with **g** = 1-2-1. Both of these are consistent with **b** = [-1-11]. As the dislocations are curved, the line vector is constantly changing, so it is difficult to determine the exact slip plane of the dislocations or if parts of the dislocations are on different slip planes due to cross slip.

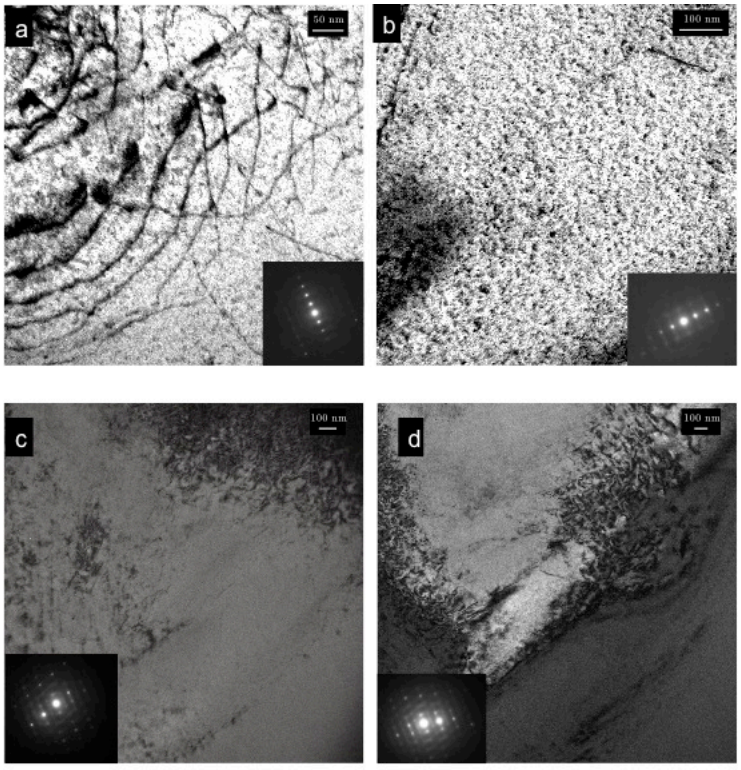

	X tilt	Y tilt	g vector	Zone	Visible?	g.b
a	-3.7	1.9	110	(001)	yes	111 OR -1-11
b	1.6	-12.6	1-10	(001)	No	111 OR -1-11
c	7.2	13.3	-211	(1-13)	yes	-1-11
d	6	11.4	1-2-1	(1-13)	No	-1-11

Figure 5.8: g.b analysis performed for the "Web"-type dislocations reveals they have a Burgers vector of [-111].

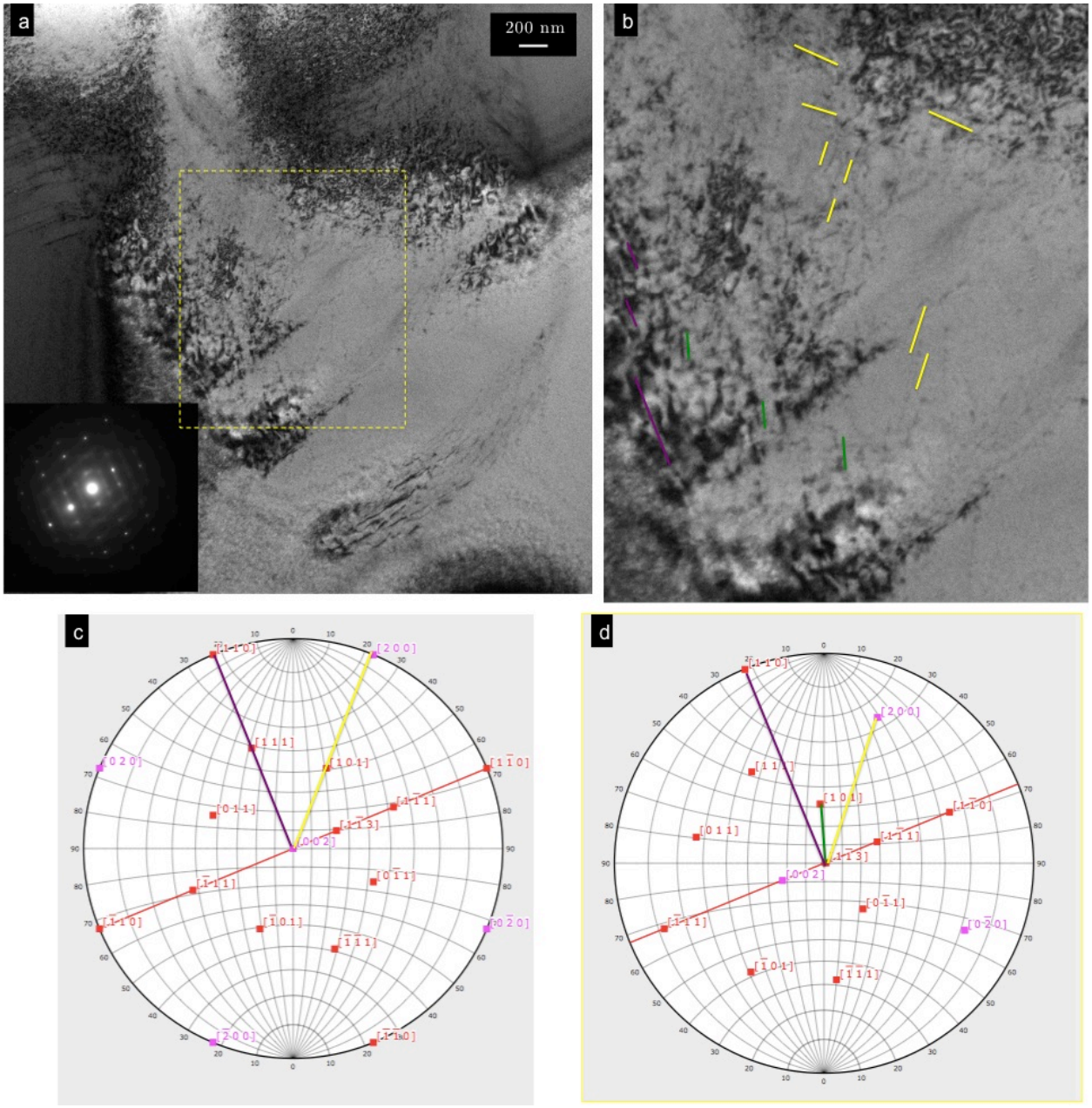

Figure 5.9: A lower magnification image of **Figure 5.8**c is given in a. b. provides a magnified view of the region of interest, in which SL+SR types (yellow) and V type can be observed. This image, taken with **g** = -211, reduces the Burgers vector and line direction possibilities for these types. Stereographic projection of [002] and [1-13] zone axes are given in c and d, respectively. As the V-type is visible, the burgers vector must be [111]. Since the projected line direction of each type did not change upon tilting to [1-13] zone axis, the line vectors are [200], [020], and [110] for SR, SL, and V, respectively. We deduce H-type, since it has same projected line length as V, has a [1-10] line direction (as opposed to [1-11]).

A lower magnification image of Figure 5.8c at the same imaging condition (**g** = -211) is given in Figure 5.9a. From this image, taken with **g =** -211, we notice SR and SL (yellow), and V (purple) type dislocations are visible. The possible Burgers vector for SR and SL from Figure 5.7are consistent with the fact they are visible in Figures 5.9a, but does not narrow down the possibility to single Burgers vector for either type. Figure 5.9b gives a magnified view of the outlined region. A few of the dislocations have lines drawn adjacent

to them as a guide to the eye since the dislocations in this imaging condition appear very faint. We also can observe their projected direction, and find that the SR and SL maintain the same projected direction of [100] and [010] respectively, as visualized in the stereographic projections of Figure 5.9c and 5.9d. The lines drawn on the stereograph projection would be the apparent observed projection of the dislocation as visualized from the respective zone axis of the given stereographic projection, which is [001] in Figure 5.9c and [1-13] in 5.9d. We thus determine that since the projected line direction does not change upon tilting to [1-13] zone, that **u** = <100> for SR+SL types. Furthermore, we find that the V-dislocations, outlined in purple (similar to that shown in Figure 5.5), are visible in the image, and thus have a Burgers vector of [111]. The projected line direction remains as [110], and we determine that the slip system for V-dislocations would be (-110)<111>. We note there are other dislocations that were not observed previously that are outlined in green, seemingly unrelated to the types analyzed here.

5.3.2.1.4 Summary

Results of the dislocation analysis are summarized in Figure 5.10, and are consistent with the finding by Withey et al [39] that the observed dislocations emanating from the indent pit are of <111> type. All dislocation types imaged are consistent with a {110}<111> -type slip system operating. The results seem reasonable with the fact that {110}<111> slip systems are most commonly observed slip system in BCC as they require the least activation energy compared to other systems.

Type	b	u	Slip System
H	1-11	1-10	(110)[1-11]
V	111	110	(-110)[111]
SL	-111 OR 1-11	010	(101)[-111] OR (-101)[1-11]
SR	-111 OR 1-11	100	(01-1)[-111] OR (011)[1-11]
Web	-1-11	Curved	----

Figure 5.10: Summary of **g.b** analysis.

Lastly, we would like to note that no twinning or stress-induced martensitic phases were observed in the sample, and that dislocations were the only defect structure observed in conventional TEM imaging experiments.

5.3.3 ADF and HAADF STEM data

We use atomic resolution STEM imaging and lower magnification ADF/HAADF imaging to understand the nature of pinning points found by Withey et al [39], and to observe the dislocations with minimal diffraction contrast effects, such as bend contours. This will enable a better qualitative understanding of the true dislocation density and dislocation

interactions in STGM that occur upon nanoindentation of STGMs. Camera length or inner collection angle will be specified where necessary, and the typical collection angle for these images is 22mrad (ADF condition) where not specified.

5.3.3.1 Dislocation-Dislocation Interactions underneath nanoindent

In Figure 5.11, we see an overview of the nanoindentation cross-section under HAADF/ADF conditions, and note that the dislocations in dark field imaging conditions appear white.

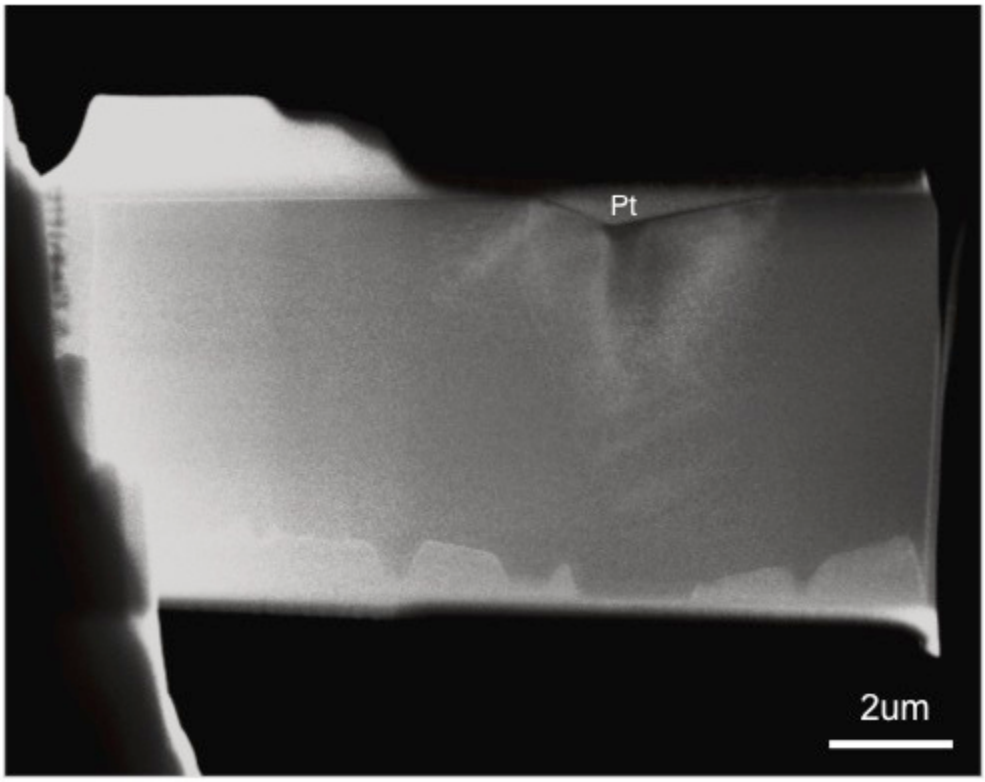

Figure 5.11: Overview of nanoindent taken with HAADF detector in STEM mode.

In Figure 5.12, we present magnified views of particular regions of the indent to demonstrate the very high dislocation density present underneath the nanoindent. We observe many dislocations are most likely interacting, but as the image is only a projection of the sample, it is difficult to determine if they are actually interacting despite apparent overlap. We note the absence of bend contours in the HAADF image, allowing dislocation image interpretation to be less complex. However, most regions, as shown in figures b, c, and d, contain too high a dislocation density to provide a clear, unambiguous picture of these dislocation-dislocations interactions. We also note that the “H” and “V”-type dislocations imaged in the previous section are visible in Figure 5.12b and the “SL”, “SR”, and “Web” types are all visible in Figure 5.12c

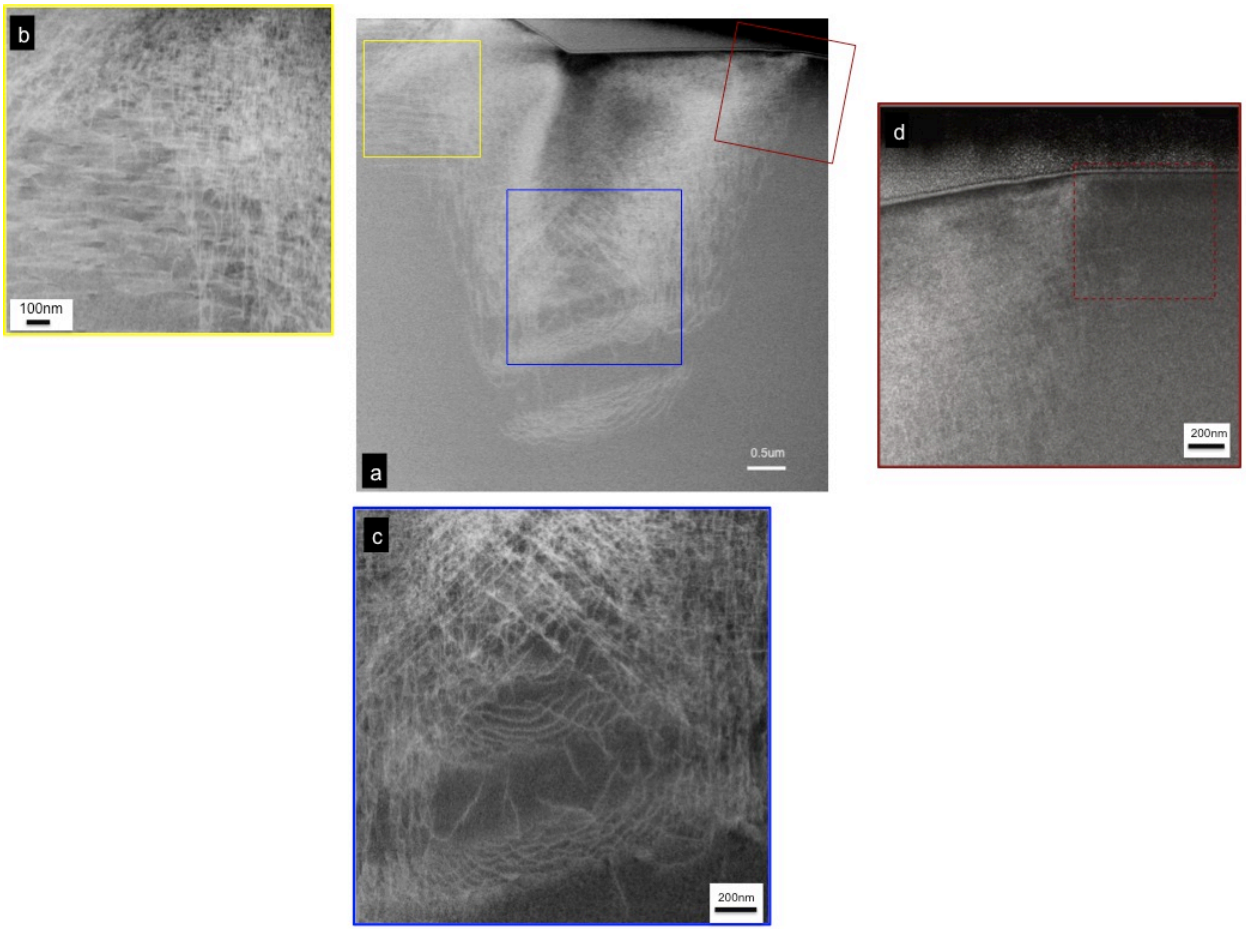

Figure 5.12: Higher magnification images of various regions underneath the nanoindent in a) are provided in b), c) and d). Image demonstrate complex extremely high density of dislocations are present underneath the nanoindent. Region outlined in d) is analyzed in the following figure.

To understand these interactions further, we image a region with a lower dislocation density, as outlined in Figure 5.12d and presented in Figure 5.13, with a and b imaged with 22mrad inner collection angle, and c and d with 27.5mrad, which are considered ADF conditions. We find in Figure 5.13a what appears to be a bowed dislocation, reminiscent of the bowed dislocations found by Withey et al. [39]. In b), we image the dislocation at higher magnification, and we observe a possible "particle" ahead of the bowed region of the dislocation. Increasing the magnification further, we find the "particle", or pinning point, exhibits dipole black/white contrast and is most likely the structure responsible for the dislocation bowing. In d), we present a magnified view of the particle imaged in c) to demonstrate the superlattice that is present in the "particle", in which an extra peak position is present in between every row and column. A motif is presented in the image, where the red circles represent the BCC matrix atomic column positions, and the blue circles represent atomic columns of the super structure.

We analyze the Fourier transform of the images to determine more precisely the periodicity of the superstructure, and whether it may be associated with a particular phase or ordered structure. Figure 5.13c is shown again in Figure 5.14a, with the Fourier transform included in the inset. We find the superstructure does yield extra reflections, but

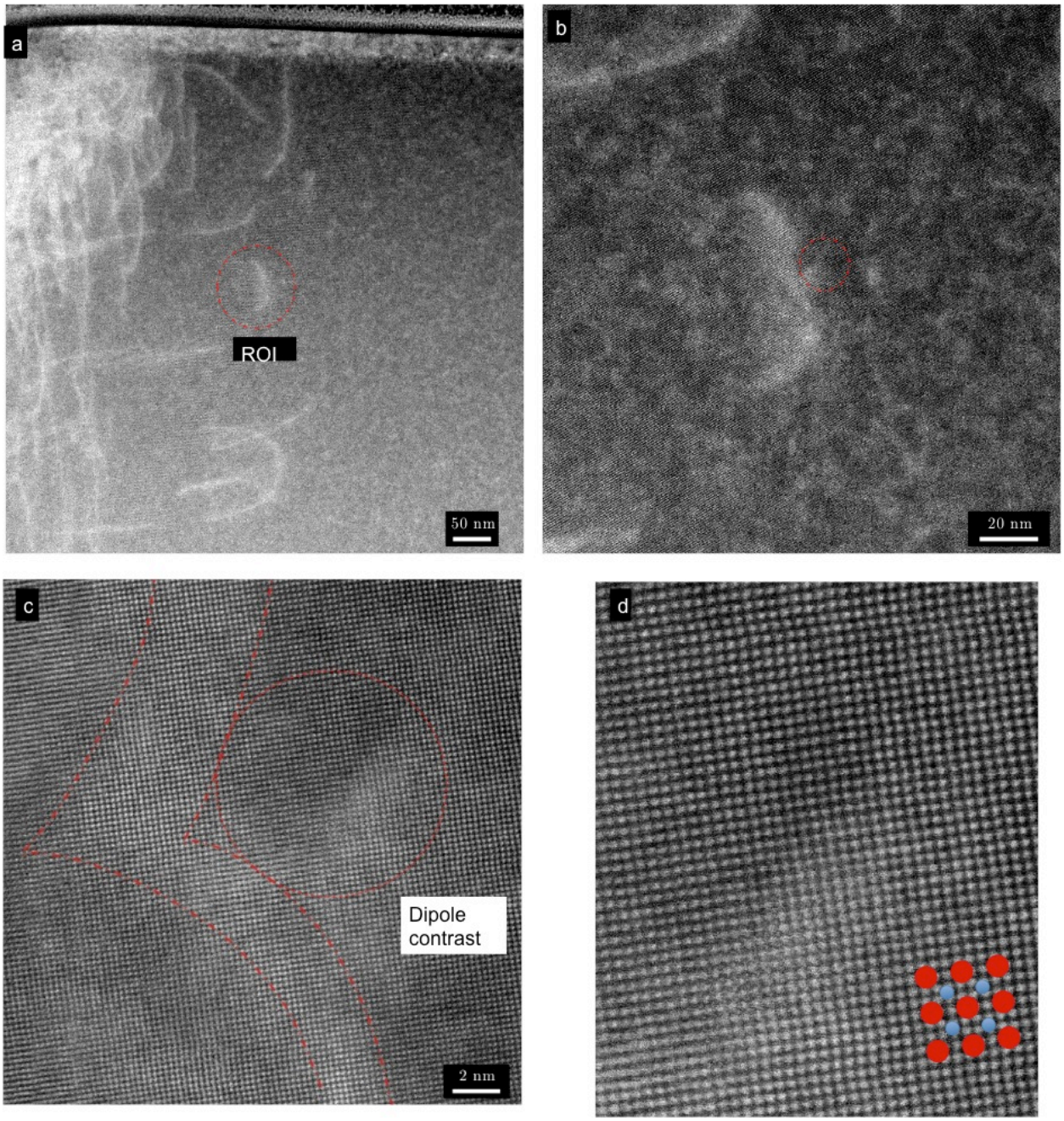

Figure 5.13: In b-d, we present ADF images of increased magnification of the ROI outlined in a. The bowing of the dislocation is apparent from the white contrast that gives an approximate position of the dislocation line. We find the bowing of the dislocation is due to a pinning point that contains dipole contrast (c) and superlattice peaks (d).

not in any positions associated with a different structure than BCC; instead it appears that the (-110) and (1-10) reflections are rotated about the 000 reflection. These rotated reflections are quite faint, and the other reflections are not seemingly rotated. Another pinning point, also exhibiting superlattice peaks and observed near a bowed dislocation, is given in Figure 5.14b. However, as the superlattice peaks are nearly exactly half the plane spacing, the superlattice reflections are probably superimposed on the fundamental reflections in the FFT. We note, though, that it is difficult to be certain that there are no extra reflections, given the large amount of streaking present in the FFT from the scanning

artifact in STEM mode. We also note here that the superstructure lattice encountered in Figure 5.13c is actually present in much of the image, not just in the region of the pinning point. This point will be discussed following a demonstration that the superstructure is not originating from a diffraction contrast effect or a thickness effect.

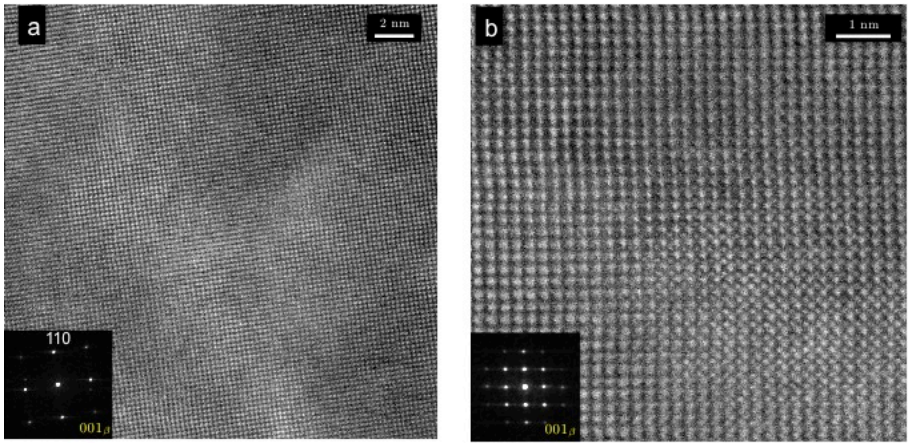

Figure 5.14: a) Image in **Figure 5.13**c is reshown here with an included FFT that indicates extra reflections that appear to be the -110 and 1-10 rotate about the central beam. Another particle, also adjacent to a bowed dislocation, also exhibits superlattice peaks, but no extra reflections are found in the FFT, as the peaks seem to be almost exactly half the lattice spacing, an thus most likely any "extra" reflections that would originate from the motif, fall on fundamental spots in the FFT.

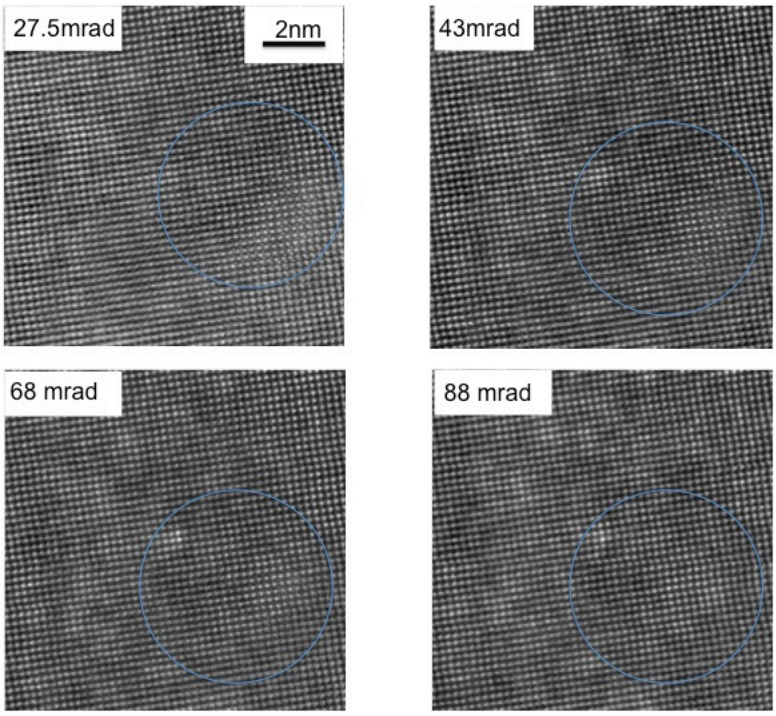

Figure 5.15: ADF/HAADF images are taken of a region exhibiting superlattice reflections at increasing inner semi-collection angle as specified in the image. The superlattice reflections are still clear at 68mrad, while only a few peaks are noticeable at 88mrad. Since the superlattice reflections are still apparent under HAADF conditions, we do not attribute the superlattice peaks to a diffraction effect.

We performed imaging of another region containing these superlattice reflections at different camera lengths, to see if the superlattice reflections disappear as the imaging

condition becomes dominated by quasi-elastic incoherent scattering or thermal diffuse scattering (TDS) as expected under HAADF conditions, and as scattering from coherent, elastic interactions, or diffraction effects, is diminished. The respective collection semi-angle is given for each camera length used, and we find that as the camera length is decreased, and the signal is dominated by thermal diffuse scattering, the intensity of the peaks become dimmer, but do not vanish entirely. Even the region imaged at 88mrad contains a few superlattice peaks, and thus the peaks are visible even under "true" HAADF conditions. Thus, since the superstructure motif did not vanish entirely and was clearly present at 68mrad, we do not think it is a diffraction effect, but rather originates from the presence of real atomic columns.

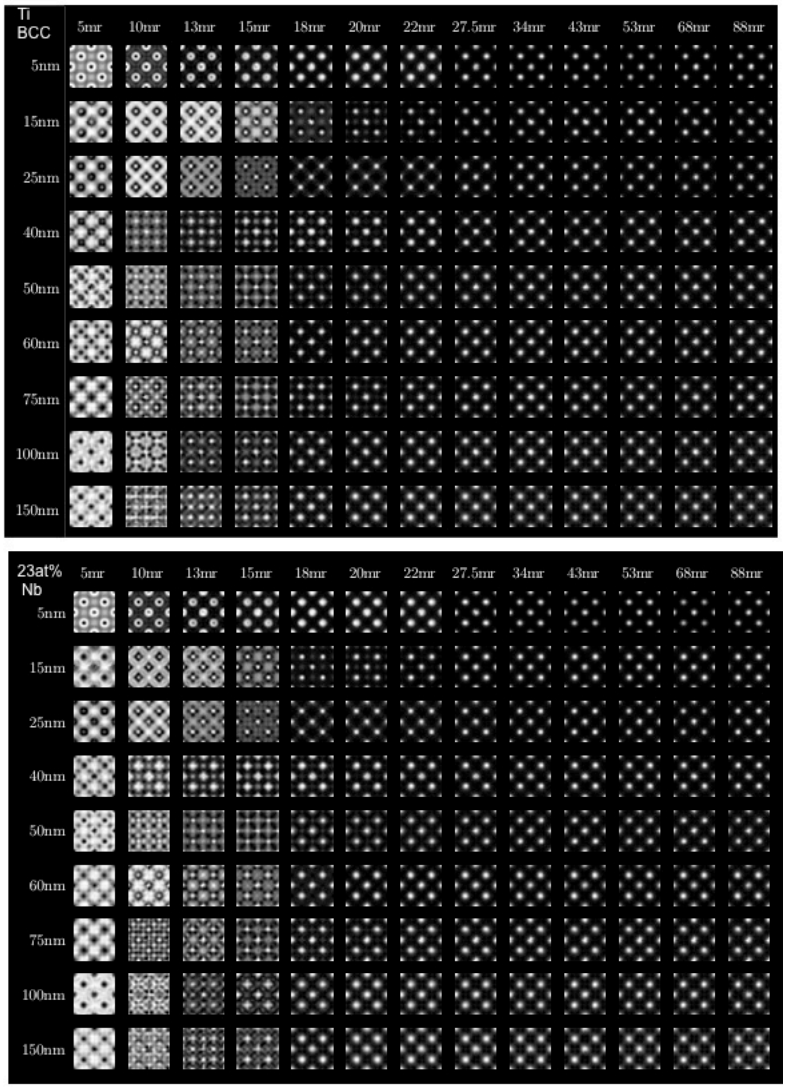

Figure 5.16: Multislice STEM simulations (with similar parameters used for simulations in Chapter 2) are presented for [001] direction of BCC –Ti(top) and a randomly ordered 23at%Nb Ti alloy (bottom). A range of thicknesses with different inner collection semi-angles was simulated. We find that the experimental ly observed superstructure peaks are not found at 68mrad at any thickness in the simulation, and only the case of 22mrad at 75nm thickness exhibits a similar motif. Thus, as the motif was clearly observed at 68mrad, we conclude it is unlikely that superstructure peaks are caused by a diffraction, thickness, or alloying effect.

Multislice STEM simulations (**Appendix A.1**) of the sample in a [001]β orientation performed at different thickness and collection semi-angles are presented in Figure 5.16, and indicate that superstructure peaks are not related to a thickness effect or a diffraction effect at the imaging conditions used. All imaging is performed at collection semi-angle of 22mrad or above in the current study, and the thickness of the sample is approximated to be between 50 and 100nm. The simulations in Figure 5.16(top) are for a Ti BCC matrix, and the simulations in the bottom of the figure are for a Ti BCC matrix with 23at% Nb populating random matrix sites. We do find that a similar superlattice is possible under certain imaging conditions from the simulation, especially in BF to ADF conditions, 18-22mrad, for certain thicknesses. However only the 75nm thick, 22mrad case for both materials demonstrates the superlattice motif, which are parameters consistent with those used in this experiment, although the superstructure peaks appear very faint compared to the matrix peaks in the simulation. Most interestingly, we find that at 68mrad no thicknesses exhibit a superstructure pattern as is clearly observed in Figure 5.15c. Thus we determine, for the imaging conditions used and thickness of the sample, the observed motif does not originate from diffraction contrast or a thickness effect, nor is there an effect from the niobium alloying that would cause the superstructure peaks.

Through imaging at different camera lengths and performing multislice simulations, it has been established that the extra columns are not likely to be due to imaging artifact, thickness effect, or alloying effect. We then performed EDS at 200kV on a FEI Titan on the sample to determine whether the atoms are simply columns primarily of titanium atoms or indicate atomic ordering or clustering. We do not present the results here as they were not near atomic resolution. However, results did not indicate the presence of any atomic clustering of any kind, including gallium, which we checked for as the sample had been made with the FIB.

Thus we determine that secondary phases, atomic clustering, and typical imaging artifacts cannot account for the superstructure peaks. We note the dipole contrast of the pinning point, and hypothesize the structure may be a dislocation with a screw component that is oriented in a way that it is being imaged nearly end-on. The extra atoms in the motif could originate from a surface relaxation phenomenon termed “Eshelby twist”, in which the lattice planes surrounding a screw dislocation core relax at the surfaces of a thin foil [93]. This relaxation would result in the twisting of atomic planes at the surfaces of the foil in opposite senses, and result in atomic displacements normal to the dislocation line. Similar rotations of atomic columns yielding rotated peak positions were observed in aberration-corrected ADF-HRSTEM optical sectioning of GaN foils containing dislocations with screw component normal to foil plane [94]. In this study, conducted by Lozano et al., the authors argue that it is the finite depth of field of the microscope that allows the Eshelby twist to appear as a simple rotation upon optical sectioning through the depth of sample, and that the resultant images can be interpreted as projections over the depth of field centered at the focal plane. Typically, it is thought there is strong channeling effect in STEM imaging that would conceivably diminish the effect of a twist that is largest at surfaces of the specimen. However, we imagine a similar situation to that observed in the Lozano et al. study is occurring at the focal value used, where the atomic columns are twisted through

the foil, and it is the projection of the twist over a limited depth about the focal plane that results in the extra peak positions in the final image.

If Eshelby twist is the true origin of the extra peaks in the motif, this would imply the pinning point imaged has a screw component normal to the foil surface. We reason, from the results of the previous section, that the pinning point is a mixed dislocation with a nominally [001] line direction and a Burgers vector of <111> type. Thus, there is both screw and edge component, for which the screw component is responsible for the extra peak positions in the motif. We deduce this is why superstructure peaks are prevalent in many regions in image Figure 5.13a: two dislocations are present in the image, and both may be exhibiting the Eshelby twist phenomenon. We also note that a previous study by Grillo et al. [95] observed that ADF images of slightly mis-tilted samples containing end-on screw dislocations in GaN also exhibit a dipole contrast similar to that which has been observed here.

We present other images that demonstrate the bowing of dislocations around other dislocations. In Figure 5.17(left) we observe the curved projection of a dislocation line, and find an extra half plane near where the dislocation is curving (the dislocation line given by white contrast only gives an approximate location of the dislocation core). We do not observe any extra atomic motif in the vicinity of the edge dislocation, but we do in the

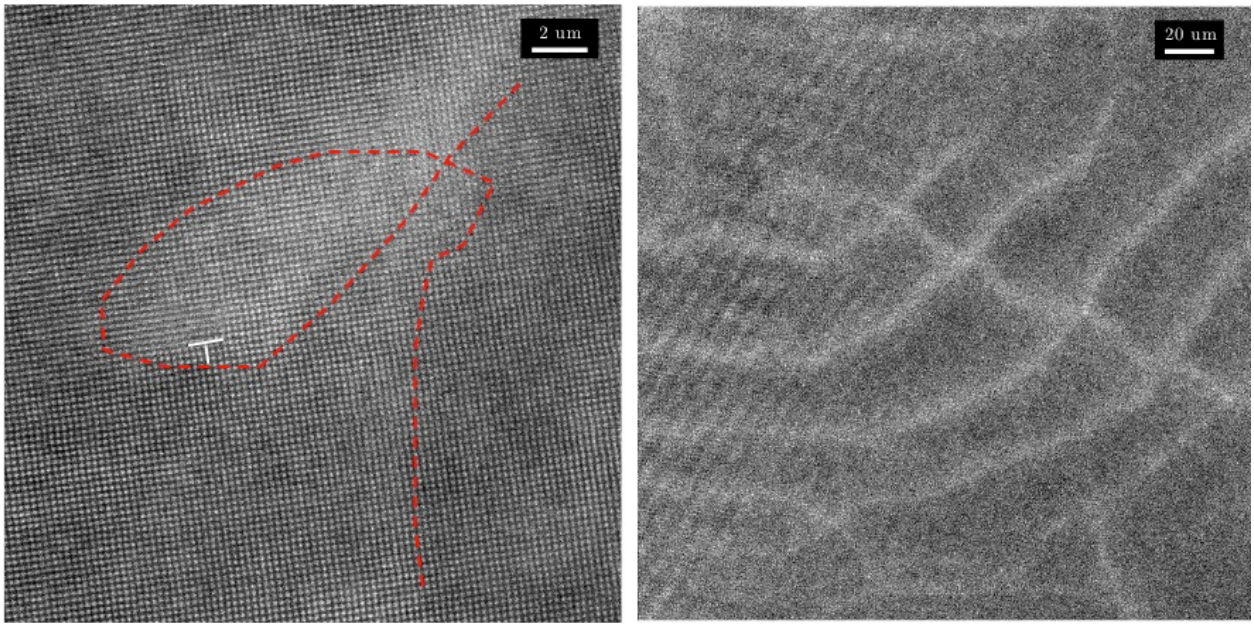

Figure 5.17: (left) we observe dislocation-dislocation interaction, where the projection of dislocation line is shown to be curved around a region containing an extra half plane. (right) Another image demonstrating dislocation bowing due to interaction with a series of dislocations.

white region of the twisted dislocation. In Figure 5.17 (right), we observe curving of a dislocation in a region of "Web" dislocations (as defined in the previous section). These results, along with the observation that the FFT of the regions contain superstructure peaks exhibiting rotation, are consistent with our reasoning that the bowed dislocation in Figure 5.13 is interacting with another dislocation. The pinning dislocation contains a screw component that results in Eshelby twist as the origin of extra atomic columns in the

image. Dipole contrast of the dislocation under ADF conditions further confirms it contains a screw component and is being imaged nearly end-on.

5.3.3.1.1 Summary

Using aberration correction, atomic scale ADF imaging, we have identified the pinning points that cause characteristic dislocation bowing, as observed by Withey et al. [31]. We find discrete examples where the bowing (projected in plane) is caused by dislocations with a line normal to the TEM foil. We find one dislocation with screw component and the other with an apparent extra half plane. We are able to conclude that the pinning point in the first example was a screw dislocation by ruling out typical STEM artifacts and noting the rotation observed with respect to the extra atoms was most likely due to Eshelby twist. The presence of dipole contrast in ADF conditions is a typical contrast motif exhibited by dislocations lines with screw component imaged at a slight tilt with respect to the electron beam.

5.3.4 Continuous Lattice Rotations in STGM: Nanoprobe diffraction and HRSTEM results

To complete our analysis of the deformation features of STGM generated from nanoindentation, we turn to the regions closer to the nanoindent, where higher stresses are endured. We find upon imaging these regions in HRSTEM that the dislocations are too dense to be observed singularly, especially near the tip of the indent as can be observed in Figure 5.12a

Based on the results of Withey et al. [39], there is some previous evidence indicating that STGMs under nanoindentation exhibit a continuous rotation about specific axes within the nanoindentation pit. To explore the nature of these lattice rotations and quantify them, we perform nanoprobe diffraction experiments on specific regions of the nanoindent, which yield strain and in-plane rotation maps for the regions investigated. As a reminder, the diffraction patterns are acquired simultaneously with the HAADF, and we will define **u** as the scanning direction and **v** as the direction the probe moves to start the next row. Thus, for the data presented in Figure 5.18, we use a 50nm step size for both **u** and **v** with 128x128 probe positions. The foil normal is very close to a [001] zone, and we tilt to this zone axis during acquisition of diffraction patterns. We also note that the x and y directions are defined to be in the [1-10] and [110] directions of the reference lattice (consistent with the indexing of the diffraction pattern in Figure 5.4). We observe that only the region adjacent to the indentation site has sustained the most lattice rotation, and these rotations near the indent appear to be divided in to four rotation zones of opposite sense to each adjacent zone. This observation is similar to the results found in EBSD maps of serially-sectioned, conically-indented copper (up to ~1μm depth), where the region directly beneath the indentation area sustains adjacent lobes of rotations and counter-rotations [96]. However, we find no large rotation – free areas directly adjacent to the nanoindent impression, as was found in the previous study. A large rotation, about 20° in-plane, is observed on the left side of the indent between the two left rotation zones. We observe in the strain maps very large tensile elastic strains are sustained within the sample, up to +/- 8% in local regions, with the largest compressive zones occurring directly beneath the indenter tip as expected. We also note that the initial front of the dislocation cell networks formed in the lower part of the indented region have sustained tensile and

compressive strains about the trace of the front. Lastly we note a large change in the sense of shear strain on the left side of the indentation. We also note that as the Berkovich tip is not self-symmetric, the resultant rotations and strain maps are not symmetric.

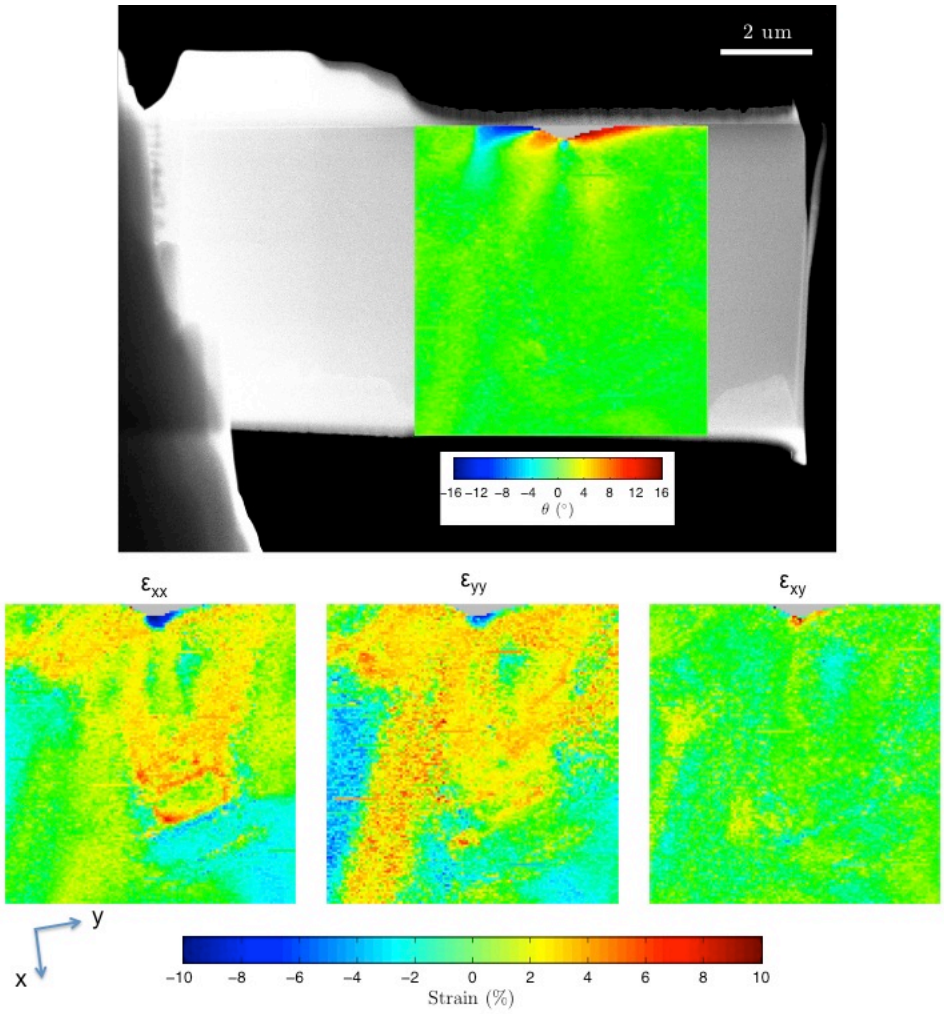

Figure 5.18: Nanoprobe diffraction results are given for overview of indent. Data taken with 128x128 probe positions at a ~50nm step. (top) Rotation map reveals four rotation lobes of opposite sense to the adjacent lobe, where the region nearest to the indent has sustain the largest amount of rotation. (bottom), strain maps show tensile strains of up to +/-8% have been endured in the sample with the largest compressive strains occurring underneath the indentation apex.

As we are interested in the continuous nature of the lattice rotations underneath the indent, we performed further nanoprobe diffraction experiments about the two rotation lobes on the left side of the indent at a higher spatial resolution. This region of interest is outlined in Figure 5.19a, and the rotation map with respect to the location of the indent is provided in Figure 5.19b (note the indent has been rotated in the image, such that the left side of the indent lays horizontally). For this data set we used 32x32 probe positions at a step size of approximately 40nm. In Figure 5.19b, we indeed find a very large rotation of slightly greater than 20° has been sustained adjacent to the indent. We can calculate from this in-plane rotation map the specific components of Nye's dislocation tensor to estimate the

geometrically necessarily dislocation (GND) densities to sustain this rotation. We calculated these components using a MATLAB script based on the derivation by Pantleon (2008) for calculation of Nye's dislocation density tensor from similar rotation data acquired from EBSD data sets [97].

In the calculation, we used a Burgers vector of $2.85*10^{-9}$m ($a_0/2*<111>$). The results are shown in Figure 5.19c, and we find the densities associated with this rotation are on the order of $10^{15}/m^2$ for both α_{xz} and α_{yz}. This calculated density, while large, is not unreasonable for a heavily deformed material, and serves as an indicator that the measured rotation data is reasonable.

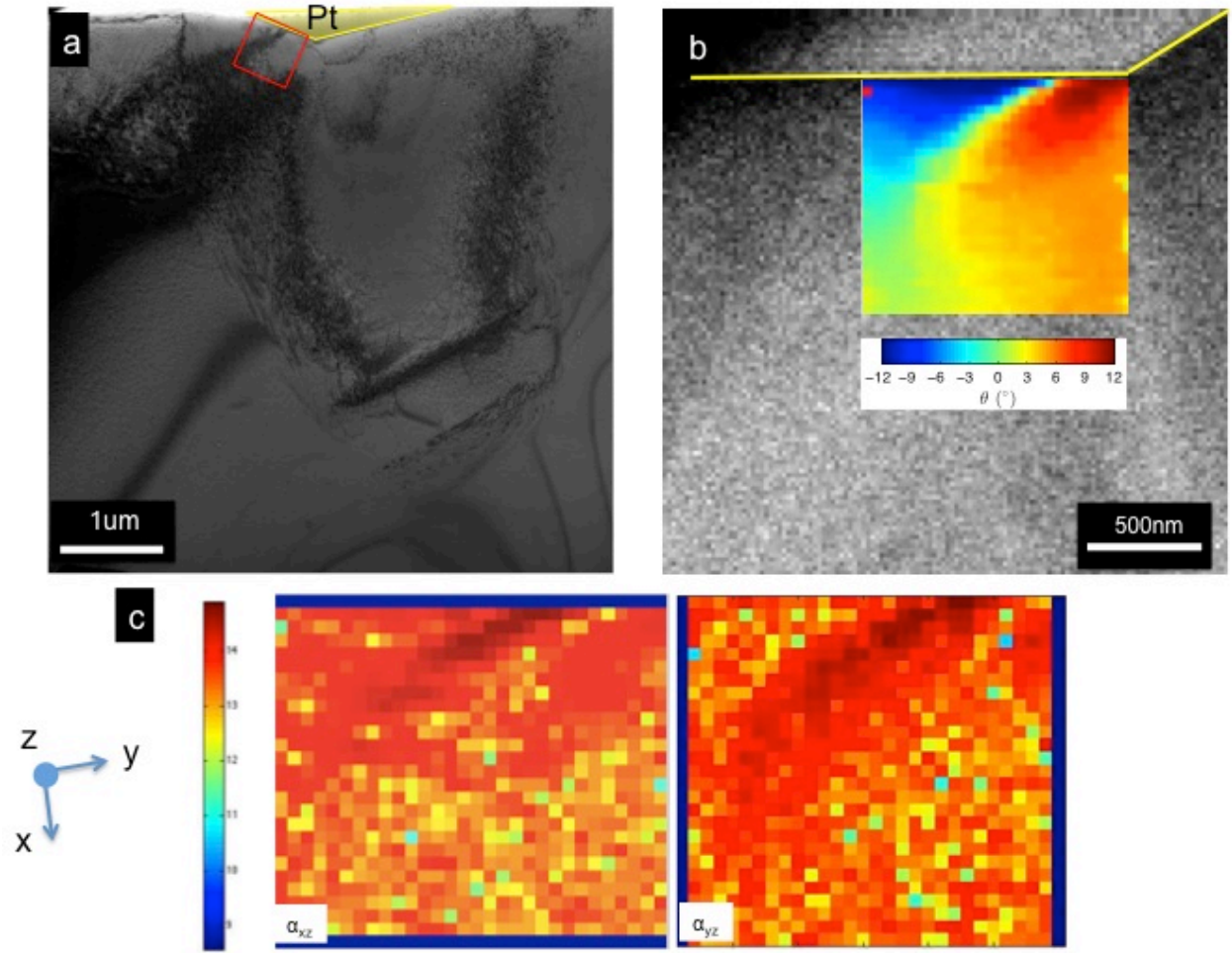

Figure 5.19: Analysis of region adjacent to indentation impression. a) region of interest is outlined in red b) Rotation map of region using 32x32 probe position, 40nm step size, demonstrate continuous nature of lattice rotations, except directly adjacent to the indent boundary, where a small angle grain boundary seems to be have partly formed.

We are able to perform nanoprobe diffraction at even higher spatial resolution due to the small, ~1nm size probe achievable on the TitanX, and investigate the nature of the large rotation gradient on the side of the indent that could possibly be originating from small-angle grain boundary feature that has formed upon nanoindentation. We also want to determine how continuous these lattice rotations are and at what length scale they may become discrete. Figure 5.20a shows the rotation map result from a nanoprobe diffraction

experiment of 6.7nm step size in **u** and a 13.4 nm step size in **v**, with 128x32 probe positions, where u and v are as given in the figure. We find that even at this step size, the lattice rotations are seemingly continuous, except right at the indentation boundary, where, again it seems as if a discrete change in rotation sense is observed. The corresponding strain maps associated with this data set are given in Figure 5.20b, and we observe positive tensile stresses on the order of 2-3% through the region, and overall almost no shear strain endured. It is sensible that there may be tensile strain endured on the side of the

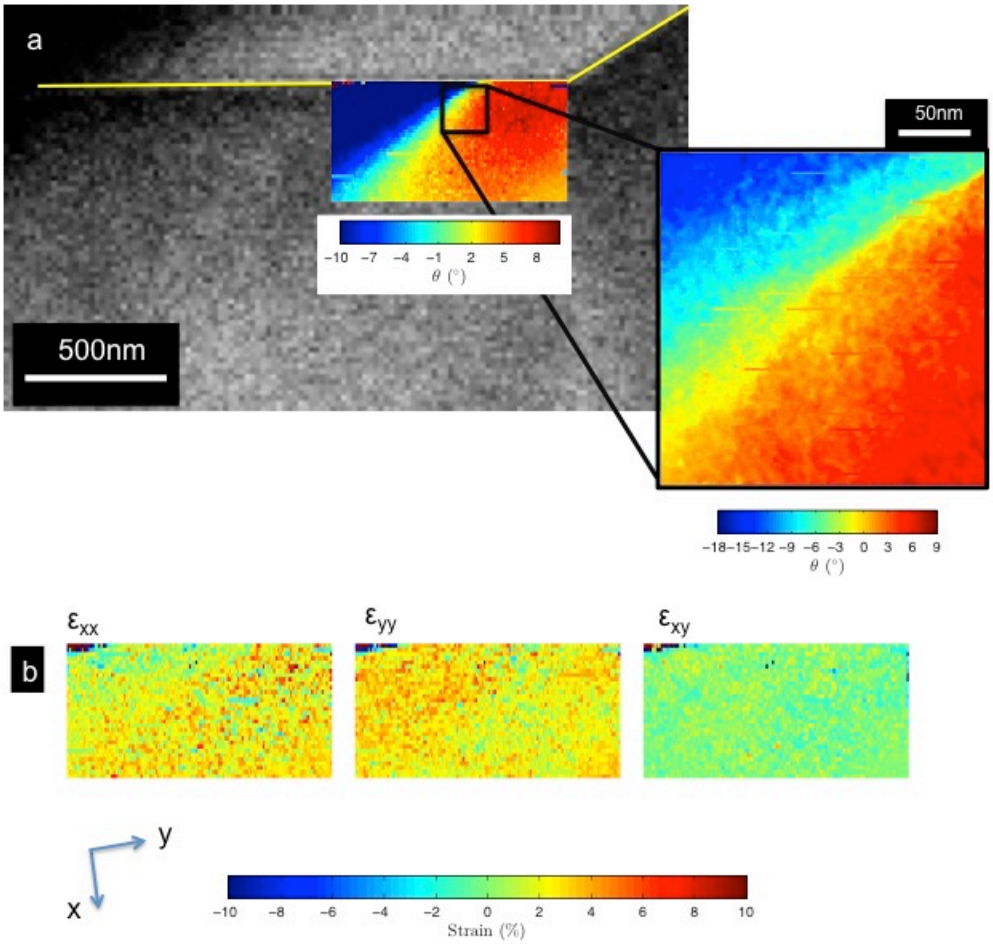

Figure 5.20: a) Another rotation map was acquired at 128x32probe positions at 6.7nmx13.4nm step size to reveal mostly continuous nature of rotations, with a small discrete boundary adjacent to the indent. (Inset) region containing boundary was mapped at 128x128 probe positions, 1.2nm step size, and demonstrates that the boundary becomes diffuse. b) strain maps of the region mapped in a) show tensile strains are present in the region.

indentation: as the material directly beneath the indenter tip is being compressed, material is being "pulled away" from material on the sides of the indent, leading to a tensile state of stress on the side of the indent, presumably. The region containing the discrete boundary was analyzed with 128x128 probe positions at a step size of 1.2nm. Here, we find the interesting observation that the lattice rotation appears discrete at the indenter boundary, jumping from 0° to -6° within a couple of nanometers. However, this discrete boundary

quickly becomes more diffuse away from the indentation boundary, until it is seemingly continuous at the nanometer scale.

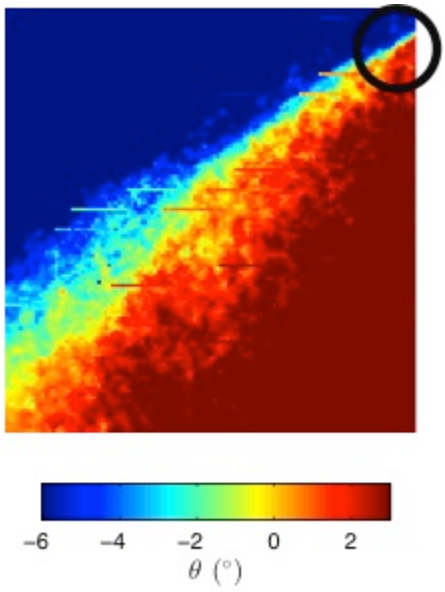

Figure 5.21: Inset rotation map in **Figure 5.20** is re-plotted with a different scale bar to demonstrate discrete nature of the boundary as it emanates from the nanoindentation surface. It appears to contain a jump of ~8°.

To ensure that the boundary adjacent to the indent contains a discrete rotation, we re-plot the inset figure with a different scale, and we find the rotational jump to be 8-9° as shown in Figure 5.21.

To provide an idea of what these lattice rotations may look like in real space, we imaged regions adjacent to the nanoindent in conventional TEM and atomic resolution HRSTEM. Images are provided in Figure 5.22. Figure a shows the respective regions from which the images were taken, and we find in Figure 5.22b that dislocations are indeed present adjacent to the indent and are most likely responsible for the lattice rotations observed. Due to the constantly changing orientation condition within this part of the sample, not all parts of the region have visible dislocations at a given time, but upon tilting the specimen we can observe their presence in all regions adjacent to the indent. We also performed atomic resolution HAADF imaging directly beneath the indentation tip, and find seemingly continuous lattice rotations as well. In Figure 5.22c, we find that the (110) plane traces do not follow the path of the straight red line through the region, but are instead seemingly curved continuously, where the rest of the (110) plane trace follows the blue line. While it may appear that there are no obvious dislocation lines in this region mediating this lattice curvature, we find at least one extra half plane above the region with heavily curved lattice planes. Thus, there is evidence suggesting that typical dislocations may be responsible for the continuous lattice rotations.

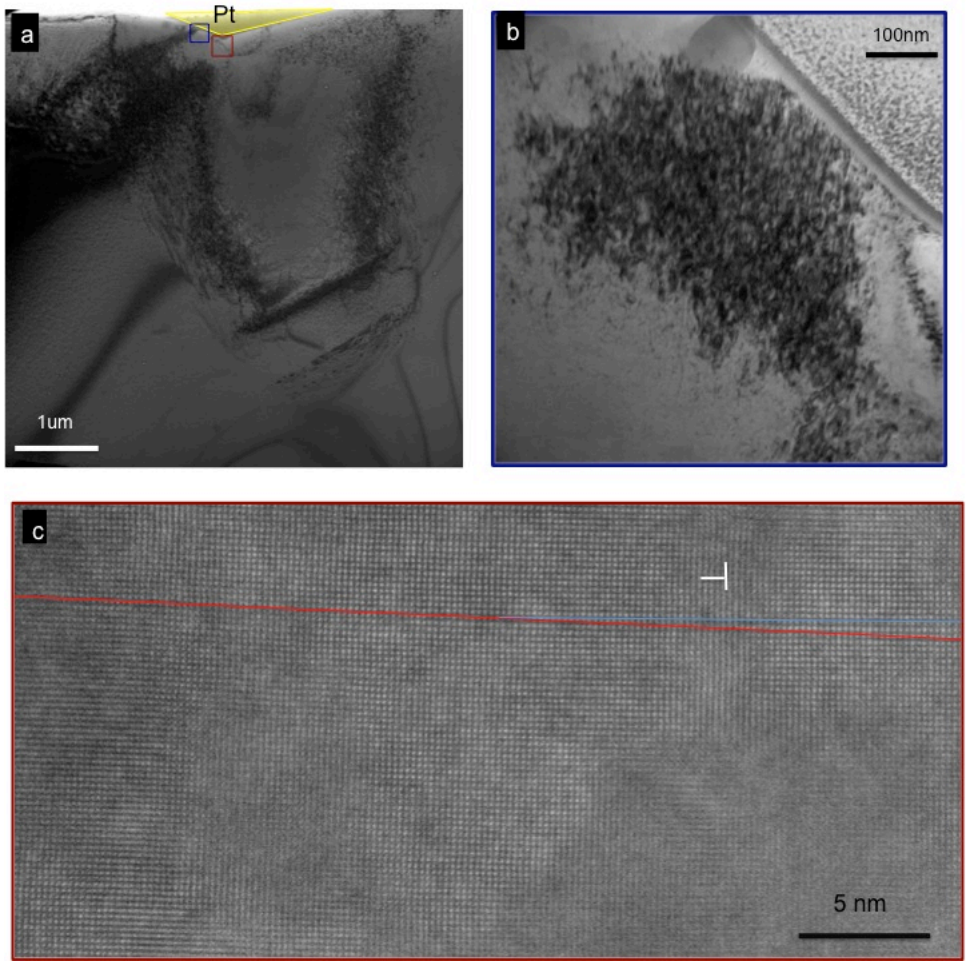

Figure 5.22: Real- space conventional TEM image (b) and HRSTEM image (c) are provided for regions outlined in a) that show the existence of dislocations in regions of large lattice curvature, implying that typical dislocations are at the least partially responsible for the large rotations endured in the material.

5.3.4.1 Discussion

Our original question was whether continuous and large lattice rotations, as previously observed qualitatively in nanoindented STGM [39], could be physically accommodated by a reasonable density of dislocations. The data presented here can very well be explained by conventional slip and crystal plasticity. Similar continuous rotations have been observed and simulated in the literature, and most authors agree lattice reorientations near the indent are due to slip. It is only in the present investigation that, for the first time, we have experimentally probed at the nanoscale to show how fine these lattice rotations really are. Only a few previous studies of a similar nature have been performed regarding quantification of lattice rotations underneath indents. The most notable studies are a survey of deformation mechanisms induced by nanoindentation by Lloyd et al. [98], a study by Zaafarani et al., in which the authors performed EBSD mapping of serially-section nanoindented copper [96], and another EBSD study of nanoindented copper by Rester et al. [99]. In the study by Lloyd et al., many types of materials were investigated, including metallic glass, spinel, silicon and copper. In all but the silicon sample, large crystal rotations were observed accompanied by shear, similar to the results found in this study.

Furthermore, the authors speculated that the crystal rotations observed may be due to an atomic rearrangement similar to martensitic shuffling. In the study by Zaafarani et al., the authors demonstrate through FEM simulations and experimental data that the origin of the lattice rotation/counter-rotation lobes surrounding the indent, as observed in this study, is due to the changing loading axis upon indentation that activates different slip systems. Rester et al. also found characteristic reorientation zones flanking the indent impression, and reasoned that for large indents, pre-existing defects and sources generate the necessary dislocations to accommodate the shape of the indenter, and that dislocation pile-up occurs at locations near zero-shear stress thereby generating small angle grain boundaries.

Thus, many features observed here, including rotational lobes, are consistent with those found in previous studies. It is only in the present study that, for the first time, we are able to truly demonstrate the continuous nature of these rotations at the nanoscale through the powerful technique of nanoprobe diffraction. We do not believe the continuous nature is necessarily unique to that of gum metal, but, perhaps the extent of the in-plane lattice rotation and size and character of the rotational lobes may be. We also are able to directly observe the ubiquitous presence of dislocations that may be mediating these nanoscale rotations, as concluded in [96] and [99], and have furthermore directly imaged via atomic scale ADF imaging, the nature of these interactions.

We also note that in spite of the large plastic deformation sustained by the sample, no secondary phases or twinning structures were found. This is interesting given that secondary phases have been imaged in heavily cold worked gum metals, and in the current study we specifically find evidence of the alpha phase. We reason as to why this might be the case. The Gum Metal alloys are designed to be metastable with respect to the α HCP transformation. It has been observed previously that metastable β-Titanium alloys cold worked at room temperature may exhibit "partial reversion" to the α phase, as the equilibrium state for these alloys is an $\alpha + \beta$ mixture [27 p. 21]. Thus, as the plastic deformation involved in nanoindentation happens for a very short time, this process probably does not provide enough time or locally elevated temperatures to activate the nucleation of α, and as such we do not observe this phase.

5.4 Summary of STGM under nanoindentation results

We have performed extensive characterization of a FIB lift-out cross section of a nanoindented STGM sample using conventional TEM analysis, including "**g.b"** analysis**,** ADF/HAADF STEM, and the powerful nanoprobe diffraction technique. We can conclude the following

- Slip systems observed for the major groups of dislocations are those typically observed ones for bcc, {110}<111> system.
- Where discrete dislocations are observed, we find they strongly interact with other dislocations and pin each other.
- Pinning points of dislocations indirectly observed by Withey et al. [39] are most likely dislocations with line direction normal to the plane to TEM foil.

- Rotational lobes of opposite sense are observed in the immediate vicinity of the indent, consistent with previous studies.
- With nanoprobe diffraction technique, we can directly observe and quantify, for the first time, the truly nanometer scale of the lattice rotations that occur in materials upon indentation.
- Large, ~20-23°, lattice rotations are observed adjacent to the indent, accompanied by dislocations, providing a very strong link between dislocation motion and rotations observed

6 Conclusions

The following conclusions are drawn from the thorough microstructural characterization by conventional TEM imaging and aberration-correction HRSTEM imaging and by investigation of defect structures resulting from nanoindentation of different gum metal alloys.

We find, as expected, that the solution treated Ref-1 compositions contain ω particles, and that the alloys with exact gum metal composition do not due to their increased β-stabilizing content. Indeed, we find no secondary phases in solution treated gum metal, but do find the presence of α particles in gum metals that have undergone swaging. These particles are thought to form during the swaging process due to the slightly elevated temperature that may occur during cold working as the alpha particles do not seem to have a martensitic morphology. These particles could possibly explain the pseudo-elasticity found in gum metals via variant reorientation. Furthermore, they may act as further obstacles to dislocation motion in cold worked gum metals. Dislocations were also observed as dislocation cell network structures within cold worked gum metals, and this high density of dislocations along, submicron grain size, and the presence of nanometer sized coherent α particles may explain why the yield strength in cold worked gum metals increases over the solution treated condition.

We understand the effect of β-stability on the deformation mechanism by performing nanoindentation on niobium-lean alloy, ST Ref-1. We find the defect structures to be {112}<111> type twinning with ω particle nucleation on the twin boundary. {112}<111> type twinning is expected, as the alloy is unstable with respect to the ω transformation. It is this intrinsic lattice instability that is thought to promote twinning. ω nucleation on the twin boundary is activated via applied shear stress and not from spontaneous transformation. It is thought to accompany twinning due to their similar crystallographic characteristics and mechanism of transformation: where the applied shear stress activates twinning, it may then also activate ω formation.

The deformation mechanism of cold worked gum metal, deformation nanotwinning, was surprising. If cold worked gum metal is understood to be a severely plastically deformed metal with a nanocrystalline grain structure, then the deformation nanotwinning observation is consistent with previous studies of nanocrystalline materials. The mechanism could be either via emission of partial dislocations from grain boundaries, or, in the case of large indenter loads, could be explained by an ideal shear mechanism. The results in this study cannot distinguish whether one or the other is occurring, but it is noted the results do not necessarily rule out the possibility that an ideal shear mechanism is operating.

Lastly, we find large, continuous lattice rotations in solution treated gum metals directly beneath the indentation, consistent with previous results of materials deformed via nanoindentation. We also observe rotation/counter-rotational lobes directly underneath

the indent, as consistent with previous studies. It is only through analysis via nanoprobe diffraction technique that we are able to demonstrate for the first time the truly nanoscale nature of the lattice rotations. This is confirmed by HRSTEM imaging of curved lattice planes, and we note the presence of dislocations in these highly rotated regions. Through calculation of the geometrically necessary dislocation (GND) densities from the rotation maps, we find a physically realistic quantity of dislocations can account for the observed rotations. We find no evidence of twinning or stress-induced phases, and believe the operating deformation mechanism is conventional slip.

We observe many examples of dislocations pinning other dislocations further beneath the indent, and determine that the pinning points indirectly observed by Withey et al. [39] are not nanodisturbances, secondary phases, or chemical clustering, but rather other dislocations oriented with the direction line normal to the TEM foil. Thus, the higher yield strength of CWGMs over STGM is most likely due to an increased dislocation density leading to strong dislocation-dislocation interactions, and possibly due to the presence of α particles that may act as dislocation obstacles as well.

References

[1] P. Laheurte, F. Prima, A. Eberhardt, T. Gloriant, M. Wary, E. Patoor, Journal of the Mechanical Behavior of Biomedical Materials **3** (2010).
[2] M. Niinomi, T. Hattori, K. Morikawa, T. Kasuga, A. Suzuki, H. Fukui and S. Niwa, Mater. Trans. 43 (2002) p. 2970.
[3] H. Y. Kim, H. Satoru, J.I. Kim, H. Hosoda and S. Miyazaki, Mater. Trans. 45 (2004) p. 2443.
[4] T. Saito, T. Furuta, J.H. Hwang, S. Kuramoto, K. Nishino, N. Suzuki, R. Chen, A. Yamada, K. Ito, Y. Seno, T. Nonaka, H. Ikehata, N. Nagasako, C. Iwamoto, Y. Ikuhara and T. Sakuma, Science 300 (2003) p.464.
[5] C.R. Krenn, D. Roundy, J.W. Morris Jr., M.L. Cohen, Mater. Sci. Eng. A 319–321 (2001) 111–114.
[6] T. Li, J. W. Morris, Jr., N. Nagasako, S. Kuramoto, D. C. Chrzan, PRL **98** (2007).
[7] H. Ikehata, N. Nagasako, T. Furuta, A. Fukumoto, K. Miwa, T. Saito, PRB **70** (2008).
[8] S. Kuramoto, T. Furuta, J.H. Hwang, K. Nishino, and T. Saito, Met and Mat Trans A **37A** (2006).
[9] M.Y. Gutkin, T. Ishizaki, S. Kuramoto and I.A. Ovid'ko, Acta Mater. 54 (2006) p.2489.
[10] "Titanium and Titanium Alloys: Fundamentals and Applications", Christoph Leyens and Manfred Peters (eds.), Wiley-VCH (2003).
[11] "Phase Transformations: Examples From Titanium and Zirconium Alloys", S. Banerjee and P. Mukhopadhyay, Elsevier Ltd (2007
[12] "Binary Alloy Phase Diagrams: Volume 2", T. D. Massaski, J. L. Murray, L. H. Bennet, H. Baker (eds.), Metals Park, OH: American Society for Metals (1986)
[13] T. W. Duerig, J. Albrecht, D. Richter, P. Fischer. Acta Metall. 30. (1982). p. 2161-2172.
[14] Sikka et al., Progress in Materials Science Vol. 27. (1982) p. 245 - 310.
[15] S. Hanada, O. Izumi, Met. Trans. A. **17A** (1986), p. 1409.
[16] E.W. Collings. The Physical Metallurgy of Titanium Alloys. ASM, Metals Park, OH (1984).
[17] A. M. Minor, S. A. Syed Asif, Z. Shan, E. A. Stach, E. Cyrankowski, T. Wyrobek, and O. L. Warren, Nature Materials, 5, (2006), p. 697-702.
[18] S. Ankem, C.A. Greene, Materials Science and Engineering A **263** (1999) p.127–131.
[19]"Transmission Electron Microscopy: A Textbook for Materials Science", D. B. Williams, C. B. Carter, Springer (2009) p. 311-313.
[20] T. Furuta, S. Kuramoto, C. Rong, J. Hwang K. Nishino, T. Saito, M. Ikeda, J. Japan Inst. Metals, **70** No. 7 (2006) p. 579-585.
[21] "Physical Metallurgy: 3 Volume Set", Eds. D. E. Laughlin and K. Hono, Elsevier (2014) p. 1113.
[22] T. Furuta, S. Kuramoto, J. Hwang, K. Nishino, T. Saito, Mater Trans, **46** No. 12 (2005), p 3001-3007.
[23] W. Guo, J. Sun, X. Li, J. Wu, Trans Nonferrous Met. Soc. China, **17** (2007) p. 55-59.
[24] T. Furuta, S. Kuramoto, J. Hwang, K. Nishino, T. Saito, Mater Trans, **48** No. 5 (2007), p. 1124-1130.

[25] D. L. Moffat and D. C. Larbalesiter, Metall. Trans, 19A (1988).
[26] D. de Fontaine, Met Trans A **19A,** 1988.
[27] "Materials Properties Handbook: Titanium Alloys", Eds. G. Welsch, R. Boyer, E. W. Collings, ASM International (1993) p. 43.
[28] A. Devaraj, S. Nag, R. Srinivasan, R.E.A. Williams, S. Banerjee, R. Banerjee, H.L. Fraser, Acta Mater. 60 (2012) p. 596–609.
[29] "Phase Transformations: Examples From Titanium and Zirconium Alloys", S. Banerjee and P. Mukhopadhyay, Elsevier Ltd (2007) p. 492.
[30] C. W. Dawson and S. L. Sass, Met Trans **1** (1970).
[31] R. J. Talling, R. J. Dashwood, M. Jackson, D. Dye, Acta Mater, **57** (2009) p. 1188-1198.
[32] D. de Fontaine, N. E. Paton, J. C. Williams, Acta Metall. **19**, (1971).
[33] Y. Hanlumyuang, R. P. Sankaran, M. P. Sherburne, J. W. Morris Jr., D. C. Chrzan, PRB, **85** (2012).
[34] "Investigations and Applications of Severe Plastic Deformation", Eds. T. C. Lowe, R. Z. Valiev, Springer Science+Business Media Dordrecht (2000). p. 122-124.
[35] Talling RJ, Jackson M, Dashwood RJ, Dye D. In: Niinomi M, Akiyama S, Hagiwara M, Ikeda M, Maruyama K, editors. Titanium- 2007 science and technology. Sendai: The Japan Institute of Metals; 2007. p. 631.
[36] "Severe Plastic Deformation: Toward Bulk Production of Nanostructured Materials" B. Alta, Nova Science Publishers, Inc. (2006) p. 254-255.
[37] R. J. Talling, R. J. Dashwood, M. Jackson, D. Dye, Scripta Mater, (2008).
[38] X. Wu, M. Zakaria, M. Loretto, Philos. Mag. 84 (2004) p. 3411–3418
[39] E. Withey, M. Jin, A. Minor, S. Kuramoto, D. C. Chrzan, J. W. Morris, Jr., Mat. Sci Eng. A 493 (2008) p.26-32.
[40] P.D. Nellist, M.F. Chisholm, N. Dellby, O.L. Krivanek, M.F. Murfitt, Z.S. Szilagyi, A.R. Lupini, A. Borisevich, W.H. Sides and S.J. Pennycook, Science 305 (5691) (2004) p.1741.
[41] S.J. Pennycook and D.E. Jesson, Phys. Rev. Lett. 64 (8) (1990) p.938.
[42] "Transmission Electron Microscopy and Diffractometry of Materials" Brent Fultz, James M. Howe, Springer-Verlag (2013) p. 568.
[43] E.M. James and N.D. Browning, Ultramicroscopy 78 (1999) p.125.
[44] R. P. Sankaran, C. Ophus, B. Ozdol, V. Radmilovic, A. Minor, J. W. Morris, Jr., Phil. Mag, **94**, Iss. 25 (2014).
[45] C. Sabol, C.J. Marvel, M. Watanabe, T. Pasang, W.Z. Misiolek, Scr. Mater. 92 (2014) 15.
[46] J.M. Bennett, J.S. Barnard, H.J. Stone, P.A. Midgley, D. Rugg, N.G. Jones, Scripta Mat (2015)
[47] E.J. Kirkland. Advanced Computing in Electron Microscopy. New York: Plenum (1998).
[48] J.L. Murray, Phase Diagrams of Binary Titanium Alloys, ASM, Metals Park, OH (1987).
[49] A.T. Balcerzak and S.L. Sass, Metall. Trans. 3 (6) (1972) p.1601.
[50] T. Yano, Y. Murakami, D. Shindo, S. Kuramoto, Acta Mater **57** (2009).
[51] S. Koppoju, M. Ohnuma, Y. Ohba, S. Kuramoto, T. Furuta, Abstract of 147th fall JIM meeting (2010) p. 521.
[52] "Quenching Theory and Technology", Second Edition, Eds. B. Liscic, H. M. Tensi, L.C.F. Canale, G. E. Totten, Taylor & Francis Group (2010) p. 90.

[53] P. Castany, M. Besse, T. Gloriant, Dislocation mobility in gum metal β – titanium alloy studied via *in situ* transmission electron microscopy, *PRB*, **84** (2001)
[54] W. Y. Guo, H Xing, J. Sun, X. L. Li, J. S. Wu, R. Chen, Met and Mat. Trans. A **39A** (2008)
[55] H. Xing, J. Sun, MSF **654-656** (2010) p. 867-870.
[56] H. Xing and J. Sun, APL **93** (2008).
[57] M.J. Lai, C.C. Tasan, J. Zhang, B. Grabowski, L.F. Huang and D. Raabe, Acta Mater **92** (2015).
[58] H. G. Paris, B. G. LeFevre, and E. A. Stark, Jr., Met. Trans. A. 7A (1976) p. 273-278.
[59] F. Sun, J. Y Zhang, M. Marteleur, T. Gloriant, P. Vermaut, D. Laille, P. Castany, C. Curfs, P. J. Jacques, F. Prima, Acta Mater, **61,** (2013) p. 6406-6417
[60] W. Christian and S. Mahajan, Prog. In Mater. Sci **39** (1995).
[61] "Crystallography and Crystal Defects, " A. A. Kelly, K. M. Knowles, John Wiley & Sons (2012) p. 343.
[62] H. Tobe, H. Y. Kim, T. Inamura, H. Hosoda, S. Miyazaki, Acta Mater, 64 (2014) p. 345-355.
[63]Y. Yang, G. P. Li, H. Wang, S. Q. Wu, L. C. Zhang, Y. L Li and K. Yang, Scripta Mat, 66, (2012).
[64] "Springer Handbook of Experimental Solid Mechanics," W. N. Sharpe Editor, Springer US (2008).
[65] W. C. Oliver and G. M. Pharr, J. Mater. Res, **7** No. 6 (1992).
[66] "Nanomechanical Analysis of High Performance Materials," A. Tiwari, Springer Science & Business Media (2013).
[67] Fisher-Cripps, Anthony, *Nanoindentation,* Spring Science: New York (2011).
[68] Z. Ma, S. Long, Y. Pan and Y. Zhou, J. Mater. Sci. Technol., **25** No.1, (2009) p. 90-94.
[69] "Handbook of Nanoscience, Engineering, and Technology," Eds. W. A. Goddard III, D. Brenner, S. E. Lyshevski, G. J. Iafrate, CRC Press (2002). p. **24**-20.
[70] N. Zaafarani, D. Raabe, F. Roters, S. Zaefferer, Acta Mater, 56 (2008) p. 31-42.
[71] A. Shibata, T. Murakami, S. Morita, T. Furuhara, T. Maki, Mat. Trans., **49** No. 6 (2008). p. 1242-1284.
[72] Dislocations in Solids: Vol 12, Eds. H. P Lirth and F. R. N. Nabarro. Elsevier: Amsterdam (2004).
[73] "Turning Points in Solid-state, Materials and Surface State," K. D. M. Harris, P. P. Edwards (2008).
[74] Metal-Ceramic Interfaces: Proceedings of an International Workshop. Eds. M. Rühle, A.G. Evans, J.P. Hirth, Michael F. Ashby, Pergamon Press: Oxford (1989) p. 212-213.
[75] S. Hanada, M. Ozeki, O. Izumi, Met. Trans. A. **16A** (1985).
[76] L. M. Hsiung and D. H. Lassila, Acta Mater **48** (2000).
[77] "Atomic Force Microscopy, Scanning Nearfield Optical Microscopy and Nanoscratching: Application to Rough and Natural Surfaces," G. Kaupp, Springer Science & Business Media (2006), p. 179.
[78] Personal Communication with Hysitron Inc. July 2015.
[79] M. Ikeda, M. Ueda, R. Matsunaga, M. Ogawa, M. Niinomi, Mat. Trans. **50** No. 12 (2009).
[80] B. S. Hickman, J. Mater Sci **4** (1969).

[81] T. Saito, T. Furuta, J.H. Hwang, S. Kuramoto, K. Nishino, N. Suzuki, R. Chen, A. Yamada, K. Ito, Y. Seno, T. Nonaka, H. Ikehata, N. Nagasako, C. Iwamoto, Y. Ikuhara and T. Sakuma, Mater Sci Forums**, 426-424** (2003) p.681-688.
[82] http://www.nanomechanicsinc.com/index.php/Service-Lab/nano-versus-micro-indentation-hardness.html. Accessed July 2015.
[83] "Materials: engineering, science, processing and design," M. F. Ashby, H. Shercliff, D. Cebon, Elsevier Ltd. (2014) p. 153.
[84] M. Y. Gutkin, T. Ishizaki, S. Kuramoto, I. A. Ovid'ko, Int. J. Plasticity (2007).
[85] J.P. Cui, Y.L. Hao, S.J. Li, M.L. Sui, D.X. Li, and R. Yang, PRL **102** (2009).
[86] E.A. Withey, A.M. Minor, D.C. Chrzan, J.W. Morris Jr., S. Kuramoto, Acta Mater. **58** (2010).
[87] H. Xing, J. Sun, Q. Yao, W. Y. Guo, R. Chen, APL **92** (2008).
[88] I. A. Ovid'ko, APL **99** (2011).
[89] X. Y. Zhang, X. L. Wu, A. W. Zhu, APL **94** (2009).
[90] J. Mayer, L. A. Giannuzzi, T. Kamino and J. Michael, MRS Bulletin 32 (2007) p.400.
[91] N.J. Higham, SIAM J. Sci. Stat. Comput., **7**(4), 1986.
[92] "Dislocation Dynamics and Plasticity," T. Suzuki, S. Takeuchi, H. Yoshinaga, Berlin: Springer Verlag (1991), p. 7.
[93] J.D. Eshelby and A.N. Stroh, Phil. Mag. 42, 1401 (1951).
[94] J. G. Lozano, H. Yang, M. P. Guerrero-Lebrero, A. J. D'Alfonso, A. Yasuhara, E. Okunishi, S. Zhang, C. J. Humphreys, L. J. Allen, P. L. Galindo, P. B. Hirsch, and P. D. Nellist, PRL **113** (2014).
[95] V. Grillo, K. Mueller, K. Volz, F. Glas, T. Grieb, A. Rosenauer, Journal of Physics: Conference Series **326** (2011).
[96] N. Zaafarani, D. Raabe, F. Roters, S. Zaefferer, Acta Mater **56** (2008).
[97] W. Pantleon, Scripta Mater. **58** (2008) p.994–997.
[98] S. J. Lloyd, A. Castellero, F. Giuliani, Y. Long, K. K. McLaughlin, J. M. Molina-Aldareguia, N. A. Stelmashenko, L. J. Vandeperre and W. J. Clegg. Proc. R. Soc. A **461** (2005).
[99] M. Rester, C. Motz, R. Pippan, Acta Materialia 55 (2007) p. 6427–6435.
[100] "Tribology of Diamond-like Carbon Films" C. Donnet, A. Erdemir, Springer Science (2008).
[101] M. R. Vanlandingham, J. Res. Natl. Inst. Stand. Technol. **108** (2003) p. 249-265.
[102] M. F. Doerner, W. D Nix, J. Mater. Res., **1**(4) (1986).
[103] G. J. Swadener, J-Y Rho, G. M. Pharr, J. Biomed. Mater. Res, **57**(2001) p. 108-112.
[104] C. A. Schuh, Materials Today, **9**(5) (2006).

Appendix

A Matlab Codes

A.1 Linked Fourier Transform

Gatan Digital Micrograph and MacTempas both have Linked FFT GUIs. However, 1) these remain a black box to the user, as it is unclear as to what processing happens on the initial image before Fourier Transform is applied, 2) Gatan DM, while free, only works on Windows OS, and 3) MacTempas, while it works in Mac environment, is not free. Thus, I felt there was a need to create my own GUI.

```
function [] = LinkedFFT( I)
%LinkedFFT   Draggable box on image giving updated FFT
%           [] = LinkedFFT(I) computes the FFT of image I
%           contained in a ROI box. FFT is presented under I
%           in same image window. The box may be dragged with
%           mouse, and the FFT automatically updates.
%           FFT is smoothed by convolving with Gaussian
%

h = figure(1);
clf
set(gcf, 'outerposition', [800 350 350 800])
initialPosition = [256 256 512 512];
h1 = axes('position', [0 .5 1 .5]); %Image
h2 = axes('position', [0 0 1 .5]); %fourier transform
set(h, 'currentaxes', h1)

Iscale = [.003 .9999];
Iint = sort(I(:));
Imax = Iint(round(length(Iint)*Iscale(2)));
Imin = Iint(round(length(Iint)*Iscale(1))+1);
Is = (I' - Imin)/(Imax-Imin); %Scales image from 0 to 1
Is(Is<0) = 0;
Is(Is>1) = 1;
imagesc(Is);

axis equal off
colormap(gray(256));
hh = imrect(gca, initialPosition);
hh.addNewPositionCallback( @(pos)Callback(pos,h2,Is))
Callback( initialPosition , h2, I)
end

function Callback(position,axesHandle, I)
posi = round(position);
Nxy = [posi(3), posi(4)];
w = hanning(Nxy(1))*hanning(Nxy(2))';

Ifft = abs(fftshift(fft2(I(posi(1):(posi(1)+posi(3)-1), posi(2):(posi(2)+posi(4)-1))
Ifft = Ifft/max(Ifft(:));
sm = fspecial('gaussian', 15, 1.5);
Ifft = conv2(Ifft,sm,'same');


if isempty( get(axesHandle,'Children'))
    imagesc(Ifft,'Parent',axesHandle);
    set(gcf,'CurrentAxes',axesHandle);

    % where axes_handle is the handle to the subplot you want. From:
    caxis([0 0.03]); % set the clim
    axis equal off
else
    imHandle = get(axesHandle,'Children');
    oldSize = size(get(imHandle,'CData'));
```

```
    if ~isequal(oldSize, size(Ifft))
        imagesc(Ifft,'Parent',axesHandle);
        set(gcf,'CurrentAxes', axesHandle);

        % where axes_handle is the handle to the subplot you want. From:
        caxis([0 0.02]); % set the clim
        axis equal off
    else

        set( imHandle,'CData', Ifft);
    end
end
end
```

A.2 Multislice Simulation for embedded precipitates: variable collapse and ordering, uses ProjPot (fparams given in Kirkland (1998))

```
function [emdSTEM] = Ti2NbSTEMROH(numFP)
%Ti2NbSTEMROH Multislice Simulation
%           [emdSTEM] = Ti2NBSTEMROH(numFP) computes a struct emdSTEM for a
%           input number of frozen phonons (numFP).

%           emdSTEM.data is [5-D double] Matrix of Intensities at the given
%           location in parameter space: [xp, yp, fracNb, fracCollapse,
%           collection semiangle] and is computed via
%           multislice method as outlined in Kirkland (1998).
%
%           emdSTEM further includes following fields for record of
%           sumulation parameters
%           emdSTEM.xySize: A/pix
%           emdSTEM.E0:  Microscope Voltage
%           emdSTEM.lambda: Microscope wavelength
%           emdSTEM.s: interaction parameter
%           emdSTEM.fractionNbArray: Niobium amounts simulated
%           emdSTEM.collapseArray:  Different amounts of collapse
%           emdSTEM.numFP: Frozen phonons
%           emdSTEM.dz: slice thickness
%           emdSTEM.xp: number of probes in x
%           emdSTEM.yp: number of probes in y
%           emdSTEM.thickness: thickness;
%           emdSTEM.numUC: Number of unit cells simulated
%           emdSTEM.intData
%
%    Reference: E.J. Kirkland. Advanced Computing in Electron Microscopy.
%               New York: Plenum (1998).
%
%
%

%Simulation Parameters
DW = 1; %0 = no DW, 1 = DebyeWaller factor included
numUC = [3 2]*2;
thickness = [0 90 210]; % in A
potBound = 1.25; %Angstroms: how far out potential is constructed
% It decreases very fast away from nucleus
psize = .05*4; %A/pixel
fractionNbArray = 0:.25:1;
collapseArray = 0:.25:1;
f_plotPot = 0;
f_plotAtoms =0;

%Cell dimenstions

a = 3.29; %Angstroms
cellDim = [sqrt(3) sqrt(6) sqrt(2)]*a; %x y z angstroms
dz = cellDim(3)/2; %Multislice width; matters greatly

% Electron Microscope
E0 = 300e3; %voltage of microscope in V
cS  = 0; %spherical aberration
defocus = 0; %delta f
```

```
alphaMax = 17.2/000; %the setting of the objective aperture constrains...
%                       the convergence angle of the probe

%Calculate relativistic wavelength
m = 9.109383*10^-31;%kg
e = 1.602177*10^-19; %C
c = 299792458; %m/s
h = 6.62607*10^-34; %m^2*kg/s
lambda = h/sqrt(2*m*e*E0)/sqrt(1 + e*E0/2/m/c^2) ...
    * 10^10; % wavelength in A (relativistic)
s = (2*pi/lambda/E0)*(m*c^2+e*E0)/(2*m*c^2+e*E0);
%interaction parameter in rad/(V-A)



%probe positions:
Nprobes = [12 17]*2;
xp = linspace(0, cellDim(1), Nprobes(1)+1); %linspace includes the
%end points, so if 34 probes is desired, the 34th will be redundant to
%0 position because of wraparound, so calculate 35, and cut off the last
%one
xp(end) = [];
yp = linspace(0, cellDim(2), Nprobes(2)+1); yp(end) = [];


% % Testing, single probe
% xp = 0;
% yp = 0;


%%%%%%%%%%%%%%%%%%%%%%%%%%%%%%%%%%%%%%%%%%%%%%%%%%%%%%%%%%%%%%%%%%%%%%%
%SPECIMEN DESCRIPTION
%%%%%%%%%%%%%%%%%%%%%%%%%%%%%%%%%%%%%%%%%%%%%%%%%%%%%%%%%%%%%%%%%%%%%%%
% -111_beta || 001_ Ti2nb, where x = [1 -1 -1]beta, y= [-11-2]
% and z = [110]beta

%1. atomic positions [unit cellshould be rectangular coordinate
% system For ease of FT coordinates
%b - atomic positions in unit cell x,y,z and atomic number

b = [ 0   0   0  41;
    1/2  0   0  41;
    1/6 1/6 1/2 22;
    2/6 2/6  0  22;
    0  1/2 1/2 41;
    1/2 1/2 1/2 41;
    1/6 4/6  0  22;
    2/6 5/6 1/2 22;
    4/6 1/6 1/2 22;
    5/6 2/6  0  22;
    4/6 4/6  0  22;
    5/6 5/6 1/2 22];
%db - collapse magnitude
db = [0   0 0 0;
    0   0 0 0;
    1/12 0 0 0;
```

```
    -1/12 0 0 0;
    0  0 0 0;
    0  0 0 0;
    1/12 0 0 0;
    -1/12 0 0 0;
    1/12 0 0 0;
    -1/12 0 0 0;
    1/12 0 0 0;
    -1/12 0 0 0];

%2. Cell Dimensions


%In Angstroms, specify sample thickness [matrix ppt matrix]

% thickness = [0 30*10 0]; % in A
% Estimates total number of unit cells in z
thickCells = round(thickness/cellDim(3));
thickTotal = sum(thickCells);


[xuc, yuc, zuc] = meshgrid(0:numUC(1)-1, 0:numUC(2)-1,1:thickTotal);
%Alternatively
%[xuc, yuc, zuc] = meshgrid(0:numUC(1)-1, 0:numUC(2)-1,0:thickCells-1);
%then take these coordinates and each row will id the coords
%of the unit cell being referred to(that is each column is
%x, y, z, atom number.  All possible combinations covered
p = [xuc(:) yuc(:) zuc(:) zeros(length(xuc(:)),1)];

%pcollapse is a truthtable
pcollapse = p(:,3) >thickCells(1) & p(:,3) <= sum(thickCells(1:2));
%so determine atom positions corresponding with each unit cell
% per uniquely identified / positioned unit cell
%pa is each unit cell to correspond to atom positions
%ba is each atom position numbered for each unit cell
[pa, ba] = meshgrid(1:size(p,1), 1:size(b,1));
% coordinate system for the whole structure, changes b to greater
%fraction of a unit cell.

%atomsInit= [x y z atomID] in Angstroms for thickness specified
%as number of rows and atoms/UC.

atomsInit = p(pa(:), :) + b(ba(:),:);

%Shift atoms in the sandwich only: gives matrix of atoms shifts
%in the correct unit cells: same size as AtomsInit, later
% coordinates added to atomsInit
atomsShift = db(ba(:),:).*repmat(pcollapse(pa(:)), [1,4]);
%change all Nb in the Matrix to Titanium
atomsInit(~pcollapse(pa(:)),4) = 22;

%make Unit cell fractions into actual angstroms
atomsInit(:,1) = atomsInit(:,1)*cellDim(1);
atomsInit(:,2) = atomsInit(:,2)*cellDim(2);
atomsInit(:,3) = atomsInit(:,3)*cellDim(3);
atomsShift(:,1) = atomsShift(:,1)*cellDim(1);
```

```
atomsShift(:,2) = atomsShift(:,2)*cellDim(2);
atomsShift(:,3) = atomsShift(:,3)*cellDim(3);

%check atoms are/look correct
if f_plotAtoms ==1
    at = unique(atomsInit(:,4));
    at1 = zeros(length(atomsInit), length(at));
    c = zeros(length(atomsInit),3);
    for a1 = 1: length(at)
        at1(:,a1) = atomsInit(:,4)==(at(a1));
        if a1==1
            ind= find(at1(:,a1));
            for a2 = 1: length(ind)
                c(ind(a2), 1:3) = [0 1 0] ;
            end
        end
    end
    figure(1)
    clf
    scatter3(atomsInit(:,1), atomsInit(:,2), atomsInit(:,3),...
        20, c, 'filled')

    set(gca,'position',[0 0 1 1])
else
end

%
% Sampling: Number od angstrom's / pixel. Typically use
% 1A/Pixel to start
% Typical: psize = 0.025; %A/pixel

%Determine Total Pixels for the super cell
Nx = ceil(numUC(1)*cellDim(1)/psize/2)*2;
Ny = ceil(numUC(2)*cellDim(2)/psize/2)*2;

%Recalculate the actual sampling (step size in a/pix*(pix coord) =
%coordinate in Real space (Angstroms).  Previously had determined
%a rough estimate of the A/pix , now recalculate actual step size
xSize = numUC(1)*cellDim(1)/Nx;
ySize = numUC(2)*cellDim(2)/Ny;
xySize = [xSize ySize];


emdSTEM = struct();
emdSTEM.xySize = xySize;
emdSTEM.E0 = E0;
emdSTEM.lambda = lambda;
emdSTEM.s = s;
emdSTEM.fractionNbArray = fractionNbArray;
emdSTEM.collapseArray = collapseArray;
emdSTEM.numFP = numFP;
emdSTEM.dz = dz;
emdSTEM.xp = xp;
emdSTEM.yp = yp;
emdSTEM.thickness = thickness;
emdSTEM.numUC = numUC;
```

```
%Fourier Coordinate System
a1 = Nx*xySize(1);
b1 = Ny*xySize(2);
kx = circshift(((-Nx/2):(Nx/2-1))/a1,[0 -Nx/2]);
ky = circshift(((-Ny/2):(Ny/2-1))/b1,[0 -Ny/2]);
[kya, kxa] = meshgrid(ky,kx);
ksq= kxa.*kxa + kya.*kya;
k1 = sqrt(ksq);

%Propagator and Anti Aliasing the wavefunction to 1/2kmax
%R. Kilaas  and Okeefe (Citation [181] in Kirkland to eliminate
%aliasing
AA = k1;
AA(k1>=(max(kx)/2)) =0;
AA(k1< (max(kx)/2)) =1;

%propagator: equation 6.32 in Kirkland
prop= exp(-1i*pi*lambda*dz*ksq);


%objective aperture to constrain probe
%Chi Probe ~0 equation 2.8 in Kirkland
chiProbe = (2*pi/lambda)*(-1/4*cS*lambda^4*k1.^4-1/2*defocus...
    *lambda^2*k1.^2);
%Objective aperture function equation 3.46 in Kirkland

kMax = alphaMax/lambda;
A = k1;
A(k1>=kMax) = 0;
A(k1<kMax) = 1;

%Construct Detector with respect to milliradians
dalphaDet = 1; %mrad, you could do this other than 1 mrad
alphaDet = k1*lambda*1000;
c = alphaDet< dalphaDet/2;
alphaDet(c) = dalphaDet/2;


detMax = floor(((max(kx)/2*lambda)/dalphaDet)*1000)*dalphaDet;%round(alpha
% max/spacing) *spacing to
if dalphaDet <1
    a1=dalphaDet;
else
    a1=1;
end
rDet = a1:dalphaDet:detMax;
det = zeros(Nx,Ny, length(rDet));
for a0= 1:length(rDet)
    Adet = abs(alphaDet-rDet(a0));
    im= Adet<=(dalphaDet/2);
    det(:,:,a0) =  im.*rDet(a0);
end
```

```
det = sum(det,3);

detmask = det>0;
det= det(detmask);
emdSTEM.rDet = rDet;

%Construct Projected Potential
%1. Integration of atom in pixels (local coordinates of atom
%in doing the integration of potential in x y space for an atom
%in Pixels
xyLeng = ceil(potBound./xySize); %pixels, Number pixels integrated
%RADIUS LENGTH
xvec = -xyLeng(1):xyLeng(1);
yvec = -xyLeng(2):xyLeng(2);
xr = xvec*xySize(1); %(angstroms)
yr = yvec*xySize(2);
potTi = projPot(22,xr,yr);
potNb = projPot(41,xr,yr);%gives potential in Volts/Ang in local coords
%for  x,y array
%in Angstroms

%4. Slice up Sample
%zVals contains z values of all the atoms in the
%the planes of sample, then determines unique values (slices)
%Later on, slice number is determined

zVals = round((atomsInit(:,3)-min(atomsInit(:,3)))/dz +.5);
zPlanes = unique(zVals);

%Debye Waller Coefficients
uTi = 0.08163*DW;
uNb = 0.07636121*DW;


if f_plotPot == 1
    potSum = zeros(Nx,Ny);
end

%Main Loops
emdSTEM.data = zeros(length(xp), length(yp), length(collapseArray),...
    length(fractionNbArray), length(rDet));
emdSTEM.intData = zeros(length(zPlanes),2);
       psi = zeros(Nx, Ny, length(xp), length(yp));
progressbar(0,2);
tic
for a0 = 1:length(collapseArray)
    c = collapseArray(a0);
    atoms = atomsInit +c*atomsShift;

    for a1 = 1: length(fractionNbArray)
        fracNb = fractionNbArray(a1);

        for a2 = 1:numFP

            %initialize probes
```

```
%             psi = zeros(Nx, Ny, length(xp), length(yp));
            for a3 = 1:length(xp)
                for a4 = 1:length(yp)
                    probefft = exp(-1i*chiProbe +2*pi*1i*(kxa*(xp(a3))...
                        +kya*(yp(a4)))).*A;
                    probefft = probefft/sqrt((sum(sum(abs(probefft).^2))));
                    psi(:,:,a3,a4) = probefft;
                end
            end

            for a3 = 1:length(zPlanes)
                aSub = atoms(zVals==zPlanes(a3),:); %submatrix of atoms .
                %on that particular zPlane)

                %Slice Potential
                pot=zeros(Nx,Ny);
                for a4= 1:size(aSub,1)
                    if aSub(a4,4)==22;
                        x = mod(xvec+round((aSub(a4,1)+randn*uTi)...
                            /xySize(1)),Nx)+1;
                        y = mod(yvec+round((aSub(a4,2)+randn*uTi)...
                            /xySize(2)),Ny)+1;
                        pot(x,y) = pot(x,y) + potTi;
                    elseif aSub(a4,4) == 41
                        if rand>fracNb
                            x = mod(xvec+round((aSub(a4,1)+randn*uTi)/...
                                xySize(1)),Nx)+1;
                            y = mod(yvec+round((aSub(a4,2)+randn*uTi)/...
                                xySize(2)),Ny)+1;
                            pot(x,y) = pot(x,y) + potTi;
                        else
                            x = mod(xvec+round((aSub(a4,1)+randn*uNb)/...
                                xySize(1)),Nx)+1;
                            y = mod(yvec+round((aSub(a4,2)+randn*uNb)/...
                                xySize(2)),Ny)+1;
                            pot(x,y) = pot(x,y) + potNb;
                        end
                    end
                end
                %bandwidth limit the slice potential:
                %empty for now because there is controversy on how to make
                %circular bandpass filters in rectangular arrays with
                %rectangular pixels.
                if f_plotPot == 1
                    potSum = potSum + pot;
                end

                trans = exp(1i*s*pot); %transmit term
                for a4 = 1:length(xp)
                    for a5 = 1:length(yp)
                        psi(:,:,a4,a5) = fft2(ifft2(...
                            psi(:,:,a4,a5)).*trans).*prop.*AA;
                    end
                end
                %remember, emdSTEM.intData will be divided by num FP
                emdSTEM.intData(a3,:) = emdSTEM.intData(a3,:)...
```

```
                    + [dz*a3 sum(abs(psi(:)).^2)/(length(xp)*length(yp))];

                comp = (((a3/length(zPlanes)+a2-1)/numFP+a1-1)/...
                    length(fractionNbArray)+a0-1)/length(collapseArray);
                progressbar(comp,2);
            end

            %Integrate results on the detector
            for a3 = 1:length(xp)
                for a4 = 1:length(yp)
                    I = psi(:,:,a3,a4);

                    emdSTEM.data(a3,a4,a0,a1,:) = ...
                        squeeze(emdSTEM.data(a3,a4,a0,a1,:)) ...
                        + accumarray(det, abs(I(detmask)).^2,...
                        [length(rDet) 1]);
                end

            end

        end
    end
end
emdSTEM.data = emdSTEM.data/numFP;
emdSTEM.intData = emdSTEM.intData/numFP/length(collapseArray)/...
    length(fractionNbArray);


if f_plotPot == 1
    figure(2)
    clf
    imagesc(potSum)
    axis equal
    colormap(hot(256))
end
toc

end
```

```
function [pot] = projPot(atomID,xr,yr)
% Projected potential function - potentials from Kirkland (1998).
% projPot Computes projected potential of atom in local coordinates xr, yr
%         Input: atomID is Z number of atomic element
%                xr, yr are local coordinates of atom position
%         Output: pot is potential given in Volts/Ang in local coords
%                  for  x,y array in Angstroms
%         requires fparams from Kirkland (1998) already be loaded.
%
%
%
% Version 02 - separate function
% potMin is now gone, instead set from outside edge

ss = 8;  % Super sampling for potential integration (should be even!!)

% Get fparams file
load('fparams.mat');

% Constants
a0 = 0.5292; %bohr radius
e = 14.4; %electron volt angstroms
term1 = 4*pi^2*a0*e;
term2 = 2*pi^2*a0*e;

% Make supersampled 2D grid for integration
dx = (xr(2) - xr(1));
dy = (yr(2) - yr(1));
sub = (-(ss-1)/ss/2):(1/ss):((ss-1)/ss/2);
[x1,x2] = meshgrid(xr,sub*dx);
xv = x1(:) + x2(:);
[y1,y2] = meshgrid(yr,sub*dy);
yv = y1(:) + y2(:);
[ya,xa] = meshgrid(yv,xv);
r2 = xa.^2 + ya.^2;
r = sqrt(r2);

% Compute potential (D.20)
ap = fparams(atomID,:);
potSS = term1*( ...
    ap(1)*besselk(0,2*pi*sqrt(ap(2))*r) ...
    + ap(3)*besselk(0,2*pi*sqrt(ap(4))*r) ...
    + ap(5)*besselk(0,2*pi*sqrt(ap(6))*r)) ...
    + term2*( ...
    ap(7)/ap(8)*exp(-pi^2/ap(8)*r2) ...
    + ap(9)/ap(10)*exp(-pi^2/ap(10)*r2) ...
    + ap(11)/ap(12)*exp(-pi^2/ap(12)*r2));
% Integrate!
potMid = zeros(length(xr),length(yr)*ss);
for a0 = 1:ss
    potMid = potMid + potSS(a0:ss:(end+a0-ss),:);
end
pot = zeros(length(xr),length(yr));
for a0 = 1:ss
```

```
    pot = pot + potMid(:,a0:ss:(end+a0-ss));
end
pot = pot / ss^2;
% Cut off radius for potential (to remove edge discontinuities)
% pot = pot - potMin;
% pot(pot<0) = 0;
% Compute potMin from edge
[~,xInd] = min(abs(xr));
[~,yInd] = min(abs(yr));
dx = round(sqrt(2*xInd-1));
dy = round(sqrt(2*yInd-1));
xv = [xInd-dx xInd+dx xInd-dx xInd+dx 1 1 length(xr) length(xr)];
yv = [1 1 length(yr) length(yr) yInd-dy yInd+dy yInd-dy yInd+dy];
potMin = max(pot(sub2ind(size(pot),xv,yv)));
pot = pot - potMin;
pot(pot<0) = 0;

end
```

B Kinematical Diffraction Pattern Simulations

Using Crystal Maker Software Suite, kinematical diffraction patterns are synthesized easily using the Single Crystal package.

B.1 Omega variants: [110]β and [-120]β DP simulations

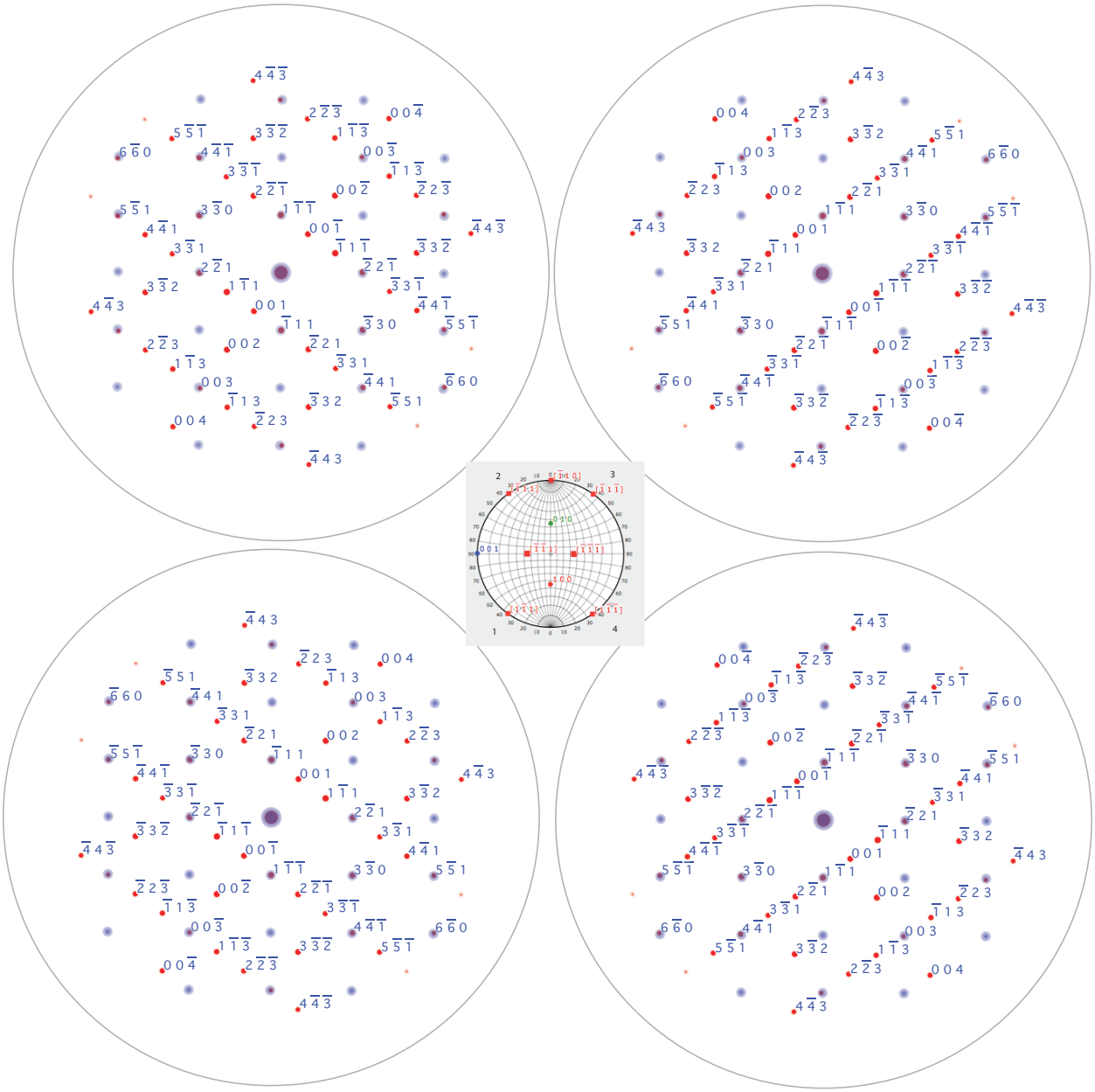

Orientation relationship between β and ω is given by $\{111\}_\beta \,||\, (0001)_\omega$; $\langle 10\text{-}1\rangle_\beta \,||\, \langle 11\text{-}20\rangle_\omega$. Since there are a total of four $\{111\}_\beta$ – type planes, there are four possible ω variants. $[11\text{-}20]_\omega$ Diffraction pattern of each variant overlaid with the matrix BCC is given in the following figure, with the stereographic projection of the $[10\text{-}1]_\beta$ given in the middle. Each $\langle 111\rangle_\beta$ – type direction in the stereographic projection is identical to the position of the

(0001) $_{\omega}$ pole for each variant. The figure clearly shows only two identical diffraction

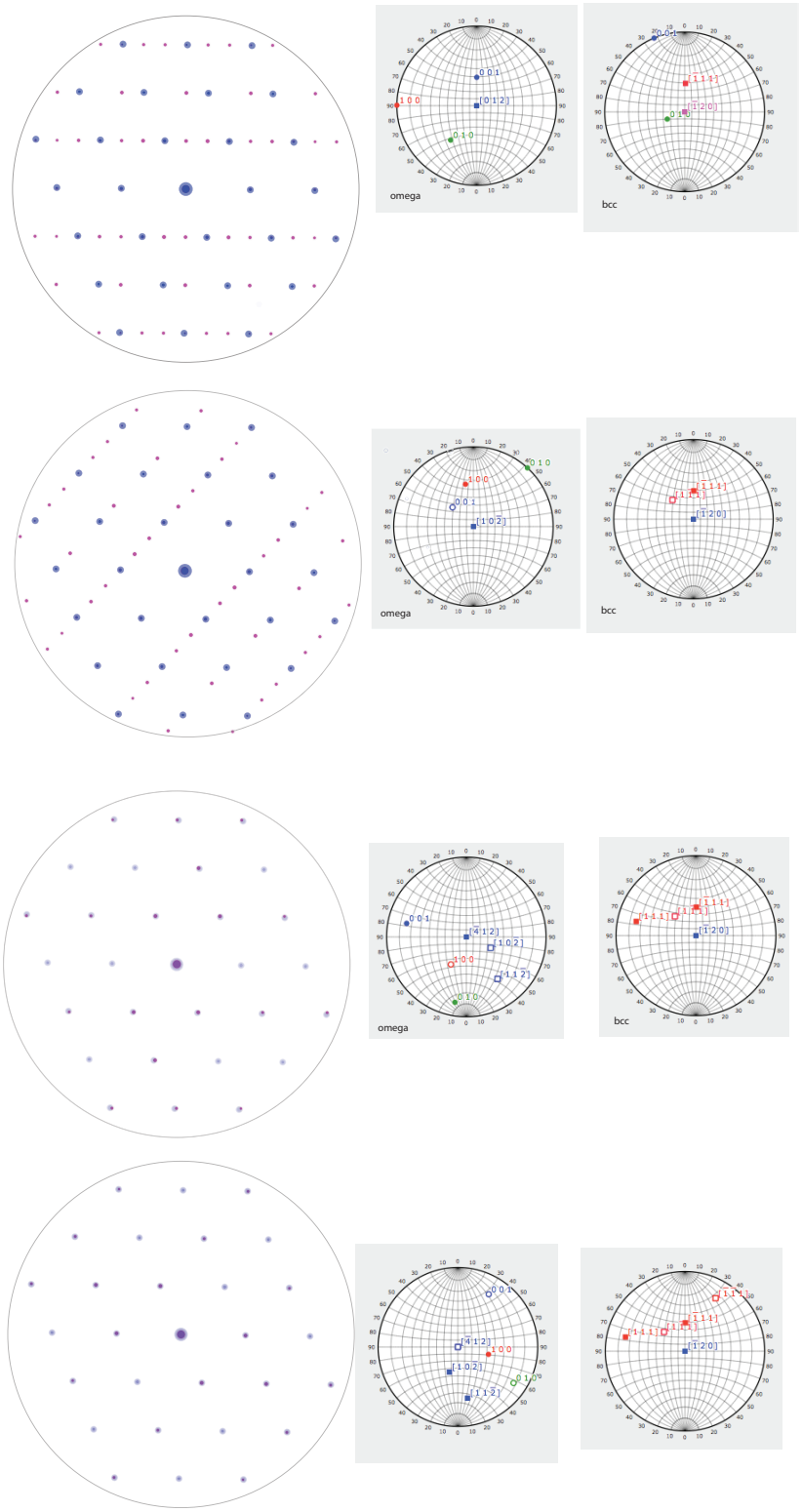

Figure B.1: [210]β diffraction pattern with simulations for all four variants and their respective orientation relationship with the beta phase seen in the adjacent stereographic projections. Total DP given in Figure 2.6

patterns: thus only 2 variants are degenerate in the [110]$_\beta$ –type ZA. Total Diffraction Pattern for [110]β is given in Chapter 2: Figure 2.5. Note that Crystal Maker uses 3 index hexagonal notation.

C Results – Other

Many TEM images were taken of the gum metal samples in completion of this work, but not all were appropriate to put into the dissertation body. Presented here are some extra images of the samples that may serve to give a more complete description of gum metal samples performed in this study. Samples are prepared in a similar manner as described in main chapters, unless otherwise specified.

C.1 As received ST-Ref1, JEOL 2011 (UC BERKELEY, Dept. of MSE)

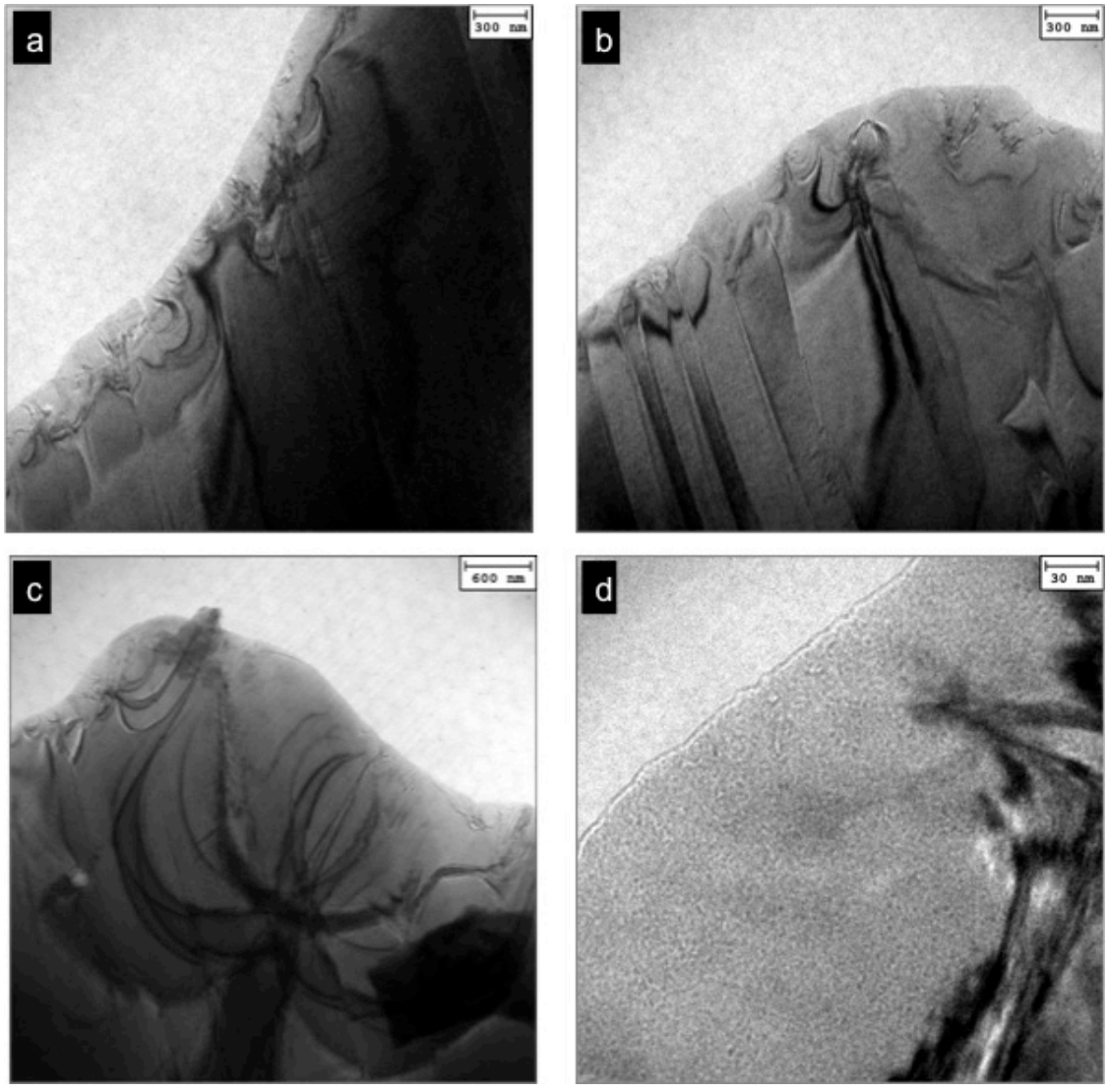

Figure C.1: Extra Bright Field TEM images of as received ST-Ref1, jet polished. a) an b) show streaking most likely caused by twinning due to jet polishing. Typically line defects emanating from the coastline, are dislocations pinned by surface oxide that try to glide out of the materials upon electrolytic thinning, however, the bend contours within some regions do not appear to be continuous, leading us to believe they are twins. c) Some regions exhibit only very thin twin regions and show large bend contours from bending of the thin sample. d) Jet polishing can produce amorphous regions near the coastline. Note ω particles not immediately visible without dark field imaging. Images taken on JEOL 2011 at UC Berkeley

C.2 As received ST-GM, JEOL 2011 (UC BERKELEY, Dept. of MSE)

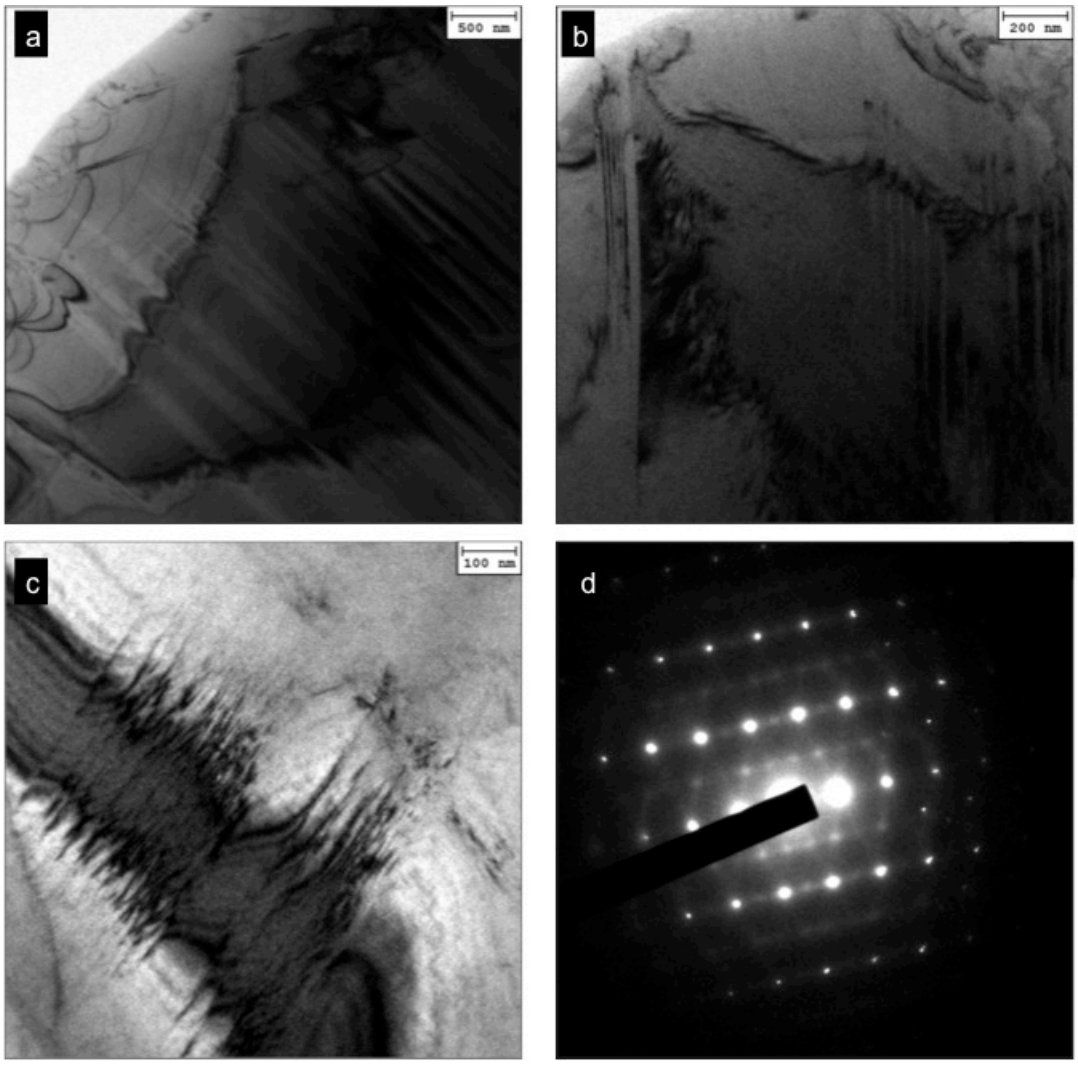

Figure C.1: a), b), c) conventional BF images. a) and b) twinning artifact/dislocations pinned by oxide still present after jet polishing. Later samples contained minimal twinning after increasing amount of perchloric acid in etchant (current images were etched with 2.74% perchloric in butanol/methanol solvent) c) line defect that is not straight enough to be stacking fault or dislocation. d) DP taken from {113}β zone axis of ST GM reveals further reciprocal lattice streaking, consistent with the conclusion there are no secondary phases in the material. Where the intensity increases in localized areas is thought to happen from overlap of reciprocal lattice streaks

D Nanoindentation overview

Similar to macro-indentation and micro-indentation testing, nano-indentation testing involves applying a force with a material of known mechanical properties to the surface of a material with unknown properties. The main experimental parameters that set nanoindentation apart from other indentation tests are the length scale and applied load: the displacement of the loaded material is on the order of nanometers, and typically the applied force is on the order of millinewtons. Furthermore, in contrast to conventional hardness tests in which only the peak applied force is known, the force and displacement during indentation can be specified and recorded through the full unloading/loading cycle. Thus nanoindentation is frequently referred to as "instrumented indentation" or "depth sensing indentation".

Traditionally, indentation testing is used for determining hardness, the resistance of a material to permanent deformation. Hardness itself is not a fundamental materials property, but does give an idea of a material's relative mechanical properties, notably yield strength [100]. Indentation hardness is typically defined as $H = P/A$, where P is the applied load and A is the plastically deformed projected area.[3] In nanoindentation, knowledge of load-displacement history (penetration depth) and indenter geometry allows for indirect measurement of contact areas on the order of nanometers, as visual determination of lengths smaller than a micron is infeasible. Contact areas in traditional indentation tests are typically on the order of millimeters and thus measured visually [67, 101]. Knowledge of the load-displacement history also allows for measurement of elastic properties, which cannot be deduced from conventional, non-instrumented indentation methods. Nanoindentation is widely used to find hardness values and elastic moduli due to ease of sample preparation and relatively non-destructive nature compared to traditional hardness measurements and tensile testing.

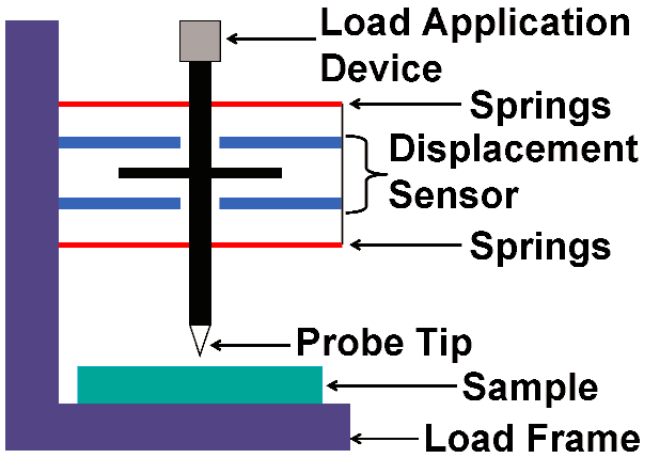

Figure D.1: Setup for Instrumented Indentation allowing for recording of depth and force (taken from [101])

[3] This hardness value calculated with projected area is also known as "Meyer Hardness". Brinell Hardness Numbers are based upon the actual area of the residual impression.

Finding hardness and modulus from Loading/Unloading cycle

Force is typically applied electrostatically via a transducer that converts the voltage to a known force. The transducer is shown schematically as the "load application device" in Figure D.1. The displacement is then measured through the motion of capacitive plates. The raw force/displacement data is typically coupled by springs as seen in Figure D.1 [1].

During an indentation loading/unloading cycle, force is applied to the column that has a probe, typically a diamond tip of known geometry, attached to the end. The probe tip approaches the surface of the sample, makes contact, compresses the sample and finally retracts from the sample through load reversal [100]. Initial contact with the specimen is elastic in nature and the following compression at larger loads involves plastic flow of material. If yield has occurred, the unloading portion of load-displacement curve will not follow the loading portion resulting in hysteresis as shown in Figure D.2(right). Elastic recovery of the material will initiate immediately as unloading begins. Upon complete unloading, if yield has occurred, a residual impression of the probe will be left in the sample [67]. The maximum depth of penetration, h_{max}, the maximum load, P_{max}, and the slope of the unloading curve at maximum load, S=dP/dh[4], are the raw values used to calculate hardness and elastic modulus values. These values are labeled on the P-h curve in Figure D.2(right).

For most indenter tips, the contact depth of penetration, shown as h_c in Figure 2(a), can be estimated from h_{max} with the following relation: $h_c = h_{\max} - .75(P_{\max}/S)$[5] [65]. In nano-indentation, the projected deformed area, A_p, which is needed for the estimation of H and E, is determined indirectly from knowledge of the contact depth, h_c. Knowing the geometry of the indenter, one can relate the contact depth of penetration to the projected area of deformation by calibrating a tip area function $A_p(h_c)$ obtained by indenting a material with known elastic properties to different depths. From the P-h curve we can easily obtain h_{max} and P_{max} and thus calculate the projected deformed area, A_p, of the indent [102]

Hardness is simply calculated through the indenter hardness relation, $H = P_{\max}/A_P(h_c)$.

From elasticity theory, we know that for a rigid indenter in contact with an elastic half-space (Sneddon, 1965)

$$E_r = \frac{dP}{dh}\frac{\sqrt{\pi}}{\sqrt{A_P(h_c)}}\frac{1}{2},$$

[4] The contact stiffness, 'S', is calculated by assuming the unloading curve has a power law form: $P = \alpha(h - h_f)^m$ (Oliver & Pharr, 1992)

[5] This equation form is derived from elasticity modeling of rigid punches indenting elastic half-spaces. The coefficient of 0.75 is based on the geometry on the indenter and generally applies to commonly used shapes. (Oliver & Pharr, 1992)

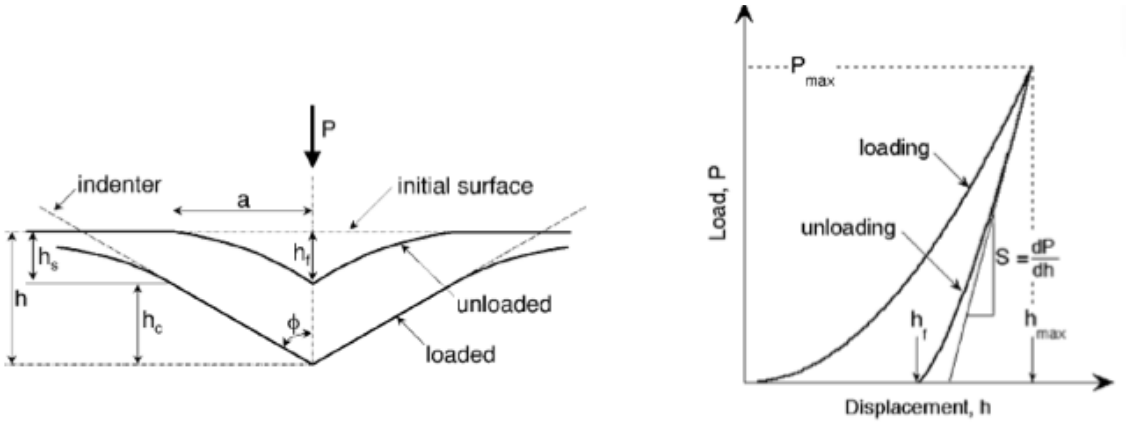

Figure D.2: Cross section of indentation experiment (a) and typical resultant loading/unloading , or P-h, curve (b) [65]

where E_r is the reduced modulus and dP/dh is the contact stiffness 'S' determined from the load-displacement data in Figure D.2. From the reduced modulus we can calculate the elastic modulus of the material using an equation derived from contact mechanics: $E_r = (1-\upsilon_i^2)/E_i + (1-\upsilon_s^2)/E_s$, where 's' denotes substrate parameters (unknown) and the subscript 'i' denotes the indenter. From these two equations, E_s may be determined. While Figure D.2(left) seems to indicate a complex multiaxial stress state, it turns out that the modulus measured, while averaged over all directions, is heavily weighted in the direction of nanoindentation [103].

For evaluating the elastic modulus, this analysis assumes that unloading is purely elastic (Hertzian) and that no pile up of material occurs on the side of the indenter - that is, no material undergoes a rigid displacement and rather is homogenously deformed. Furthermore, dP/dh from the load-displacement curve includes the stiffness of the load frame. Thus, care should be taken when comparing these values to those generated by other mechanical testing methods.

Nanoindentation has found wide popularity for:

- studying the mechanical properties of microstructural or local features in a material
- ability to test a wide range of materials and geometries – easy sample preparation
- thin films
- nondestructive testing
- exploring deformation mechanisms at the smallest scales: e.g. dislocation nucleation
- ability to gather a wide range of mechanical properties: strain hardening exponent, fracture toughness, viscoelastic properties

Understanding the elastic-plastic transition

While the majority of nanoindentation experiments are used to determine hardness and elastic modulus values, its next most popular use in fundamental materials science research is in determining the nature of the elastic to plastic deformation response, also termed "incipient plasticity." It turns out that local features of the P-h curve can correspond to "discrete" deformation events occurring under the indenter tip. Using the

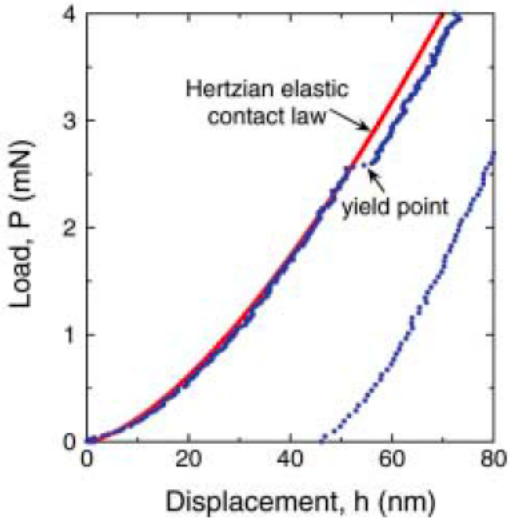

Figure D.4: Deviation from elastic contact is indication of a plastic event. Taken from [104].

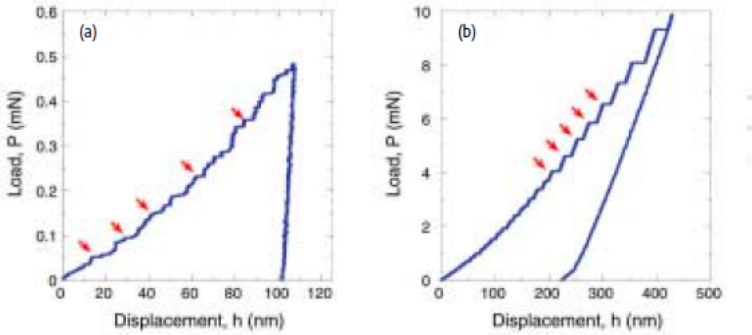

Figure D.3: Discontinuities in P-h curve are indicated by red arrows and indicate plastic activity. Single crystal platinum (a) demonstrates further dislocation activity beyond initial yielding. Pd-based metallic glass shows evidence of shear banding indicated by serrated curve(b). Taken from [104].

theory of Hertzian contacts, the loading curve should follow a power law form. Any deviation from this relation is indicative of a local plastic event as indicated in Figure D.4. The deviation from an elastic contact is termed a "pop-in" event. During a load-controlled test, these pop-ins occur when the displacement increases without an increase in load. Dislocation multiplication is presumed to be the source of initial pop-in events.

Further pop-in events may indicate a particular plastic deformation mechanism at work. In Figure D.3(left) dislocation activity is observed in single crystal platinum subsequent to initial yielding. Figure D.3(right) contains a characteristic serrated curve indicative of

shear band formation in bulk metallic glass. The precise deformation mechanism responsible for pop-in events, however, is difficult to determine using P-h curves alone. To gain a full physical understanding of incipient plastic behavior, *in-situ* TEM and SEM indentation techniques are currently being researched [104].